Doctoral Thesis

To obtain the Title of: Ph.D. and D.Sc.

Specialty: Life and Health Sciences

Delivered by: CY Cergy Paris Université and Tampere University

Prepared within

Doctoral School n°417 Sciences and Engineering and the Equipe de Recherche sur les Relations Matrice Extracellulaire – Cellule (ERRMECe) Laboratory

And

Tampere University Doctoral School at Faculty of Medicine and Health Technology - Doctoral Programme in Medicine, Biosciences and Biomedical Engineering

Development of organic-inorganic innovative scaffolds for bone tissue engineering based on polymer honeycomb membrane and bioactive glass-based mineral phase

By Audrey DERAINE COQUEN

Directed by Pr Emmanuel PAUTHE and Pr Jonathan MASSERA

Presented to a jury composed of

Pr. Cédric BOISSIERE	Sorbonne Université, France	Reviewer
Pr. Pekka VALLITTU	University of Turku, Finland	Reviewer
Pr. Didier LUTOMSKI	Sorbonne Université, France	Examiner
Dr. Valérie BENSOUSSAN-COHEN	Chirurgien-dentiste, France	Examiner
Pr. Emmanuel PAUTHE	CY Cergy Paris Université, France	Supervisor
Pr. Jonathan MASSERA	Tampere University, Finland	Supervisor
Pr. Minna KELLOMÄKI	Tampere University, Finland	Co-supervisor
Dr. Michel BOISSIERE	CY Cergy Paris Université, France	Co-supervisor

Abstract

When a significant bone defect develops as a result of trauma, bone resection owing to malignancy or infection, or both, bone needs aid from a substitute to regenerate while preventing the invasion of fibrous tissue into the defect. To prevent the implant site invasion by fibrous tissue, barrier membranes have been fabricated from naturally sourced or synthetic polymers. One characteristic of major importance, to consider in the fabrication of a barrier membrane, is its porosity. The pores in the membrane should allow appropriate nutrient and waste flow while preventing the cells from entering the defect. However, the currently available membranes degrades faster than the bone regeneration occurs. To overcome this challenge, focused has been made on materials able to accelerate bone regeneration in order to close the gap between the membrane degradation and the bone regeneration rate. For this purpose, one strategy is to use bone graft in combination with a barrier membrane, although it implies a two-step procedure with two distinct materials which can be challenging for surgeons. As bone graft, bioactive glasses (BG) have made a breakthrough the past decade since they are able to degrade, bond to bone, and induce osteogenesis. Materials for bone graft should have suitable porosity to allow the neo formed bone to colonize the structure and eventually replace it. Processing BG into 3D porous scaffolds has revealed to be challenging but not impossible.

This thesis project has been designed with the aim to propose a new biphasic material that would avoid the fibrous tissue in-growth and the two-steps surgical procedure by directly linking the graft and the barrier membrane.1) The membrane, made of poly-L-co-D, L-lactic acid (PLDLA), was created at the surface of the materials by the Breath Figure Method (BFM) to give it a honeycomb-like porous structure, in order to prevent cell migration while maintaining nutrients migration and waste removal. 2) The membrane was generated on chosen BG, namely the S53P4, also known as BoneAlive® S53P4, and the 13-93B20, an experimental BG composition containing boron (B), or a decellularized bone matrix (DBM) to support bone regeneration.

The impact of BG surface chemistry on membrane adhesion has been studied and revealed that, the conditioning of the BGs induces calcium phosphate (CaP) precipitation at their surface which results in a stronger attachment of the membrane.

Successively, our assemblies were sterilized through gamma irradiation and, although irradiation induced some changes in physicochemical properties of both the polymer and BG, cell-material interactions were found unaffected.

Finally, a 3D printed 13-93B20 scaffold was specifically designed to generate the honeycomb PLDLA membrane at its surface. After immersion in simulated body fluid (SBF), the assemblies were found to be able to precipitate hydroxyapatite (HA). When put in contact with osteoblast-like cell, the assemblies were found to support cell adhesion and growth while providing an effective way of segregating osteoblasts-like cells and fibroblasts thanks to the honeycomb membrane.

In summary, a new biphasic scaffold based on an inorganic and an organic phase directly linked together was successfully developed. The material showed a great cohesiveness during the immersion and revealed itself to be able to support hydroxyapatite precipitation. Furthermore, it showed great capacity to support cell adhesion, growth and proliferation while providing an effective space delimitation for osteogenic and fibroblastic cells.

This scaffold paves the way toward new devices allowing space separation and cells segregation in order to improve bone regeneration while avoiding the deleterious fibrous tissue ingrowth.

Résumé

Lorsqu'une perte osseuse significative survient suite à un traumatisme, à une résection osseuse liée à une malignité ou à une infection, un apport extérieur est nécessaire pour favoriser la régénération osseuse tout en évitant l'invasion de tissu fibreux dans la zone affectée. Pour prévenir cette invasion, on utilise des membranes « barrière » composées de polymères, naturels ou synthétiques. Un aspect crucial dans la fabrication de ces membranes est leur porosité. Les pores de la membrane doivent permettre la circulation adéquate des nutriments tout en empêchant les cellules d'envahir la zone.

Cependant, les membranes actuellement disponibles se dégradent plus rapidement que la régénération osseuse n'a lieu. Pour surmonter ce défi, les chercheurs se sont penchés sur des matériaux capables d'accélérer la régénération osseuse afin de réduire l'écart entre la dégradation de la membrane et le taux de régénération osseuse. Une stratégie consiste à utiliser une greffe osseuse en combinaison avec une membrane « barrière », bien que cette approche implique une procédure en deux étapes et des matériaux distincts.

Les verres bioactifs (BG) se sont avérés prometteurs en tant que matériaux de greffe osseuse, car ils sont capables de se dégrader, de se lier à l'os et d'induire l'ostéogenèse. Cependant, la transformation des BG en structures poreuses en 3D s'est avérée être un défi. Ce projet de thèse vise à proposer un nouveau matériau biphasé qui limite l'invasion de tissu fibreux et la procédure en deux étapes en liant directement le greffon et la membrane « barrière ».

La membrane, composée d'acide poly-L-co-D, L-lactique (PLDLA), est générée en surface des matériaux grâce à la méthode Breath Figure (BFM), créant une structure poreuse en nid d'abeille pour empêcher la migration cellulaire tout en permettant la circulation des nutriments. Cette membrane est déposée sur des BG spécifiques, tels que le S53P4 (connu sous le nom de BoneAlive® S53P4) et le 13-93B20, une composition expérimentale de BG contenant du bore, ainsi que sur une matrice osseuse décellularisée (DBM) pour favoriser la régénération osseuse.

L'impact de la chimie de surface des BG sur l'adhérence de la membrane a été étudié, montrant une meilleure adhérence après une étape de conditionnement grâce notamment à la topographie de surface qui montre la présence de précipité de calcium-phosphate (CaP). Les assemblages ont été stérilisés par irradiation gamma, sans altérer les interactions cellules-matériaux.

Enfin, une structure (scaffold) 3D imprimée en 13-93B20 a été spécifiquement conçu pour supporter la génération de la membrane en nid d'abeille en PLDLA à sa surface. Après immersion dans un milieu simulé fluide biologique, les biomatériaux font l'objet d'une précipitation d'hydroxyapatite en surface. Ce qui n'a pas inhibé l'adhérence, la croissance et la prolifération des cellules ostéoprogénitrices, tout en limitant physiquement la migration des cellules (effet barrière).

En somme, ce nouveau matériau biphasé offre une approche prometteuse pour améliorer la régénération osseuse tout en prévenant l'invasion de tissu fibreux nocif.

Acknowledgments

Words cannot express my gratitude to all my supervisors, **Pr. Emmanuel Pauthe**, **Pr. Jonathan Massera**, **Pr. Minna Kellomäki** and **Dr. Michel Boissière**. Your invaluable patience, feedback and encouragement through-out the journey of my PhD are the reason why we are here today. Your support meant everything to me, and I cannot thank you enough for that. I thank you all for the trust you put in me to conduct this PhD project and for the opportunity to work under your supervision. I also wish to extend my gratitude to **Pr. Cédric Boissière** for his suggestions and guidance during my follow-up group meetings.

I would like to express my gratitude to the examiners and reviewers **Dr Bensoussan-Cohen, Pr. Cédric Boissière**, **Pr. Pekka Vallitu** and **Pr. Didier Lutomski** for their efforts in reviewing the work of this thesis.

I would like to extend my gratitude to **Dr. Maria Teresa Rebelo Calejo**, you were the first to introduce me to the honeycomb films and the first brick in this incredible adventure I lived the past 4 years. Your kindness, understanding and encouragements were a blessing for the young master and doctoral student I was then.

I would like to express my deepest gratitude to my co-authors, **Pr. Laeticia Petit** who gave me the opportunity to work under her supervision and gave me invaluable advice and support, **Dr. Bartosz Bondzior** for the time spent on the photoluminescence measurements, **Dr. Credson Langueh** as co-author and friend for his help on the experiments for my last publication and for all the fun times spent in the office and **Dr. Rosa Calendro-jacinto** as co-author and friend for her invaluable help in the cell experiments and the great times spent together in the office.

I am extremely grateful to **Heikki Liejumäki**, **Suvi Heinämäki** and **Pasi Kauppinen** for all the help they provided me in the lab during my numerous stays in Tampere, and to **Remy Agniel** and **Lamia El-guermah** for their help and guidance during my work at ERRMECe. A special thanks to **Remy** for the many and long hours spent imaging my samples with the SEM and the confocal microscopes. Thank

you for explaining to me the principles of this techniques, although I was yawning most of the times I promise you I listened as carefully as I could to all the knowledge you were willing to share with me.

A particular thanks to interns who I worked with, **Suvi Huhtanen** and **Rose Emilien**, thank you for your help in obtaining results and investigating parts of my subject I could not do on my own.

To all my dear colleagues and friends of Tampere, from the Bioactive glass group, **Virginia**, **Sonya**, **Anastasia** and **Agata** your presence, help, smile and all the times we spent together will stay in my mind forever, you made me feel like I had a family in Tampere and for that I am eternally grateful. To my colleagues from the 5th floor in the SM wing, **Mart**, **Christine** and **Maiju**, thank you all for the help you have provided me with, and a special thanks to Christine who also became a friend through our common guild, ESN INTO. I will never forget how I felt welcome in Tampere thanks to you and our friends at INTO. A particular thanks to **Arnaud** and **Nicole** for their happiness, joy and friendship, for making me go to the gym, for listening to me whenever I had a heartache and for making me go out sometimes. My stays in Tampere would not have been this happy without you.

To all my colleagues at ERRMECe, I spent less time with you thanks to our dear friend the Coco19, but I still thank you all for the times we spent together and the help you gave me during my PhD. A special thanks to **Amel Houaoui**, as a newbie PhD student I would have been lost without your help. You welcomed me in your home at one of the hardest moments of my PhD and your watchful eye has been a real support, thank you. To **Credson**, **Alphonse**, **Sarah**, **Mathilde**, **Amaranta**, **Pierre**, **Anamar** and **Rosa** our lunches with impromptu talks about Napoleon, women rights, coypu, platypus and other rodent were the funniest I ever had (thank you for all those eclectic subjects Alphonse). Thank you for your happiness and kindness, you are the best. To **Clotilde** and **Mathilde R.** a special thank for your help during my pregnancy for immunostaining experiments and when the confocal did not work (because the key was on the "off" button).

To my friends and relatives, **Benji**, **Sandra**, **Ophélie**, **Galaad**, **Justine**, **Cassandre**, **Corentin**, **Corinne**, thank you all for your support, your kind words, thank you for changing my mind with endless walks and making me go out from my "cave". A special thanks to **Clara**, you are my best friend, your

encouragement meant the world to me, our talks driving us always further in dreams are among my favorite moments.

I am eternally grateful to my parents, my mother **Elizabeth**, my stepdad **Nicolas** and my father **Thierry**, without whom I would have never been able to go this far in my studies, or in my life. Your support and unconditional love have always been my rock and even more during the hardest endeavor of my life as of today: doing a PhD. I love you forever and ever and I hope I made you proud. To my sisters and brother, **Ingrid**, **Anastasia** and **Paul-Antoine**, I love you and your support meant the world to me, I hope I made your proud too.

Finally, to my husband, **Matthieu**, I know I made your life a living hell. I know I can be unbearable sometimes and yet; you gave me your love, support, and encouragement during all this endeavor. You even accepted to marry me! Despite all the hard times we had. And then, our world has been shattered by the arrival of our wonderful little boy, **Nolann** who has put our world upside down and yet brought us the purest love of all. Living together these past few months has been hard, we are not always on the same page, but we stand together in this hardship. I cannot thank you enough for supporting me and loving me through all of this. I love you and I hope I made you proud.

To **Nolann**, my son, the sun of my nights, I know you do not understand everything yet, but I hope one day you will be proud of your mum, as much as I am proud of calling you my son. I love you to the moon and back and beyond.

Meulan-en-Yvelines, October 2023

Audrey Deraine Coquen

Table of Contents

x

List of publications and communications

Publications

1. **Deraine, A.,** Rebelo Calejo, M. T., Agniel, R., Kellomäki, M., Pauthe, E., Boissière, M., & Massera, J. (2021). Polymer-Based Honeycomb Films on Bioactive Glass: Toward a Biphasic Material for Bone Tissue Engineering Applications. ACS Applied Materials and Interfaces, 13(25), 29984−29995. https://doi.org/10.1021/acsami.1c03759

2. **Coquen, AD**, Bondzior, B, Petit, L, Kellomäki, M, Pauthe, E, Boissière, M, & Massera, M, Evaluation of the sterilization effect on biphasic scaffold based on bioactive glass and polymer honeycomb membrane. J Am Ceram Soc. 2023; 00–00. https://doi.org/10.1111/jace.19406

3. **(Submitted) Coquen, AD**, Calderon-jacinto, R, Langueh, C, Agniel, R, Kellomäki, M, Massera, J, Boissière, M & Pauthe, E, Creation of a polymer-based honeycomb membrane on an 3D inorganic matrix bioactive glass or bone-based: toward a new generation of scaffolds for bone tissue engineering

Oral communications

1. **A. Deraine**, M. Boissière, M. Kellomäki, M. T. Calejo, J. Massera, E. Pauthe Deposition of a polymer-based membrane on bioactive glass as a biphasic scaffold for bone tissue engineering applications, **World Biomaterials Congress**, December 2019, Glasgow, Scotland

2. **A. Deraine**, M. Boissière, M. Kellomäki, MT. Calejo, J. Massera, E. Pauthe Polymer-based honeycomb membrane on bioactive glass as an innovative biphasic scaffold for bone tissue engineering, **MET Research Day**, November 2021, Tampere, Finland

Poster presentation

1. **A. Deraine**, M. Boissière, M. Kellomäki, MT. Calejo, J. Massera, E. Pauthe Deposition of a honeycomb-like polymer-based film on bioactive glass as a biphasic scaffold for bone tissue engineering application, **MET Research Day**, November 2019, Tampere, Finland

2. **A. Deraine**, M. Boissière, M. Kellomäki, J. Massera, E. Pauthe Deposition of a polymer-based honeycomb-like membrane on 3D printed bioactive glass scaffold and decellularized bone matrix as scaffolds for bone tissue engineering, **European Society for Biomaterials**, September 2022, Bordeaux, France – presented by Michel Boissière

Author's contribution

Publication 1.   The author was responsible for planning the work, analyzing the data and writing the paper with co-authors. The author produced all the samples used in the experiments. The author conducted all the experimental tests as the main author except the zeta potential measurement and participated in the SEM imaging.

Publication 2.   The author was responsible for writing the paper, planning the work, and analyzing the data with co-authors. The author produced all the samples used in the experiments. The author conducted all the experimental tests as the main author and participated in the photoluminescence measurements. The author also performed the cell experiments.

Publication 3.   **(Submitted)** The author was responsible for writing the paper, planning the work, and analyzing the data with co-authors. The author produced all the samples used in the experiments. The author conducted all the material characterization experiments and participated in the atomic force microscopy imaging and the cellular experiments. The author realized all the ICP-OES analysis and participated in SEM imaging and EDX analysis. The author made the analysis and validated the data of the water contact angle measurements and the X-ray microtomography images.

List of figures

List of tables

Abbreviations

°C: degree Celsius

%: percent

3D: 3 dimensions

µCP: microcontact printing

AFM: Atomic force microscopy

AMT: additive manufacturing technology

APTES: 3-Aminopropyltriethoxysilane

ATR: Attenuated Total Reflectance

B: boron

BCP: block copolymer

BFM: Breath Figure Method

BG: Bioactive Glass

BO: bonding oxygen

BSA: Bovine Serum Albumin

BTE: Bone Tissue Engineering

B_2O_3: boron oxide

Ca: calcium

$CaCO_3$: calcium carbonate

CAD: computer assisted design

$(CaHPO_4)(2(H_2O))$: calcium phosphate dibasic dihydrate

CaO: calcium oxide

CaP: calcium Phosphate

cm: centimeter

CSD: critical size defect

DAPI: 4',6-diamidino-2-phénylindole

DBM: decellularized bone matrix

DOPE: dioleoyl phosphatidylethanolamine

ECM: extracellular matrix

EDX: energy dispersive X-ray spectroscopy analysis

FBR: foreign body reaction

FTIR: Fourier Transform Infrared

g: gram

GBR: Guided Bone Regeneration

h: hours

H_3BO_3: boric acid

HA: hydroxyapatite

HCA: hydroxycarbonated apatite

hMSC: human mesenchymal stem cells

ICP-OES: Inductively Coupled Plasma – Optical Emission Spectroscopy

IR: infrared

K: potassium

K_2CO_3: potassium carbonate

K_2O: potassium oxide

Mg: magnesium

MgO: magnesium oxide

µL: microliter

µm: micrometer

MCT/Micro-CT: x-ray microtomography

mA: milliampere

mg: milligram

mL: milliliter

mm: millimeter

mM: millimolar

min: minutes

N: Newton

Na: sodium

Na_2CO_3: sodium carbonate

Na_2O: sodium oxide

NBO: non-bridging oxygen

NC: network connectivity

$NH_4H_2PO_4$: ammonium phosphate monobasic

NH_2: amine

nm: nanometer

OH: hydroxyle

P: phosphorous

PBS: phosphate buffer solution

PCL: polycaprolactone

PDLA: poly-D-lactic acid

PFA: paraformaldehyde

PGA: poly-glycolic acid

PLLA: poly-L-lactic acid

PLDLA: poly-L-co-D,L-lactic acid

PMMA: poly(methyl methacrylate)

PU: polyurethane

P_2O_5: phosphorous pentoxyde

RH: relative humidity

RP: rapid prototyping

RT: room temperature

SAM: self-assembled monolayer

SAMIM: solvent-assisted micro-molding

SEC: size exclusion chromatography

SEM: scanning electron microscopy

SFF: solid freeform fabrication

Si: silicon

SiC: silicon carbide

$Si(OH_4)$: silicic acid

SiO_2: Silicon oxide

β-TCP: β-tricalcium phosphate

Tg: glass transition temperature

Tx: crystallization temperature

WCA: water contact angle

I. Introduction

Bone is a complex and active tissue responsible for the support and protection of vital organs and the nervous system. Bone is also responsible for the production of blood cells via the bone marrow and for some inorganic ions homeostasis, like calcium (Ca) [1]. Bone has an intricate structure, made of an organic and an inorganic matrix, highly intertwined that can regenerate via the activity of the osteoblast, osteoclasts, osteocytes and bone lining cells [2].

Bone remodeling is the process through which bone is renewed and is active throughout the life of an individual. Bones are naturally subjected to stress, but sometimes important stress can cause fractures and, through the bone remodeling process, small fractures can normally heal by themselves [3]. However, **medical condition** (e.g. cancer, bone infection) or stress, greater than the bone resistance, can endanger bone integrity and create bigger fractures and/or **critical size defect**. In that case, the spontaneous bone healing and remodeling is compromised, and external intervention is required to help the bone repair and regenerate [4], [5].

Worldwide it is estimated that more than 2 million procedures, involving **bone graft,** take place every year which makes bone the second most transplanted tissue after blood [6], [7]. The **gold standard** for bone graft is currently considered to be **autologous bone graft,** taken from the iliac crest and/or fibula of the patient. However, this procedure has several drawbacks like its cost, donor site morbidity, pain and limitations in quantity of bone available, for example [8]. Other options include **allograft** or **xenograft** but they bear the risk of diseases transmission, donor rejection, a high cost and limited supplies in regards of the required histocompatibility between donor and receiver that remains limitations for these procedures [8], [9]. Consequently, synthetic biomaterials have been developed, especially ceramics, to favor bone reconstruction.

Biomaterials developed for **bone tissue engineering** (BTE) purposes face numerous requirements and challenges. For instance, biomaterials should be **osteoinductive**, **osteoconductive**, promote **osteogenesis** and allows **osteointegration**. These are the fundamental characteristics essential to

achieve bone repair. In this context, bioactive and bioresorbable biomaterials were developed. **Bioactivity** refers to the ability of a material to induce a biological response resulting in the formation of a close bond between the implanted scaffold and the surrounding tissue [10]. **Bioresorbable** materials gained interests because they gradually degrade to leave the space for the newly formed tissue and therefore allow to avoid a second removal surgery, contrary to the inert first-generation biomaterials [11]. **Bioactive glass** (BG) was the first of a new generation of materials that reached clinical use in the mid-80's [12], [13]. The bioactive glass developed by L.L. Hench, known as 45S5 Bioglass ®, was the first material to really bond with the surrounding tissue without being "isolated" by a fibrous capsule [14]. BG composition can be easily modified to meet the need of specific application. Especially, it allows to tailor the degradation rate of the BG that can ultimately be entirely converted to hydroxyapatite (HA) and integrated into the tissue. In recent studies, BG were found to be able to stimulate certain cellular response such as cell differentiation and angiogenesis thanks to their ability to leach ions beneficial for the cell fate [15]–[18]. The possibility to easily modify or dope with trace elements BG composition, made them particularly interesting for applications ranging from wound healing to bone regeneration [14]. Furthermore, the availability of BG compared to the gold standard autograft make them tremendously attractive. Indeed, more than 25 BG composition are approved today for clinical use, demonstrating their attractiveness [19]. Among all, the S53P4 is a silicate-based BG, manufactured as a bone graft substitute, under the name of BoneAlive® (BonAlive Biomaterials Ltd., Turku, Finland), has drawn significant interest [20], [21]. Several studies have highlighted the potential of S53P4 to stimulates angiogenesis and showing antimicrobial properties [22], [23]. Nowadays, the S53P4 is used in a large variety of clinical applications ranging from cranio-maxillofacial surgery to spine surgery or in the treatment of osteomyelitis, for instance [21]. However, the degradation process for silicate-based BG is slow and it can take years for the BG to degrade in-vivo. Furthermore, silicate-based BG do not dissolves completely and particles stay encapsulated in the newly formed tissue [21]. Furthermore, it is very hard or even not possible to sinter scaffolds made of S53P4 without crystallization which results in a lower bioactivity and lower dissolution rate [24]. To overcome the fast crystallization kinetics of the glass S53P4, 13-93 bioactive glass has been developed [25], [26]. However, this glass, while having improved sintering ability, degrades much slower than S53P4. Boron

(B) in BGs has not only been found to increase BG dissolution rate but also to increase the hot forming domain, thus enabling sintering without significant crystallizations [27], [28]. Furthermore, studies showed that, although the boron presence in the borosilicate composition might decrease cell proliferation, it still promotes osteogenesis and angiogenesis [17], [29]–[31]. In our group, the 13-93B20 (where 20% of the silica (SiO_2) in the 13-93 is substituted for B_2O_3) was developed to promote HA precipitation while releasing B ions in proportion amenable to cell viability and differentiation into bone cells [29].

Nevertheless, despite all the advantages of using BGs compared to autograft, for either material, one major challenge remains: **fibrous tissue ingrowth** [32]. Indeed, regardless of the nature of the material used as bone graft, researchers and surgeons have identified the fibrous tissue ingrowth as a major drawback. Fibrous tissue ingrowth refers to the scar tissue that invades the bone grafting site and where fibrous tissue takes the place of the bone tissue, resulting in an incomplete bone regeneration [32], [33]. In the attempt to minimize the fibrous tissue ingrowth and maximize the bone regeneration, researchers have tried to combine the inorganic grafting materials with membranes to produce a mechanical barrier to the fibrous tissue invasion, especially in large defects [14, 15]. The use of a **barrier membrane,** to isolate the bony defect from fibrous tissue infiltration, is designated as **Guided Bone Regeneration** (GBR), first presented by Dahlin et al. in 1988 [35], [36]. In GBR, the barrier membrane is considered to be a key factor for the success of the bone regeneration. The barrier membrane must have good mechanical properties while resorb at an adequate rate compared to the regenerating tissue, be biocompatible, cell-occlusive while having a porosity allowing nutrient flow, maintain the space it is intended to protect (i.e. the membrane should not collapse into the defect) and integrate to the tissue [33], [37]. One of the major characteristics of the membrane is its porosity. Indeed, the porosity of the membrane in GBR is the feature that defines how nutrient, oxygen, bioactive substances and degradation products can diffuse [38], [39]. **Porosity** is essential to tailor in the production of barrier membrane since large pores could impair the barrier property of the membrane while too small pores could reduce the angiogenesis [40]. The membrane is typically either a natural or synthetic polymer. While natural polymers generally exhibit too fast degradation, synthetic polymers degradation can be

tailored to match the regeneration of the bone. Poly-L,D-lactic acid (PLDLA), which is a co-polymer made of the L and D isomers of the PLA, has a degradation rate that can be tailored by modifying the stereoregularity [41]. To produce such membranes, in the 90's, a well-known nature-inspired method has made a breakthrough: the **Breath Figure Method** (BMF) [42]–[44]. The interest for the BFM resides in the simplicity and versatility of the approach. The method is based on the use of a humid air flow directed on a solution of the polymer used for the membrane dissolved in a water-immiscible and fast evaporating organic solvent. While the solvent evaporates, water droplets form at the surface of the solution and organize themselves in an ordered hexagonal lattice to reduce the free energy. After complete water and solvent evaporation, a thin membrane with a honeycomb-like structure is created [42]. The method has several advantages such as: 1) simplicity (it does not require complex setup), 2) cost (it does not require complex equipment and so is inexpensive), 3) rapidity (numerous porous membranes can be prepared in a limited time), 4) tailorability (by modifying the process parameters (e.g. relative humidity (RH), polymer solution concentration, polymer type) the pore size can be tailored) [42].

Nevertheless, a membrane alone cannot allow a quick and qualitative bone regeneration, especially in large bone defects [45], [46]. For this reason, surgeons have combined the barrier properties of the membrane and osteopromotive properties of grafting material as two different materials in a two-step procedure and, to the best of this authors knowledge, a single material, combining both phase (i.e. the barrier membrane and the grafting material), for a single step procedure does not exists.

It is in this context that this thesis was conducted, with the **aim to develop a single material combining a polymer-based honeycomb membrane as organic phase and an inorganic phase made of BG or decellularized bone matrix (DBM).**

PLA is one of the few polymers yielding amorphous or crystalline material by mixing different amount of its stereoisomers [47]. Poly-L-lactic acid (PLLA) for instance has a high crystallinity and a long degradation time, up to 5 years. In the other hand, **poly-L-co-D,L-lactic acid** (PLDLA) has a lower crystallinity and a faster degradation rate compared to PLLA since it can be completely degraded in 12 months [41]. However, its degradation products can create an acidic environment that would lead to

inflammatory response. BG upon degradation releases alkali ions that results in a high pH locally which can counteract the acidic species of the PLDLA degradation [47].

Therefore, in this thesis, the PLDLA was chosen as polymer to produce the honeycomb membrane while S53P4 and 13-93B20 BGs were chosen as the inorganic phase, along with DBM, to produce a biphasic scaffold for bone regeneration.

Broadly, this thesis is composed of a literature review on the field of bone regeneration, barrier membranes and synthetic inorganic grafting materials. The aims of the project are then described and followed by the materials and methods used during the thesis. The following results and discussion section is organized in two chapters:

1) the first covering the development of a biphasic bulk material based on BG and the honeycomb membrane and the effect of the sterilization applied on the assembly. In this part, the results showed that by carefully tailoring the surface topography and chemistry it is possible to obtain a strong adherence of the membrane on bulk discs of BGs and that sterilization does not significantly influences the assembly properties,

2) the second discussing the development of a 3D-printed material and DBM associated with the honeycomb membrane. In this part, the results showed that it is possible to deposit the membrane at the surface of a 3D-printed BG-based scaffold and of a DBM. Furthermore, it has been showed that the membrane does play its role in the assembly by separating spaces and segregating fibroblast from osteoprogenitor cells.

Finally, a conclusion summarizes the work of this thesis and perspectives are provided.

II. Literature review

A. Bone dynamic and healing

There are more than 200 bones in the body with all types of shapes and length, e.g. from the flat bones of the thoracic cage, to the irregular bones of the skull and the long bones of the leg. Bone tissue has three main functions:

1. Mechanical: bone is a strong and hard connective tissue that provides support and protection while enabling movement due to its rigidity [1].

2. Metabolic: Bone is a dynamic tissue that undergoes continuous remodeling in response to mechanical forces. This remodeling process involves the release or storage of mineral salts. Consequently, bone plays a crucial role in maintaining the body's phosphocalcic homeostasis [2].

3. Hematopoietic: the blood cell lines are created in the hematopoietic marrow, which is contained within the medullary region of the bone [1], [2].

1.1. Structure and composition

Microscopically, the composition of the bone extracellular matrix (ECM) is a mixture of organic and inorganic elements. Most of the organic matrix is made of collagen and particularly type I but it also contains collagen type III, V, X and XII, along with other proteins such as fibronectin, osteocalcin, osteopontin and proteoglycans. The inorganic matrix of the bone is composed of nanosized leaf-like crystals of calcium hydroxyapatite that bind to the collagenous matrix and give the bone its stiffness. The inorganic matrix of the bone serves as an ion reservoir especially for the calcium and phosphate for which bone is responsible for 99% and 85%, respectively, of the storage in the body [2]. The storage of those inorganic compounds has an essential role in the regulation of the homeostasis. Some other trace elements can be found in bone such as magnesium, sodium, potassium, fluoride, chloride, copper, aluminum, strontium, silicon or boron.

A variety of specialized cells, including osteoblasts, osteocytes, and osteoclasts, are encased in the mineralized collagenous extracellular matrix of the bone. The periosteum, endosteum, and marrow are closely related structures [1].

As they secrete the bone matrix, osteoblasts are in charge of its synthesis, deposition, and mineralization. They change into osteocytes after becoming enmeshed in the rigid mature bone matrix. On the other hand, the bone matrix resorption is mediated by osteoclasts. Their roles are closely linked since one regulates the other and vice versa [1], [2].

The most common cells in bone are osteoclasts, occupying lacunae in a functional unit called osteon (**Figure 1**), which is made of concentric mineralized lamellae of ECM, scattered throughout the matrix. An intricate network of tiny passageways known as canaliculi connects lacunae, allowing osteocytes to transmit cytoplasmic or dendritic processes. This organization of the osteocytes in lacunae interconnected through canaliculi in the bones make them the primary mechanosensory cell-type for the bone's response to mechanical forces [2], [48].

Macroscopically, the inner part of bone is structured with large cavities where the bone component is reduced to trabeculae, a latticework of bars and plates name trabecular or cancellous bone (**Figure 1**), while the outer part is as dense as ivory, and name compact or cortical bone. A thick cortex is typically needed to offer strength while bending, which is the case in the mid-diaphysis of a long bone. The epiphyses of long bones or the vertebral bodies of the spine, for example, are usually rich in trabecular bone, which provides strength in compression [1], [2].

The presence of cortical bone is especially noticeable in the diaphysis, where it creates a substantial cortical shell (cortex) that protects a bone marrow-filled medullary canal. By distributing bone mineral away from the bending axes, this tube-like structural design significantly increases bending resistance without also increasing bone weight. This gives long bones the strength and rigidity needed for weight bearing and muscular action, but also the lightness needed for energy-efficient mobility. Although cortical bone is solid, it does have small pores, called Harvesian canals inside osteons, that allow for nutrient delivery, vascular and neuronal supply [2]. Contrary to cortical bone, which has low porosity,

trabecular (or cancellous) bone has significant porosity, with pores accounting for 50% to 90% of the total volume of trabecular bone. Its purpose is to expand the surface area of bone that connective tissues, blood vessels, and red bone marrow can interact with. This makes bone's function in hematopoiesis and mineral homeostasis easier. Although trabecular bone lacks the strength of cortical bone, it nonetheless plays a mechanical role by offering internal support. Particularly close to joints, this supporting function makes it easier for bone to appropriately distribute stress and absorb energy [2].

Between cortical bone and the underlying soft tissue or musculature, the periosteum, a specialized connective tissue, acts as a transitional fibrous layer. With the exception of articular surfaces, tendon insertions, and the surfaces of sesamoid bones, it covers the external surfaces of the majority of bones. You can distinguish two different layers of the periosteum. The outer most "fibrous" layer contains fibroblasts, collagen, and elastin fibers and also characteristic nerve and microvascular network. The inner "cambium" or "cellular" layer is in close proximity to the surface of the bone. It contains differentiated osteogenic progenitor cells, fibroblasts, micro vessels, and sympathetic nerves in addition to mesenchymal stem cells (MSCs), which can develop into osteoblasts and chondrocytes [2].

A similar tissue covering the inner medullary canal of bone is called the endosteum which is a membrane across the endocortical and trabecular bone surfaces to surround the bone marrow. The endosteum, contrary to the periosteum, is made of a single thin layer of bone-lining cells (mature quiescent osteoblasts) and osteoblasts. Osteoclasts can also be found in the endosteum but only in regions with an active bone resorption [2].

The inner medullary canal of bones, especially long bones, contains bone marrow. Although they seem to be two distinct anatomical structure, bone and bone marrow have a clear functional connection. Haematopoietic and non-haematopoietic stem cells can be found in bone marrow, and these cells give rise to osteoclasts and osteoblasts notably [1], [49]. In addition, non-osteogenic cells contained in the bone marrow are involved in the regulation of bone remodeling while angiogenesis in bone marrow and osteogenesis are closely related processes [49].
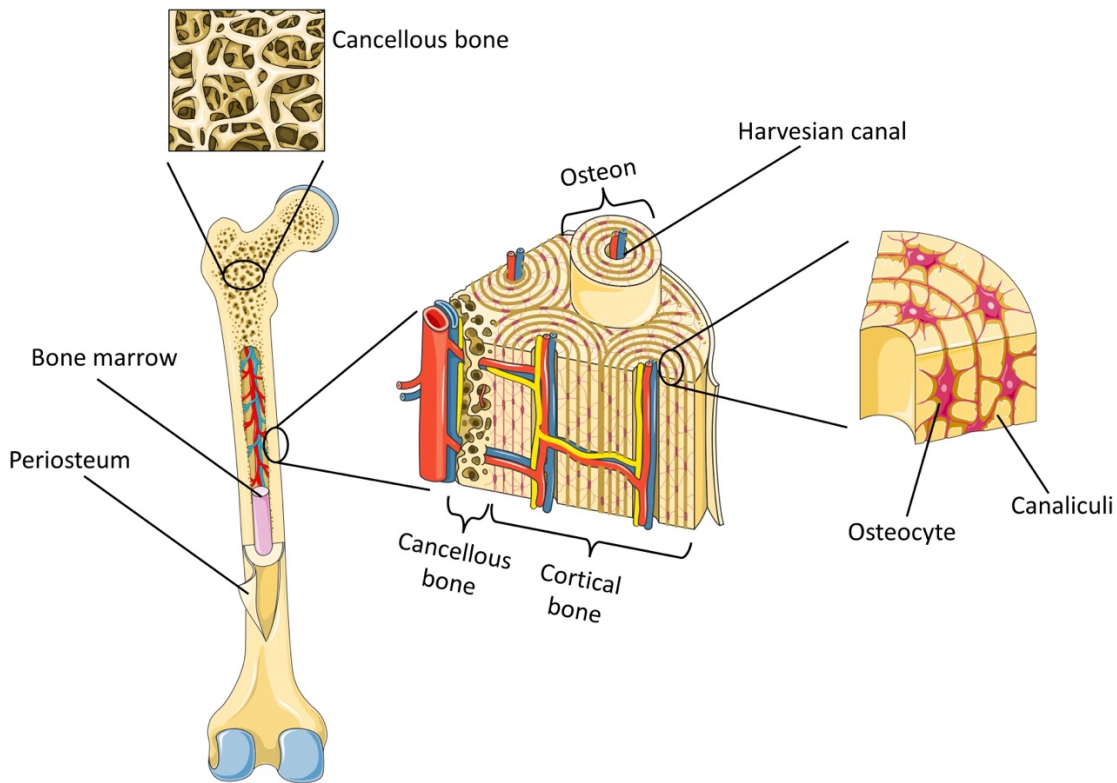
Figure 1. Schematic of the structure and composition of bone (made using Servier Medical Art)

1.2. Bone remodeling

Bone, which appears to be inert, is in reality a highly dynamic organ that is constantly being resorbed by osteoclasts and neoformed by osteoblasts. Furthermore, there is evidence that osteocytes control and coordinate this bone remodeling process as mechanosensors [48]. This process is responsible for the good health of the bone and is highly complex. It is called "bone remodeling" and has three major phases [2], [48] (**Figure 2**):

(1) The initiation of the bone resorption by osteoclasts,

(2) The transitional phase from resorption to new bone formation, also called "inversion",

(3) The bone formation, that starts with osteoblasts secreting an unmineralized version of the bone matrix: the osteoid.

The bone remodeling process is essential for fracture healing and adaptation to mechanical demands on the skeleton as long as mineral homeostasis. However, it can sometimes be imbalanced and cause diseases like osteoporosis which results from a higher rate of bone resorption compared to neoformation

of bone, or osteopetrosis if there is more neo formed bone compared to resorbed bone [48]. Therefore, the balance in bone remodeling is essential to bone health and the functions associated. Consequently, the regulation of the bone remodeling process is of high importance and is mediated, notably, by hormones, cytokines, and biomechanical stimulation.
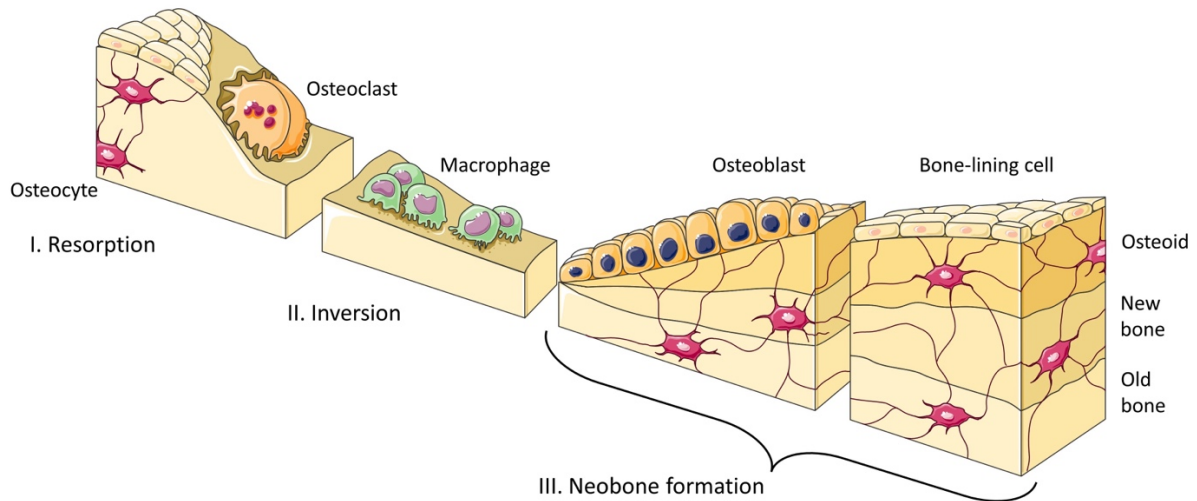
Figure 2. Schematic of the bone remodeling process (made using Servier Medical Art)

1.3. Bone healing

Contrary to other tissues, most skeletal injuries or fractures heal without the development of scar tissue, and bone is rebuilt with most of its pre-existing qualities restored, eventually becoming indistinguishable from the uninjured bone nearby [4].

In case of fracture, there are two types of fracture healing [50], [51]:

(1) Non-contact (or indirect or secondary) fracture healing

(2) Contact (or primary or direct) fracture healing

On one hand, non-contact fracture healing is the most common type of fracture healing happening naturally. This type of healing does not require reduction or rigidly stable conditions. On the other hand, the contact fracture healing requires anatomical restoration and strong fixations in order to minimize as much as possible the gap between the two sides of the bone fracture and the movement to ensure a close contact and allow the bone to regenerate. Bone healing occurs in essentially 3 steps (**Figure 3**):

1) Inflammatory step

2) Healing

3) Remodeling

The inflammatory phase starts with the formation of a hematoma and then, through signaling molecules like interleukines 1 and 6 (IL-1 and IL-6), tumor necrosis factor and tumor-derived growth factor (TNF-α and TNF-β) and bone morphogenic proteins (BMP) like BMP-2, the callus formation is initiated[50], [52]. In the meantime, cells are also recruited and proliferate at the site of the injury, like mesenchymal stem cells, and new blood vessels are created, which happen along with chondrogenesis in the case of endochondral ossification [53]. In the case of a small subperiosteal defect, the healing happens through intramembranous osteogenesis. The intramembranous osteogenesis consists of the recruitment of MSCs coming from the periosteum, adjacent soft tissue, and bone marrow. The MSCs differentiate into osteoblasts, and they will secrete and mineralized the ECM to form a hard callus directly under the periosteum [53]. In the case of endochondral osteogenesis bone forming cells and osteoclast will resorb the mineralized cartilage and continue neo-vascularization. The final step is the remodeling and reconstruction of the bone marrow [50], [52]. This final step happens through a longer period on which the callus is continuously resorbed and regenerated (i.e. remodeled). It may take several months for the bone to regenerate to its original state.

Although this process generally suffices for the bone repair, it sometimes fails. In such situation, fractures may take longer to heal than expected, heal in an undesirable anatomical position, or possibly develop into pseudo-arthrosis or non-unions [50].
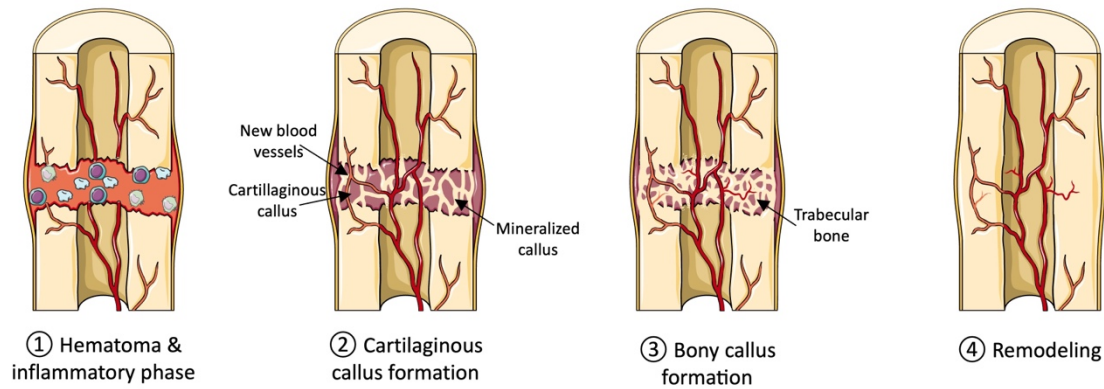
Figure 3. Schematic of the bone healing process through endochondral osteogenesis following a fracture (made using Servier Medical Art)

B. Situations requiring medical intervention and strategies for bone repair

1. Defects requiring medical intervention

Certain pathologies or traumatisms can cause such an important bone loss that the natural ability of bone to repair itself is hindered. Past a certain defect size, a medical intervention is necessary to help the bone to regenerate. This is the so called "Critical Size Defect" (CSD). The definition of such defect is controversial, and no consensus is found in the literature. Generally, CSD is considered as the critical size for which natural bone healing is inhibited. According to Schemitsch [54] general guidelines found in the literature define the critical size as a defect length greater then 1-2 cm and a loss greater than 50 % of the bone circumference. However, Schemitsch emphasizes that this is highly dependent on the location of the defect, the tissue environment surrounding it and patient related characteristics (comorbidities, age, diseases etc.) [54]. Another definition from P. Baudet, orthopedic surgeon, is that below 6 mm a bone defect does not need medical intervention while between 8 to 12 mm the defect can be considered as critical sized [55]. In a more general definition Li et al. have defined the critical size defect as a "segmental bone deficiency of a length exceeding 2-2.5 times the diameter of the affected bone" [56]. The causes of CSD are various and range from tumor resection, to developmental deformities, infection, age or important traumatisms [57].

1.1. Traumatic defects

Bone is a material able to withstand important mechanical stress [52]. A fracture is caused when the resultant strain from the stress applied on the bone is such that the bone is deformed beyond its elastic limit and breaks [51]. The term "fracture" includes all loss of continuity; i.e. from bone broken in several fragments to microscopic fracture [55].

A traumatic fracture or stress fracture occurs when bone receive an impact or a stress it cannot resist and break [55], [58].There are different type of traumatic fracture depending on the type and importance of the strain applied to the bone [51], [59]:

1.2. Defects due to a pathophysiological context

A pathological fracture is defined as "a fracture occurring on an abnormal bone, independently of the constraint that caused the fracture". Those fractures can be caused by cancer or pathologies acquired such as osteoporosis, for example [55]. Defects can also be caused by infections (osteomyelitis) that can require bone debridement if antibiotics are not sufficient [60].

1.2.1. Age

Although bone is a tissue with the capacity to regenerate and remodel, this ability decreases with aging. Cellular processes and molecular pathways are less efficient in the bone remodeling, and this can lead to pathologies such as osteoporosis or osteoarthritis [61].

Osteoporosis is a major public health problem happening more often in post-menopausal Caucasian woman but both sexes are affected. It Is estimated that the number of patient suffering from osteoporosis worldwide is more than 200 million [62], [63]. Osteoporosis is characterized by a generalized loss of bone mass, strength, and microarchitecture that makes fragility fractures more likely. Fractures due to osteoporosis commonly occur in the spine, hip or wrist but can also concern other bones like the ribs. In a patient point of view, the subsequent loss of mobility due to a fracture represents a significant decline in life quality. Furthermore, fractures in hip or spine can be life threatening [63].

1.2.2. Cancer

The vast majority of primary bone tumors, which are tumors that develop directly into the bone and are benign, are asymptomatic. Therefore, diagnosis is often made incidentally during radiographic examination for other reasons. Other bone tumors are often due to malignant cancer cells spreading to the bone. The three most common primary malignant bone tumors are osteosarcoma, chondrosarcoma, and Ewing's sarcoma and they mostly affect infants and adolescents having a significant impact on the patient's life [64], [65]. The treatment of those tumors often consists of a surgery, to remove the tumor, and chemotherapy [66], [67].

1.2.3. Infections

Bone infection, also called osteomyelitis, is caused by bacteria coming in contact with the bone. This infection can be at best limb-threatening or, in the worst-case scenario, life-threatening. Spontaneous infection of the bone is uncommon but due to increased arthroplasty rates and rising rates of diabetes, there is an increase in the incidence of prosthetic joint infection (PJI) and diabetic foot osteomyelitis. The usual treatments involve antibiotics and, depending on the case, debridement or even amputation [60].

C. Bio(materials) and strategies for bone regeneration

As said above, CSD cannot heal by themselves and often require a surgical intervention to provide elements **necessary for the bone to regenerate in appropriate conditions. For this purpose, natural biological** materials, such as autologous, allogenous or xenogenous graft, and/or biomaterials can be used. [68]. On the other hand, **biomaterials** are defined as synthetic materials created to be utilized alone or in a complex system with the aim of performing a diagnosis, treating patients, replacing or regenerating organs, tissues, or functions in human or veterinary medicine by controlling the interactions with the living organism in which it is implanted [69], [70].

In this section, natural and synthetic biomaterials for bone regeneration will be presented along with the barrier membranes used for the segregation of the fibrous and bony tissue to avoid fibrotic tissue

infiltration. Existing association of both materials (bone graft and barrier membrane) will be introduced and finally the fabrication methods for the materials sued in this thesis will be described.

Bone filling materials are either engineered or based on natural bone graft materials used to fill a CSD in bone and act as a scaffold to support the bone regeneration process. Ideally, the material used to fill the CSD should be osteoinductive, osteoconductive, promote neo-bone formation by bone forming cells and be able to fully integrate within the newly formed bone. There are hundreds of engineered materials for BTE based on many different materials, some are listed in **Table 1**. For the purpose of this work, only a few of the materials listed in **Table 1** will be detailed from natural polymers, synthetic polymers, and bioactive ceramics.

1. Natural strategies

1.1. Autograft
Autograft refers to a surgical procedure consisting of harvesting bone tissue from a donor site and used to fill the patient's defect. Usually, the donor site is the iliac crest as it is easy to access and provides good bone quality. However, harvesting bone from the iliac crest has several drawbacks, such as 1) post-operative pain, 2) increased time of surgery and 3) limited bone availability [71].

As of today, autograft is the gold standard for bone graft. Indeed, it possesses all the characteristics to perfectly promote the bone regeneration. It is osteoinductive, osteoconductive and osteopromotive and can therefore integrate rapidly and completely into the host [3].

1.2. Allograft
Allografts are tissues taken from a donor of the same species as the recipient. It is the second-best option for surgeons as it is more available than autografts, in many different forms and can be shaped to perfectly fit the patient's defect. However, it bears the risk of disease transmission, graft rejection and given that they have to go through sterilization, their properties change and they lose some of their osteoinductive and osteogenic capacity [3], [9], [71].

1.3. Xenograft

Xenograft refers to procedures that consist of taking a bone graft from a donor of a different species. This method allows using animal-based or plant-based materials, like corals or decellularized bone matrix (DBM) from porcine or bovine origin. Xenografts are usually osteocondutive and osteoinductive but lack osteogenic properties. Xenografts are even more available than allografts but they also bear the risk of graft rejection and disease transmission [5], [72].

2. Engineered strategies

2.1. Nature of the bone filling matrix

In the treatment of a bone loss, tissue engineering (TE) is the "final" option to circumvent the limitations of the presented natural strategies. TE refers to a treatment method involving the use of scaffold, biological/chemical factors and/or cells in order to restore, maintain or improve a tissue function [5], [70]. TE, and particularly BTE, relies extensively on the use of scaffolds as templates for the regeneration of the damaged tissue. Scaffolds can be made of biological (natural/organic) or synthetic (artificial) materials. Natural materials can be made of collagen or DBM for example. Synthetic inorganic materials are metals, calcium phosphate ceramics such as tricalcium phosphate (TCP) or synthetic hydroxyapatite (HA), bioactive glasses and polymers such as polyglycolic acid (PGA) or polylactic acid (PLA) and their composites [5].

Table 1. Summary of some known biomaterials used to produce scaffolds for BTE. Modified from [73]

Biomaterials	Characteristics	Advantages	Disadvantages
Metals	*Appropriate mechanical properties of biocompatible metals*	*Great mechanical properties, Biocompatible*	*Non-biodegradable* *Corrosion*
Tantalum	Bioactive and corrosion resistant	Widely used as biomaterial	Almost no degradation leading of 2nd surgery for removal
Magnesium	Porous and biodegradable implant	Similar mechanical properties to human bone, Biodegradable	Toxicity risks from ion or particle leaching
Titanium and titanium alloys	Long-lasting, biocompatible, highly corrosion resistant, similar modulus of elasticity compared to trabecular bone	High affinity with bone	Non-biodegradable
Nickel-titanium alloys	Special mechanical properties like shape memory or superelastic effects	Best material with closest properties to natural bone compared to any other metals	Mostly non-degradable, due to titanium content can cause stress-shielding
Natural polymers	*Similar to ECM, great biological properties*	*Biocompatible, biodegradable*	*Low mechanical strength*
Collagen	Major part of bone ECM, outstanding biocompatibility	Biodegradable, can take various forms	
Gelatin	Denaturalized collagen	Can form blends through crosslinking	
Silk fibroin	Outstanding mechanical properties	Biodegradable, biocompatible	Long degradation time, elicits foreign body reaction (FBR) [74]
Chitosan	Cationic polysaccharide, biocompatible, resistant to bacteria	Biodegradable, non-toxic, antioxidant, hemocompatible [75]	Poor osteoinduction properties

Table 1. (contd.)

Biomaterials	Characteristics	Advantages	Disadvantages
Alginate	Negatively charged polysaccharide	Can be crosslinked and print by injection	
Synthetic polymers		*Tunable mechanical and physico-chemical properties*	*FBR due to acidic degradation products*
PLA, PLDLA (poly lactic acid)	Aliphatic polyester, FDA approved for medical applications	Tunable crystallinity, mechanical properties and degradation time by adjusting isomers content [76]	Can trigger FBR[76]
PGA (poly glycolic acid)	Aliphatic polyester	Biodegradable, Biocompatible [77]	Low mechanical properties [77]
PCL (polycaprolactone)	Aliphatic polyester, very flexible	Crosslinkable in situ and print by injection	Long degradation rate
PVA (polyvinyl acohol)	Synthetic hydroxylated polyvinyl acetate	Easily shaped into various forms of implant with different porosity and degradation ate	
Polyurethane (PU)	Great mechanical properties		
Bioinert ceramics	*Unable to link with living tissues after implantation*		
Aluminum (e.g. aluminum oxide Al_2O_3)		Great mechanical properties	No biological activity
Zirconia		Possibility to produce interconnected structures	No biological reaction with living tissues
Bioactive ceramics (bioceramics)	*Able to bond to living tissue (hard or soft)*		
Hydroxyapatite (HA)	Main component of the inorganic ECM of bone	Outstanding biocompatibility, non-toxic, osteoconductive	Non-biodegradable

Table 1. (contd.)

Biomaterials	Characteristics	Advantages	Disadvantages
β-Tricalcium phosphate (β-TCP)	Similar calcium to phosphorous ratio compared to natural bone	Biocompatible, no rejection reaction from the host	Degradation rate and osteogenic promotion are inconsistent
Calcium sulfate (CaSO$_4$)	Good material after tumor resection		
Akermanite (Ca, Si, Mg)	Great mechanical properties	Controllable degradation rate, enhanced osteogenic properties compared to β- TCP	
Bioactive glass	Biocompatibility depends on the composition, main components Si, Ca, P, Na and/or B, Biodegradable, hard and soft tissue bonding	Tunable composition for tunable properties, osteoinductive, osteoconductive, Tunable degradation rate [78]	Brittle, low fracture toughness [79]
Composites	*Depending on the materials used to form the composite*	*Tunable physico-chemical and biological properties*	*Same disadvantages as the materials forming the composite*
Glass fiber reinforced composites (FRC)	Can have a matrix made of metal, ceramic or polymer containing fibers organized in two directions to enhance the mechanical properties [80]	Important variety of matrices and types of fibers can be combined and FRC can even be combined with particles, like BG particles (FRC-BG) [81], [82]	

2.1.1. Inorganic

o   Synthetic hydroxyapatite

Synthetic hydroxyapatite (HA), with the formula $[Ca_{10}(PO_4)_6OH_2]$ is a crystalline material with a calcium-to-phosphate ratio of 1.67 and has a structure which is the closest to the natural bone apatite [83]. It has excellent biocompatibility and osteoconductivity properties and therefore has been used successfully as a bone filler in various forms such as cement, granules, porous scaffold or as coating of metallic implants [83], [84]. However, synthetic HA presents low mechanical properties and extremely long degradation rate which has limited its use as a scaffold for BTE [84]. However, it can be associated with other materials to improve its mechanical and physical properties, or doped with different atoms such as fluor to produce fluoridated hydroxyapatite (fluorapatite) to inhibit infections or with zinc to enhance its resorption rate for instance [83].

o   β-tricalcium phosphate (β-TCP)

β-TCP has presented itself as an alternative to the highly crystalline synthetic HA and has been used as bone substitute for more than 25 years now, mainly for orthopedic and dentistry applications [85]. It is, like synthetic HA, a calcium phosphate ceramic. Its resorption is cells mediated meaning that, it is by the action of cells, especially osteoclasts that, by creating an acidic environment, β-TCP degrades [86]. β-TCP degrades very slowly and takes 13 to 20 weeks to completely resorbed. Despite having a sufficient mechanical resistance, β-TCP does not match the mechanical properties of cancellous bone or a bone allograft [67], [78].

o   Bioactive glass (BG)

"Why, if scientists are capable of making materials withstanding high energy radiation exposure, they are not able to produce materials that can survive the human body environment?"

It is this question, asked to Pr. Larry Hench in the 60's by a colonel met on the way to a conference, that led him to focus his research on materials with a better biocompatibility. This resulted in the discovery of the very first material able to integrate, bond and promote neo-bone formation: bioactive glasses (BG) and particularly the 45S5 also called Bioglass® [14], [87], [88]. This class of material has

since then been described as "bioactive" according to the following definition: "A bioactive material is one that elicits a specific biological response at the interface of the material which results in the formation of a bond between the tissues and the material "[89]. The particularity of those glassy materials resides in the fact that, unlike crystalline solids, they only show a short-range arrangement of their atoms that depends on their composition [78]. This molecular structure directly affects many properties of the BGs notably their stability, density, solubility and ability to release ions in aqueous environments. Thanks to this particularity, by modifying the glass composition – adding specific elements in order to trigger specific properties, changing the former/modifier oxides ratio or the molar ratio – it is possible to design BG with variable degradation rate to match that of neo-bone formation. Furthermore, added properties can be imparted to the BGs by adding appropriates ions, i.e. anti-bacterial (Cu, Ag) or angiogenic (B, Cu) properties [78], [79]. Hence, many different BG compositions have already been synthetized and studied, which led to the development of three main classes of BGs: phosphate, borate or silicate-based BG [90]. In this thesis, only silicate and borosilicate glasses have been used. Hence, only silicate, borate and borosilicate BG will be described.

Silicate BG are made of successive SiO_4 tetrahedra (**Figure 4**). One SiO_4 tetrahedra can be linked to a maximum of 4 other tetrahedra with Si-O-Si link. In such glasses, network modifiers are used to reduce the melting temperature and reduce the production cost, such as NaO, but also to modify the network connectivity (NC) and play with the durability of the glass. In silicate BG, the addition of modifier disrupts the NC and the breaking of Si-O-Si bonds creating non-bridging oxygens (NBO) which are oxygens not linked to another tetrahedra (Si-O⁻). The different possibilities for tetrahedra structures are commonly described using the "Qn" notation where "n" depict the number of bridging oxygen (BO) on a tetrahedron. "n" varies from 0 to 4 (**Figure 4**) [78].

Q$_4$ (0 NBO)   Q$_3$ (1 NBO)   Q$_2$ (2 NBO)   Q$_1$ (3 NBO)   Q$_0$ (4 NBO)
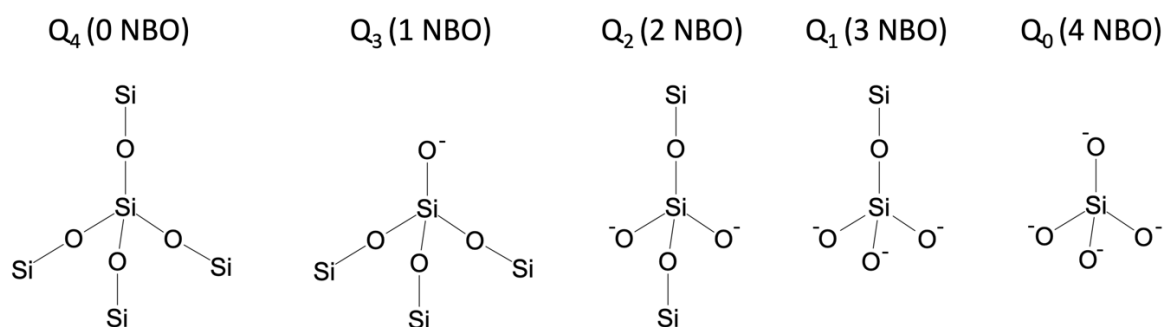
Figure 4. Schematic representation of the Qn structural units in a silicate BG

Some well-known silicate BGs include the 45S5 (Bioglass ®), but also the S53P4 or BoneAlive ®, discovered by Anderson et al. [91], and the 13-93 for instance (**Table 2**). Those compositions, due to their different silica content have a different behavior when it comes to dissolution and crystallization. However, their dissolution mechanism remains identical.

Table 2. Common and investigated BGs composition in mol%. The investigated BGs are written in bold case. Based on reference [92] and [29].

Glass	mol%						
	SiO$_2$	Na$_2$O	CaO	P$_2$O$_5$	K$_2$O	MgO	B$_2$O$_3$
45S5 (Bioglass®)	46.1	24.4	26.9	2.6	-	-	-
13-93	54.6	6.0	22.1	1.7	7.9	7.7	-
S53P4 (BoneAlive®)	**53.9**	**22.7**	**21.8**	**1.7**	**-**	**-**	**-**
13-93B20	**43.7**	**6.0**	**22.1**	**1.7**	**7.9**	**7.7**	**10.9**

The dissolution steps of BGs are as follow and illustrated in **Figure 5** [89], [93], [94]:

1) Rapid exchange of alkali ions (e.g. Na$^+$, K$^+$) from the glass surface with H$^+$ or H$_3$O$^+$ from the solution and pH augmentation,

2) Breaking of siloxane bonds and formation of Si-OH (silanol) groups at the glass surface and loss of soluble silica in the form of silicic acid Si(OH$_4$),

3) Repolymerization of a highly hydrated SiO2 rich layer at the surface of the glass which provides large surface area for future calcium phosphate nucleation,

4) Migration of Ca^{2+} and PO$_4^{3-}$ from the glass to the solution and recondensation at the glass surface in the form of an amorphous calcium phosphate layer,

5) Crystallization of the amorphous calcium phosphate layer incorporating OH$^-$ and CO$_3^{2-}$ eventually forming a hydroxycarbonated apatite (HCA) layer.
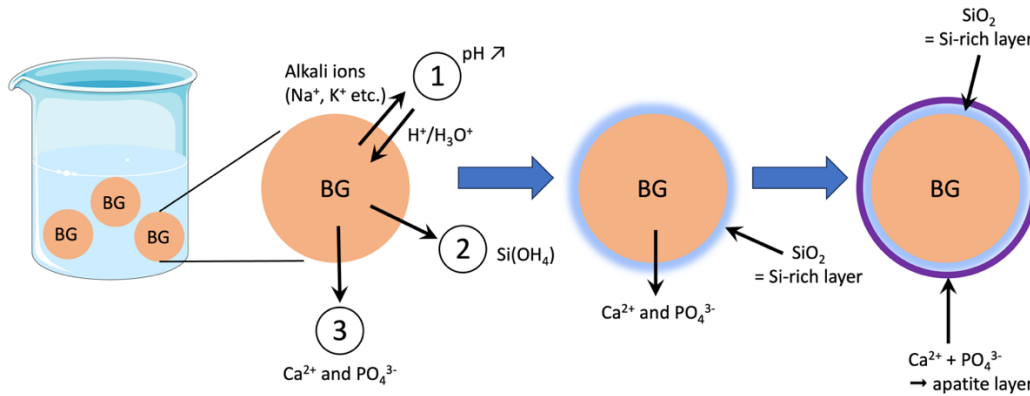
Figure 5. Schematic of the BG reaction upon immersion in aqueous environment (modified after reference [67])

Following the formation of the chemically reactive layers at the BG surface, interactions with the tissue/BG are initiated – the different steps of the BG surface reactions are recapitulated in **Figure 6**. The very first step in this process consist of the adsorption of growth factors and other biological molecules (like collagen) on the forming HCA layer. Later, macrophages and stem cells step in, although macrophages action in this step (step 7, **Figure 6**) is still unclear [89]. Afterwards, stem cells arrives to the bone/BG interface and attach (step 8), they differentiate, proliferate (step 9-10), produce their matrix (step 10) and finally the matrix can crystalize into the new bone (step 11) [89], [95], [96].
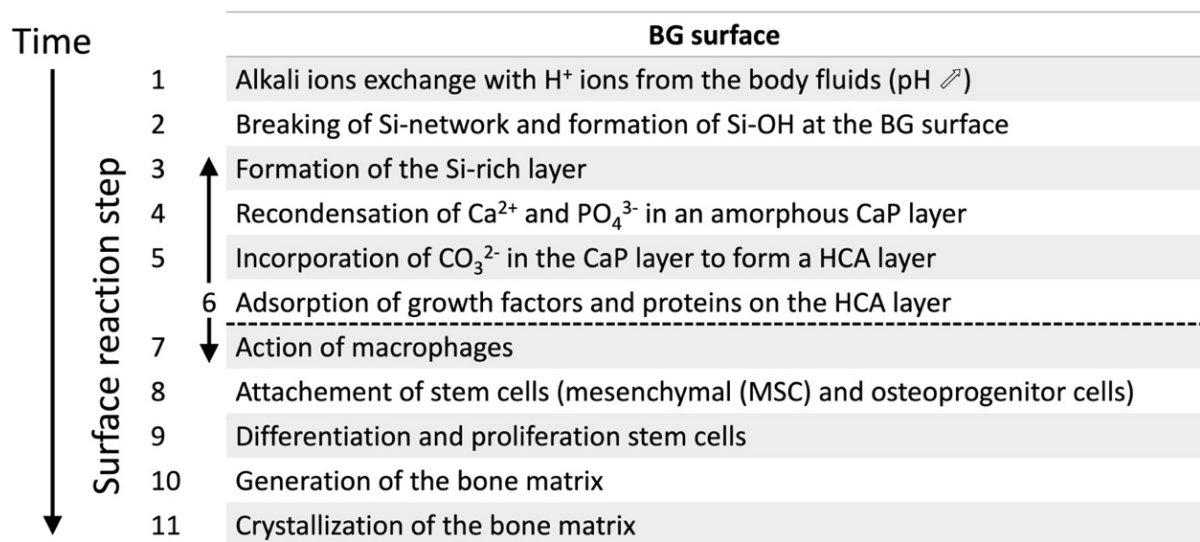
Figure 6. Sequence of reactions at the BG surface leading to the bonding with bone (modified from reference [96]).

However, traditional silicate BGs (45S5 and S53P4) have drawbacks. the main drawbacks lies in 1) their non-congruent dissolution mechanism that leads to glass remnants, even 14 years post-surgery [97] and 2) their fast and uncontrolled crystallization that, not only decrease the material bioactivity [98], but also inhibit glass particles sintering, when 3D scaffolds are being sought [99]. Owing to its high silica content, the BG 13-93, dissolve at a lower rate than 45S5 and S53P4 but is more resistant to crystallization [92].

In order to overcome the incomplete conversion of silicate BG into HA and further prevent crystallization during hot forming, borosilicate and borate glasses have been developed [24], [100]. It is commonly admitted that borate-based BG follow the same steps as silicate-based BG however, they do not form a "boron-rich layer", and the HCA layer forms directly at the surface of the BG due to their rapid dissolution behavior [101]. Huang et al. [100] and Yao et al. [102] investigated the dissolution behavior of silicate-based BG with varying amount of boron. They both found that the borosilicate-based BG produced converts faster and more completely to HA compared to their silicate counterparts. The poor mixing between the silica and the borate phase is the cause of the enhanced conversion rate of borosilicate-based glasses. While the borate phase will encourage hydrolysis, resulting in a faster dissolving rate and a higher amount of ions in solution, the silica phase will produce a Si-rich layer, permitting better cell adhesion and proliferation. Therefore, by varying the B_2O_3/SiO_2 ratio, it is theoretically possible to tailor the dissolution and HA conversion rate of BGs in order to match the bone regeneration rate in-vivo [67]. Furthermore, borate-based BG leaks boron which is as trace element in humans. The total of boron in human body ranges from 3 to 20 mg the majority of which is found in bones, nails and hair. Studies have revealed that boron interacts with vitamin D, calcium and magnesium which are all essential for bone metabolisms processes and a boron deprivation has been shown to be detrimental for the processes involved in bone formation and maintenance [17]. Furthermore, it has been demonstrated that boron plays an important role in angiogenesis, which makes it a very interesting element to use in a BG [16]. Nevertheless, just like Si, the exact mechanisms of action of boron in its metabolic functions has not yet been fully understood [103]. Consequently, Fu et al. [104] demonstrated a faster bone regeneration in-vivo for the borosilicate BG compared to silicate-BG. In addition to

improving the cell-material interactions, it has been proven that borosilicate BGs have an larger sinterability window, since boron not only decrease the activation energy for viscous flow but also reduces the crystallization tendency, which makes them highly interesting materials for additive manufacturing of BGs [14], [98], [99].

In the borosilicate BG family, a new composition investigated by Houaoui et al. [29] and reported for the first time in 2020, revealed to be an interesting composition for bone regeneration applications: the 13-93B20. The 13-93B20 is a variation of the 13-93 silicate BG of which 20% of the silicate content was replace by boron. They have reported that, used in a PLA/13-93B20 composite, the 13-93B20 releases ions beneficial to the cell fate and evidenced differentiation from C2C12 cells to a bone lineage upon culture in contact with PLA/13-93B20 composites and deposition of a mineralized matrix. One must keep in mind that high concentrations of boron have been reported to be toxic for the cells. However, when cultured in dynamic conditions or in-vivo, this effect disappears thanks to the dilution of the borate ions released from the BG [14].

Despite all the potential of BGs for BTE, there are still some drawbacks of using BGs, notably their brittleness and weakness to fracture [14]. That is why their use must be carefully considered depending on the targeted application. For instance, BGs have been successfully used in non-load bearing applications, maxillofacial surgery or as coatings on implants intended for load-bearing applications [105]. Nevertheless, there are ongoing research aiming at producing composites using BGs and polymers for load bearing applications.

2.1.2. Organic

For BTE, polymers are extremely interesting materials. Indeed, depending on their origins (natural or synthetic) they can yield different properties like bioactivity and biodegradability with variable mechanical properties and degradation rate. Due to their facile processing, they can be shaped in various structures from paste, to fill bone defects, to fixation devices like screws or even barrier membranes.

In orthopedic applications, the first bioresorbable polymer-based implants were introduced in the 70's. Those implants permitted an early limb mobilization after fixation thanks to a sufficient stability and

anatomical reduction, i.e. proper fracture fixation and reconstruction by the surgeon. Thanks to their biodegradability property, a second operation to remove the implant or repair soft tissues is not required because it entirely vanishes from the fracture site, which also allow to gradually transfer the mechanical strain, leaving healthy and strong bone in the place of the implant [106]. Furthermore, to provide a perfect implant for every patient, the implant can be trimmed to a customized form during surgery. Because there is no metal implant in the patient's body, CT scans exhibit less image distortion and MRI imaging in various locations of the body is feasible. The inflammatory reactions, restricted mechanical qualities, high costs, and specific storage conditions due to their bio-resorbable properties are known drawbacks of bioresorbable implants [106].

Polymers for orthopedic implants can be classified as natural or synthetic, both with their own advantages and drawbacks. Some examples are listed in **Table 1** and a few of them are described below.

o   Natural polymers

The intrinsic benefits of using natural polymers include bioactivity, good biocompatibility, the capacity to deliver receptor-binding ligands to cells and sensitivity to proteolytic degradation driven by cells. Nevertheless, those advantageous properties have their own drawbacks depending on the polymer [67], [107].

➢   Protein

♦   Collagen

Collagen, the most abundant protein in the human body, plays a vital role in the bone's extracellular matrix and is of great interest in designing biomaterials for bone tissue engineering [75], [108]. Collagen is biodegradable, biocompatible, and non-toxic to cells, making it a suitable biomaterial. However, it has low elasticity and mechanical strength, which can be improved through treatments [107], [108]. There are numerous types of collagens, with type I being the most prevalent in both the body and bone matrix [48], [107]. Despite its advantages, collagen sourcing from natural origins, such as bovine or porcine skin or tendons, can lead to quality variations and high costs [75], [107], [108]. Nonetheless, collagen is used in bone regeneration applications, as exemplified by the bone graft substitute Infuse[MC]

(Medtronic) [109]. In summary, collagen is a valuable biomaterial for bone tissue engineering due to its biocompatibility, despite challenges related to its natural sourcing and mechanical properties.

♦ Silk fibroin

For biomaterials, silk from silkworms like Bombyx mori and orb-spiders like Nephila clavipes have been studied. The silk produced by these organisms has outstanding mechanical properties in addition to a great biocompatibility, environmental stability, it is also biodegradable, flexible and easy to obtain in large quantities [110], [111]. One should note that, silk from B.mori has been used as material to produce sutures for centuries. It is also FDA approved since 1993 and therefore is of high interest to produce biomaterials [110], [111].

Silk is primarily made of 2 proteins: 1) silk fibroin (SF) a semi-crystalline fibrous protein made of 2 subunits: an amorphous light chain called silk I, and a heavy chain, also called silk II, organized in β-sheets giving SF its semi-crystalline structure, and 2) sericin, a globular protein acting as a "glue" between SF fibers. Although sericin has been reported to be biocompatible, the interaction between SF and sericin has been said to induce allergic reactions. Therefore, for the use of silk as biomaterials, the sericin is removed by a thermochemical treatment of the silk cocoon known as "degumming" [111]. However, this process induces slight modifications in the mechanical properties of SF notably a higher tensile strength. Nonetheless, even after degumming, SF keeps a similar Young's modulus [111]. Being a protein, SF has been shown to be susceptible to proteolytic degradation by various enzymes such as protease XIV, alphachymotrypsin and collagenase IA. The amino acids that are produced as SF is broken down can be absorbed in vitro or in vivo, which is advantageous for biomedical applications. The degradation rate of SF depends on the species it is produced by and can be tailored by chemical or thermal treatment for instance. Particularly, with increasing amount of silk II, the degradation rate of SF increases too. This allows to obtain a tunable degradation rate ranging from a few days to several months [75], [111].

SF offers a wide range of properties and can be processed using aqueous or organic solvents to be prepared in various forms like sponges, hydrogels, films or membranes and even chemically modified to be used in various biomedical applications [75].

In one study, Meinel et al. [112] demonstrated that SF sponges can be successfully used to heal CSD in rats femur. In another study, Kim et al. [113] demonstrated the formation of trabecular bone-like structures after 28 days of culture in osteogenic media with human mesenchymal stem cells (hMSC) in contact with an SF sponge.

➢ Polysaccharides

♦ Chitosan

Chitosan is a cationic polysaccharide made of glucosamine and N-acetylglucosamine, extracted and modified from chitin which is mainly found in the exoskeleton of crustaceans, mollusks and insects [75], [108], [114]. To obtain chitosan, chitin must be deacetylated and depending on its degree of acetylation (DA), chitosan's properties can vary [108]. Chitosan is a biocompatible, biodegradable, non-toxic, antioxidant, anti-inflammatory and hemocompatible material. It has the unique property of being able to attract both positively and negatively charged molecules thanks to the amine and hydroxyl groups in its chemical structure. Those features make it a highly interesting material for biomedical applications. Chitosan can easily be shaped into different forms including membranes, hydrogels, sponges and fibers and chemically modified with other molecules [75].

Chitosan production is inexpensive, easy and can offer more control over its final properties. It can degrade through human enzymes such as lysozymes, it is pH-sensitive and dissolves easily at low pHs but is insoluble at higher pHs. This property makes chitosan highly interesting as a delivery matrix for other molecules [77]. However, the poor osteoinduction properties of chitosan causes the bone formation to only occur over long period of time, from months to years. Therefore, it is necessary to combine chitosan with other molecules, such as growth factors, or bioactive material to shorten the bone-forming time and improve the chitosan-based materials efficacy [77].

♦ Hyaluronan /Hyaluronic acid

Hyaluronic acid, also called hyaluronan (anionic form present in-vivo), is a polysaccharide composed of alternating disaccharide units of D-glucuronic acid and N-acetyl glucosamine. Hyaluronan belongs to the family of glycosaminoglycan and can be found throughout the human body in the ECM [109], [115]. Hyaluronan can be found in most connective tissues ECMs like cartilage, synovial fluids,

umbilical cords, dental pulp or the dermis. Hyaluronan acts as a lubricant, keeps the tissues hydrated and helps to maintain the physical form of the ECM [77], [115]. Hyaluronan, through interactions with cell receptors, plays a role in tissue morphogenesis, regeneration, cell migration and differentiation [77], [109].

Due to its unique viscoelastic properties, biocompatibility and non-immunogenicity, hyaluronic acid uses have been centered on cartilage, bone, and osteochondral tissue engineering, most probably because of its crucial role in the ECM [77].

In 2010, Baldini et al. [116] investigated the use of a composite graft made of hyaluronic acid and autologous bone graft for the repair of post extraction dental bone defect. They evidenced that the use of hyaluronic acid combined with the autologous bone graft increased the injectability of the paste in the defect site. They also showed that bone regeneration, angiogenesis and the remodeling were enhanced with the paste.

o   Synthetic polymers

As opposed to natural polymers, which have several drawbacks, synthetic biomaterials are typically physiologically inert, have more predictable properties, batch-to-batch homogeneity, and have the special advantage of having tailored property profiles for specific applications. In general, hydrolytically degradable polymers are favored as implants because they exhibit less variance from site to site and patient to patient than enzymatically degradable polymers [107]. Polyesters are amongst the most studied polymers for orthopedic applications due to their favorable properties like great mechanical strength, durability and degradability [117]. Therefore, in this section, focus will be made on some polymers in the polyester family used for orthopedic applications such as poly-glycolic acid (PGA), poly-caprolactone (PCL) and poly-lactic acid (PLA) (**Figure 7**).
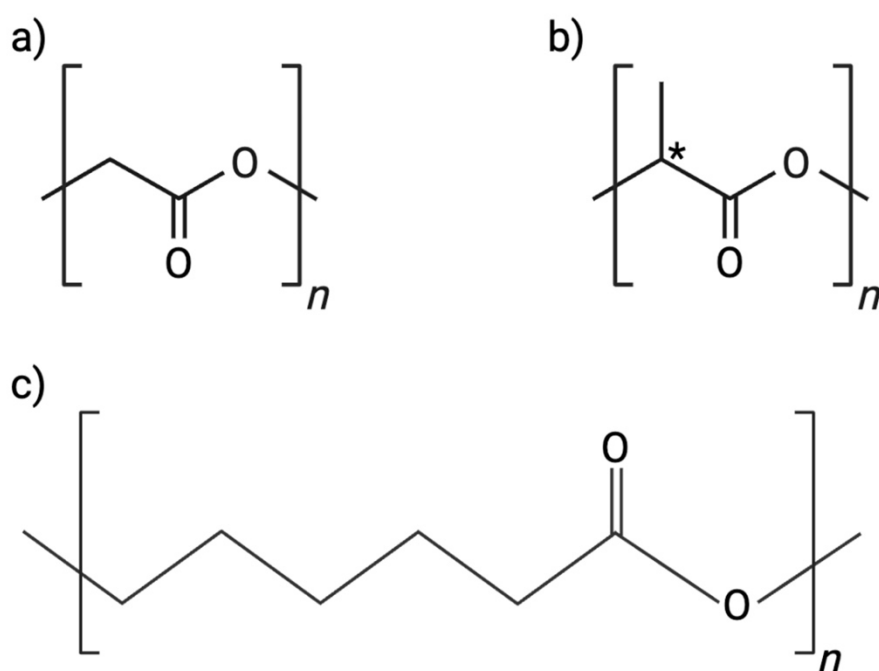
Figure 7. Illustration of the chemical structure of a) poly-glycolic acid, b) poly-lactic acid with its chiral center mentioned with * and c) polycaprolactone (produced using BioRender, BioRender.com).

  ◆ Poly-glycolic acid

Poly-glycolic acid (PGA) is the simplest linear aliphatic polyester made of repeating units of glycolic acid (**Figure 7a**) [118]. PGA is a highly crystalline polymer (crystallinity > 50%) due to the absence of side groups [117]. PGA is biodegradable and starts to degrade in-vivo within a few weeks, it loses mechanical strength rapidly, around 2 to 4 weeks post-implantation, and is entirely degraded within a few months thereby reducing the need of a second removal intervention and the infection risks associated [75], [119], [120]. The PGA degradation by-products are biocompatible and non-toxic, although they can elicit an inflammatory response due to their acidic nature. Thanks to its high tensile strength, PGA is suitable for various uses such as sutures, surgical mesh, scaffolds for TE, barrier membrane and even in textile technologies for instance [75], [119]. Furthermore, it is possible to improve mechanical properties of PGA material by combining it with other materials, such as collagen or calcium phosphate, and produce composites. In addition the high thermal stability and high melting point of PGA makes it quite resistant and suitable for heat-sterilization processes [75]. Since its FDA

clearance in 1969, PGA has been marketed as synthetic sutures under the trade name Dexon®. It is regarded as the first synthetic biodegradable polymer for biomedical applications [117].

♦ Polycaprolactone

Poly-ε-caprolactone, or polycaprolactone (PCL) to simplify, is an aliphatic polyester obtained by ring-opening polymerization and is a long chain without side groups (**Figure 7c**). The degradation rate of PCL is quite long and range from 2 to 3 years [117].PCL is biocompatible, it has a low tensile strength and high elongation which makes it suitable for drug delivery devices and TE scaffolds [117]. However, PCL can easily be blended with other polymers such as polycarbonates, polybisphenol or natural rubber for instance which in turns improves its properties, notably, copolymers of PCL and poly-D,L-lactic acid (PDLA) have been synthetizes with the aim to reduce its degradation rate [129, 130]. Nevertheless, due to its properties unsuitable for its use in orthopedic applications, there is no medical device listed as only composed of PCL but more made of blend of PCL and other polymer [118].

♦ Poly-lactic acid

Poly lactic acid (PLA) is also an aliphatic polyester and is made of repeating units of lactic acid. Because of its superior biocompatibility and mechanical qualities, PLA has become one of the most studied and used materials for tissue engineering. It is also one of the most commonly used biopolymers for medical devices like screws, plates, valves, and other items [120]. Lactic acid is a chiral molecule, meaning that it can be found either as an L or D isomer and PLA can be found as poly-L-lactic acid (PLLA), poly-D-lactic acid (PDLA) or as a racemic mixture giving poly-D,L-lactic acid (PDLLA) (**Figure 7b**). PLA can be produced either by chemical synthesis or biologically. The biological approach for producing PLA is based on the fermentation of carbohydrates by an engineered bacterial strain of Lactobacilli. This method has been proven to be more cost-effective than the chemical route and is therefore preferred nowadays to produce PLA. Different bacterial strains can produce either D or L-lactide [117], [120]. PLLA and PDLA, due to their different stereochemistry yield different physical properties, notably their degradation behavior, resulting in different applications. PLLA is a semi-crystalline polymer with a degree of crystallinity close to 40% and the crystallinity of the polymer can be adjusted by changing the processing conditions. PLLA has a high modulus, approximately 4.8 GPa, good tensile strength and

a low extension which are considered appropriate characteristics for load-bearing applications. Many orthopedic devices have been produced with PLLA here are some examples: Phantom Soft Thread Soft Tissue Fixation Screw®, Phantom Suture Anchor® (DePuy), BioScrew®, BioAnchor®, Meniscal Stinger® (Linvatec) and Clearfix Meniscal Dart® (Innovasive Devices) [117]. PDLA on the other hand is amorphous and degrades faster than PLLA which requires more than 2 years to completely degrade [118]. PDLA low modulus (around 1.9 GPa) and faster degradation rate makes it a favored material for scaffolds, degradable sutures or drug delivery systems [117]. It is possible to make a copolymer with PLLA and PDLLA called the poly (L-co-D,L-lactic acid) (PLDLA) which present particularly interesting properties combining the strength of PLLA and the faster degradation rate of PDLLA. The ratio between PLLA and PDLLA can be tailored which allows to obtained specific properties with varying degradation rate and mechanical strength [121], [122]. Despite all the advantages in using PLA for biomedical devices, the degradation products of PLA can elicit an inflammatory reaction due to their acidic nature even though they are eventually eliminated from the body [75].

Whichever polymer is chosen, natural or synthetic, they lack either mechanical strength or bioactivity. On the other hand, inorganic materials, particularly bioactive glasses, are very brittle which limits their use, particularly in load bearing applications. Therefore, single component scaffolds are less interesting, and researchers have tried to find a way to enhance materials properties by combining organic and inorganic compounds into composites.

2.1.3. Composites organic/inorganic for bone tissue engineering

Bone is made of an organic matrix combined with inorganic particles of hydroxyapatite. This makes bone a natural composite. BG is a highly interesting material for BTE thanks to its outstanding bioactivity compared to other bioceramics. Furthermore, the possibility to tailor the BG composition by incorporating specific ions is a highly interesting property to boost some physiological processes such as angiogenesis. However, the brittleness and low mechanical strength of BGs and the difficulties to shape it in the desired structure are a major drawback for BG uses as a single component material. One strategy to get around these drawbacks is to combine BG with polymers to create a composite scaffold that optimizes the use of both components [84]. The aim is mainly to improve the processability,

mechanical properties, printing performances and bioactivity of the scaffolds produced [73]. For example, both natural and artificial polymers, such as collagen, polylactic acid (PLA), polyglycolic acid (PGA), copolymers made by grafting PLA and PGA (PLGA), or polycaprolactone (PCL), demonstrated qualities that made them appropriate for use in BTE to produce composite scaffolds [123]. The BG can be used either as a coating of the polymer part or as a filler in a polymer matrix to produce scaffolds with varying porosity with techniques such as 3D printing or electrospinning [124].

Among natural polymers used to produce composites, collagen is a common choice since it composes 90% of the total weight of bone ECM [124]. However, the low mechanical properties of collagen make it unsuitable for the fabrication of load-bearing scaffolds. Therefore, to counterbalance its weak mechanical properties, it can be used in composites with bioactive glass particles as filler [125]. Long et al. [126] reported on the fabrication of a scaffold base on collagen fibers and bioactive glass fabricated by a slurry-dipping technique. The scaffold prepared was highly porous with a porosity of $81 \pm 4.6\%$ and has a much lower water absorption compared to the collagen scaffold alone. The mechanical properties of the scaffold prepared was close to the trabecular bones' with a compression strength of 5.8 ± 1.6 MPa and an elastic modulus of 0.35 ± 0.01 GPa.

There are other options in the natural polymer family to produce composites such as chitosan or silk, which are among the most investigated ones for the production of composites with BG. With silk for example, the outstanding strength, elasticity, biodegradability and low FBR it provokes makes it a highly interesting material for BTE but silk lacks osteogenesis potential which limits its application in BTE. Therefore, combining it with BG can counterbalance this lack of bioactivity for bone regeneration [125]. Du et al. [127] investigated the properties of a mesoporous BG/SF 3D printed scaffold and demonstrated a better compressive strength than the control as long as an increased expression of osteogenic biomarkers in human bone marrow stem cells (hBMSC). Chitosan on the other hand, is a polysaccharide with great biocompatibility, biodegradability and antimicrobial properties that has great potential as scaffold for BTE. However, like collagen, it lacks mechanical strength and therefore its use as a composite with BG can also increases its mechanical properties [125]. For example, Yang et al. [128] developed a 3D porous scaffold based on chitosan fibers prepared by needle punching and then

dip-coated with BG. The prepared scaffold had a great porosity of 77.52% and a pore size around 50 μm. They showed that with BG the fabricated scaffold had a water absorption tremendously decreased from 570% to 59% and the mechanical properties were also similar to that of trabecular bone with a compression strength of 7.68 ± 0.38 MPa and an elastic modulus of 0.46 ± 0.02 GPa. They also reported a good biocompatibility of their scaffold with hBMSC [128].

Using natural polymers in a composite scaffold with BG has many advantages such as the great biocompatibility and enzymatic degradability of the polymers and the enhanced mechanical properties thanks to the BG phase. However, the common disadvantage of using natural polymers for composite is that it is difficult to have reproducible batches of natural polymer since they are naturally sourced and extracted [90]. Nowadays, it is possible to produce tough composites using synthetic biodegradable polymers as the matrix and BG as the filler phase. As synthetic polymers, the most often used are PLA, PGA and a co-polymer of PGA and PLA the poly lactic-co-glycolic acid (PLGA) [90]. One example of composite with 45S5 and PLGA investigated by Lu et al. [129] has a Young's modulus of 51 ± 6 MPa which is double that of the PLGA alone but has a comparable compressive strength of 0.42 ± 0.05 MPa. Here, the compressive strength of the composite is too low, highlighting the fact that, although the goal of making composites is to enhance both materials properties, adding BG particles can sometimes have detrimental effects on the construct [90]. But there are some examples of promising composites such as the PDLLA-45S5 Bioglass® loaded foams produced by thermally induced phase separation (TIPS), a variation of the freeze-drying process [130], [131]. The prepared foams had tubular pores of ≈ 100 μm in diameter, interconnected with pores of 10 to 50 μm and an overall porosity > 90%. The thin walls of the foam allowed the exposition of the BG particles, but it also contributed to low mechanical properties. For instance, the foams prepared with 15 vol% of BG presented a Young's modulus of 1.2 MPa and a compressive strength of 0.08 MPa. The authors concluded that the low mechanical properties were probably due to the low loading of the composite with the BG particles [131]. The first composite fabricated with 13-93B20 and PLA by melt-extrusion was proposed by Houaoui et al. [29]. It demonstrated interesting properties notably its osteoinduction properties, the ability to induce cells differentiation towards the osteogenic lineage and the ability to withstand bone

matrix synthesis by cells. It also demonstrated a similar Young's modulus compared to the scaffold of polymer single component around 3.5 GPa but a decrease of the shear stress force from 46.6 MPa to 32.1 MPa [29].

Some other options using non-degradable polymer matrix exists and are investigated. One example of fiber-reinforced composite with BG S53P4 was fabricated by Vallittu *et al.*[82] and showed great outcomes for cranial bone reconstruction. The fiber glass reinforced composite was made of biostable glass fiber laminates and a dimethacrylate polymer matrix in a sandwich structure. The space between the inner and outer laminates was filled with S53P4 particles to act as bioactive agent. They demonstrated the beneficial effect of the BG particles loaded in the implant to improve the ossification post-cranioplasty. Indeed, after careful analysis of the implant after extraction, they demonstrated the presence of neo-vascularization in the implant and biomineralization which are markers of denovo bone formation. However, one should note that, in this study, only one patient received the prototype material and infection at the scalp wound area made necessary the removal of the implant. Furthermore, such material is not biodegradable due to the glass fiber and polymer matrix nature. Therefore, removal is eventually necessary for this type of material.

Therefore, although composites are promising construct for BTE, their properties must be scrupulously studied and the clinical context related to each patient must be carefully considered, since all combination of polymer-BG do not always have a synergistic effect between the qualities of each single component.

As demonstrated above, there are various materials available to produce bone filling bio(materials). Such variety of materials nature results obviously in a large diversity of processing methods to produce bone filling scaffolds. In the following section this subject will be addressed.

2.2. Fabrication method

In terms of engineered methods for the fabrication of bone filling materials, a variety of options are available. There is essentially 2 main groups: 1) the commonly used techniques, consisting of solvent casting, phase separation methods or electrospinning for instance, and 2) the advanced techniques,

which are often based on computer-aided design (CAD) and 3D printing [124]. However, especially for BGs, all methods are not necessarily applicable and must be adapted to allow the production of a scaffold with the appropriate properties [159]. For fabricating a BG porous scaffold, the minimum parameters for allowing tissue ingrowth and tissue function are typically thought to be interconnected pores with a mean diameter (or width) of 100 µm or higher and open porosity of > 50%. In the conventional methods applied to the fabrication of BG porous scaffolds, we can find sol-gel foaming, organic phase burning out (with porogen for instance), foam replication or freeze casting for example (**Table 3**). In the advance methods, we find 3D-printing methods like selective laser sintering, stereolitography or direct ink writing techniques such as robocasting (**Table 3**). The latter being the method we have chosen to prioritize for elaborating 3D porous BG-based structures, the other methods will be described in the annex with their advantages and disadvantages (**Annex 1**) [132].

Table 3. Summary of the available manufacturing methods to produce glass-based scaffolds for bone tissue engineering. Adapted from [132]

Group	Technological class	Adapted method to glass-ceramic scaffold production
Conventional methods	Foaming techniques	Gel-casting foaming, sol-gel foaming, H2O2 foaming
	Thermal consolidation of particles	Organic phase burning out: polymeric porogens, starch consolidation, rice husk method
	Porous polymer replication	Coating methods, foam replication
	Freeze-drying	Freeze-casting of suspensions, ice-segregation-induced self-assembly
	Thermally induced phase separation	
	Solvent casting and particulate leaching	
Advance techniques (additive manufacturing)	Selective laser sintering (SLS)	
	Stereolitography	
	Direct ink writing	3D printing, ink-jet printing, robocasting

Robocasting can be considered to be the most powerful direct ink writing technique based on the continuous extrusion of an ink filament. The set-up involves the use of a cartridge containing the ink that is extruded by pressurized air under the form of a filament through a computer-controlled head, which follows a CAD file, onto the building platform (**Figure 8**). The ink used for robocasting is slurry of a homogeneous colloidal suspension of the glass ceramic particles and a polymeric binder. The ink must have very specific properties for the process to be successful. Those properties have been described by Cesarano in 1999 [133] and are still applicable. Namely, the ink must:

1) Be pseudoplastic to allow the ink to flow through the small orifice of the nozzle while generating minimal shear stress.

2) It must setup into a non-flowable mass. Meaning that the ink must somehow solidify enough to keep the rod-like filamentous structure even after it has been printed on the building platform.

3) It must be able to withstand the weight of other layers without deformation.

Therefore, the robocasting method relies on the ink's capacity to change its viscosity through physical and/or chemical processes in order for the ink to become strong enough to support the printing of the superior layers. During the ink preparation, the first aim to achieve is to produce an ink with the highest particle/binder ratio possible in order to have as much particles as possible to reduce the drying shrinkage. However, and regardless of the ink properties, direct air extrusion has some disadvantages, one of which is the potential for uneven shrinkage brought on by various air flows within the structure [132].

Other than the inks' intrinsic properties, there are quite a few other factors that can influence the final result of the printing process. For instance, the diameter of the extruded rod, which is not only determined by the size of the nozzle but also by the pressure required to extrude the rod from the cartridge and the printing speed. Indeed, an important printing speed and a low extruding pressure would cause the rod to brake during the printing process due to a lack of material. On the other hand, a low printing speed and a high pressure would cause the rod to be enlarged and deformed, therefore

destroying the structural features. Consequently, those two parameters, the extruding pressure and printing speed, must be adjusted in real time to obtain a constant shape [132]. Another parameter to control is the spacing along the z-axis which is fundamental to allow the correct adhesion of each new layer to the underlaying one while avoiding the deformation of the structure. In addition, the printing substrate (surface on which the ink is extruded) has a crucial role. Indeed, it must be absolutely plane and enable attachment of the ink during the printing process, while still allowing to detach the completed and dried object without damage to the structure [132].
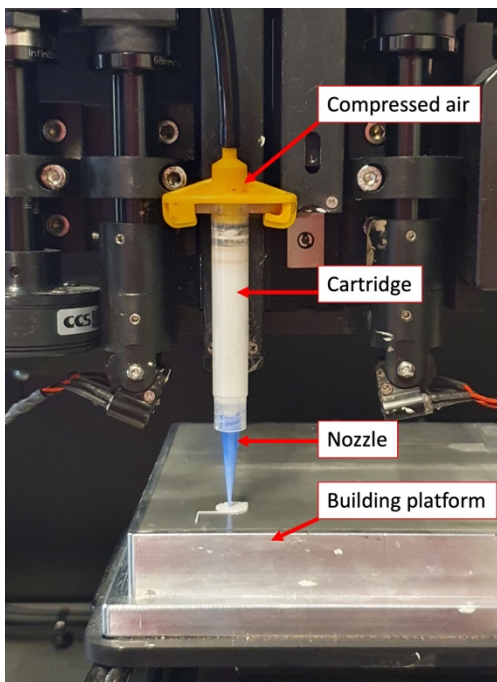
Figure 8. Experimental robocasting setup to produce BG scaffolds, photo credit: Audrey Deraine Coquen

The robocasting method was first used by Franco et al. in 2010 [134] when they managed to print a hydrogel-based ink with calcium phosphates (HA and β-TCP) particles. In their work, they proposed the use of Pluronic, a surfactant block co-polymer (polyethylene oxide [PEO]–propylene oxide [PPO]-PEO), as the binder and dispersant to create the ink. They emphasize the fact that using a large size distribution of the particles allows the smaller particles to rearrange the bigger ones which permitted to load more particles and reduce the pressured needed for printing [134].

Robocasting has proved to be a very powerful tool in the fabrication of glass scaffolds for bone regeneration and even in load bearing site. Indeed, robocast glass scaffolds have been fabricated exhibiting extremely high compressive strength, sometimes even higher than that of cortical bone, ranging from 13 to 142 MPa. Furthermore, by tailoring the particles and nozzle size, it is possible to produce glass scaffolds with a porosity ranging from 50 to 70 vol% with pore dimension varying from hundreds of micrometers to half a millimeter. In addition, the method allows an incredibly easy control of the scaffolds structure and the possibility to produce functionally graded porous devices [132].

However, regardless of the material used to produce the bone filling scaffold, or the method of fabrication, they all present the disadvantage of not being able to protect the defect from fibrous tissue ingrowth, eventually resulting in a suboptimal bone regeneration and even sometimes implant failure. For this reason, barrier membranes have been developed to guide the tissue regeneration, and cover the defect to avoid any deleterious fibrous tissue infiltration. The clinical concept of using barrier membranes for bone regeneration is called "guided bone regeneration" (GBR) and was first introduced by Dahlin et al. in 1988 [36]. In the following section, the principle of GBR will be briefly described and some common membranes used in clinical settings will be presented. Since materials used to produce barrier membranes are often the same as the bone filling bio(materials), there properties will only be evoked, and a focus will be made on the products available on the market or the results of the research on the subject. Furthermore, another section will present a few of the available fabrication methods to produce porous barrier membranes.

3. Guided bone regeneration and barrier membranes

It is in 1957 that Murray et al. [135] first reported on their investigation of the use of a "plastic cage" in spinal fusion made to create a secluded space in the bone to prevent fibrous tissue to infiltrate the defect which would preclude the bone regeneration in the defect. They hypothesized that the soft tissue cells were faster proliferating than the bony cells to form the new bone. Therefore, they suggested that by

creating a secluded space to keep the soft tissue out and allow the bony cells to proliferate it is possible to obtain a better bone regeneration [135]. After this study, many followed but it is not until the 80's that the GBR therapeutic potential was recognized, and Dahlin and colleagues spearheaded the research on the use of GBR for jaw and mandibular defect repair. It is Dahlin's group that suggested the clinical protocol for the use of barrier membranes in GBR [35], [136]. The GBR procedure consists of the surgical installation of a cell occlusive membrane facing the bone surface in order to physically seal off the skeletal location that needs regeneration (**Figure 9**). Meanwhile, the membrane preserves and establishes a closed-off area, giving the osteoprogenitor cells an environment favorable for their recruitment, proliferation, differentiation along the osteoblastic lineage, and expression of osteogenic activity to eventually regenerate the lost bony tissue [137]. In the GBR procedure, the membrane can be used either alone or in conjunction with a particulate bone graft and/or bone substitute in order to enhance the bone regeneration. There are 4 principles that must be met to ensure a successful GBR procedure, 1) the soft tissue surrounding the defect must be correctly excluded, 2) the membrane must have appropriate mechanical properties to ensure space maintenance and not collapse in the defect as long as being easily handled in a surgical setting , 3) the fibrin clot must be stable and kept inside the created space and 4) the surgeons must be able to close the wound properly following the membrane placement [35], [138]. Furthermore, the barrier membrane must have the appropriate porosity to allow nutrient flow while still providing a secluded space to keep each cell type apart [45]. In the following section, some polymers used to produce barrier membranes for GBR procedures will be presented along with their advantages and drawbacks.
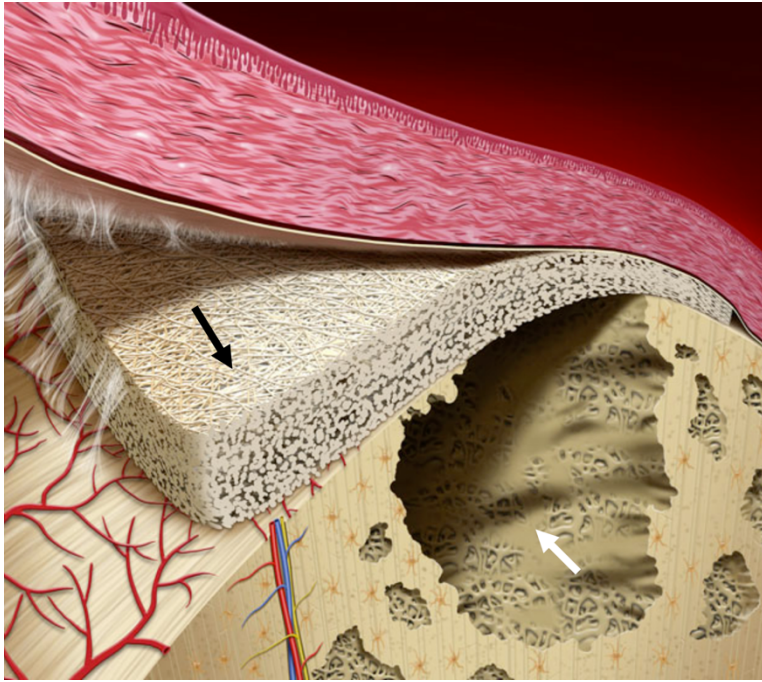
Figure 9. Schematic of the principle of the GBR procedure, black arrow = barrier membrane, white arrow = bone defect protected by the barrier membrane. Reproduced and modified from [38].

3.1. Nature of the barrier membrane

3.1.1. Non-resorbable barrier membranes

The first proposed membranes with a barrier function were non-resorbable and either made of polymer - polytetrafluorethylene (PTFE) - or metals such as titanium and titanium alloys or even alumina and it's alloys [139]. PTFE and some titanium barrier membranes will be presented in the following section.

3.1.1.1. Polytetrafluorethylene

Polytetrafluorethylene (PTFE) is a fluorocarbon polymer (**Figure 10a**) biocompatible, inert and it does not elicit a FBR in humans. However, PTFE is non-porous, therefore less interesting for barrier membrane because, although the membrane must ensure proper cell segregation, it must stay porous to allow nutrients and waste flow to ensure appropriate healing of the defect. Therefore, expanded PTFE (e-PTFE) was developed. PTFE and e-PTFE are identical chemically, but e-PTFE has the advantage of being porous, therefore allowing proper flow of fluids [35]. The e-PTFE is the first synthetic polymer reported for its use in GBR procedures. Thanks to the e-PTFE chemical stability, and mechanical properties, it maintains the tissue exclusion property of the membrane through time even in the very

corrosive environment of the body. However, its excellent mechanical properties can also be their downfall since their excessive rigidity can cause membrane exposure leading to complications. Indeed, when exposed to the oral cavity, bone augmentation and osseointegration can be impaired because of bacterial infection and the migration of microorganism [38], [75]. Furthermore, because e-PTFE membranes are not resorbable, a second surgery is required to remove the membrane which can also cause complications and damage the newly formed bone.
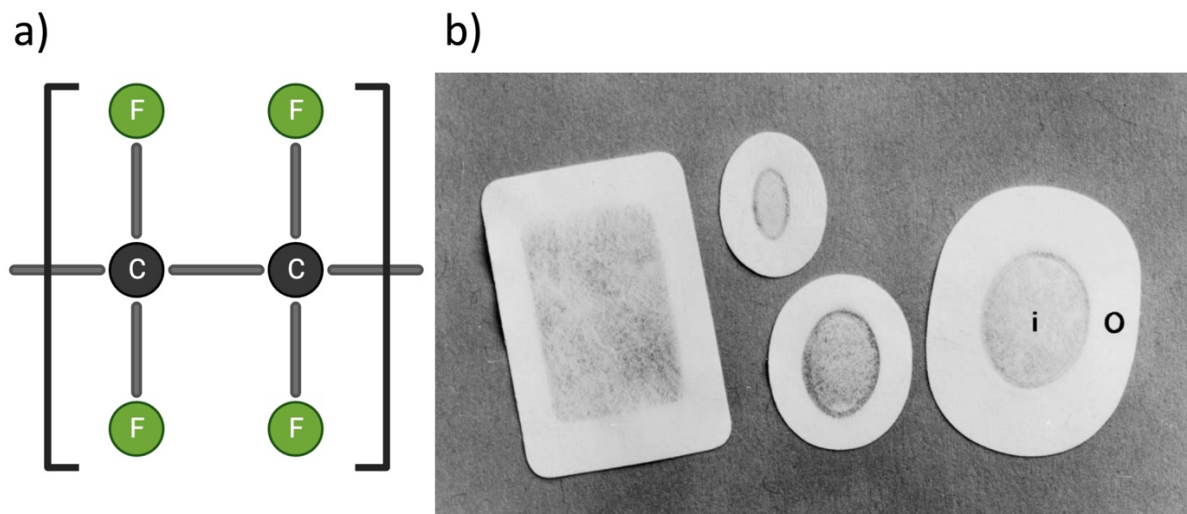
Figure 10. a) Chemical structure of polytetrafluoroethylene (produced using BioRender, BioRender.com) and b) example of e-PTFE membrane (Gore-Tex® membrane) from [35].

3.1.1.2. Titanium mesh and cages

Titanium is one of the most used metals as a biomaterial, especially in the context of bone because out its outstanding mechanical properties. Titanium meshes are traditionally used to maintain a graft in place and ensure volume maintenance, not to provide a barrier function because of its large pore size. However, it has been used as a barrier membrane and has shown great results in alveolar bone reconstruction. Titanium mesh is usually combined with PTFE or collagen membrane in clinic. The titanium mesh providing volumes stability and the membrane space maintenance. Nevertheless, researchers tried to enhance the clinical suitability of the titanium meshes and used 3D-printing to produce what is called "titanium cages". This enables a precise fit to the bone deficiency and prevent the negative effects of improper implantation [140]. Nonetheless, either titanium meshes or cages are

not resorbable and therefore must be removed after bone regeneration which bears the risk of damaging the neo-bone formed and causing other complications.

These drawbacks of non-resorbable membranes lead researchers and surgeons to try to find other options, to avoid the second surgery notably. They found alternatives with resorbable polymers that allows a procedure in only one surgery since the membrane completely degrades with time.

3.1.2. Resorbable barrier membranes

Just like bone filling materials, barrier membranes can be made of non-biodegradable of biodegradable polymer. The most common are presented in the following section with their respective advantages and drawbacks.

3.1.2.1. Natural polymer-based barrier membranes

♦ Collagen

As mentioned before, collagen is one of the most abundant proteins in the human body. It is a structural protein playing a crucial role in the structure of the ECM in bone notably. Indeed, bone ECM is composed of collagen fibrils on which hydroxyapatite crystals have precipitate. Therefore, collagen is one of the most relevant proteins to use to produce barrier membranes. Indeed, it is biocompatible, biodegradable and has osteoinduction properties. However, the low mechanical properties of collagen and its susceptibility to degradation are the main drawbacks in the use of collagen as component of barrier membranes [75], [140].

Collagen membranes come in a wide variety of forms and are employed in clinical settings. Some examples include Bio-Gide® (Geistlich Pharma AG, Wolhusen, Switzerland), Jason® (botiss biomaterials GmbH, Zossen, Germany), Ossix® (Datum Dental, Lod, Israel), and Periogen® (Collagen Corporation, Palo Alto, CA, USA) (**Figure 11**). These collagen membranes have distinct chemical and physical structures as a result of the various collagen sources and extraction techniques [140].

Figure 11. Examples of collagen membranes available on the market, namely Bio-Gide® (Geistlich Pharma AG, Wolhusen, Switzerland), Jason® (botiss biomaterials GmbH, Zossen, Germany), Ossix® (Datum Dental, Lod, Israel).

There are other options than collagen that have been investigated by researchers, like chitosan or silk fibroin membranes, but those have not yet reached the market, like chitosan or silk fibroin.

♦ Chitosan

Chitosan as described above is extracted from chitin through deacetylation and is a polymer composed of glucosamine and N-acetylglucosamine [38], [75]. Chitosan as very interesting properties as a biomaterial as it is biocompatible, biodegradable, it has a low immunogenicity and also presents anti-microbial (bacteriostatic) properties. Furthermore, it has the unique property of being able to attract both positively and negatively charged molecules due to the amino groups present in its chemical structure. This feature allows to crosslink chitosan with various proteins or drugs to modify its properties. This is especially interesting to enhance chitosan's mechanical properties. Indeed, the low mechanical properties of chitosan and the limited control over the degradation rate has been a limitation to its use in clinic [38], [75]. That is why nowadays chitosan is more often use in composites with other polymers and/or molecules.

For GBR applications, chitosan can be processed through solvent casting, freeze drying or electrospinning for example. As of today, and to the best of this authors knowledge, there has not been any membrane approved for GBR procedures based on chitosan. However, chitosan-based barrier membranes have been tested in-vitro and on in-vivo and have shown encouraging results. In rats, compared to individuals in the control group, individuals treated with chitosan membranes demonstrated effective cell occlusion and a positive osteogensis impact [141]. The same outcomes were also seen in rabbits with cranial defects treated with chitosan nanofiber membranes; new bone filled the defects and bonded to the old bone after 4 weeks [142]. More recently, a chitosan/polyurethane nanofibrous membrane loaded with silver nanoparticles showed great biocompatibly and anti-microbial properties in-vitro [143].

♦   Silk fibroin

As described above, silk fibroin is a protein that can be produced by various species, but the most used silk for biomaterials comes from Bombyx mori. Silk fibroin has suitable mechanical properties to be used as membrane, it is also biocompatible and biodegradable and degrades completely over a period 12 months [144]. There are several ways to make silk membrane, including electrospun technique, casting technique, and straightforward separation approach. In the rat or rabbit calvarial defect model, silk fibroin membrane demonstrated good bone repair and reduced inflammation, regardless of the production process [145].

However, the biggest drawback of employing silk fibroin in GBR applications is that it can dry out and become brittle. Its mechanical strength and durability can be compromised, making it difficult to handle. Adding plasticizers or raising the water content are examples of solutions to this issue that aim to prevent the creation of hard β-sheet structures. Additionally, the mechanical characteristics of silk fibroin membranes may be impacted by variations in temperature and pH [75]. Nevertheless, silk fibroin remains an excellent candidate for biomaterials fabrications. Indeed, along its valuable mechanical properties, it contains many active sites that can act as bonding spots for potential drugs, bioactive molecules or cells to enhance the osteogenic properties of silk and promote the bone regeneration [75].

Silk membranes can be produced through various techniques such as electrospinning, freeze drying, micropatterning or bioprinting and can be incorporated in composites with polymers, hydroxyapatite or even magnesium oxide which is also an option to increase the osteogenic properties of silk [75].

One example of material is the composite membrane investigated by Ghafouri et al. [146] made of silk fibroin and poly(ethylene oxide) electrospuned fibers. A functionnaly graded membrane (FGM) was created by mechanically pressing two layers of the membrane pattern together. The tight layer had a superior barrier effect, preventing epithelial tissue growth into bone defects, whereas the loose layer was intended to direct osteogenic cell proliferation and bone regeneration. The fabricated membrane presented great mechanical properties, no cytotoxic effect on human dental fibroblasts and retained its bilayer configuration after 8 weeks suggesting that the construct might be of interest for a use as barrier membrane in GBR. Another study by Sankar et al. [144] investigated for the first time the use of silk fibroin membrane, in combination with a xenograft, in human for the treatment of periodontal disease. They demonstrated that, compared to the use of a collagen membrane, using a silk fibroin membrane in conjunction with a xenograft had a better outcome with an increased bone regeneration. Furthermore, compared to collagen membrane, their silk membrane can be stored at RT and be sterilized through ethylene oxide, autoclave or irradiation which would bring the overall cost of the intervention down. However, the authors emphasize that more clinical studies are required with a bigger patient group notably and other parameters to confirm their findings.

Natural polymers have many advantages especially the fact that they retain their natural biological properties that can more or less promote osteogenesis. However, the inherent cost of their extraction can make the cost for the patient increase drastically. Furthermore, their mechanical properties are not always suitable and because they are extracted, their use carries the risk of disease transmission although processes in place allows to control this risk. Therefore, researchers have investigated the use of synthetic bioresorbable polymers, to produce barrier membranes.

3.1.2.2. Synthetic polymer-based barrier membrane

Most barrier membranes developed from synthetic polymers nowadays are made of aliphatic polyesters, especially PLA, PGA, PCL and their copolymers. The most interesting property of those polymer is the possibility to tailor their degradation rate by making co-polymers [40]. Overall, synthetic bioresorbable membranes have the following benefits: 1) they enable for a one-step procedure; 2) they are radiolucent, allowing imaging; and 3) their biodegradability eliminates any potential stress shielding effects. In contrast, the rate of the membrane resorption, which is governed by elements including the regional pH and material composition, is variable and uncontrollable [33].

♦ Poly(glycolic acid) (PGA)

PGA is the simplest aliphatic polyester with the highest degradation rate. It is biocompatible and degrades into carbon dioxide and water in the human body. However, due to its fast degradation rate it is rarely used as a separate barrier membrane but more often used as a copolymer, especially PLGA, and in combination with other materials, such as calcium phosphate cements or hydroxyapatite [75], [139]. It has a high tensile strength and high thermal stability and melting point which makes it suitable for many biomedical applications notably as sutures and as GBR membrane.

Poly(lactic-co-glycolic) acid (PLGA) is more often used in biomedical applications because it has a higher degradation rate compared to PGA single component materials. Both subunits of PGA and PLA are biocompatible and biodegradable and the degradation rate and mechanical properties of the copolymer can be tailored by adjusting the polymers ratio [75]. Several barrier membranes made of PLGA are available on the market. Some examples are Cytoflex® Resorb from Unicare Biomedical (**Figure 12a**) or Tisseos® from Biomedical tissues (**Figure 12b**). Nevertheless, degradation product of PGA and PLGA can cause an inflammatory response due to their acidic nature, although they are not toxic to the cells [75].

♦ Polycaprolactone (PCL)

PCL is a biodegradable, biocompatible, biobased aliphatic polyester with an amorphous structure. It is a thermoplastic polymer, like PGA or PLA, which means that it can be melted and molded in different shapes and can be reheated and remolded, although this can alter its physicochemical properties [75].

Thanks to these characteristics, PCL has great toughness yet is flexible and has a low melting temperature and a low degradation rate (2-3 years) which makes it attractive for biomedical purposes [75], [140], [147]. Nevertheless, the long degradation time of PCL can be a downside and therefore efforts have been done to combine PCL with other components like hydroxyapatite or other polymers, like gelatin, to decrease this degradation time and increase PCL's mechanical properties. One example of membrane available on the market based on PCL is made of a copolymer of PCL and PDLLA, Vivosorb® from Polyganics (**Figure 12c**). This membrane was used as nerve guide but, some studies have revealed its potential as GBR membrane [148].

♦ Poly(lactic acid) (PLA)

As described above PLA is an aliphatic polyester that has two stereoisomers, L- and D-lactic acid. The PLLA has a low degradation rate while the PDLLA (racemic mixture of D- and L-lactic acid) has a faster degradation rate. The degradation rate can be further tailored by using a mixture of the different stereoisomers like with the poly-L-co-D,L-lactic acid (PLDLA). All the isomers of PLA are biocompatible and biodegradable with variable degradation rate and mechanical properties depending on the isomer and the isomer ration in stereocopolymer. PLDLA is especially of great relevance in the biomedical industry since it combines the mechanical properties of the PLLA and the shorter degradation rate of the PDLA [121]. One example of a PDLLA available membrane on the market is the Epi-Guide® from Curasan (**Figure 12d**) membrane made of a PDLLA in a unique three-layer configuration. Another example is a bilayered membrane made of a sprayed layer of copolymer of PDLLA and PGA and another dense layer of PCL, Activioss™ from Noraker (**Figure 12e**), fabricated by a French patented jet-sprayed technology [149].

Figure 12. Examples of synthetic resorbable barrier membranes for guided bone regeneration, a) Cytoflex® Resorb from Unicare Biomedical, b) Tisseos® from Biomedical tissues, c) Vivosorb® from Polyganics, d) Epi-Guide® from Curasan and e) ActiviossTM from Noraker.

All the above-mentioned membranes have an intrinsic porosity, they are not made porous on purpose. However, it is crucial to manage the membrane's porosity and topology in order to prevent the fibrous tissue from migrating while still allowing for cell attachment and nutrient flow [42]. Controlling the membrane's porosity is also crucial because mechanical characteristics and porosity are inextricably linked [39]. Therefore, it is crucial to fabricate membranes with controlled surface topography and porosity in order to get the best barrier membrane for successful GBR.

There are various methods to produce barrier membranes. The choice of fabrication method is crucial depending on the considered application of the membrane since different fabrication methods will yield different properties. Typical methods to produce barrier membranes include: electrospinning, chemical crosslinking or phase inversion methods for instance [139]. However, the membranes fabricated with those methods do not present a controllable porosity. As said above, controlling the porosity and topography of the membrane is of tremendous importance.

In terms of topography and porosity, honeycomb-like structures have been extensively investigated for centuries and are extremely attractive. Indeed, honeycomb structures have found applications in various domains ranging from architecture to mechanical engineering, chemical engineering and, in the recent years, in biomedicine [150]. In the last two decades, researchers have made tremendous progress in understanding how the honeycomb topography influences cells behavior and cell fate. Indeed, there are encouraging results showing that honeycomb patterned materials can induce the differentiation of stem cells toward a specific lineage without the need of biochemical cues [42].Therefore, honeycomb patterned films and membranes have gained interest and researchers have developed and studied honeycomb patterned materials as scaffolds for tissue engineering [42], [151].

In the following section, fabrication methods to obtain orderly porous membranes with a honeycomb-like pattern will be presented. First top-down approaches will be introduced and described followed by the bottom-up approaches, along with their advantages and drawbacks.

3.2. Fabrication method

There are several methods available to produce structured porous membranes which can be divided in two groups: 1) top-down approaches among which some of the most used are photolithography or soft lithography, and 2) bottom-up approaches from which some of the most utilized are block-copolymer self-assembly and the Breath Figure Method (BFM) [152], [153]. In a simplified manner, top-down approaches consists of "removing" parts from a material to build the desired shape while bottom-up approaches consists of using construction blocks as bricks to build up the desired form. Here, we will detail only the method we have chosen to create structured porous membranes, the Breath Figure method which is a bottom-up approach. The other methods are explained in the **Annex 2**.

As a bottom-up approach, the Breath Figure method (BFM) represents a powerful tool to produce nano- to microscale honeycomb structured porous membranes and films. It is designated as "breath figure" or "water droplet templating" method because it uses water droplets in humid air (fog) as template for the formation of pores at the surface of an evaporating solution [42]. It was observed for the first time by François et al. [43] in 1994 when his team observed the formation of honeycomb patterned pores after

evaporating carbon disulfide with star-shaped polystyrene or polystyrene-polyparaphenylene block copolymer solutions, under a flow of moist air. The mechanism of the formation of the honeycomb pores via the BFM are not completely understood yet. However, there is a consensus on some of the steps involved in the honeycomb formation process via BFM [44].

Briefly, a polymer is dissolved in a volatile, water-immiscible organic solvent. The solution is then casted on a surface, or substrate, under high relative humidity (RH). The solution surface cools down while the solvent evaporates, water condense from the moisture in the air forming small and disorganized droplets on the surface. The water droplets grow and self-assemble in an ordered and closely packed hexagonal array on the entire solution surface in order to reduce the free energy. In this configuration, the polymer is situated at the water droplet-solvent interface. Finally, the solvent and water evaporates completely, leaving the well-known hexagonal array of the honeycomb on the dry membrane (**Figure 13**) [42], [44].
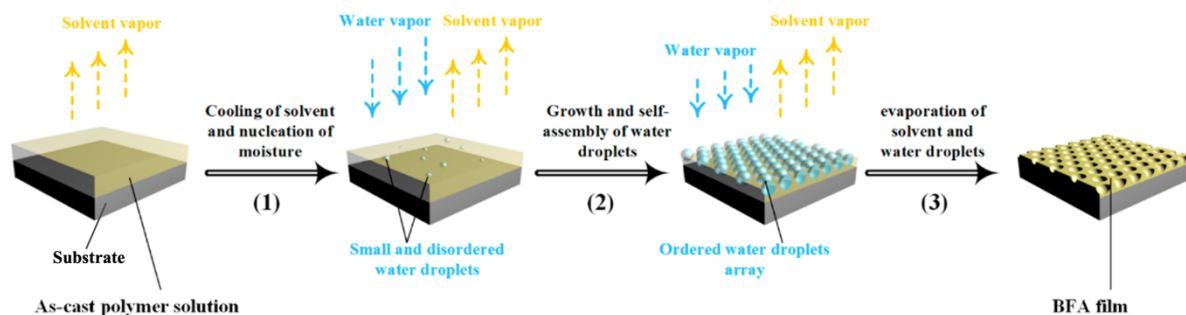
Figure 13. Schematic of the mechanism of formation of honeycomb array on a film or membrane by the breath figure method (BFM). Modified and adapter from [44]

The formation of honeycomb patterns through the BFM is controlled by complex mechanisms, heat, and mass transfer, which are further dependent on experimental conditions like temperature, humidity, the solution concentration and viscosity, the solvents physical properties and the nature of the substrate notably. Due to the complexity of the process, the slightest modification in one or more of the above mentioned parameters can drastically change the final result of the BFM [44].

Nevertheless, compared to other methods like the different lithography approaches or μCP, BFM has multiple advantages for the fabrication of porous membranes. Namely:

i)   It is a simple method that does not require complex set up or multiple steps.

ii)   It is far less expensive than many other methods since it does not require the use of costly equipment's like master molds. Indeed, there is no standard way of making BFM and most of the experimental results reported in the literature have been obtained with homemade set-ups.

iii)   It uses water as templating medium which is non-toxic.

iv)   It is possible to obtain the porous membranes quite fast and a large surface area can be prepared,

v)   An important diversity of polymer can be used to obtain the honeycomb array through this method.

vi)   By controlling the parameters, such as the RH and solution concentration, it is possible to tune the pores size and shape.

Those numerous advantages made the BFM one of the most widely applied method to fabricate orderly porous polymer membranes and films [42].

III. Aims

BGs have revealed themselves as one of the most promising bone filling materials for bone regeneration and bone repair. However, and like most of the other bone filling materials, they are not able to prevent fibrous tissue ingrowth in the bone defect which can eventually impair the bone regeneration and implant stabilization. Therefore, they must be used in conjunction with barrier membranes. Although the available barrier membranes on the market degrade faster than the bone regeneration occurs, their combination with a bone graft can reduce the gap between bone regeneration and membrane degradation. This would allow the bone enough time to heal properly, without deleterious fibrous tissue ingrowth. Nevertheless, as of today BG graft and barrier membrane are two distinct materials. During a surgical procedure, while the graft needs to stay in place, the membrane needs to be adapted to match the defect size and shape. The surgical procedure is therefore composed of 2 distinct steps which can be challenging for surgeons.

Therefore, this thesis aims to develop a two-in-one material composed of an inorganic phase made of BG (or xenogenic DBM) and an organic porous membrane phase made of PLDLA structured in honeycomb. The material produced must be able to withstand immersion in aqueous condition without dehiscence of the membrane while allowing the BG phase to degrade and produce HA. Furthermore, the membrane phase must be able to actually maintain cells at its surface, demonstrating its capacity to really prevent the fibrous tissue ingrowth.

To achieve these goals, the work endeavored here aims to answer the following questions:

1) Is it possible to produce a honeycomb membrane at the surface of a BG substrate (porous or not)? On DBM?

2) Does the membrane stay attached to its substrate while immersed? Is it necessary to functionalize the substrate to ensure membrane adhesion? If so what kind of functionalization works best?

3) Does the biphasic scaffold allow proper ion dissolution from the BG phase and retain its bioactivity emanating from the BG phase?

4) Is it possible to sterilize the scaffold and how does it impact the scaffolds?

5) Is the biphasic scaffold biocompatible and does the membrane really prevent cell migration?

IV. Materials and Methods

1. Bioactive glass materials and bone matrix

1.1. Bioactive glass materials synthesis and manufacturing

S53P4 and 13-93B20 BG were prepared from analytical grade K_2CO_3 (Alfa Aesar, Thermo Fischer, Kandel, Germany), Na_2CO_3, $NH_4H_2PO_4$, $(CaHPO_4)(2(H_2O))$, $CaCO_3$, MgO, H_3BO_3 (Sigma Aldrich, Saint-Louis, MS, USA) and Belgian quartz sand. The nominal oxide compositions of the experimental BGs are presented in Table 1 in mol %.

Table 4. Investigated BGs composition in mol%

Glass	mol%						
	Na_2O	CaO	P_2O_5	SiO_2	K_2O	MgO	B_2O_3
S53P4	22.66	21.77	1.72	53.85	-	-	-
13-93B20	6.0	22.1	1.7	43.7	7.9	7.7	10.9

The reagents were melted in a platinum crucible at 1450 °C in an electrical furnace. The molten glass was either casted into a pre-heated graphite mold to obtain a rod (S53P4 and 13-93B20 in **Part A** of the Results and Discussion) with a diameter of 14 mm or in a disc form graphite mold at RT (only 13-93B20 in **Part D** of the Results and Discussion). The glass rods or discs were annealed overnight at 500 °C and let to cool down to room temperature before storage. The rods were cut into 2 mm thick discs and polished with SiC paper (grit #320, #500, #800, #1200, #2400 and #4000, from Struers, Copenhagen, Denmark). The 13-93B20 glass bulk discs were used for crushing and 3D printing (**See 1.2**). All samples were dried and kept in a desiccator until further use.

1.2. Bioactive glass 3D printing

Method used in **Part D** of Results and Discussion.
For 3D printing purposes, the 13-93B20 were crushed into a powder of particle size inferior to 38 μm with a Pulverisette 7 planetary micro mill machine (Fristch GmbH, Germany) followed by a sieving step using sieves ranging from 1mm to 38 μm sieves. In the meantime, a solution of Pluronic 30% was

prepared from Pluronic® F127 (Sigma Aldrich, Saint-Louis, MS, USA) and deionized water. Then the ink for printing was prepared from a mixture of 30 wt% of Pluronic 30% and 70 wt% of 13-93B20 powder. In order to homogenize the ink, it was alternatively vortexed for 30sec then cool for 30 sec in an ice bath 6 to 7 times. When ready, the ink was poured inside a syringe and allowed to gel at RT for at least 1h before use. Cylindrical grid-like scaffolds (nominal diameter 7.4 mm, 17 layers of which the last 2 were dense) were then print using a 3Dn-Tabletop printer (nScrypt Inc., Orlando, Florida, USA), and controlled via the Machine Tool 3.0 system software. Scaffolds were specifically designed with 2 final dense layers in order to obtain a non-porous surface on one side of the scaffold. When printed, scaffolds were incubated for 24h at 40°C in a static incubator before sintering. After drying, the scaffolds were put upside down at RT in an oven and then sintered in air with a temperature rising to 650 °C at a 1°C/min rate. When reached, the temperature was kept for 1h before cooling down to RT. Scaffolds were then stored in a desiccator until further use.

1.3. Bioactive glass materials surface treatments

Membranes were directly generated onto untreated or surface-modified BG discs or scaffolds. Discs with both BGs compositions (S53P4 and 13-93B20) were surface treated by either silanization or conditioning. 3D scaffolds of 13-93B20 were only conditioned. The surface treatment protocols are as follow:

1.3.1. Silanization with 3-aminopropyltriethoxysilane

Method used in **Part A.A** and **Part A.B** of the Results and Discussion.

Polished BG discs were silanized with 3-Aminopropyltriethoxysilane (APTES) (Thermo Fischer Scientific, Germany), according to the protocol used by Massera et al. [154] (Publication I). Briefly, BG discs were first washed for 5 min in acetone and distilled water (three times), in a sonicating bath. After washing, BG discs were immersed in ethanol (150 mL) with APTES (70 µL) for 6 hours and, successively, dried at 100 °C for 1 h. In order to remove the loosely bound APTES, the BG discs were then washed again in ethanol for 5min in the sonicating bath and further dried for 30 min at 100 °C.

1.3.2. Conditioning

Method used in **Part A** and **Part D** of the Results and Discussions.

Polished BG discs were immersed in TRIS buffer solution and incubated at 37 °C for 24 h. TRIS solution was prepared from Trisma base® and Trisma HCl® (Sigma Aldrich, Saint-Louis, MS, USA) at pH 7.38 ± 0.02 at 37 °C ± 0.2 °C. After incubation, the solution was removed, and BG discs were allowed to dry in a fume hood overnight before membrane deposition.

1.4. Bone matrix

Only used in **Part D** of the Results and Discussion.

Sow cortical or cancellous bone treated through the BIOBank Supercrit® process was kindly supplied by BIOBank inc. The bone pieces received were square shaped with varying height. In order to obtain a similar shape to the 3D printed scaffolds, the bone pieces were further shaped (cut and polished only on 3 of the faces of the pieces to keep one "natural" face) with a Dremel 4000 (Dremel, Illinois, USA) to obtain rounded shape pieces with a height varying from 8 to 4 mm and a diameter of approximately 8mm ± 1mm.

2. Honeycomb membrane deposition

Method used in **Part A** and **Part D** of the Results and Discussion.

Honeycomb membranes were fabricated from a 10 mg.ml^{-1} solution of 96/04 poly L-lactide/D-lactide copolymer (PLDLA) containing 0.1 mg.ml^{-1} of the surfactant dioleoyl phosphatidylethanolamine (DOPE) in chloroform. PLDLA purified, medical grade, PURASORB PLD 9620, was purchased from Corbion Purac, The Netherlands and, DOPE from Sigma Aldrich, Japan.

The honeycomb membranes were produced by the BFM as described in **Figure 14** and as previously reported in [155]. Briefly, the polymer solution was deposited drop by drop onto BG discs or 3D scaffolds or xenogenic DBM, and then the solvent was allowed to evaporate in a humidity chamber at 80 % ± 5 % RH, under airflow. The samples were air dried at RT and then washed twice with 70 % ethanol in order to remove the surfactant. Samples were air-dried again and stored in a desiccator until further use.
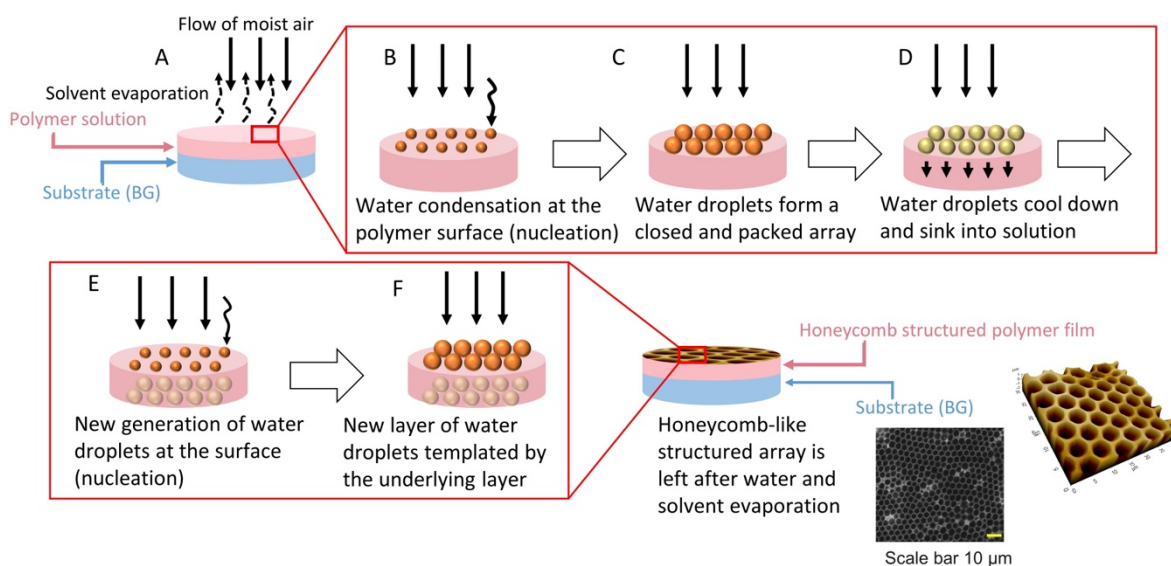
Figure 14. Schematic of the membrane deposition process, using the BFM. A) deposition of the polymer solution on the substrate (BG) and placing the construct under a flow of moist air, B) water droplets start to condense at the surface of the polymer solution, C) water droplets grow and form a closed and packed array, D) The droplets cool down and sink into the solution, E) a new generation of water droplets is formed at the surface, F) the process continues until the end of the reaction under the flow of moist air and each new generation of water droplets is templated by the underlying layer.

3. Samples names

Samples <u>without any treatment</u> were simply designated by their name (**S53P4**, **13-93B20**, **Bone**). Samples <u>silanized</u> (only in **Part A.A** and **A.B** of the Results and Discussion) were named **S53P4s** and **13-93B20s**. <u>Conditioned</u> samples were named **S53P4c** and **13-93B20c**. When the samples have the membrane at their surface, they have the "**M**" suffix attached. Samples without the membrane are collectively referred to as "**substrates**" while samples with the membrane are collectively referred to as "**membrane/substrate assemblies**". All samples regardless of the presence of the membrane are collectively referred to as "**materials**".

Table 5. Recap table of the different sample's names depending on the treatment and presence of the honeycomb membrane

Sample type / Membrane	S53P4			13-93B20			Bone
	untreated	*silanized*	conditioned	untreated	*silanized*	conditioned	untreated
Without membrane	S53P4	S53P4s	S53P4c	13-93B320	13-93B20s	13-93B20c	Bone
With membrane	S53P4M	S53P4sM	S53P4cM	13-93B320M	13-93B20sM	13-93B20cM	BoneM

4. Sterilization

Method used in **Part A.0** and **Part D** of the Results and Discussion.

Before irradiation, the membrane/substrate assemblies were disinfected in two successive EtOH 70% baths and stored in homemade individual plastic pockets and then irradiated at room temperature using a ^{60}Co gamma cell (2000 Ci) as source of gamma radiation having a dose rate under 28 kGy. The gamma irradiation was performed by IONISOS.

5. Materials characterization

5.1. Bioactive glass surface topography and composition

5.1.1. Scanning electron microscopy and energy dispersive X-ray spectroscopy

Method used in **Part A** and **Part D** of the Results and Discussion.

Scanning Electron Microscopy - Energy Dispersive X-ray Spectroscopy analysis (SEM/EDX) was conducted using a Gemini SEM 300 (Carl Zeiss, Germany) equipped with an EDS Bruker Quantax (Bruker, USA) for EDX spectroscopy. Samples were metalized with nickel (for EDX analysis) or with a 4 nm thick platinum layer using a Leica ACE600 (Leica, Wetzlar, Germany) (for SEM imaging).

5.1.2. Atomic force microscopy

In **Part A.A** and **Part A.B**, topographical features of the honeycomb membranes were analyzed using an atomic force microscope (AFM) XE-100 Park System Corp, USA. An image size of 30 µm x 30 µm was scanned in noncontact mode, in air and at room temperature. Acquired images were analyzed using image analysis software (XEI, Park System, USA). The pores size was estimated from the AFM images using the software Fiji.

In **Part D**, topographical features of the 3D scaffolds with or without membrane were analyzed with AFM as follow. Samples (n=3) were analyzed using an atomic force microscope (AFM Workshop TT2). An image size of 25 μm × 25 μm was scanned in noncontact mode, in air and at room temperature (RT). Acquired images were analyzed using image analysis software (Gwyddion).

5.1.3. Surface roughness and 3D topography

Method used in **Part D** of the Results and Discussion.

Surface roughness was investigated using a roughness tester (PCR-RT-2300) equipped with a diamond-tipped micro-sensor and a removable feed unit, with the following parameters: 1.5 mm travel and 320 μm measuring range (-160 μm +160 μm). The sensor exerts a maximum pressure of 4 mN on the sample surface. Average roughness (Ra) measurements are carried out on samples (n=3) in accordance with ISO 16610-211. The pore depth was also measured with the roughness tester through the same protocol.

5.2. Structural property

5.2.1. Zeta potential

Method used in **Part A.A** of the Results and Discussion.

An electrokinetic analyzer for solid surfaces (SurPASS^{TM} 3, Anton Paar, Austria) was employed to measure the Zeta potential of the untreated and treated BG discs by means of the streaming potential technique [156]. An adjustable gap cell was used for the measurements and a 1 mM KCl solution was used as the electrolyte. Measurements were carried out at pH = 7.

5.2.2. Shear stress test

Method used in **Part A.A** and **Part A.0** of the Results and Discussion.

Two aluminum plates were clamped to a TA1 texture analyzer (Lloyd materials testing, AMETEK, Pennsylvania, USA) equipped with a 20 N or 100 N load cell, depending on the force to be applied. The specimen to be tested was fixed in-between the plates, by solvent-free double-sided tape (tesa® ECO FIXATION). Freshly prepared samples were used for the measurement. Shear force on the membrane was created by pulling the upper plate at 1 mm.min^{-1} while the bottom aluminum plate remained fixed. The design of the set-up can be found in [157]. The test was performed on 5 to 7 samples.

5.2.3. Fourier transform infrared

In **Part A.A** of the Results and Discussion, the Fourier Transform Infrared (FTIR) absorption spectra of the untreated or treated BG discs were recorded using a Bruker Alpha FTIR in attenuated total reflectance (ATR), to see the effect of the treatments on their surface chemical properties. All IR spectra were recorded within the range 400–4000 cm^{-1} with a resolution of 2 cm^{-1} and 64 accumulation scans. All spectra were corrected for Fresnel losses and normalized to the band with maximum intensity.

In **Part A.0** of the Results and Discussion, before measuring the IR spectra of the BGs, the membrane was removed by polishing, and the BGs were subsequently crushed by hand in a mortar to obtain a powder. The IR spectra were recorded using a Spectrum Two FTIR spectrophotometer Perkin Elmer (PerkinElmer) in attenuated total reflectance mode with a diamond crystal puck, to assess the possible changes induced by the sterilization. All IR spectra were recorded within the range of 400–4000 cm^{-1} with a resolution of 2 cm^{-1} and 64 accumulation scans. All spectra were background corrected and normalized to the band with maximum intensity and presented from 600 cm^{-1} because of the air absorption that makes the signal below 600 cm^{-1} unreliable.

5.2.4. Photoluminescence

Method used in **Part A.0** in the Results and Discussion.

Photoluminescence (PL) spectra were recorded with an FLS-1000 (Edinburgh Instruments, UK) spectrofluorometer equipped with double excitation and emission monochromators and with a 450 W xenon lamp as excitation source. Spectra were recorded from 300 nm to 920 nm and excitation wavelength was 266 nm. Spectra were normalized to the band at 700 nm.

5.2.5. UV vis absorbance

Method used in **Part A.0** in the Results and Discussion.

The UV vis absorption spectra of the glasses were measured using a spectrophotometer (UV-3600 Plus, Shimadzu) in the 200 to 1800 nm range with a step of 0.5 nm.

5.2.6. Size exclusion chromatography

Method used in **Part A.0** in the Results and Discussion.

Size exclusion chromatography (SEC) was used to determine the molecular weight loss of the polymer membrane following gamma irradiation. On 12 samples the membranes were dissolved in 2mL of Tetrahydrofurane (THF, Fischer scientific, Illkirch, FR) in order to analyses the polymer molecular weight before and after irradiation. A Merck Hitachi 7000 series was used to analyze the samples, equipped with a L-7200 autosampler taking 20 µl of solution to analyze, a L-7100 pump, a L-7350 column oven set at 35°C and a RI 5450 detector. Solutions were eluted in THF at a 1 ml/min rate.

5.2.7. Inductively Coupled Plasma - Optical Emission Spectroscopy

Method used in **Part A.B**, **Part A.0** and **Part D** of the Results and Discussion.

Inductively Coupled Plasma - Optical Emission Spectroscopy (ICP-OES) analysis was conducted with an Agilent 5110 instrument (Agilent technologies, USA) equipped with a SPS 4 autosampler, in order to quantify the presence of phosphorus (P), sodium (Na), calcium (Ca), silicate (Si), and boron (B), potassium (K) and magnesium (Mg) (only for 13-93B20) in the medium collected during the immersions in TRIS buffer, SBF or cell culture medium as described below. Samples in TRIS buffer solution and SBF were diluted in nitric acid, while samples in cell culture medium were diluted in water for the analysis. Wavelength values for the analysis were as follows: P 213.618 nm, Na 589.592 nm, Ca 317.933 nm, Si 250.690 nm (in **Part A.B**) or 288.158 nm (in **Part A.0**), B 249.678 nm, K 766.491 nm and Mg 279.800 nm.

5.2.8. X-ray microtomography

Method used in **Part D** of the Results and Discussion.

The internal structure of the samples was investigated with X-ray microtomography (µCT). The images were acquired with MicroXCT-400 (Carl Zeiss X-ray Microscopy, Inc., Pleasanton, CA, USA) device. X-ray tube voltage was 100kV and current 100µA. Two magnifications were used, low resolution with a pixel size of 14.25 µm for an overall view of the sample, and high resolution with a pixel size of 2.28 µm for a more detailed view. 1601 projections were taken with exposure times of 3 and 7 seconds. The projections were reconstructed to 3D volume with the manufacturer's XMReconstructor software. Image processing and visualizations were performed with Avizo 2020.2 software (Thermo Fisher Scientific, Waltham, MA, USA).

5.2.9. Water Contact Angle

Method used in **Part D** of the Results and Discussion.

The wettability of the membrane/scaffold assemblies was assessed by water contact angle (WCA) measurements carried out using an optical tensiometer (Bioline TethaFlex TF300). Water droplets of 5 μl, under air and at room temperature are deposited on the surface of each sample (n=3) in sessile drop mode (drop rate 2 μl/s) monitored by a camera with an acquisition time of 10s at 10% (33 FPS). Acquired images were analyzed using analysis software (OneAttension) with Surface tension (Young-Laplace) as secondary analysis mode.

5.2.10. Stability of the membrane in dry conditions

The method was used in **Part A.A** of the Results and Discussion.

Samples (n = 3) were dried and kept at room temperature in a desiccator (20-40% RH) inside multi-well plates for up to 4 weeks. Topographical features of the honeycomb membranes were analyzed through AFM as described above in **section 5.1.2.**

5.2.11. Stability and membrane/substrate assemblies' behavior in wet conditions

5.2.11.1. Immersion in TRIS buffer solution

The method was used in **Part A.B and Part D** of the Results and Discussion.

Samples (n = 12) were immersed in 5ml of TRIS buffer solution before being incubated at 37 °C in static conditions (without agitation). The buffer solution was refreshed at 3 h, 6 h, 24 h, 48 h, 5 days, 7 days, 9 days, 14 days and 21 days to prevent saturation of the immersion solution with ions released from the BG substrate. The assembly (membrane/BG disc) integrity was assessed by counting the number of membranes that detached (partially or totally from the substrate) during the immersion period. At 28 days (4 weeks), samples were collected and left to dry in a fume hood overnight before further analysis.

All samples were imaged by AFM and SEM/EDX, as described in **section 5.1.2** and in **section 5.1.1** of the Materials and Methods respectively.

At each time point (3 h, 6 h, 24 h, 48h, 5 days, 7 days, 9 days, 14 days,21 days and 28 days), 1 ml of the immersion solution was collected to quantify the change in ion concentration over the incubation period. Inductively Coupled Plasma - Optical Emission Spectroscopy (ICP-OES) analysis was conducted as described in **section 5.2.7** of the Materials and Methods.

5.2.11.2.   Immersion in simulated body fluid

The method was used in **Part D** of the Results and Discussion.

SBF was prepared following the methodology from the standard ISO/FDIS 23317 as described by Kokubo et al. [158]. The membrane/substrate assemblies (n=3/time point) were immersed in 5mL SBF solution for 24h, 48h, 72h, 7 and 14 days at 37°C in a shaking incubator (HT Infors Multitron) at a speed of 100 rpm. As controls, samples without honeycomb membrane (n=3) were immersed only until 14 days. During the experiment, the solution was not refreshed so that calcium phosphate precipitation could be measured. The ion concentration in the solution according to immersion time was measured by ICP-OES as previously described in **section 5.2.7** of the Materials and Methods.

6.   Membrane/substrate assemblies/cell behavior

6.1. Cell lines

Pre-osteoblastic MC3T3 cells, E1 subclone 4, (ref: CRL-2593, ATCC, Manassas, VA, USA) were cultured in Minimum Essential Medium α, αMEM, (Thermo Fischer Scientific, Germany) supplemented with 10 % Fetal Bovine Serum (FBS) and 1 % penicillin/streptomycin (P/S), designed as αCM (αMEM complete medium).

Red Fluorescent Human Dermal Fibroblasts, Red TTFluor HDFs, expressing turboFP602 protein ($\lambda_{ex}/\lambda_{em}$ = 574/602 nm) free in cytoplasm (ref: P20204, Innoprot, Vizcaya, Spain), were cultured in Fibroblast Basal Medium (ref: P60108-b, Innoprot, Vizcaya, Spain) supplemented with 2% FBS, 1% Fibroblast Growth Supplement (ref: P60108-GS, Innoprot, Vizcaya, Spain) and 1% P/S, designed as FCM (Fibroblast Complete Medium).

6.2. Impact of the gamma irradiation on the membrane/substrate assembly/cells-interactions

Method used in **Part A.0** of the Results and Discussion.

Prior to cell culture, the non-irradiated samples were disinfected in two successive EtOH bath during 1 and 2 min respectively and then allowed to dry for 10min before use. Between the baths, the samples were allowed to dry during 5 min under the laminar hood.

The irradiated and non-irradiated samples were pre-immersed in 1mL of cell culture medium for 24h before seeding the cells. Pre-osteoblastic MC3T3 cells (E1 subclone 4, from ATCC, ref: CRL-2593) were cultured in Minimum Essential Medium α (αMEM) Gibco (ThermoFischer Scientific, Germany) supplemented with 10 % Fetal Bovine Serum (FBS) and 1% penicillin/streptomycin, in a humidified atmosphere of 5% CO_2 at 37 °C.

Cells were seeded at a density of 20 000 cells/samples and 3 samples were used. The morphology of the cells was observed after 24h, 72h and 7 days of culture. At each time point, the cells were fixed with 3% (w/v) para-formaldehyde solution dissolved in PBS (Sigma Aldrich) for 15 min, then permeabilized with 0.1% (v/v) Triton X-100 (Sigma Aldrich) for 10 min. Non-specific binding sites were blocked by incubating the assembly in PBS containing 1% Bovine Serum Albumin (BSA, Sigma Aldrich) for 1 h. The cytoskeleton and nuclei of the cells were stained respectively with 1:50 FITC-labelled phalloidin (Sigma Aldrich P5282) and 1:1000 4',6-Diamidino-2-phenylindole dihydrochloride (DAPI, Sigma Aldrich D9542) in PBS-BSA 0.5% for 1 h. Each incubation with antibodies was performed in the dark in a humid atmosphere. Samples were then washed in PBS-BSA 0.5%, mounted in Prolongold (Invitrogen), and observed under a LSM710 confocal microscope (Carl Zeiss).

During the cell culture, at each time point (pre-incubation, 24h, 72h and 7 days after cells seeding), 1mL of culture medium was collected from each sample and diluted in 9 mL of deionized water to quantify the change in ion concentration over time. The pre-incubation time point is presented before 0 in the curves. Inductively coupled plasma-optical emission spectroscopy (ICP-OES) analysis was

conducted as described in **section 5.2.7** of the Materials and Methods. The results are presented as cumulative data ± standard deviation (SD).

6.3. Membrane/substrate assembly ability to control Red TTFluor human dermal fibroblasts passage through the bioactive glass scaffold

Methods described here were used in **Part D** of the Results and Discussion. **For these experiments, only membrane/13-93B20c assemblies were used.**
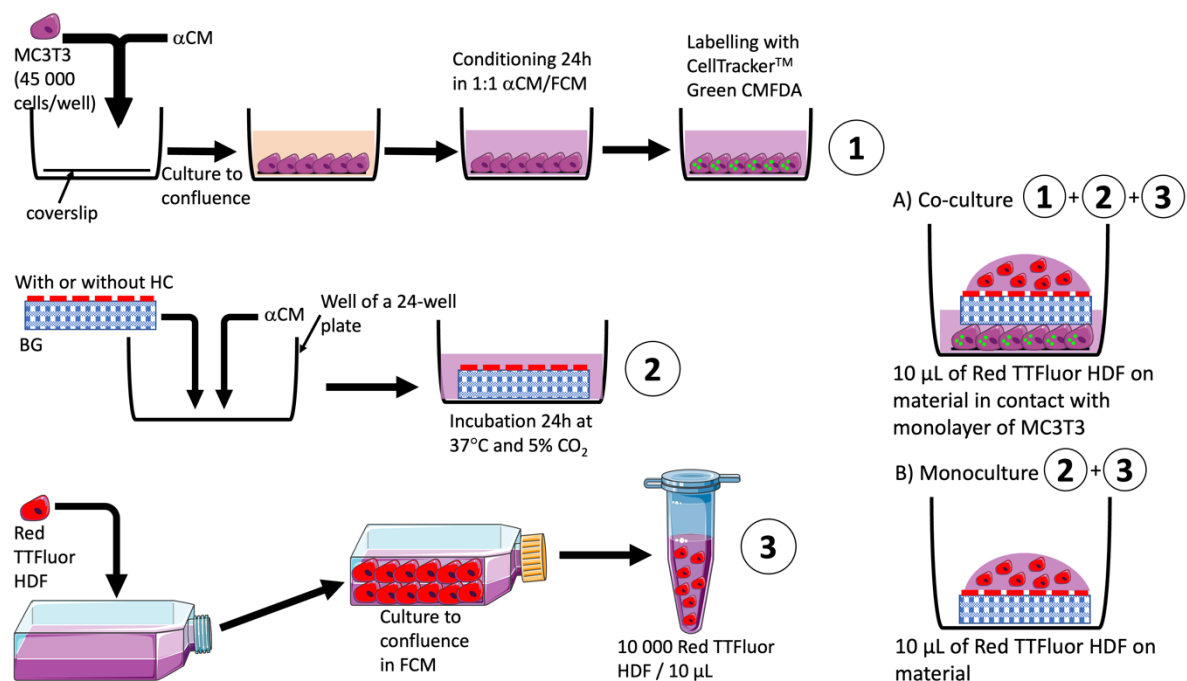
Figure 15. Schematic representation of the cell culture protocols for the tests in co-culture and mono-culture condition as described in **section 6.3.1** and **6.3.2** of the Materials and Methods

6.3.1. Under co-culture conditions

MC3T3 cells were seeded at 45 0000 cells/cm^2 in either a 24 -well plate or on glass coverslips of 14 mm of diameter and left in incubation for 24 h at 37 °C 5% CO_2.

The next day, MC3T3 monolayers were conditioned with a mixture 1:1 of αCM and FCM, for 24h. In parallel, membrane/substrate assemblies were pre-immersed in 1 mL αCM, in a humidified atmosphere at 37 °C and 5% CO_2 for 24h. Mixture of αCM and FCM was removed from the MC3T3 monolayer. Cells were labeled with CellTracker^{TM} Green CMFDA (ref: C7025, Thermo Fisher Scientific,

Germany), according to the protocol supplied by the manufacturer. In brief, the fluorescent probe was dissolved in DMSO at a concentration of 10 mM and then diluted to a concentration of 20 μM in αMEM without FBS. 300 μL of this solution were put in contact with cells for 45 min at 37°C and 5% CO_2. Then, media was removed from the MC3T3 monolayer and replaced by 100 μL of FCM.

Pre-immersed membrane/substrate assemblies were put in contact with the MC3T3 labelled monolayer. 10 000 Red TTFluor HDFs in 10 μL of FCM were seeded on the top of each membrane/substrate assembly and incubated for 2h. Observation of fluorescent cells were performed directly after the 2h of incubation using an inverted microscope DMi8 Thunder Imager (Leica Microsystems, Germany) in epifluorescence mode and equipped with a CO_2 incubator (Okolab).

6.3.2. Under Red TTFluor HDFs monoculture conditions

After the membrane/substrate assemblies immersion in 1 mL of αCM for 24h, Red TTFluor HDFs were seeded on the top of each membrane/substrate as previously described in **section 6.3.1** of the Materials and Methods. They were incubated for 2h at 37°C and 5% CO_2. After incubation, the membrane/substrate assemblies were either imaged immediately or 900 μL of FCM was added and membrane/substrate assemblies were incubated for 72h.

The membrane/substrate assemblies were imaged as follow: upper and lower parts of the membrane/substrate assemblies were observed using an inverted microscope DMi8 Thunder Imager (Leica Microsystems, Germany) in epifluorescence mode. For this, assemblies were carefully removed and put in glass bottom μ-Dish of 35 mm (Ibidi, Martinsried, Germany), with either the upper or the lower part of the assembly towards the glass side to be visualized.

6.4. Impact of membrane/substrate assembly on metabolic activity

Methods described here were used in **Part D** of the Results and Discussion. For this experiment, only membrane/13-93B20c assemblies were used.

Alamar Blue test was performed on either MC3T3 (45 000 cells/cm^2) or Red TTFluor HDFs (25 000 cells/cm^2) in contact with the membrane/substrate assemblies for 2h and 72h. MC3T3 control cells were

directly seeded on the well plate. Red TTFluor HDFs control cells were also deposited on the well plate and incubated in 10 µL of FCM and followed the same incubation times as experimental cells.

After 2h and 72h of culture, cell culture media was replaced by complete cell culture media containing 10% v/v of Alamar Blue™ HS Cell Viability Reagent (ref: A50101, Thermo Fisher Scientific, Germany). Samples were incubated for 3 h at 37°C and 5% CO_2. 150 µL samples of the cell culture media containing Alamar Blue were placed in a dark 96 well-plate and fluorescence measurements were performed using a Synergy HTX Multi-Mode Reader (BioTek® Instruments, Vermont, USA) at $\lambda_{ex}/\lambda_{em}$ = 560/590nm. Metabolic activity was calculated by comparing fluorescence values of samples to those of control cells.

6.5. Impact of membrane/substrate assembly on MC3T3 morphology

Methods described here were used in **Part D** of the Results and Discussion. For this experiment, only membrane/13-93B20c assemblies were used.

To assess the morphology, MC3T3 cells were seeded at a density of 45 000 cells/cm^2 on glass coverslips of 14mm of diameter and put in contact 2h with the membrane/substrate assembly and subsequently prepared for imaging as follow. Cells were fixed with 4% w/v para-formaldehyde solution for 15 min, then permeabilized with 0.1% v/v PBS-Triton X (Sigma Aldrich) for 10 min. Non-specific binding sites were blocked by incubating the samples in PBS containing 1% Bovine Serum Albumin (BSA) for 1h. The cytoskeleton and the nuclei of cells were stained with 1:100 diluted FITC-labelled phalloidin (ref: P5282, Sigma Aldrich) and 1:1000 4',6-Diamidino-2-phenylindole dihydrochloride (DAPI, ref: D9542, Sigma Aldrich) in PBS-BSA 0.5% v/v for 1h. Incubation was performed in the dark and in a humid atmosphere. Samples were then washed in PBS-BSA 0.5% v/v and mounted in ProLong™ Gold antifade reagent (ref: P36930, Thermo Fisher Scientific, Germany) and observed using an inverted microscope DMi8 Thunder Imager (Leica Microsystems, Germany) in epifluorescence mode.

MC3T3 cells were seeded in the well plate and no membrane/substrate assembly were put in contact with them as experimental control. They were fixed and labelled as previously described.

V. Results and discussion

In this section, results of this thesis work will be presented and discussed. The first part of the results presents the study on the evaluation of the membrane/BG discs assemblies' behavior in dry conditions to assess the impact of aging on the adhesion of membranes to the substrates. Subsequently, the membrane/BG discs assemblies were immersed to observe and understand the degradation process of the membrane/BG discs assemblies in aqueous conditions. Afterwards, the membrane/BG discs assemblies were irradiated for sterilization purposes. The impact of the irradiation on the membrane/BG discs assemblies and the membrane/BG discs assemblies-cell interactions was assessed. Finally, in a second part, a 3D functionally graded porous scaffold based on BG was 3D printed and the generation of the honeycomb membrane at its surface, and at the surface of a decellularized bone matrix, was attempted. The obtained 3D porous membrane/scaffolds assemblies were characterized through physicochemical techniques and the barrier effect of the membranes was studied with cells.

A. Generation of a honeycomb membrane on non-porous bioactive glass discs: disc treatment, deposition and characterization of the stability of the membrane in dry conditions

1. Surface treatments

First, the impact of the treatment on the surface charge of BG discs was analyzed. Zeta potential measurements are reported in.

Table 6. Zeta potential of untreated, silanized and conditioned BG disc surfaces at pH 7 (streaming potential).

	S53P4			13-93B20		
	Untreated	Silanized	Conditioned	Untreated	Silanized	Conditioned
Zeta potential (mV)	-47.8 ± 0.5	-30.6 ± 2.0	-16.9 ± 0.4	-53.2 ± 1.9	-12.2 ± 0.4	-15.5 ± 0.4

As expected, with zeta potential around -50 mV, the surface charge of the untreated samples is in agreement with the values for silicate and borosilicate glasses [159], [160]. Regardless of the BG composition, both treatments (silanized and conditioned) led to a decrease in the surface charge. In the case of silanization with APTES, the decrease in surface charge can be explained by the introduction of positively charged amine groups to the BG disc surface at pH = 7 [159]. Upon conditioning for 24 h in TRIS buffer solution, the BG discs started to dissolve which resulted in the formation of Si-OH and Si-O$^-$ groups on their surfaces. Eventually, if the dissolution/reaction in aqueous solution is rapid, a calcium phosphate reactive layer may start to precipitate [93], [161]. Using a silicate glass model, Lu et al. reported that during immersion the measured zeta potential presents a shift toward positive values, corresponding to the formation of an amorphous Ca-P layer, which can be detected as early as 1 day after immersion [162]. At longer immersion times, the amorphous Ca-P layers crystallize. The crystalline hydroxyapatite layer has been reported to have a zeta potential value close to -15 mV [161], [163]. Based on these results, the surface charge decrease observed in our study may be explained by 1) the density of positively charged amine groups at the surface of the silanized samples, and 2) the nature (composition, specific surface area) of the Ca-P layer that has possibly deposited during the pre-incubation of the BG discs for 24 h.

When comparing BG compositions, it was clear that the surface charge of the untreated and conditioned glass discs, respectively, was similar. However, silanization with APTES was found more efficient in reducing the electronegativity on the glass 13-93B20 than on the glass S53P4. Such variation in the surface charge between BGs might be correlated with their dissolution rate. Indeed, the borosilicate BGs are known to possess a borate phase with higher reactivity than the silicate BGs [28], [164]. Such a fast, early dissolution may lead to an increase in the density of Si-OH groups that are formed during

the washing step, in turn leading to a higher density of sites onto which the APTES can be attached. The higher the concentration of amine groups, the less negative the surface will be. Indeed, Ferraris et al. have reported that upon silanization, the increase of the zeta potential is dependent on the density of amine groups [159]. Therefore, the smaller change in surface charge seen for the S53P4 glass when compared to the 13-93B20 glass, can be assigned to a greater density of positively charged amine groups at the surface of the latter composition. However, one should keep in mind that the dynamic dissolution of the BG may also lead to the release of amine groups.

In order to obtain more information on the surface texture of the different BG discs and the impact of the treatments on the surface composition, BG discs were imaged by SEM/EDX (**Figure 16** and **Figure 17**).
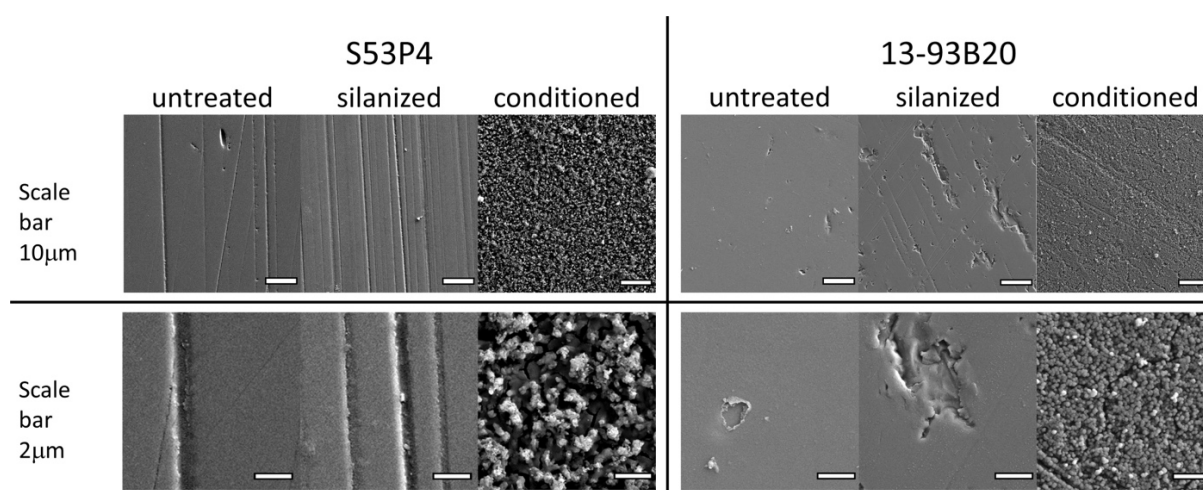
Figure 16. SEM images of the surface of untreated, silanized and conditioned BG discs, before membrane deposition.

At the microscopic level, silanization of S53P4 does not seem to have a significant impact on surface texture, whereas, in the case of 13-93B20, signs of surface degradation can be seen. In addition, a high density of nodules with sub-micrometer size can be observed on the conditioned BG discs. At higher magnification, one can see that the nodules are smaller and denser at the surface of the 13-93B20 than at the surface of S53P4. The samples cross section was analyzed by EDX (**Figure 17**) and the top surface by FTIR (**Figure 18**).
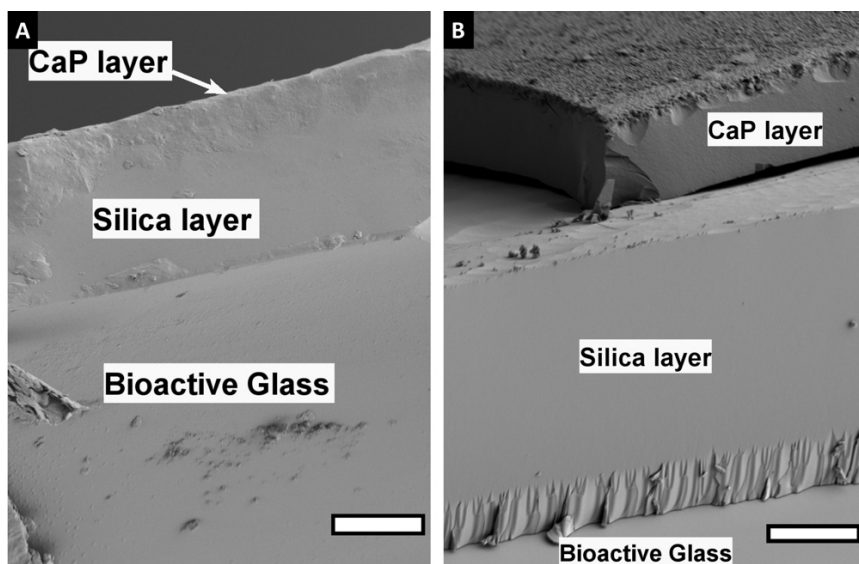
Figure 17. SEM images of cross section of S53P4 (A) and 13-93B20 (B) conditioned analyzed by EDX, scale bar: 20 μm.

SEM/EDX analysis of the conditioned samples indicated the presence of three phases: 1) the bioactive glass, 2) a silica-rich layer and 3) a reactive layer composed mainly of Ca and P. The Ca/P ratio was found to vary between 1.4 and 1.7, regardless of the BG composition. The large variation in the ratio can be assigned to the 1) high penetration depth of the electron beam (signal from the underneath BG is collected) and 2) the Ca deficiency of the early apatite layer formed at the surface of BG [160]. The formation of such layers was expected upon immersion of silicate and borosilicate BGs into aqueous solutions [28], [100], [164]. It is interesting to point out that the reactive layer at the surface of S53P4 glass had a lower density of nodules than the surface of 13-93B20 (**Figure 16**). Such a thin layer at the surface of the S53P4, formed upon immersion in TRIS buffer solution, was also reported before by Varila et al. [165].

The FTIR-ATR spectra of the top layer are presented in **Figure 18**.
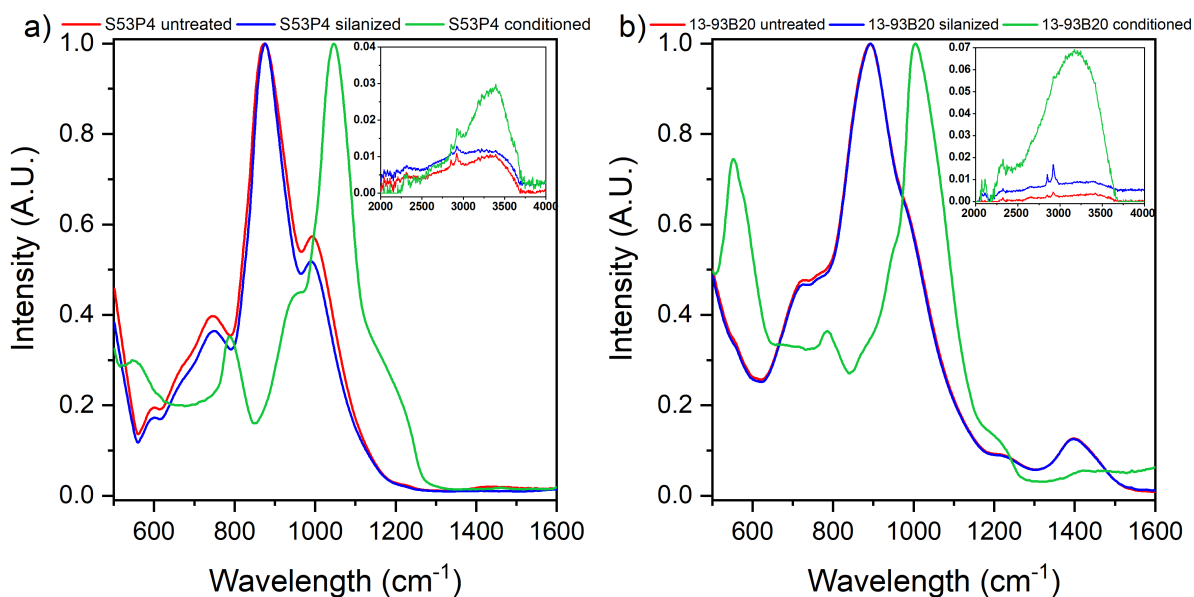
Figure 18. FTIR-ATR spectra of S53P4 (a) or 1393B20 (b), untreated (S53P4 and 13-93B20, red), silanized (S53P4s and 13-93B20s, blue) and conditioned (S53P4c and 13-93B20c, green) prior to membrane deposition. The insert in each spectrum shows the 2000-4000 cm^{-1} region.

The FTIR-ATR analysis was made to identify the chemical structure at the surface of the glasses.

FTIR-ATR spectra of the S53P4 (**Figure 18a**) and 13-93B20 (**Figure 18b**) displayed bands ~748 cm^{-1}, ~930 cm^{-1} and ~1030 cm^{-1}. These bands can be attributed to Si-O bending, Si-O⁻ (non-bridging oxygen) in the [SiO_4] units and to Si-O-Si asymmetric stretching in [SiO_4] units respectively [166], [167]. Aside from those bands, the glass 13-93B20 also exhibited bands at 1400 cm^{-1} related to the BO_3 vibrations [17], [167]. Silanization did not seem to significantly impact the surface chemistry, regardless of the glass composition. While vibration related to the amine groups (NH_2 between 1400 cm^{-1} and 1600 cm^{-1}) could be expected, they were not visible in the FTIR-ATR spectra of the silanized BG discs. The reason may lie in the low density of amine groups at the surface of the BG discs [154], [159]. However, as amine group signal is visible in the same region as BO_3 units in the 13-93B20, it is possible that those bands were covered by the boron bands in this glass.

Major changes in the surface structure occurred for the conditioned BG discs, as expected from SEM/EDX. The FTIR-ATR spectra of the conditioned samples exhibited complete disappearance of the vibration bands related to the silicate and borate network and new absorption bands at ~560 cm^{-1},

~605 cm^{-1}, ~800 cm^{-1} and ~1060 cm^{-1} as well as a shoulder at ~959 cm^{-1} appeared. The shoulder at ~959 cm^{-1} can be attributed to C-O vibration mode in CO_3^{2-} and to P-O-P bonding [166]. The bands at ~800 cm^{-1} and ~1060 cm^{-1} can be assigned to the C-O bending and P-O stretching vibration, respectively [168]. Bands at ~560 and ~605 cm^{-1}, in the conditioned BG discs spectra, attributed to the P-O resonance of PO_4^{3-}, were characteristic of an apatite structure. [100]. Furthermore, conditioned samples presented a band of higher intensity in the region 3000-3600 cm^{-1} corresponding to OH vibration indicating a hydrated layer at the BG disc surfaces (**Figure 18a** and **b** inserts) [154].

These spectra confirmed the presence of a hydroxyapatite layer at the surface of the conditioned BG discs and reveal that there were no significant differences in the surface chemistry of the silanized and untreated BG discs.

2. Deposition of poly (L-co-D,L-lactic acid) honeycomb membrane

Figure 5 presents the AFM images of the membranes deposited on the different BG discs (untreated and treated). The images, taken 24 h post deposition (**Figure 19a**), allowed us to assess the relationship between the physicochemical features of the different BG disc surfaces and the features of the membranes prepared by the BFM.
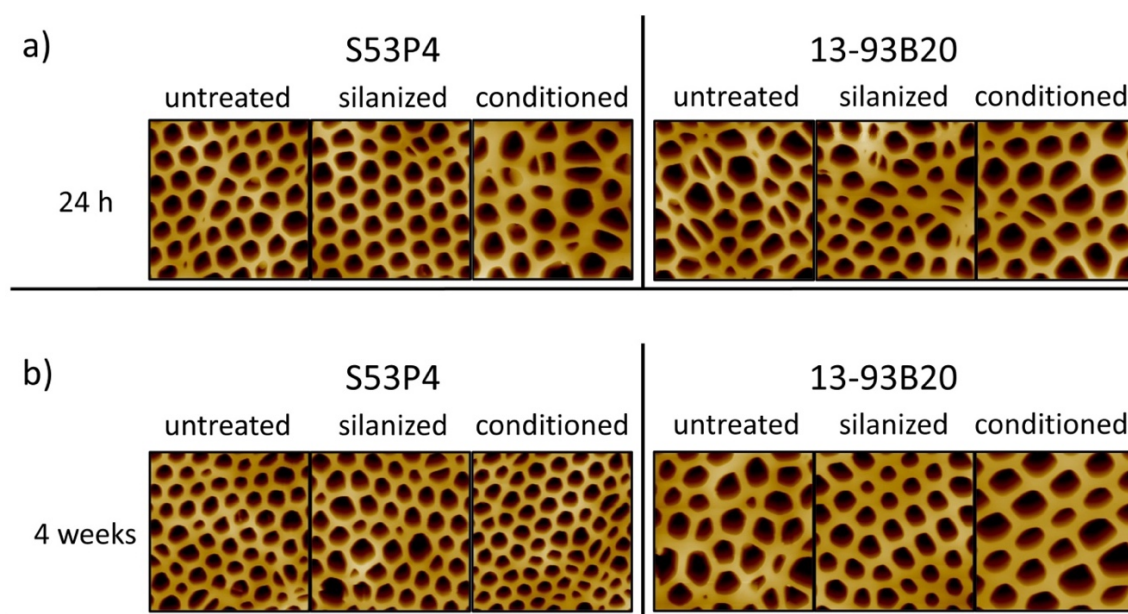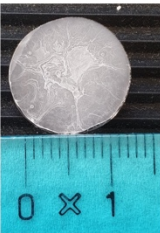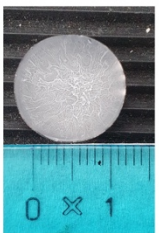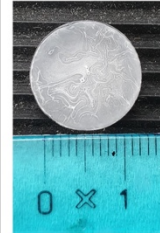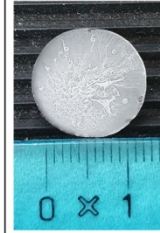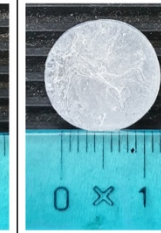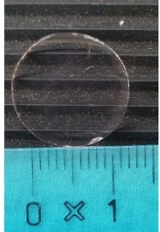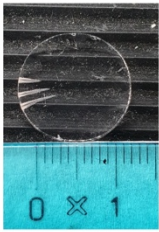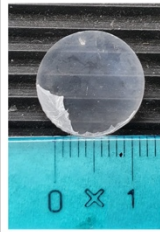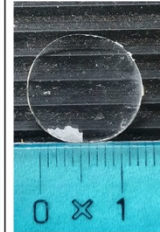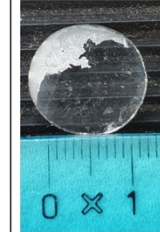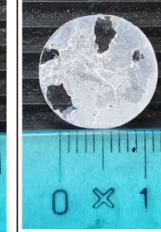
Figure 19. AFM images of the membranes deposited on the different substrates 24 h (a) or 4 weeks (b) after aging in a desiccator at 40 % RH (each image is 30 μm x 30 μm).

After 24h ageing (**Figure 19a**), regardless of the substrate, a honeycomb-like pattern was always visible, in spite of some variation in the homogeneity of the pores. Pore area was calculated and found to be 5 to 20 μm^2 (data not shown) and the thickness of the membrane was found to vary from 10 to 20 μm. Assuming that the pores had a shape close to a circle, this corresponded to a diameter of 1 to 5 μm, which was similar to the values reported in the literature for PLDLA honeycomb membranes [155]. It is well known that when using the BFM, small variations in the humidity, in the viscosity of the polymer solution or in room temperature can greatly influence the final shape of the honeycomb [44], [155], [169].

3. poly (L-co-D,L-lactic acid) membrane resistance and stability in dry conditions

The attachment of the membrane to its substrate was then evaluated by applying a shear stress on the materials and by measuring the force needed to detach the membranes. The results are shown in **Table 7**.

Table 7. Photographs of the PLDLA membrane deposited on BG discs before (upper row) and after (lower row) the shear stress test. Upon shear, the loss of the membrane is revealed by the appearance of the transparent glass substrate.

	S53P4			13-93B20		
	Untreated	Silanized	Conditioned	Untreated	Silanized	Conditioned
Before						
After						
Maximum Load (N)	0.94 ± 0.46	0.83 ± 0.63	5.56 ± 5.26	1.96 ± 1.15	13.18 ± 7.65	19.88 ± 3.79

The results showed that the membranes deposited on S53P4 and S53P4s substrates exhibited full detachment from the glass surface. In the images, almost no residues of the membrane were visible on the glass surface with a maximum load inferior to 1 N. On the other hand, membranes deposited on the S53P4c detached only partially, and the force needed to detach them was more than 5 times higher than that needed to detach the membrane from the silanized and untreated S53P4.

In the case of the 13-93B20, the untreated and silanized BGs behaved similarly, i.e. part of the membrane detached from the substrate, but some residues were observable after the test. In contrast with S53P4, silanization of 13-93B20 greatly increased the resistance to shear (more than 10 times). The attachment strength of the membranes deposited on the 13-93B20c outperformed all the other substrates and treatments. In spite of the membranes becoming mildly damaged following a maximum load of 19.88 N, a large portion of the membranes remained tightly attached to the substrate after the test, with the shear force needed to achieve detachment being greater than for all other samples. It is noteworthy that, in all the cases, the standard deviation indicated a high degree of inhomogeneity between samples. Inhomogeneities on untreated samples can be attributed to small differences in the surface finish of the samples post-polishing. In the case of silanized samples, differences may arise from the APTES physisorption. While the exposure of amine groups was the most likely event, one cannot overlook the possibility of the APTES being bound to the BG disc surface by the amine group, thus revealing ethoxy groups [170]. Upon conditioning, the texture, topography, and density of reactive layer across the surface of the disc cannot be precisely controlled, especially in the case of S53P4 where the precipitation was less prominent than for 13-93B20. Finally, as mentioned earlier, a small variation in the membrane deposition parameters (i.e. temperature, humidity etc.) can lead to small changes in membrane properties [155].

The stability of the membranes in dry conditions as a function of time and without external stress, was also studied. Membranes deposited onto the various BG disc surfaces were imaged using the AFM, 4 weeks post-deposition, as shown in **Figure 19b**. When compared to **Figure 19a**, the honeycomb structure kept its integrity for at least 4 weeks in a dry environment (desiccator). Most of the pores were found in the range of 1 to 5 μm in diameter. As stated above, a large variability in the pore dimension

was measured, which does not seem to be correlated with membrane aging nor with the treatment applied to the substrate, but rather with the processing methods and variables (humidity, polymer solution viscosity, temperature).

> **As a conclusion for this section, we demonstrated that it is possible to generate a honeycomb membrane at the surface of bulk discs of BG, regardless of the BG composition (S53P4 or 13-93B20). This section also demonstrated that the membrane attachment can be controlled by controlling the substrates surface chemistry and topography. Here, the most promising functionalization to allow proper membrane attachment seems to be the conditioning. The chemistry and topography at the conditioned BG surface, with the formation of hydroxyapatite, revealed to be favorable to a stronger membrane attachment in dry conditions. In the next section, the membrane/BG discs assemblies' properties will be studied in aqueous conditions.**

B. Stability of the membrane/Bioactive glass disc assembly in aqueous conditions

1. Assembly integrity in aqueous solution

The stability of the membrane/BG disc assembly was then studied by immersing the material in TRIS buffer solution at 37 °C, for up to 4 weeks (**Figure 20**).

—: BAG untreated, ⋯: BAG silanized, - - -: BAG conditioned
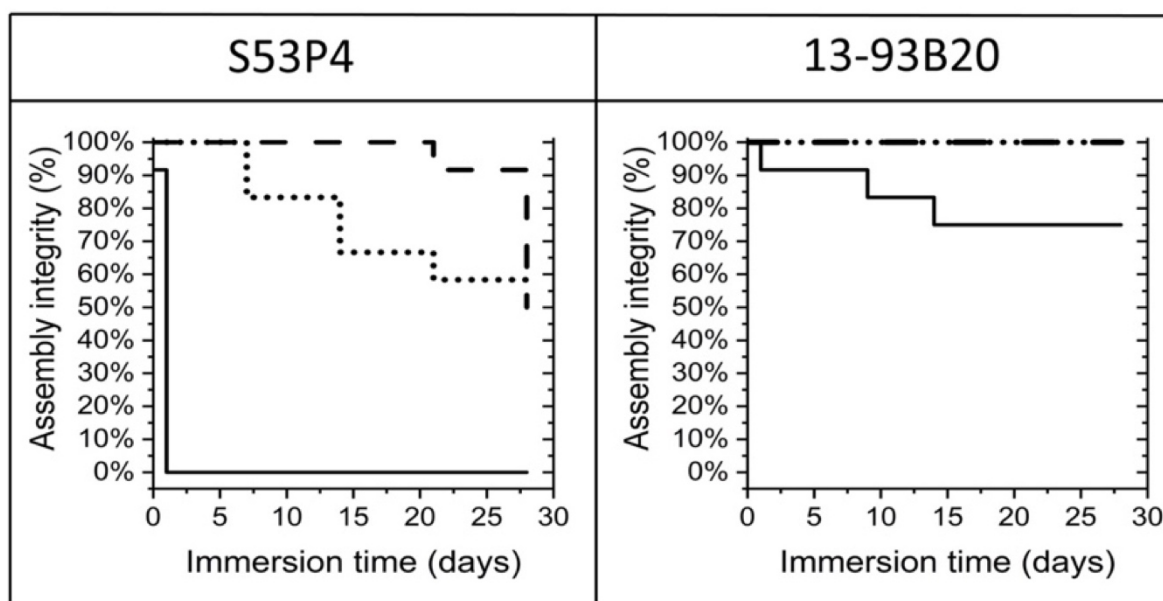
Figure 20. Assembly integrity (in %), was estimated by counting the number of membranes that did not detach (partially or totally) from their substrate, as a function of immersion time, n = 12.

All membranes deposited on S53P4 detached after 3 h of immersion. Membranes started to detach after 7 days and 21 days on S53P4s and S53P4c, respectively. Compared to the S53P4, membranes deposited on 13-93B20 were noticeably more stable. Indeed, 70 % were still attached to their substrate after 28 days of immersion. While borosilicate glass is typically considered more hydrolytically unstable than silicate glass, this is solely due to the borate phase which degrades at a faster rate than the silicate phase [167]. As per the FTIR-ATR spectra in **Figure 18**, one can see that the silicate network in the S53P4 glass has a greater number of non-bridging oxygen (ratio between the bands at ~930 cm^{-1} and ~1030 cm^{-1}), than the silicate network in the 13-93B20 glass [171]. Therefore, the initial dissolution of the SiO_2 network occurs faster for the S53P4 glass, leading to a decreased interface stability between the glass and the membrane.

Silanization improved drastically the assembly integrity, regardless of the BG composition. It is interesting to note that membranes deposited on S53P4s seemed to detach gradually over time. 60 % of the membranes remained attached to the substrate after 4 weeks of immersion, while 100 % of the membranes were still attached to their substrate on the 13-93B20s. As per the zeta potential, it is believed that the surface of the 13-93B20 was grafted with a higher density of amine groups leading to

78

a higher stability of the membrane at the glass surface. Zhou et al. reported interactions between PLDLA and hydroxyapatite, thereby hydrogen bonds forms between C=O and P-OH functions [172]. Similarly, in this study it is feasible that amines and C=O group interacts through hydrogen bonding.

Finally, on the S53P4c, membranes remained stably attached to the substrate for 20 days, with 50 % of the membranes abruptly detaching at 27 days. Membrane attachment was found to be significantly improved when 13-93B20c BG was used as the substrate, with 100 % of the membranes remaining attached at the end of the immersion period. As shown by the SEM/EDX (**Figure 16** and **Figure 17**) and FTIR-ATR analysis (**Figure 18**), the surface chemistry has changed during the immersion for 24 h in TRIS buffer solution, thereby a Ca-P reactive layer has formed at the surface of the glass. This is believed to be the reason for the stability of the assembly upon immersion.

Zeta potential, mechanical testing and immersion into TRIS buffer solution indicated that:

1) The stability of the membrane was highly dependent on the surface reactivity, i.e. in solution the more reactive surface will lead to a faster failure of the membrane.

2) Silanization improved the stability of the membrane/BG disc assembly in aqueous solution. The improvement was a function of the amine group density (i.e. surface charge). However, only at higher silanization density an increased shear stress is necessary to detach the membrane from the substrate (i.e. for silanized13-93B20, **Table 6**).

3) Membranes deposited on conditioned samples demonstrated improved resistance to shear, as well as higher stability in aqueous solutions. Such improvement in the membrane/BG disc assembly stability was linked to the precipitation of a stable Ca-P reactive layer. The thicker the layer, the more stable the membrane, probably due to an increased specific surface area and/or interactions between the hydroxy groups of the reactive layer and carbonyl groups of the polymer [172]. The impact of the specific surface area on the membrane adhesion will be studied in the future.

Overall, a controlled surface treatment of the bioactive substrates led to an improvement in the assembly integrity. This is of paramount importance in view of culturing cells without the risk of the membrane

detaching over time. Furthermore, when thinking of the application (i.e. a biphasic bone substitute), proper adhesion of the membrane to its substrate is crucial, up until the time the defects has been repaired.

2. Bioactive glass ion release, from the assembly, in aqueous solution

It is well known that BGs react and release ions upon immersion, which can have beneficial effects on cell fate [17], [173]. The release profile of Si, Ca, P and Na ions by both BGs is presented in **Figure 21**, while the release profile of B, K and Mg ions, specific to the composition of the 13-93B20 glass, is shown in **Figure 22**.

The ion release profiles for untreated samples are also reported in the figures. However, membranes deposited on the untreated S53P4 were not studied further, due to their poor stability in aqueous conditions (**Figure 20**, all membranes detaching after 3 h). Therefore, the ion release from this material does not reflect the release rate of ions through the membrane but rather from the substrate alone. The data are included to allow for comparison in dissolution kinetics between the various treatments on S53P4.

As suspected, the release of Si from the untreated S53P4 was slightly faster than the release rate observed for the 13-93B20, which confirmed that the decreased membrane stability in aqueous solution was probably due to the rapid release of ions from the glass surface. A faster Si release from S53P4, when compared to 13-93B20, was expected. Indeed, BG 13-93B20 was developed by substituting 20% of the SiO_2 with B_2O_3 in the silicate glass 13-93 [29]. The silica network, in the glass 13-93 (without boron), is more polymerized than in S53P4 and therefore 13-93 is more stable to hydrolysis [174]. In addition, the partial substitution of B_2O_3 for SiO_2, in 13-93B20, further leads to an increased polymerization of the SiO_2 network making 13-93B20 silica network less sensitive to hydrolysis compared to S53P4 [29], [175]. Upon silanization, one can see that the Si release for S53P4 did not significantly change whereas it increased for 13-93B20. This can be assigned to the pre-treatment of the materials during silanization and/or release of Si from the grafted APTES. Finally, the conditioned S53P4 BG released more Si than the silanized counterpart, whereas the Si release profile from the

conditioned 13-93B20 was similar to the Si release from the silanized 13-93B20 material. The greater Si release from the conditioned S53P4 compared to 13-93B20 can be explain by the change in surface chemistry. Indeed, as the reactive layer was thinner on the S53P4 BG, more silica gel was in contact with the solution, in turn leading to higher Si release to the surrounding medium. It is important to note that, after 3 days of immersion, the silicon release seemed to slow down. This phenomenon is in agreement with previous studies discussing the Si release from BGs [159].

Phosphorous release profile was similar for all BGs Phosphate concentration seemed to saturate, as soon as 1 week for all samples. The shape of the curve indicated that phosphate release followed a typical diffusion-controlled process. However, as the results are cumulative, this could also indicate the saturation of the solution with phosphate ions, leading to precipitation of a reactive layer [176]. The phosphorous release profile appeared to be independent of the surface treatment in 13-93B20. However, untreated S53P4 released more phosphorous than the surface treated ones. This can be attributed to the absence of the membrane in this particular condition.

Sodium release from S53P4 and 13-93B20 glass samples was consistent with the dissolution mechanism described by Hench [88], [89] for BGs Indeed, the conditioned samples seemed to release Na at a lower rate than the silanized samples. This was attributed to the fast Na^+ H^+ ion exchange occurring at the early stage of the glass dissolution, occurring during the conditioning step. The variation in concentration was less pronounced in the case of 13-93B20 due to the lower Na content in the glass composition (**Table 4**).

It is interesting to note that despite the two glass compositions having almost the same mol% of Ca, the release of this ion happened faster in the case of the borosilicate glass. Indeed, it has been hypothesized that Ca interacts preferentially with the borate network than with the silicate one, which is the least hydrolytically stable [159], [167]. All 13-93B20 BGs released a higher content of Ca compared to S53P4 BGs regardless of the treatment, but this amount was significantly higher for the silanized and conditioned 13-93B20. Given the high affinity of Ca and P toward the precipitation of apatite crystals,

the high release of Ca, irrespective of the treatment for the glass 13-93B20 is likely to lead to the precipitation of a reactive layer overtime [159], [177].
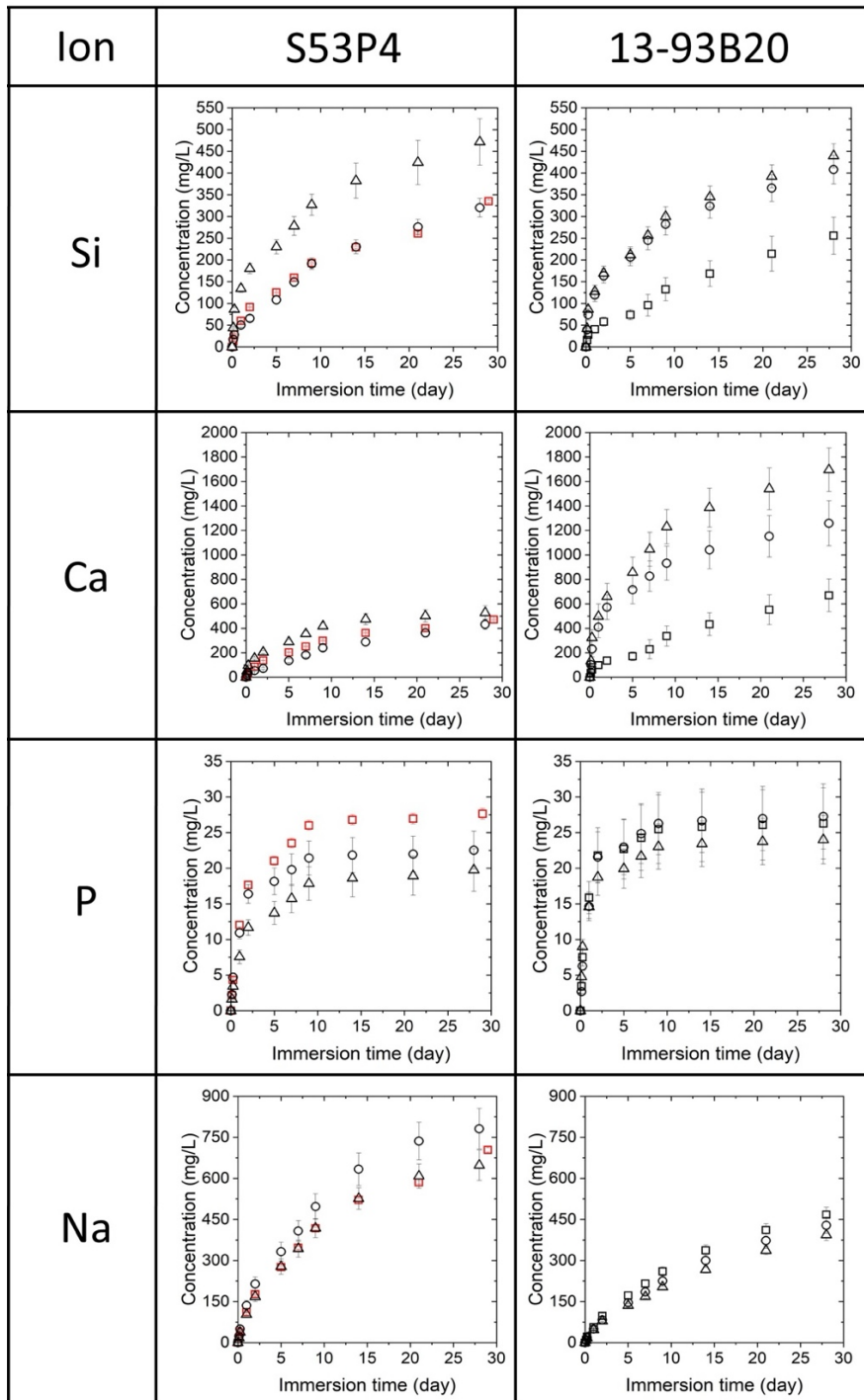
Figure 21. Silicon (Si), Calcium (Ca), Phosphorous (P) and Sodium (Na) release profile upon immersion of the membrane/BG disc assembly in TRIS buffer solution for up to 28 days. Red squares display the results of untreated S53P4 without membrane.
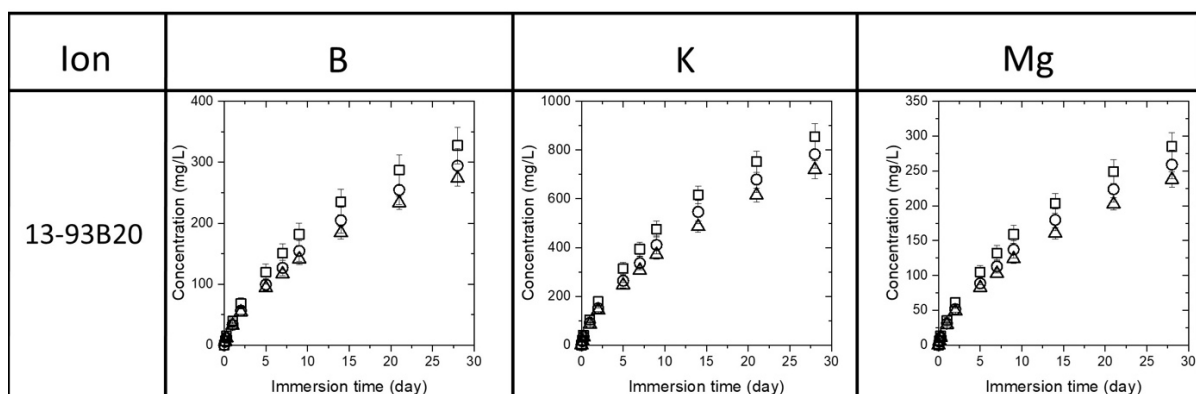
Figure 22. Ion release profile of Boron (B), Potassium (K) and Magnesium (Mg) for the three 13-93B20 -containing membrane/BG disc assembly as a function of immersion time in TRIS buffer solution.

As shown in **Figure 22**, 13-93B20 released B, K, and Mg, in a similar amount and kinetics regardless of the treatment. This suggested that the borate phase was the most soluble and was not affected by the silica-rich layer formation and Ca-P reactive layer precipitation.

Altogether, these results indicated that a) the presence of the membrane did not prevent the glass from dissolving, and therefore the ions, beneficial to the cells, were still released to the medium, b) 13-93B20 glass exhibited a rapidly dissolving borate phase and a stable silicate phase, which in turn promoted membrane stability and higher density of APTES grafting and c) 13-93B20 exhibited an ion release profile favorable to the precipitation of a reactive layer.

3. Membrane surface analysis

To assess the surface features of the membrane after immersion, samples incubated in TRIS for 4 weeks were air dried overnight and imaged by AFM (**Figure 23**).
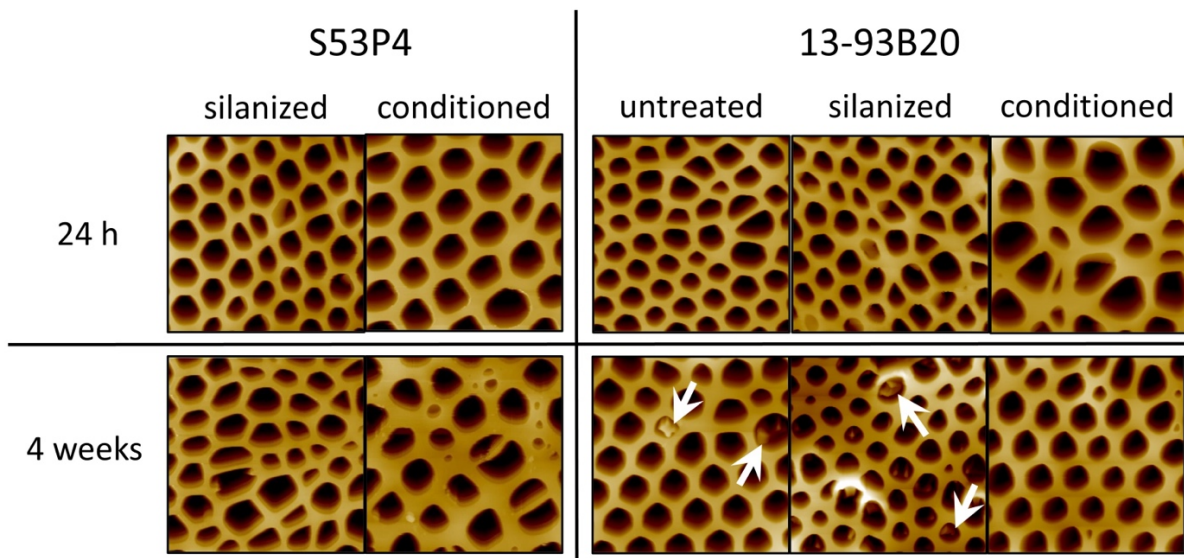
Figure 23. AFM images of the films deposited on the different substrates after incubation in TRIS buffer solution at 37 °C for 24 h and 4 weeks (each image is 30 μm x 30 μm, each image is from different samples). White arrows show precipitates.

The honeycomb structure of the membrane was preserved for at least 4 weeks of immersion in TRIS buffer solution. Images were further processed with Fiji and the pores size was estimated. Regardless of the incubation time or the substrate, pores were estimated to have a diameter in the 1 to 5 μm range. The pore size post-incubation was similar, within the accuracy of the measurement and the accuracy of the processing, to the sample pre-incubation.
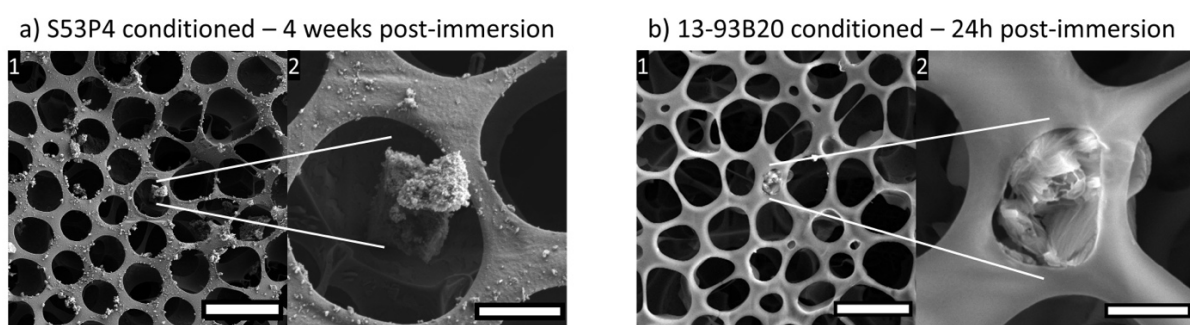
Figure 24. SEM images of the films deposited on a) S53P4c or b) 13-93B20c incubated in TRIS for 4 weeks and 24 h, respectively (a1 and b1 Scale bar 10 μm. Area of interest a2 and b2 are displayed on the right of the images, Scale bar 2 μm).

To illustrate the precipitation within the pores, **Figure 24** exhibits the membrane surface of a) S53P4c immersed for 4 weeks in TRIS and b) 13-93B20c immersed for 24 h in TRIS.

From the SEM images (**Figure 24a**), one can observe the presence of small nodules at the surface of the membranes deposited on the conditioned S53P4; similar features were also seen at the surface of the silanized S53P4 post-immersion. From **Figure 24b**, one can see that large aggregates were present within the pores of the membrane. Such aggregates were not visible in the silanized and untreated samples post-immersion. The EDX analysis revealed a high concentration of Ca and P. Those nodules, both on membrane deposited on S53P4 and 13-93B20 were due to the precipitation of a CaP, as expected upon immersion of BGs [105]. However, the small size and low density of the nodules did not enable unambiguous EDX analysis.

The previous sections showed that it is possible to generate a honeycomb membrane at the surface of BG discs and make it strongly attached, even in aqueous conditions, through careful control of the BG discs surface physicochemical properties. Furthermore, the study revealed that the membrane does not impair the BG dissolution properties and can support HA precipitation. Nevertheless, the aim of the developed material is, ultimately, to be implanted in humans. For that, sterilization is essential to ensure the safety of the product. Therefore, an investigation on the effect of the gamma irradiation on the BG, membrane and membrane/BG discs assemblies' physicochemical properties was carried out. Furthermore, the membrane/BG discs assemblies-cell interaction before and after irradiation was investigated. In this study of the effect of the gamma irradiation, only conditioned BG discs were used since the conditioning proved to be the best functionalization to obtain a strong membrane attachment.

C. Gamma irradiation effect on the membrane/BG assembly

Before discussing the impact of the gamma irradiation on various membrane/BG assembly properties (including cell- membrane/BG assembly interactions), the structural and luminescent properties of the selected BGs, S53P4 and 13-93B20, are first presented. The IR spectrum of S53P4 BG in **Figure 25a** exhibit multiple bands which can mainly be related to Si-O bonds. The shoulder at ≈ 660 cm^{-1} and the band at ≈ 750 cm^{-1} can be attributed to bending vibrations of the Si–O^{-} end groupings [159], [166], [178]. The main band at ≈ 915 cm^{-1} can be assigned to Si-O^{-} (non-bridging oxygen = NBO) asymmetric stretching vibrations of the [SiO$_4$] units [179], [180] followed by the band at ≈ 1010 cm^{-1} which is related to Si-O-Si asymmetric stretching vibration [179]. A faint shoulder can be seen ≈ 1250 cm^{-1} and might be connected to longitudinal asymmetric stretching of Si-O-Si according to Kopani et al. [181]. The band at ≈ 1465 cm^{-1} can be associated with carbonate groups presence due to an incomplete decarbonization [159], [166], [182]. The spectrum of 13-93B20 has similar bands compared to that of the IR spectrum of S53P4 while also having a few differences. The band between 600 and 800 cm^{-1}, with a pick at ≈ 720 cm^{-1}, can be associated with B-O-B bending vibrations [179]. The main bands in the 800 – 1100 cm^{-1} region can be related to a joint contribution from the previously mentioned band related to Si-O bonds and from B-O bonds in [BO$_4$] units especially at 916 cm^{-1} and 1010 cm^{-1} [179]. The shoulders at ≈ 1225 cm^{-1} can be related to BO$_2$O^{-} triangles and at ≈ 1400 cm^{-1} and ≈ 1470 cm^{-1} can be associated to BO$_3$ groups and carbonate groups whose signature might be covered by the BO$_3$ groups signal [159], [167], [183]. In summary, while S53P4 spectra mainly depict the presence of SiO$_4$ units with bridging and non-bridging oxygens, the structure of 13-93B20 present a joint contribution of the silica network, and mainly BO$_3$ along with BO$_2$O^{-} and BO$_4$ units which are fully integrated within the BG structure.

The PL spectra of the 2 investigated BGs under 266 nm excitation are presented in **Figure 25b**. They exhibit two emissions bands centered at 532 and 710 nm which can be assigned to oxygen deficient centers (ODC) [184] and non-bridging oxygen hole center (NBOHC, molecular structure: ^{o}Si-O^{-}) [185],

[186], respectively. While a larger amount of ODC is suspected in S53P4 than in 13-93B20, the 13-93B20 possesses a larger amount of NBOHC probably due to the presence of various borate units [168], [187].
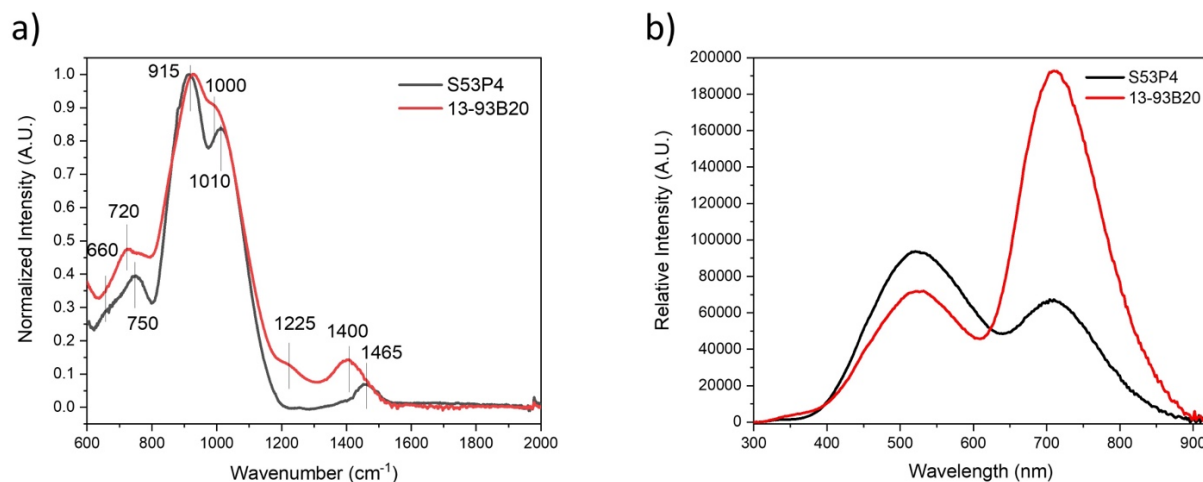
Figure 25. FTIR (a) and photoluminescence (b) spectra of the BGs as prepared (λ_{exc} = 266 nm).

4. Effect of the gamma irradiation on the bioactive glass

The investigated BGs were irradiated using gamma radiations with a dose of 26-29 kGy. After irradiation, the BGs became dark, S53P4 being less dark (**Figure 26**). The darker color of the BGs visible after radiation treatment is a clear sign of defect formation as demonstrated by Rautiyal et al.[188].
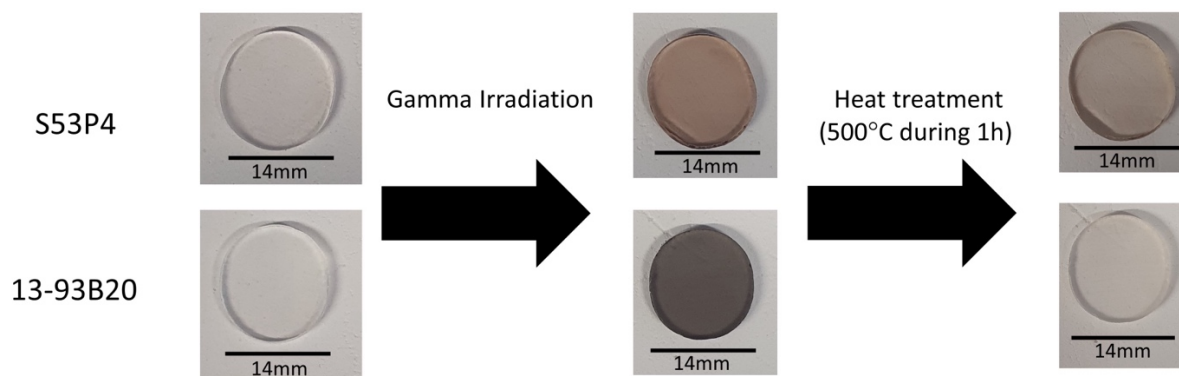
Figure 26. Pictures representing pictures of the BGs before and after irradiation and after heat treatment (in that order) showing the reversibility of the color's appearances.

As in Rautiyal et al., the formation of defects is evidenced from the changes in the UV vis absorption spectra after radiation treatment [188]. As depicted in **Figure 27ab**, the absorption coefficient in the 300 – 1000 nm range increases after irradiation, the increase being larger in the absorption spectrum of 13-93B20 BG (**Figure 27**).

The shoulder at 450-550 nm can be assigned to defects like ODC [188], [189] and the shoulder at 550 – 650 nm can be attributed to defects like NBOHC and/or peroxy radicals (POR, molecular structure: $\equiv$Si-O-O$^-$) [188], [189]. E$^-$ centers, known to have an absorption band in the range 600-730 nm, are also expected to form during the radiation treatment [190]. The absorption bands centered at 440 and 620 nm can be related to H_I and H_{II} defect centers, defined as trapped holes on one or two nonbridging oxygens on the same SiO_4 tetrahedron [191] , respectively. Similar defects were reported in silicate glasses by El-Kheshen [192]. According to Griscom et al., oxygen deficient center, peroxy linkage and/or E' centers (molecular structure: Si$^-$) with an absorption band at 300-350 nm are also expected [189]. In the 13-93B20 BG, the increase in intensity of the absorption bands at 350–450 nm could be related to boron bound oxygen hole centers (BOHC, $\equiv$B-O·-Si$\equiv$) according to Möncke et al. [193] . BOHC's or hole trapped centers with an absorption band between 500 and 600 nm are also suspected to form [187]. As depicted in **Figure 27c**, a larger amount of defects are expected to be formed during the radiation treatment in the 13-93B20 indicating that this BG is more sensitive to gamma irradiation than S53P4, probably due to the presence of BO_3 and BO_4 units. Griscom et al. [194] described a core-silicate-clad-borosilicate prototype fiber that shows a higher radiation sensitivity in the cladding material compared to the core. They state that, this higher sensitivity of the borosilicate cladding material is due to the defects formed upon irradiation and particularly the "boron E' centers". Those centers are planar BO_3 units that, upon irradiation, trap an electron and are therefore charged (-1), while the Si E' centers are not charged, which make the boron E' centers less stable than their Si counterpart. This might be what happens in our BG and can explain the higher radiation sensitivity of the 13-93B20. This is in agreement with the darker coloration of the 13-93B20 after irradiation seen in **Figure 26**.
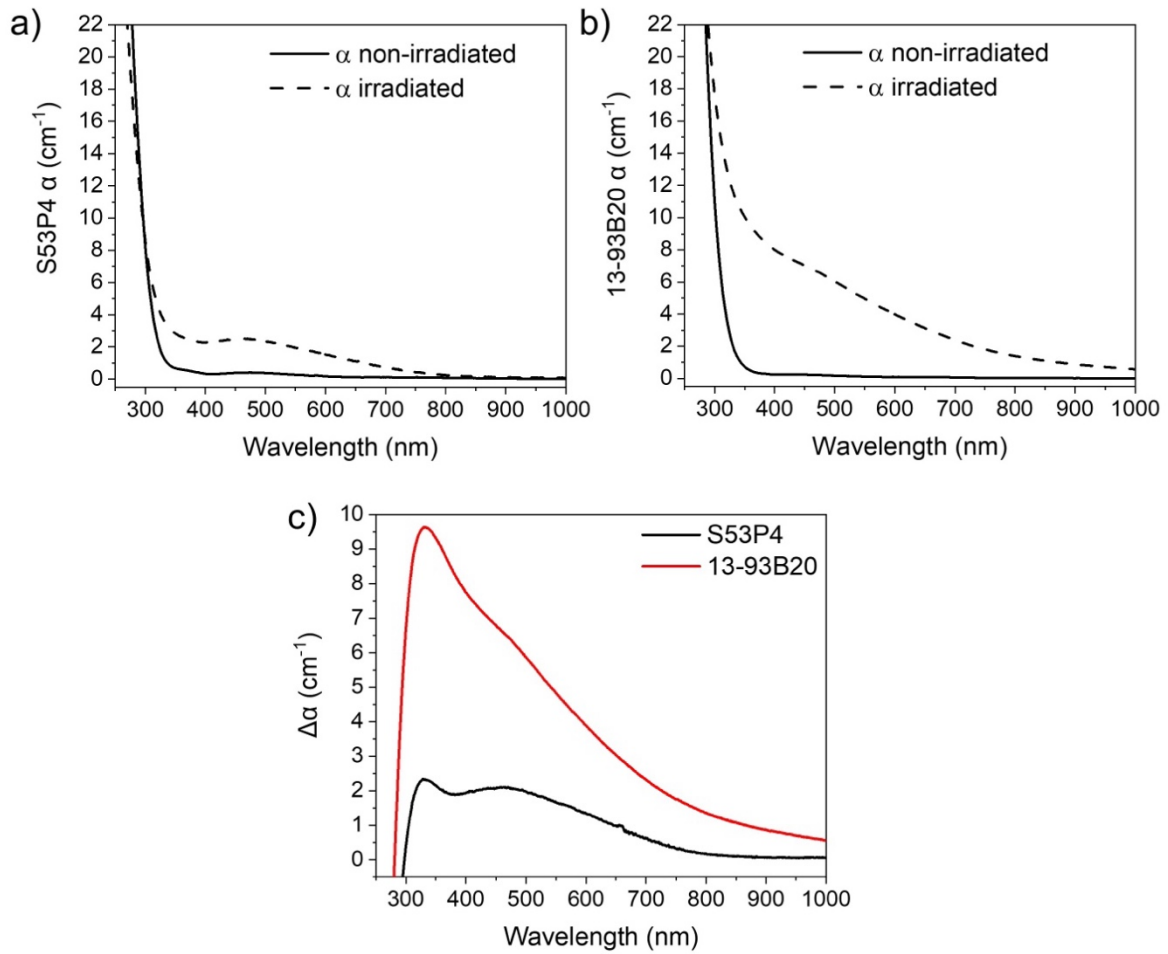
Figure 27. UV vis absorption spectra represented by the absorption coefficient of S53P4 (a) and 13-93B20 (b) as prepared or after irradiation, and spectra of the difference in absorbance coefficient (a) between irradiated and non-irradiated samples (c) ($\Delta\alpha = \alpha$ (irradiated) - α (non-irradiated))

One should point out that the formation of defects has no noticeable impact on the structure of the BGs (**Appendix 1**) although an increase in bridging oxygen (BO) at the expense of NBO was reported after radiation treatment in [195], [196]. However, the doses used in these studies were orders of magnitude higher than the dose used in our study. The radiation treatment has an impact on the spectroscopic properties but only for 13-93B20 as seen in **Figure 28**: the PL emission bands between 300 and 900 nm decreases after irradiating 13-93B20 revealing a decrease in the number of ODC and NBOHC in this glass in agreement with [195], [196]. 13-93B20 seems to be more sensitive to the irradiation than S53P4 most probably due the presence of BO_3, BO_2O^- and BO_4 units and of a large amount of NBO in its network.

Nevertheless, the identification of the defects presented here requires more investigation with other methods than FTIR and PL such as Raman spectroscopy or electron paramagnetic resonance spectroscopy (EPR) to provide more information and precisely determine the nature of each defect.
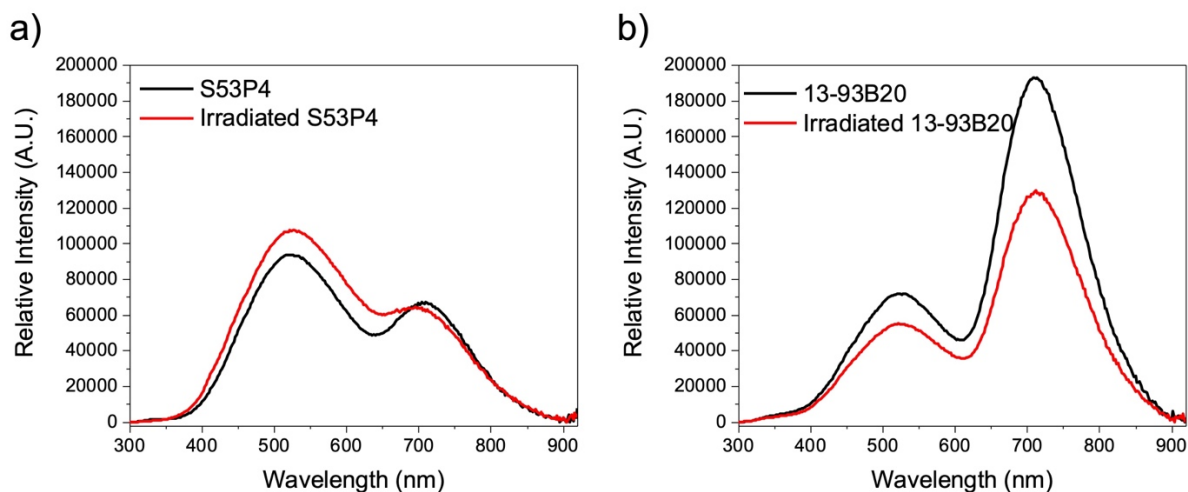
Figure 28. Photoluminescence spectra of S53P4 (a) and 13-93B20 (b) before (black curve) and after (red curve) irradiation.

To assess the reversibility of the color change post-irradiation, the irradiated samples were re-heated at 500°C for 1h (**Figure 26**). This temperature was chosen because it is lower than the T_g of the BGs and would allow relaxation without damaging the BG structure. In **Figure 26**, it can be seen that all samples recovered a color similar to their original one. This suggest that reversible structural changes are occurring during the irradiation of the samples. This reversibility of the color of the BGs induced by irradiation has already been described by Radek et al.[197] and El-Kheshen [192].

5. Effect of the gamma irradiation on the membrane/bioactive glass assembly

As seen in **Figure 29**, the polymer retains the honeycomb structure after irradiation. However, the molecular weight of the polymer decreases from ≈350.000 g/mol to ≈175.000 g/mol after irradiation, independently of the BG composition A similar decrease in molecular weight of polymer was reported by Nugroho et al. [198] and Shim et al. [199] and can be related to random chain scission. Furthermore, FTIR spectra were recorded pre- and post-irradiation, and no significant difference could be evidenced (data not shown). This agrees with a study by Shim et al. [200] who reported that, at gamma-rays doses

ranging from 25 to 500 kGy no significant difference in the polymer chain, and notably the polymer functional groups, before and after irradiation could be seen. In addition, Pèrez-Davila et al. reported a 99.8% similarity in FTIR spectra recorded pre- and post-irradiation (25kGy) of PLA 3D scaffolds.
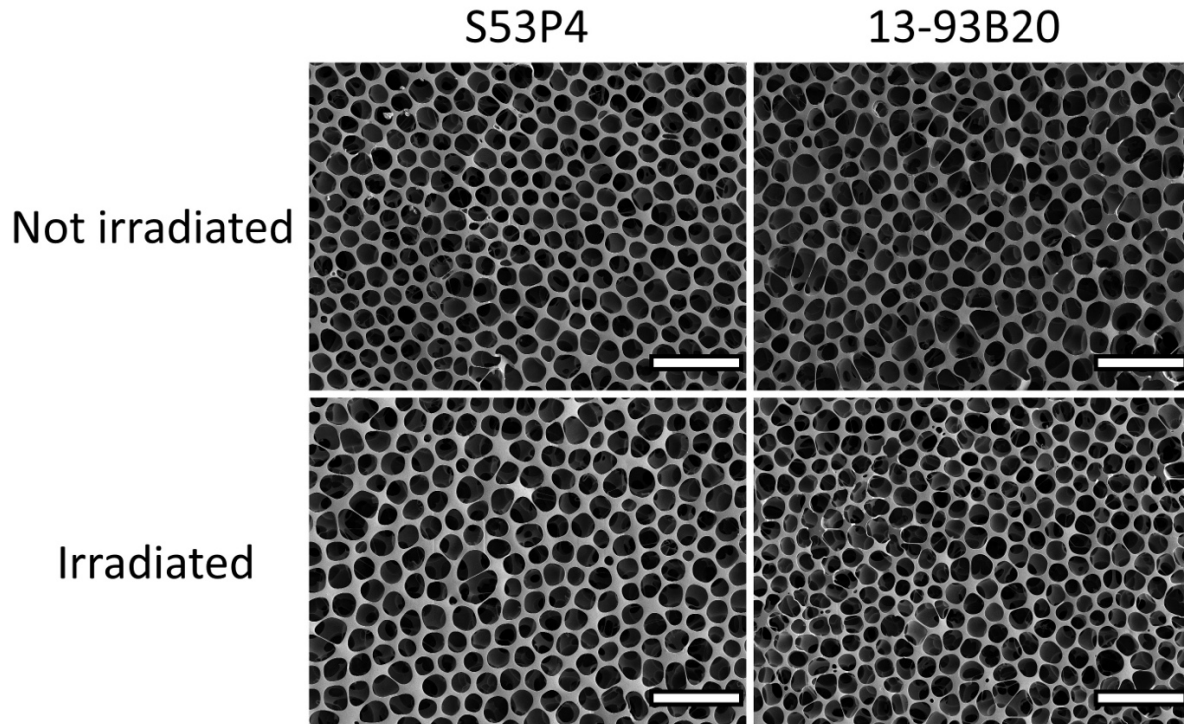
Figure 29. SEM images of the membranes deposited on the S53P4 and 13-93B20 substrates both before and after irradiation (scale bar 20μm).

Photographies of the membrane/BG assemblies after the shear stress test and surface of detachment (SOD) are shown in **Table 8**. Prior to irradiation, the SOD is comprised between 2 and 10 mm^2. When comparing the SOD of the non-irradiated S53P4 and 13-93B20 membrane/BG assemblies, we can see a larger surface area detached on the S53P4 than from the 13-93B20 (9.79 mm^2 vs 2.61 mm^2) , indicating that the membranes are better attached on the 13-93B20 than on the S53P4 due to the thicker apatite layer and it structure at the surface of the BG as explained in [201]. One should point out the attachment inhomogeneity of the membrane based on the photographies and the large standard deviation for the shear stress load. After irradiation, the SOD increases while using a lower load indicating a lower attachment of the membrane to the BG. Therefore, it is plausible to think that the radiation treatment leads to a decrease of the membrane attachment points and therefore the membrane resistance to shear stress.

Table 8. Photographies illustrating membrane/BG assemblies before and after irradiation, after the shear stress test. SOD = Surface of detachment, pointed by the white arrows, membrane total surface ≈ 154 mm^2.

		Samples	Average Maximum load (N)	Average SOD (mm^2)
S53P4	Before irradiation		42.60 ± 9.45	9.79 ± 10.89
	After irradiation		33.79 ± 13.05	30.40 ± 23.85
13-93B20	Before irradiation		49.17 ± 19.66	2.61 ± 3.27
	After irradiation		36.69 ± 7.26	10.97 ± 6.64

6. Effect of the gamma irradiation on the membrane/bioactive glass assembly-cell interaction.

MC3T3-E1 osteogenic progenitor cells were seeded on top of non-irradiated and gamma irradiated membrane/BG assembly. In order to estimate, and to discriminate, the potential and resulting effect of the irradiation onto the cell behavior, as controls, non-irradiated membrane/BG assembly samples were simply disinfected prior to cell culture. Cells were cultured on the honeycomb membrane side up to 7 days and had their nucleuses and actin filaments stained and subsequently imaged through confocal microscopy to observe their morphology (**Figure 30**). Furthermore, the medium during the cell culture was collected and analyzed through ICP to quantify the ion release from the BGs during the experiment (**Figure 31**).
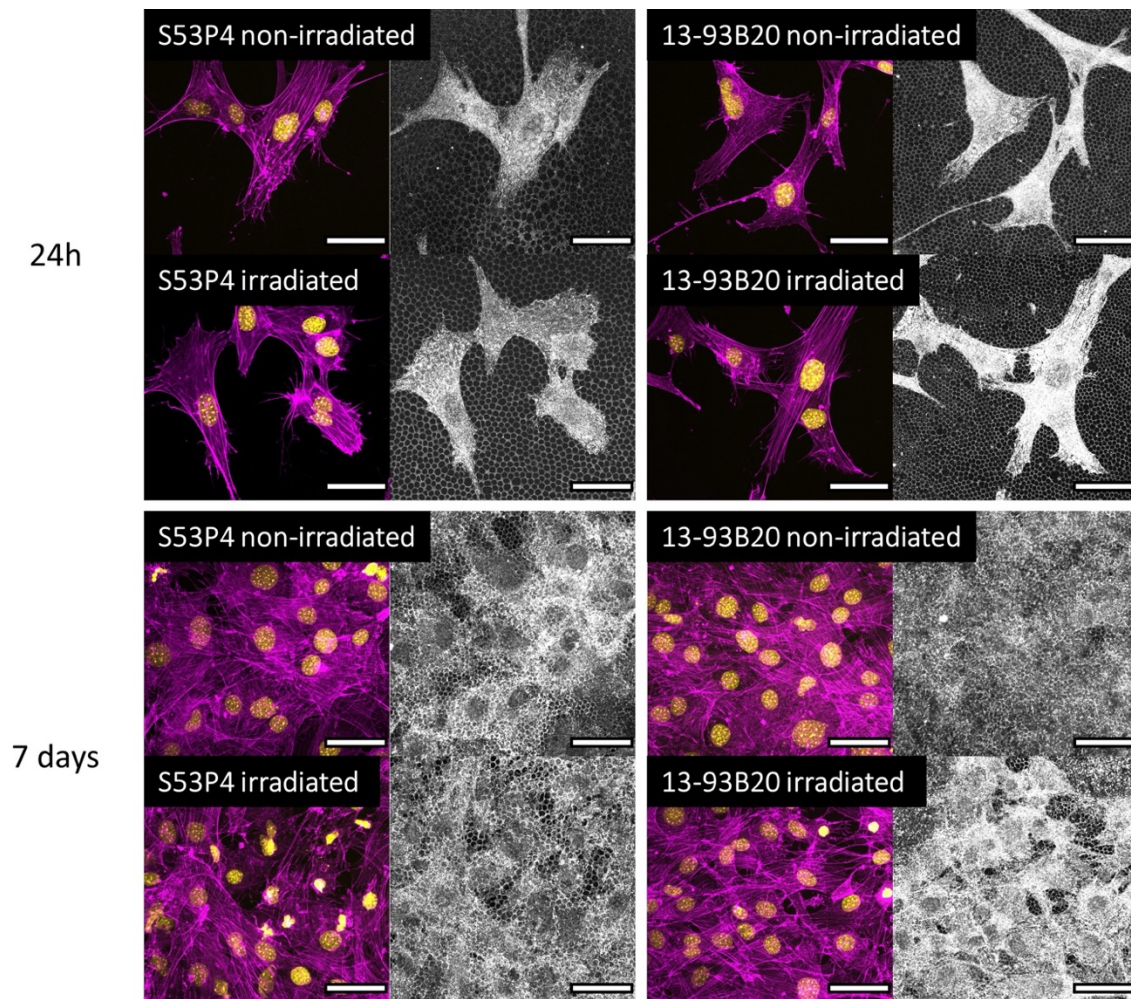
Figure 30. Confocal images of MC3T3 cells cultured on the membrane part of the materials non-irradiated (disinfected) or irradiated after 24h and 7 days, scale bars 50 µm. Gray scale images show the honeycomb membrane with a shadow of the cells on it. Magenta = actin filaments, yellow = nucleus.

After 24h, cells have adhered at the membrane surface and have spread independently of the BG composition and treatment. Actin filaments are visible and organized. Nuclei are well defined and large, showing that the cells grew at the surface of the irradiated membrane/BG assembly similarly than those on the disinfected samples. Furthermore, the honeycomb membrane, visible under the cells (gray scale images) seems to be intact, independently of the BG composition. After 7 days, cells are confluent. Actin filament organization is well visible like nuclei. The membrane is less visible underneath the cells because of the high number of cells. These results indicate that the gamma irradiation of the membrane/BG assembly, does not seem to induce deleterious or cytotoxic effect on the cells.

To confirm this finding, the medium was analyzed through ICP in order to quantify the inorganic ions released by the BGs in the medium during the experiment. The results are presented in **Figure 31**.

Looking at the ion release from the S53P4, for each considered ion, the release profile is similar irrespective of the treatment. This result indicates that, the defects, resulting from the gamma radiation, do not impact the dissolution rate of the S53P4 BG.

The silicon (Si) release profile of the 13-93B20 is similar to the release profile of S53P4 and no significant variation is observed between the non-irradiated and the irradiated samples. Considering the boron (B) release, we can observe a significant increase in its release when the BG is irradiated. The same pattern can be observed regarding the release profile of calcium (Ca), magnesium (Mg) and potassium (K). As said above, irradiation creates defects in the BGs and the 13-93B20, due to the presence of borate units like BO_3 and BO_4, is more sensitive to the radiations meaning that more defects are created in this BG. This phenomenon makes the 13-93B20 slightly more soluble when irradiated resulting in a higher release in the medium of Ca, Mg and K.

Considering the phosphorous (P) concentration, the decrease observed indicates that there is a precipitation of apatite occurring regardless of the BG [29], [166]. It is noteworthy that, contrary to P, Ca concentration does not decrease. This suggest that Ca ions saturate the solution while P can easily be consumed to form apatite structure at the surface of the membrane/BGs assemblies. Furthermore, there is no significant difference between the irradiated and the non-irradiated samples, making clear that the irradiation does not influence the precipitation speed.

Those results, in combination with the observation from the cell culture, confirm that, even though the irradiation induces the creation of defects in the BG molecular matrix that leads to some modifications in the ion release and the molecular weight of the polymer membrane that decreases, these modifications do not seem harming for the cells. Nevertheless, such observations are not sufficient to ensure that the membrane/BGs assemblies do not have a cytotoxic effect on the cells. Further experiments such as MTT and LDH assays are planned for a future study in order to further analyze the effect of the membrane/BG assemblies and the sterilization on the cells.
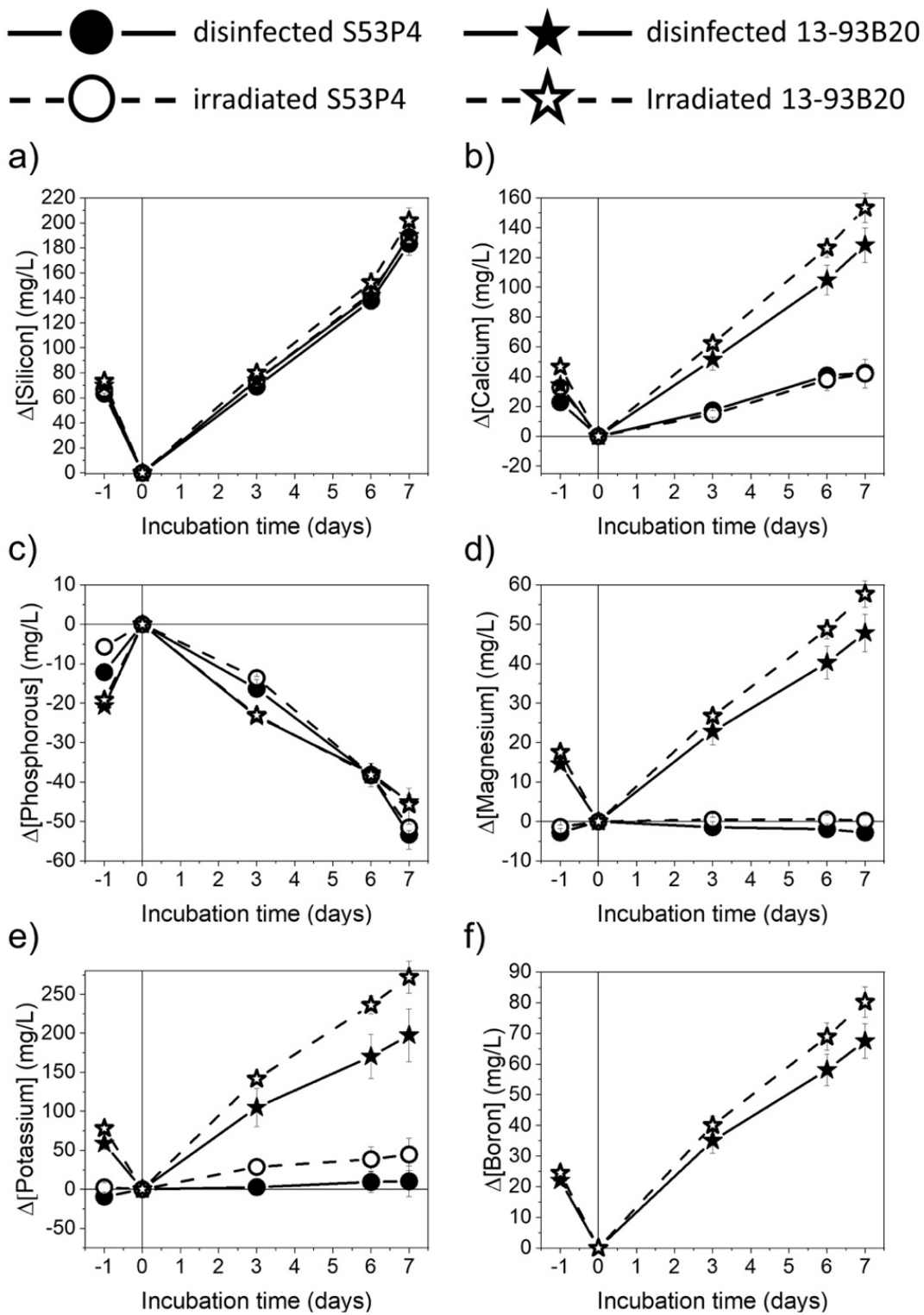
Figure 31. Ions release profile of silicon (a), calcium (b), phosphorous (c), magnesium (d), potassium (e) and boron (f) during cell culture up to 7 days of S53P4 non-irradiated (●) or irradiated (○) and 13-93B20 non-irradiated (★) or irradiated (☆). -1 represent the ion release during the pre-incubation of the materials in complete culture medium and 0 the starting point of the cell testing. Data are presented as cumulative over time.

Until now, we have proved that a bulk material made of BG can support the formation of a honeycomb membrane at its surface, maintain its bioactivity with the membrane upon immersion, and that by controlling the surface features of the bulk BG, the membrane can be strongly attached to it. Furthermore, we demonstrated that although sterilization can induce subtle changes in the BG and membrane physicochemical properties, it does not deleteriously impact the bioactivity, nor the membrane/BG assemblies-cells interactions. However, a bulk piece of BG does not seem very interesting for the purpose of bone tissue engineering. Indeed, bone is a complex porous structure, with varying porosity and density depending on if we consider cortical or cancellous bone. The bone porosity is an essential feature to allow the vascularization of the tissue and the exchange of waste and nourishing molecules. Therefore, and to mimic further the bone organization, we attempted to generate the honeycomb membrane on more appropriate bone substitutes. First, 3D printed porous BG scaffold made of 13-93B20 and second, pieces of xenogeneic decellularized bone matrix (DBM). Subsequently, the physicochemical characteristics of the prepared membrane/substrates assemblies were studied. Successively, the barrier properties of the membrane and the biocompatibility of the assemblies with relevant cells were assessed.

D. Honeycomb membrane generation on 3D printed 13-93B20: process validation, behavior in aqueous solution and material-cell behavior

Our previous work [201] aimed at demonstrating the feasibility of depositing a honeycomb membrane on inorganic synthetic biomaterials. However, to increase the relevance, the biomaterials ought to be porous. Therefore, a strategy to generate a membrane, using the BFM, on 3D printed porous BG scaffolds was developed. In this context the 13-93B20 BG was 3D printed by robocasting and the top of the scaffold was dense to 1) mimic the structure of bone (cortical/spongious) and 2) allow the

deposition of the membrane. Successively the membrane was generated on cortical bone to extend the proof of concept to xenograft.

1. Membrane deposition on the 3D porous substrates

The BG 13-93B20 scaffolds, with dense top, post-printing and post-sintering are shown in **Figure *32*a**. As in our previous study the scaffold was either untreated (13-93B20) or conditioned (13-93B20c). The roughness measurements were carried out and the average roughness of the substrates are presented in **Figure 32b**.

The untreated scaffold (13-93B20) presents a relatively smooth surface with picks and valleys formed by the 3D printed filament, accompanied by some pores in the structure. The roughness for the 13-93B20 varies from 2 to 6 µm with a mean around 4 µm (**Figure 32b**). While no significant changes in the Ra can be evidenced, for the 13-93B20c compared to 13-93B20, a "rocky" surface can be distinguished due to the precipitation of HA during the conditioning [201].
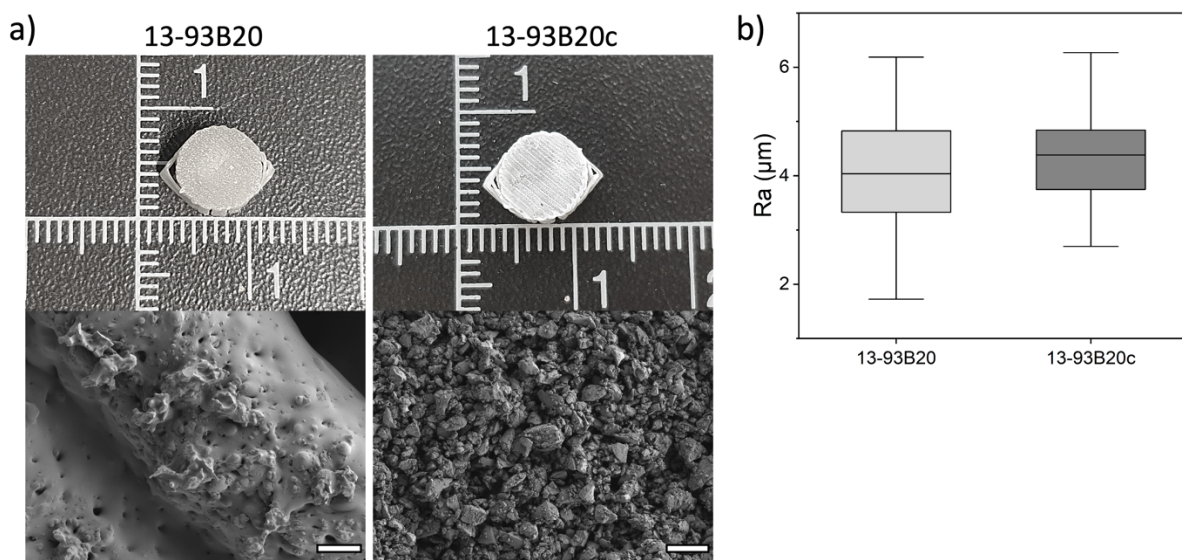
Figure 32. a) Macroscopic and SEM images of the 3D printed scaffolds before the honeycomb membrane deposition. Scale bar 50µm, b) Average surface roughness of the 3D printed scaffold.

Successively the membrane was generated on both type of scaffolds. Images of the membrane on the substrates were taken by SEM, presented in **Figure 33**. Furthermore, the average pore depth of the membrane on the membrane/substrates assemblies was measured and assessed by AFM (**Figure 34a**, **c**

and **d**) along with the membrane pore diameter distribution (**Figure 34b**) and the water contact angle (WCA) of the substrates and membrane/substrates assemblies (**Figure 35**).
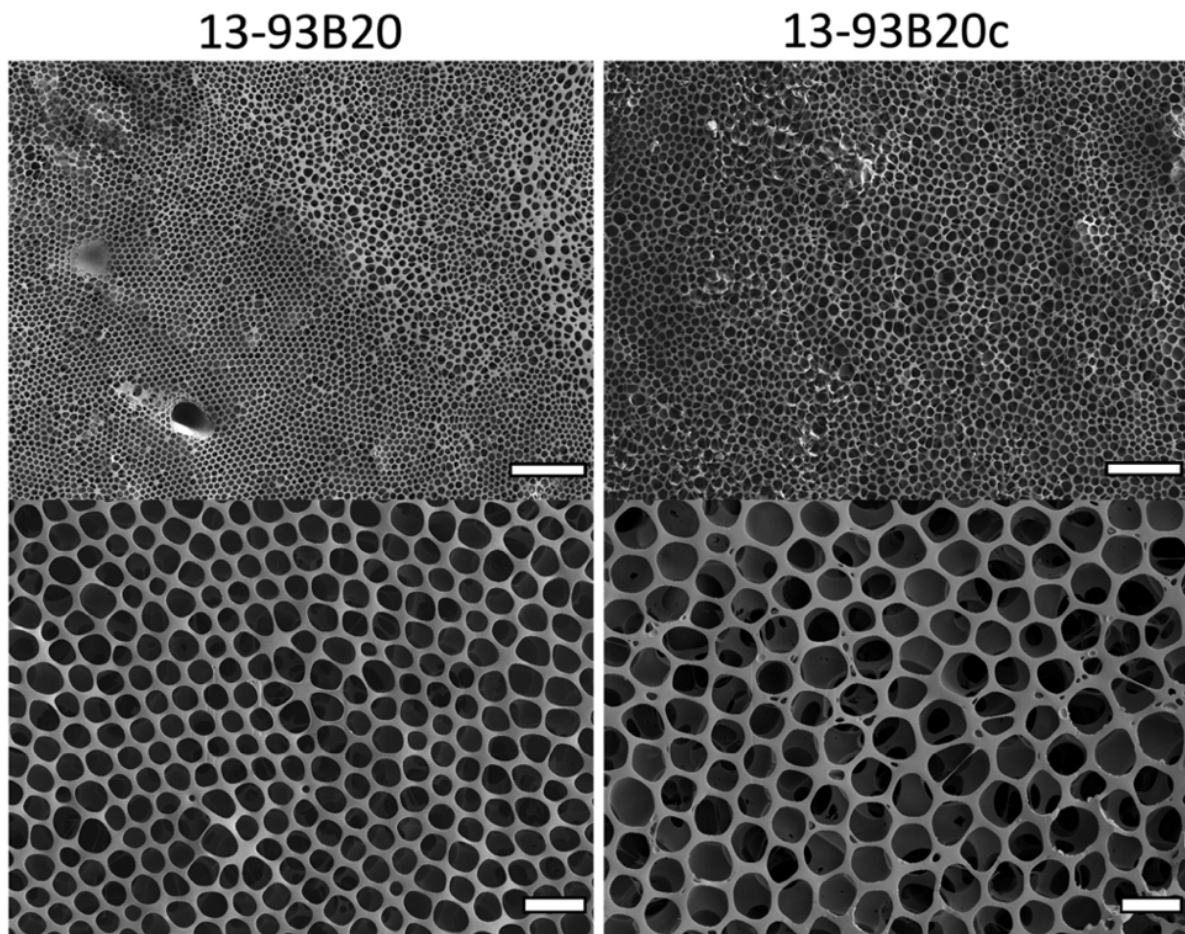
Figure 33. SEM images of membranes deposited on 13-93B20,13-93B20c from randomly imaged sample. Scale bar 50µm (1st line) and 10 µm (2nd line).

One can see that there is some subtle variability in the shape and the size of the pores on the honeycomb membrane. These variations were expected. Indeed, HC pores in membranes and films generated with the BFM are known to be affected by many parameter (RH, temperature, solution viscosity, volume) that can induce variations in the pore size, shape and organization [44], [155], [169]. Assuming that pores had a shape close to a circle, their diameter was calculated and found to vary between 2 and 7 µm (**Figure 34b**) which is similar to what can be found in the literature for PLDLA honeycomb membranes [44]. There is no significant difference between the pore diameter between the membrane/13-93B20 assembly and the membrane/13-93B20c assembly. However, one should note that pore size distribution is broader on the 13-93B20 than on the 13-93B20c. Indeed, 75% of the pore's diameter are comprised

between 2 and 5 µm on the 13-93B20, with a mean around 4 µm, while on the 13-93B20c, they are mostly comprised between 4 and 5.5 µm with a mean around 4.5 µm. The narrower pore size distribution, on the 13-93B20c, could be due to the surface topography of the substrate. Indeed, SEM images revealed pores in the structure of the 13-93B20 which can induce a capillary effect that might reduce the volume of solution in some areas at the 13-93B20 surface during the BFM process. This limited amount of solution results in a limited space for the formation of the pores which can cause the observed variations in the pore size [44]. On the other hand, the 13-93B20c does not have the pores of the 13-93B20 and therefore allows more of the solution to stay at the surface to allow the HC pores formation during the BFM process. Therefore, there is less variations in the pore size on the membranes generated at the surface of the 13-93B20c. Furthermore, we hypothesize that this capillary effect might be responsible for the variations on the pore depth (**Figure 34a**). Indeed, with the capillary effect, the solution penetrates inside the material which can cause the pores to be slightly deeper. In fact, the average pore depth measured on the membrane alone (membrane deposited on a flat nonporous petri dish) as a control, is approximately 1 µm and varies only between 0.1 and 2 µm while the depth measured for the pores on the membranes deposited on the 13-93B20 and the 13-93B20c revealed a depth varying between 2 and 5.5 µm with an average depth around 3.5µm. These measurements are confirmed by the AFM images that measures similar pore depth (**Figure 34c** and **d**). Nevertheless, no significant difference was found between the depth of the pores measured on the membrane of the membrane/13-93B20 and the membrane/13-93B20c assemblies.
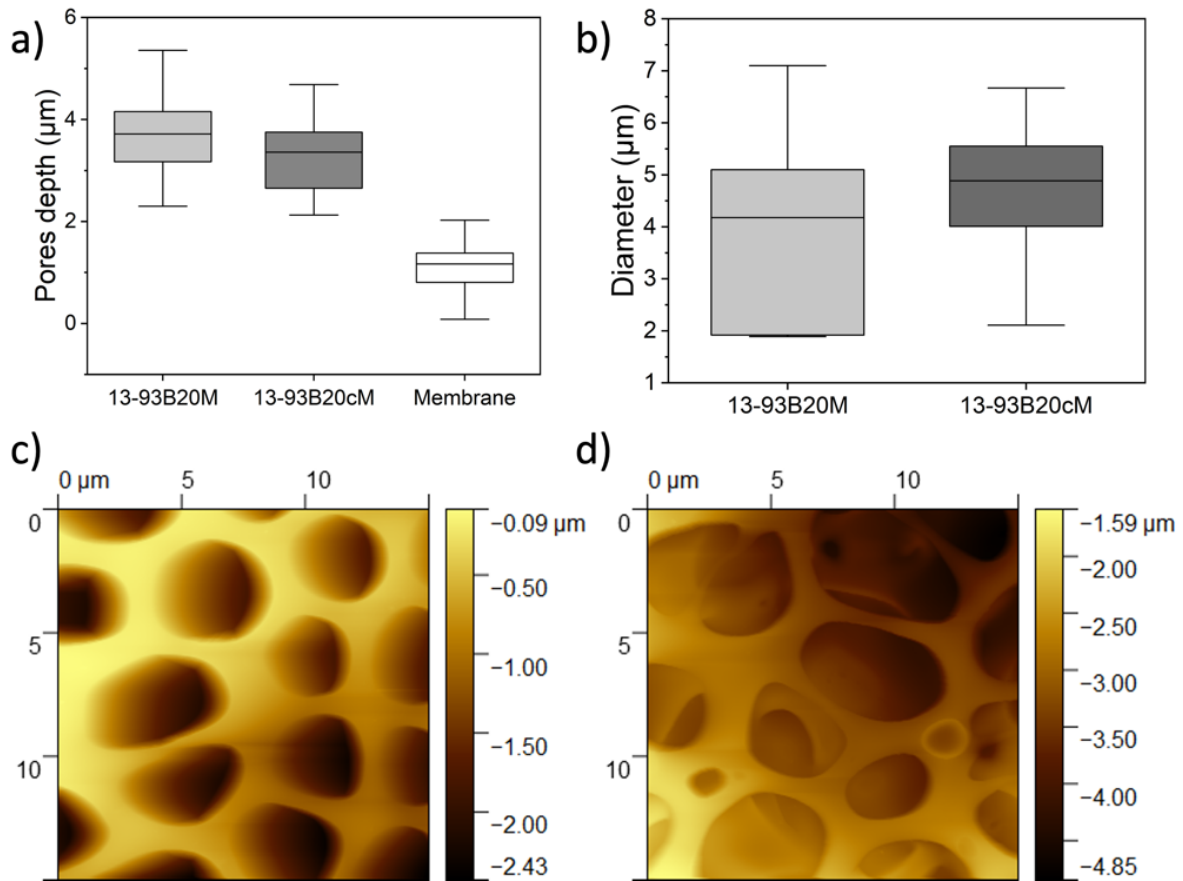
Figure 34. Box charts representing a) the pore depth variation of the HC membrane on the membrane/substrates assemblies and the membrane alone (n = 3), b) the pore diameter distribution of the membrane deposited on the different substrates (measured with Fiji based on 3 images of 3 different randomly chosen regions on 3 different sample for each substrate) and AFM images of the HC membrane generated on c) 13-93B20 and d) 13-93B20c

Along with the roughness and the surface topography, the wettability of materials is an essential feature to study since it can greatly influence the cells behavior *in-vivo* and *in-vitro* [202], [203]. The static water contact angle was measured on the samples and the results are presented in **Figure 35**. For the membrane alone, the measurements revealed a contact angle of approximately 110°, which is similar to what can be found in the literature for contact angle on HC membranes of PLDLA [151], [204]. The substrates without membrane have a contact angle below 90° which corresponds to hydrophilic surface [205]. Furthermore, 13-93B20 contact angle of ≈ 60° is significantly different from the one found on the 13-93B20c with a contact angle of ≈ 70°. This might be due to the surface topography of the 13-93B20c, due to the hydroxyapatite precipitates, or to the different chemistry between the glass surface

and the HA. Once the membrane has been generated at the surface of the substrates, the contact angle increases and become similar to the one of the membrane alone (membrane produced on a flat nonporous petri dish), namely $\approx 120°$ for the 13-93B20M and $\approx 110°$ for the 13-93B20cM. This means that, the features below the membrane do not influence its wettability once generated at the surface of the substrate.
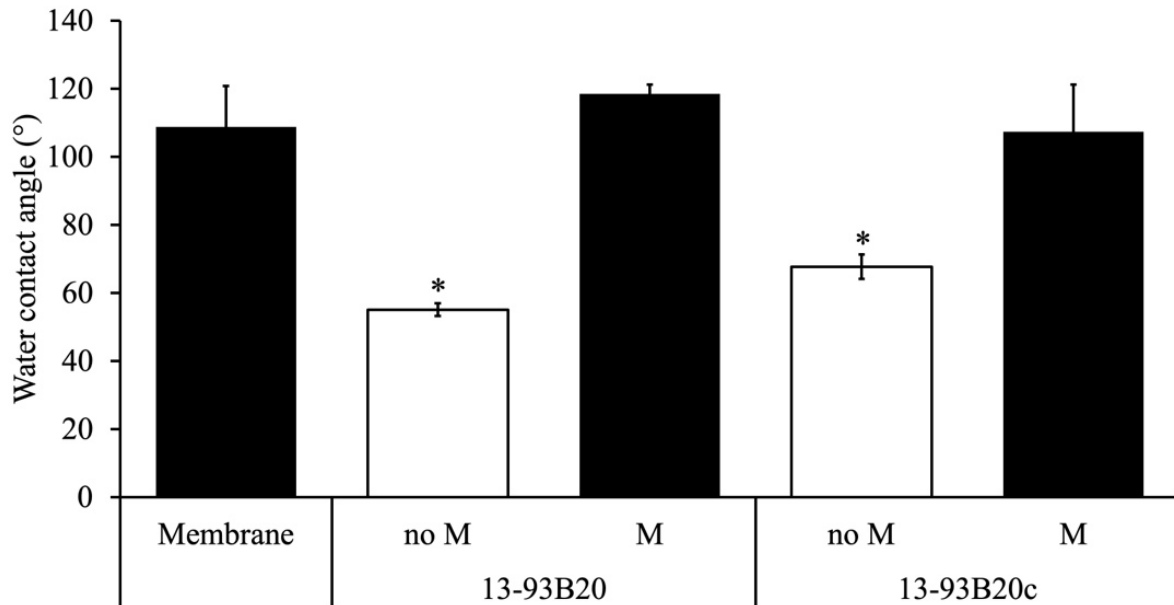
Figure 35. Static water contact angle of the membrane alone, the substrates and the membrane/substrates assemblies. * denotes a significant difference with $p < 0.05$.

In this section, we demonstrated the possibility to generate a honeycomb membrane at the surface of BG-based 3D printed scaffolds. In addition, the generated membrane/substrates assemblies present hydrophobic properties, compared to materials without the membrane. This scaffold is aimed to be in contact with fluids in the human body. Therefore, it is of outmost importance to study its behavior in aqueous solution. The following section studies the behavior and bioactivity of the scaffolds in TRIS buffer solution and simulated body fluid (SBF).

2. Behavior of the membrane/substrate assemblies in aqueous conditions

2.1. In TRIS buffer

To study the behavior of the materials in solution, BG scaffolds with and without membranes, were immersed in TRIS buffer solution for up to 28 days. The ion release was measured through ICP-OES and the formation of precipitates was investigated by SEM and μCT. The results are presented from **Figure 36** to **Figure 38**.

The membrane/substrate assemblies, regardless of the treatment, release Si, P, Ca and B. Considering the silicon (Si) release (**Figure 36a**), all the samples have a similar release regardless of the treatment and the presence of the membrane. Furthermore, the Si release seems to slow down after 2 days of immersion. This is in accordance with the Si release reported in previous studies [159], [201]. When it comes to phosphorous (P) (**Figure 36b**), as suspected, the P concentration increases and reaches a plateau quickly, at 2 days post-immersion, for all samples, regardless of the presence of the membrane. As the data are cumulative, this suggests a potential precipitation of a reactive layer [176].

When looking at the ion release of calcium (Ca) and boron (B) (**Figure 36c** and **d** respectively), the profiles seem to follow the same pattern: 13-93B20 is the sample that releases the more, the membrane/13-93B20 assembly (13-93B20M) and 13-93B20c have a similar intermediate release and the membrane/13-93B20c assembly (13-93B20cM) releases the less ions. The similar release pattern of Ca and B, compared to Si, depict the higher affinity of Ca with the borate phase compared to the silicate phase in borosilicate glasses. This phenomenon was already observed previously in our work [201]. Now, the lower Ca ion release for samples with the membrane compared to their counterpart without the membrane, especially for the membrane/13-93B20 assembly (13-93B20M), might indicate a preferential Ca/P precipitation on the membrane leaving less ions free in solution. Indeed, upon immersion, the PLDLA is subjected to hydrolytic degradation that creates carboxylic-end groups that can be used as nucleation point for HA [206], [207]. Therefore, the Ca is preferentially attracted to the membrane where it contributes to the precipitation of HA.
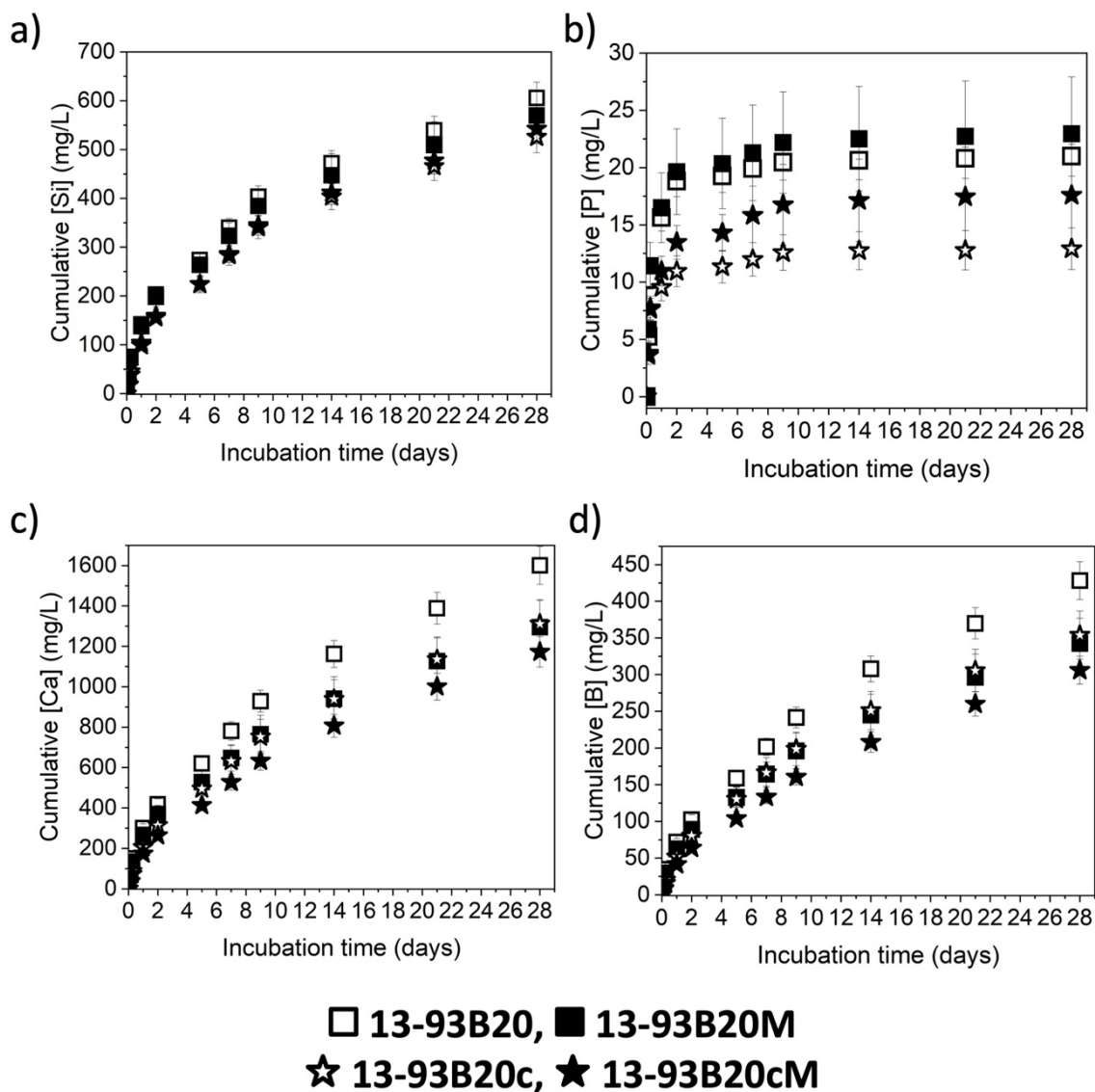
Figure 36. Ion release profile of a) Silicon (Si), b) phosphorous (P), c) calcium (Ca) and d) boron (B) in the dissolution product of 13-93B20 (□), 13-93B20M (■), 13-93B20c (☆) and 13-93B20cM (★) upon immersion in TRIS buffer solution up to 28 days, [element] = element concentration.

To assess the precipitation of a reactive layer on the materials, they were imaged using X-ray micro-computed tomography (μCT), to analyze the inner part, and SEM, to analyze their surface.

Figure 37 presents μCT images of vertical cut made in the middle of the materials before and after immersion, with and without membrane.
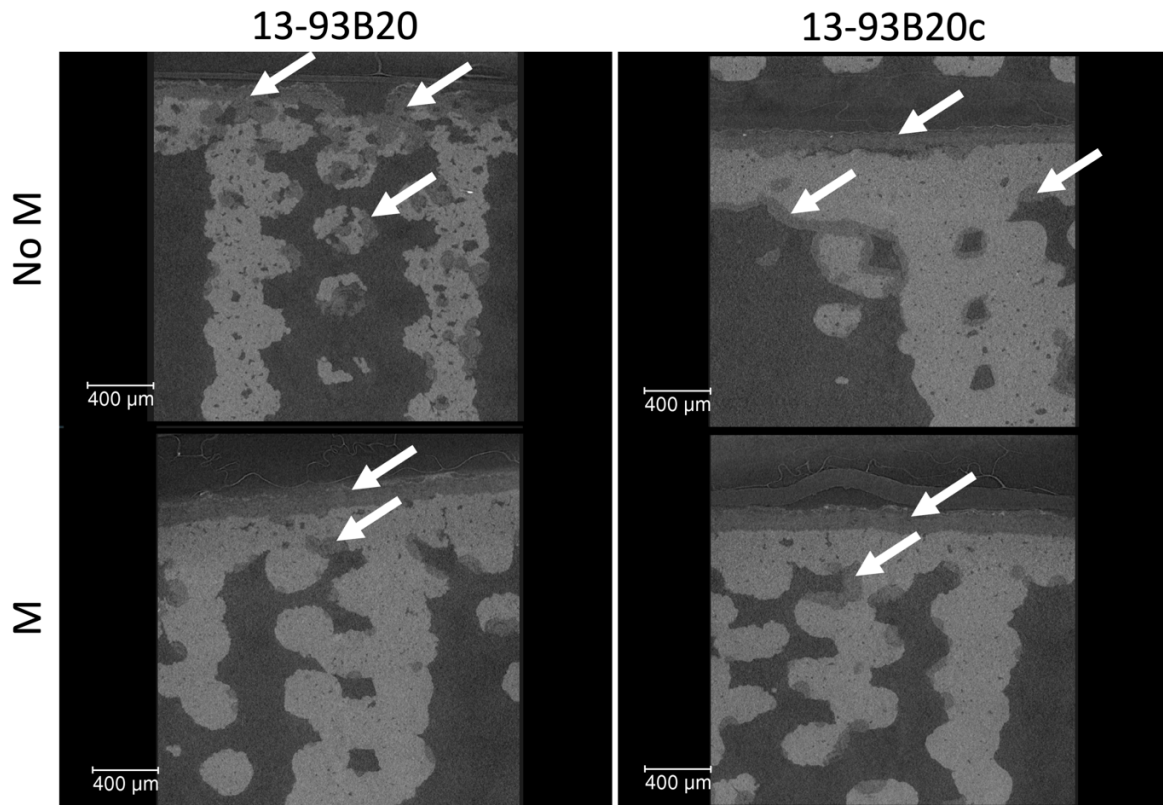
Figure 37. μCT images of vertical slice of the samples without or with a HC membrane and before or after 28 days of immersion in TRIS buffer solution. White arrows show denser areas, probably apatite precipitates. Scale bar = 400 μm

First of all, the 3D printed scaffold regardless of the treatment or the presence of the membrane, have similar inner features and the 3D printed strut seems to have a good cohesiveness revealing a successful sintering process. After immersion, regardless of the treatment, denser part appears inside the scaffolds (white arrows). In the untreated 13-93B20 (13-93B20), those dense areas are sparse and seems to appear everywhere inside the 3D porous structure without a particular pattern, and also at the surface. This suggests the apparition of precipitates, probably CaP, inside and at the surface of the material and their dispersion suggest an uneven precipitation process. On the 13-93B20c, those denser parts seem to be less sparse compared to the 13-93B20 and are more present at the surface of the scaffold and the surface of the strut inside. This is due to the conditioning that allows a first precipitation of a reactive layer at the surface of the 3D printed strut that than serves as a template for further precipitation during the immersion in SBF. In addition, those precipitates seem to be more present inside the substrates (13-93B20 and 13-93B20c) without the membrane compared to the membrane/substrate assemblies,

104

regardless of the treatment, which is consistent with the ICP results suggesting a preferential precipitation on the membrane. Furthermore, it is noteworthy that the membrane is not visible in the µCT images. This might be explained either by the fact that the polymer is radiolucent and therefore invisible on the µCT or by the fact that the membrane is extremely thin compared to the other features and cannot be seen at the scale of the images, or both [208].

To analyze the surface of the samples, SEM images were taken after the 28 days of immersion in TRIS buffer solution. The images are presented in **Figure 38** and **Figure 39**.
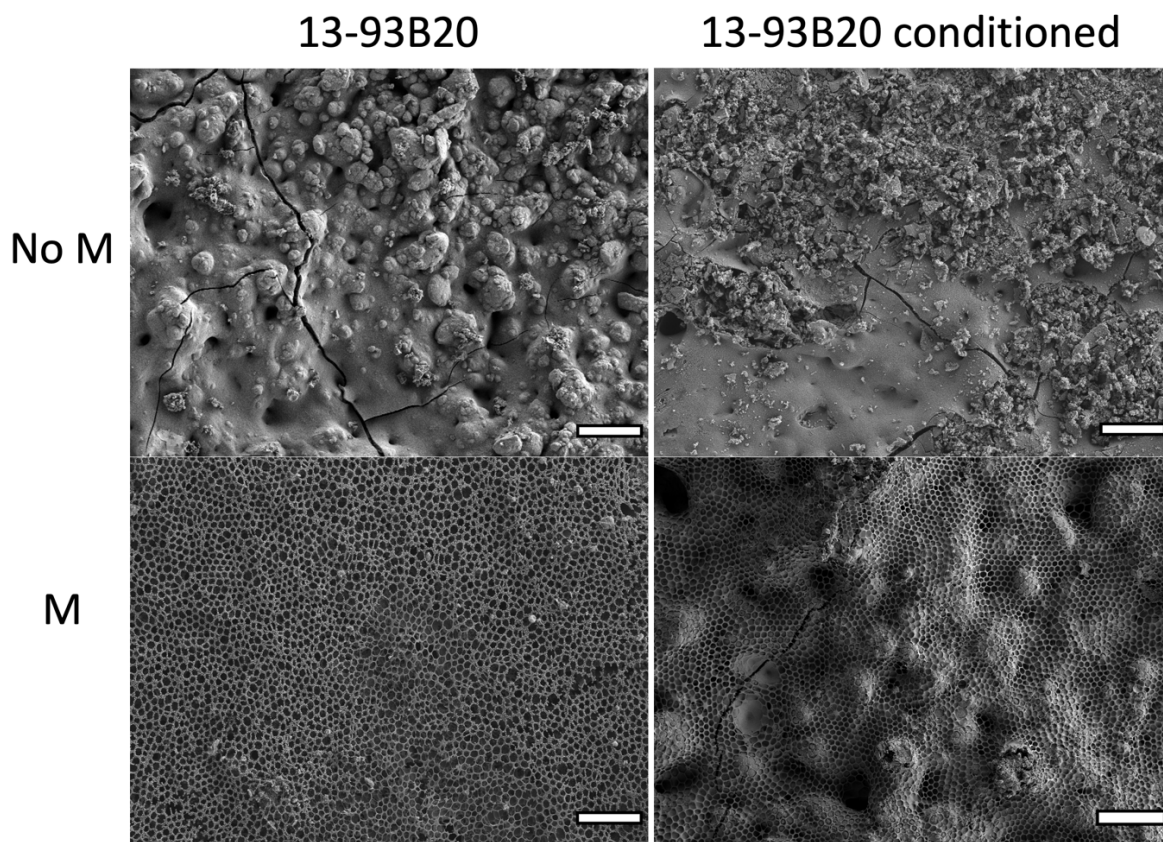
Figure 38. SEM images of samples without and with HC membrane after 28 days of immersion in TRIS buffer solution; Scale bar = 50µm

a) membrane/13-93B20 after 28 days immersion in TRIS buffer solution
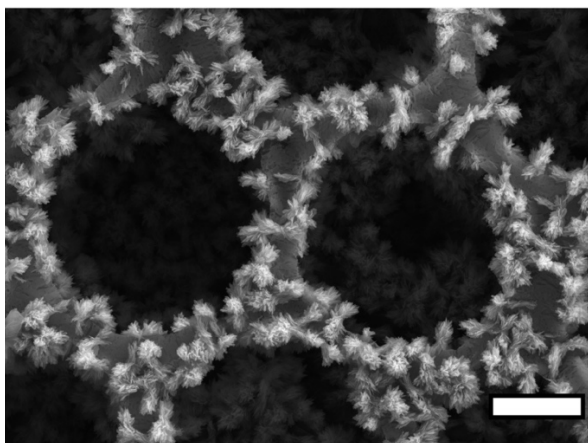
b) membrane/13-93B20c after 28 days immersion in TRIS buffer solution
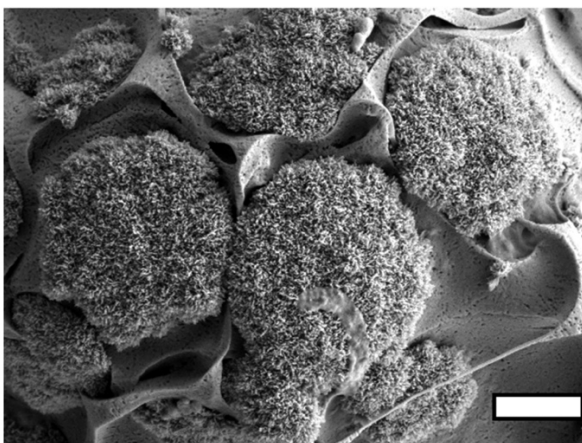
Figure 39. High magnification SEM images of the surface of a) 13-93B20M and b) 13-93B20cM after 28 days immersion in TRIS buffer solution. Scale bar 2 μm

After 28 days of immersion in TRIS buffer solution, the 13-93B20 has a similar topography compared to what was found on the 13-93B20c before the membrane generation (**Figure 33**). This confirms the precipitation of HA during the immersion in TRIS buffer solution. On the bottom left corner, one can see a layer that is cracked which most probably correspond to the Si-rich layer that forms at the BG surface when immersed [160]. The same structure is visible on the 13-93B20c after 28 days in TRIS. This suggest that apatite precipitation on the BG without membrane is not uniform. This is in accordance with the μCT images from **Figure 37** that showed an uneven precipitation.

On the membrane/13-93B20 assembly, it is possible to see small precipitates scattered on the membrane (**Figure 39a**). On the membrane/13-93B20c assembly, it is not possible to see those precipitates previously found on the membrane/13-93B20. However, one can see in **Figure 38** that some structures seem to come from beneath the membrane The higher magnification images **Figure 39** allows us to see an aggregate of precipitates that seems to come from underneath the membrane. We hypothesize that, on the 13-93B20c, because of the presence of apatite structure prior to the membrane generation, during immersion, those structure serves as nucleation points and not the membrane directly. Therefore, precipitates continue to aggregate on the previous ones and burst open the membrane to emerge at the surface.

TRIS buffer solution is interesting to study the behavior of a material and have a general understanding of the material's behavior in aqueous conditions. However, immersion in simulated body fluid (SBF) is the preferred method to assess the bioactivity of a material [29], [209]. Therefore, the materials were immersed in SBF, their ion released measured, and they were subsequently images through SEM. The results are presented in the following section.

2.2. In simulated body fluid

Precipitation of HA, upon dissolution in SBF is, according to Larry L. Hench's, the first sign of a material's bioactivity [85]. Therefore, the bioactivity of the assemblies was studied upon immersion in SBF solution up to 14 days. The solution was not refreshed during the immersion, and ICP-OES was used to quantify the ion concentration in the solution and the results are presented as the difference between the ion concentration in a control SBF solution and the ion concentration from the immersion with the materials (**Figure 40**). Following the immersion, the materials were imaged using SEM/EDX (**Figure 41** and **Figure 42**).

Regarding the silicon (Si) release (**Figure 40a**), as expected, all samples release a similar amount of Si in the solution. Although they do not follow the same pattern and are released a little more slowly than Si, boron (B) (**Figure 40b**), phosphorous (P) (**Figure 40c**) and calcium (Ca) (**Figure 40d**) are also released in a similar quantity for both membrane/substrate assembly.

Now, looking at the Ca release (**Figure 40d**), for both membrane/substrate assemblies, the Ca concentration in the solution increases with time and no significant difference can be seen between the samples. When looking at the phosphorous (P) concentration (**Figure 40c**), for all materials, the P concentration decrease in the solution over immersion time, indicating a precipitation. Usually, to confirm precipitation, we would expect the Ca to decrease and follow the trend of P [29], [210]. Here this is not the case. This is due to the high content of Ca in our BG compared to the small amount of P that is quickly used for the precipitation. Therefore, P is the limiting element here and since there is not enough P in the solution to consume the totality of the Ca released in the medium, Ca concentration increases over time.
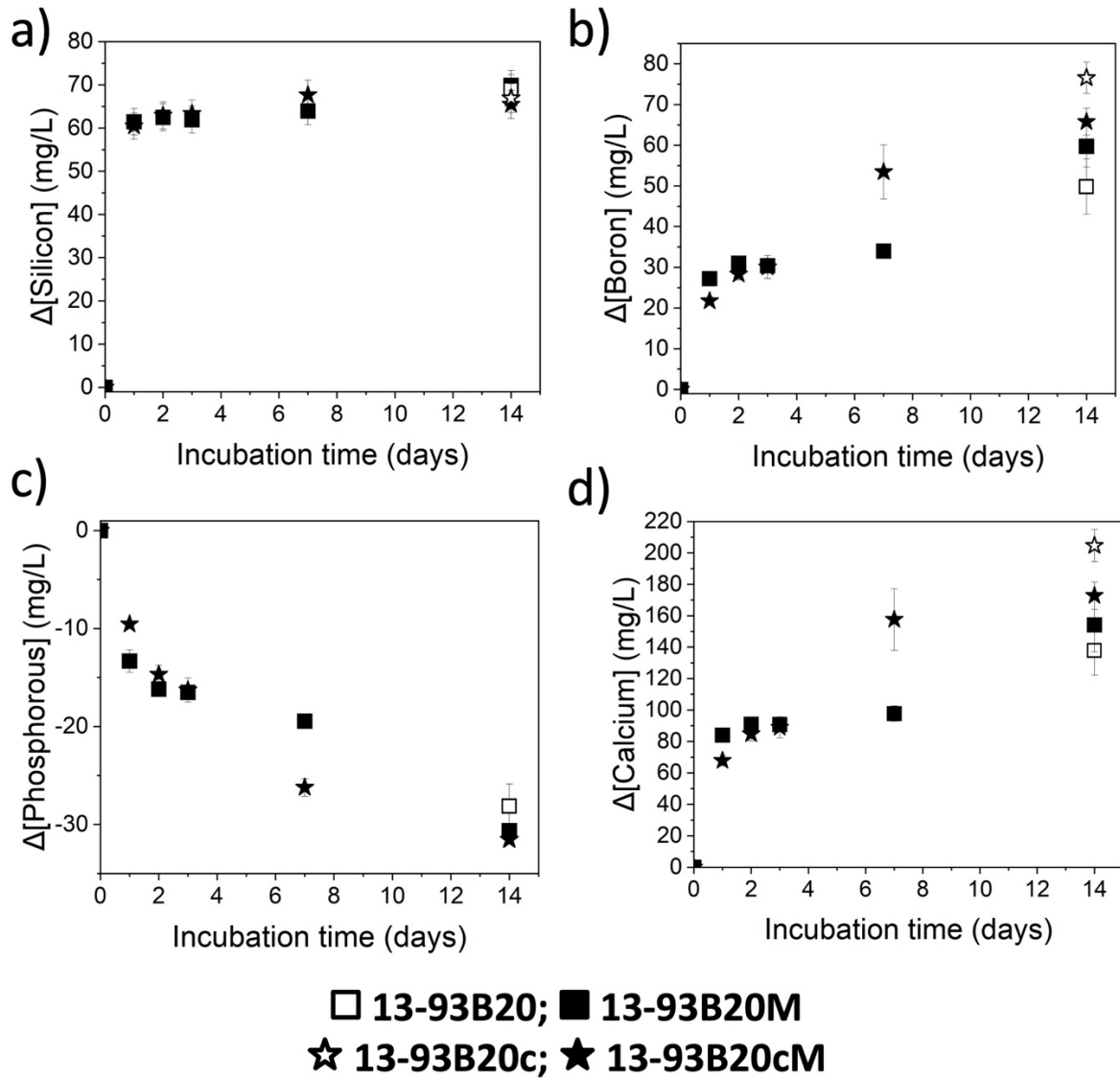
Figure 40. Ion release profile of a) Silicon (Si), b) boron (B), c) Phosphorous (P) and d) Calcium (Ca) in the dissolution product of 13-93B20 (■), 13-93B20M (■), 13-93B20c (★) and 13-93B20cM (★) upon immersion in SBF up to 14 days, Δ[element] = [element] in the SBF solution in presence of the sample – [element] in the initial SBF solution.
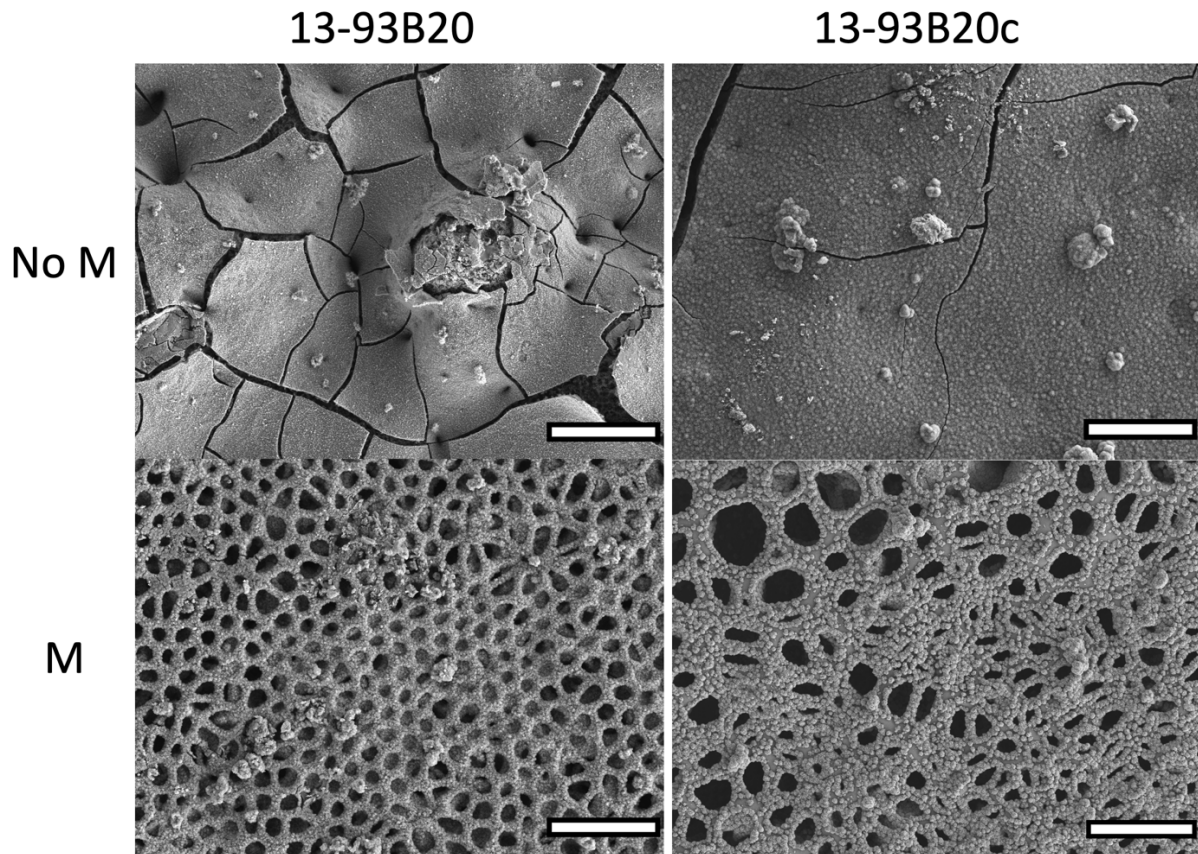
Figure 41. SEM images of the samples with and without membrane after 14 days of immersion in SBF. scale bar = 20μm

When looking at the topographical features at the surface of the samples after the 14 days of immersion in SBF, the surface of the BGs without membrane, regardless of the treatment, are similar. Indeed, we find, similarly to the results after immersion in TRIS (**Figure 38**), a layer that is cracked that can be either the Si-rich layer or a thick CaP layer. When looking at the BGs surface more closely (**Figure 42a** and **c**), it is possible to see some differences between the 13-93B20 and 13-93B20c. First, the Si-reach layer in 13-93B20 (**Figure 42a**) is clearly visible and similar precipitates, small and thin, seen after the TRIS buffer solution immersion on the membrane/13-93B20 assembly, are visible. On the other hand, the precipitates observable on the 13-93B20c (**Figure 42c**) seem to create aggregates that come together in a dense structures of plate-like crystals, contrary to the small, thin and sparse precipitates at the surface of the 13-93B20. This organization was also observed in SEM by Magyari et al. [211] after immersion of a silicate bioactive glass in SBF and were identified as hydroxyapatite precipitates. Furthermore, Drouet [212] indicate that plate-like crystals are a good indication in favor of bone-like

apatite precipitation, although it is not a sufficient indicator to unequivocally identify the nature of the apatite crystals. Those same precipitates are observable on the samples with membrane regardless of the treatment. However, they seem to be present in higher number on the membrane/13-93B20 assembly than on the membrane/13-93B20c assembly. One explanation might be because of the already important precipitation that has occurred on the 13-93B20c during the conditioning and therefore the precipitation at the surface of the membrane during the immersion in SBF is slightly slower than on the membrane/13-93B20 assembly.

EDX performed on the observed precipitates revealed a Ca/P ratio close to 2.1 for all samples except the 13-93B20 which has a Ca/P ratio of 1.68 which is very close to the hydroxyapatite ratio of 1.67 [182]. The high ratio obtained on the membrane/13-93B20 assembly, 13-93B20c and the membrane/13-93B20c assembly might be due to an additional signal from the BG underneath the surface features that increases the ratio.

Together, the results from ICP-OES showing CaP precipitation, SEM and EDX showing the plate-like morphology of the crystals and the Ca/P ratio close to HA, are good indicators that the crystals at the surface of the samples might be HA. However, although ICP-OES, EDX and SEM are valuable tools to have a hint on the composition of the observed precipitates, they are not sufficient methods to unequivocally identify the precipitates as bone-like apatite. Therefore, more experiments are needed to demonstrate the nature of these crystals. For instance, nuclear magnetic resonance (NMR) or FTIR could give more information on the composition of the precipitates [212].
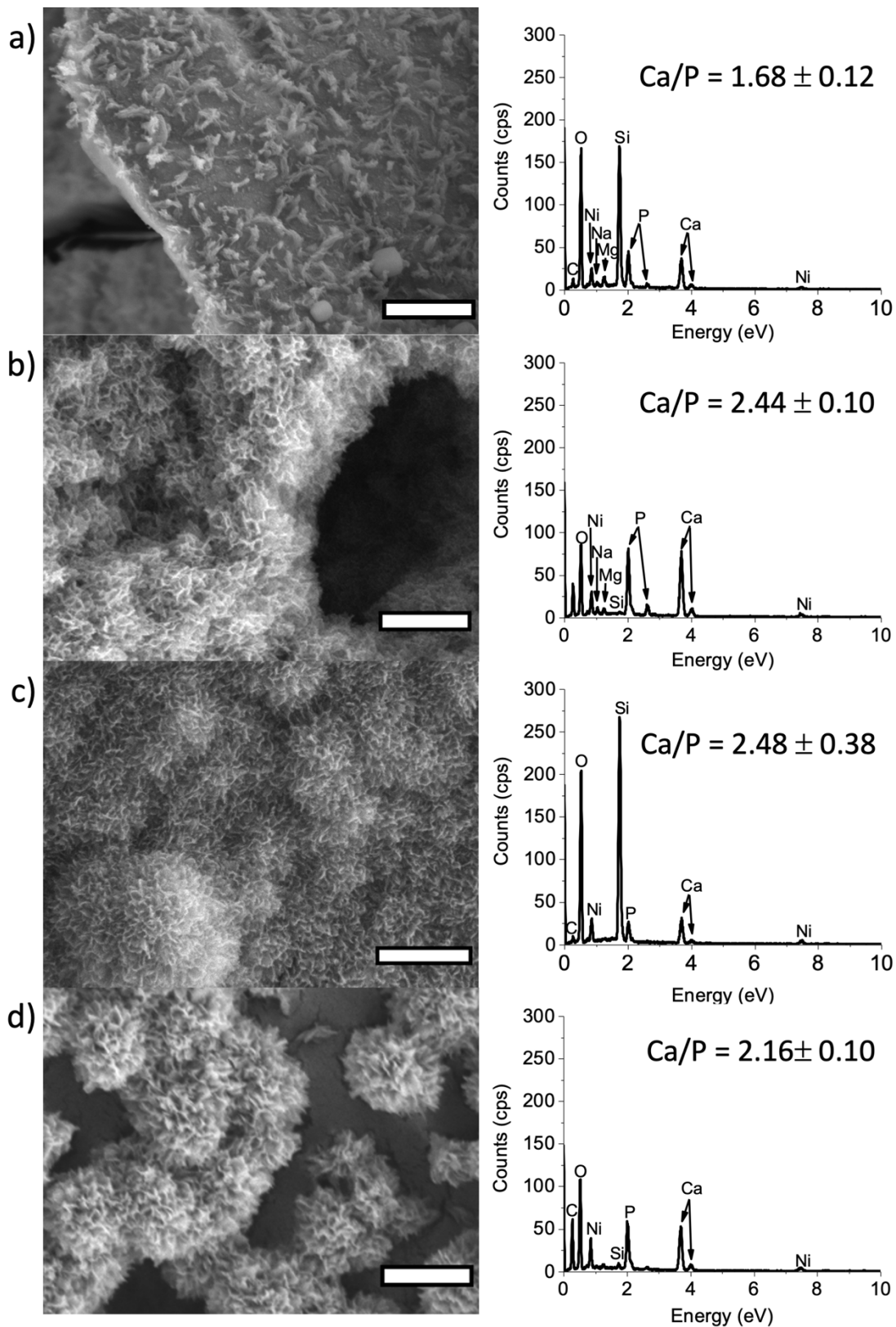
Figure 42. SEM images and corresponding EDX scans of a) 13-93B20, b) 13-93B20M, c) 13-93B20c and d) 13-93B20cM after immersion 14 days in SBF. SEM images scale bar = 1μm

As a conclusion, it has been demonstrated that the membrane/substrate assemblies degrade upon immersion and release ions that can be beneficial for the cell fate. Furthermore, the bioactivity of the membrane/substrate assemblies was demonstrated by the precipitation of HA-like precipitates. As the first sign of bioactivity have been demonstrated, it is of tremendous importance to investigate the material-cells interaction and assess the biocompatibility of the material. Furthermore, the aim of this work is to propose a material that provides a barrier membrane effect which should also be assessed. Therefore, the following section is dedicated to the investigation of the assessment of the barrier effect of the HC membrane and of the membrane/substrate assemblies-cell interactions. For these experiments, as preliminary cell investigation, only the 13-93B20c and membrane/13-93B20c assembly were used.

3. Membrane/substrate assemblies – cell behavior

Materials were placed in a 24-well plate and surfaces with or without membrane were seeded with 10 000 Red TTFluor HDFs. After 2h, the bottom of the wells was visualized under a fluorescence microscope and the number of Red TTFluor HDFs per cm^2 of scaffold surface was determined and the results are presented in **Figure 43**.

By placing 10 000 cells on a scaffold with a diameter of 0.7 cm, without considering the surface area provided by porosity, a density of 26 000 cells/cm^2 would be expected on the underside of the scaffold if there were no barrier effect. However, after 2h, as showed in **Figure 43a**, the number of fibroblasts that passed through the scaffolds without membrane is 280 cells/cm^2 (1% of the cells initially deposited), suggesting that the scaffold by itself limits the cell passage. Furthermore, the number of fibroblasts that passed through the membrane/substrate assemblies is 69 cells/cm^2, demonstrating that the presence of the HC membrane further reduces cell passage by up to 75%, thus confirming that the HC membrane on the scaffold's surface has a barrier effect. However, one should keep in mind that this experiment was conducted on a very short time (2h) and therefore only measure the "initial" passage of nonadherent

cells. Further experiments are required to measure the passage of adherent cells from the surface through the scaffold.
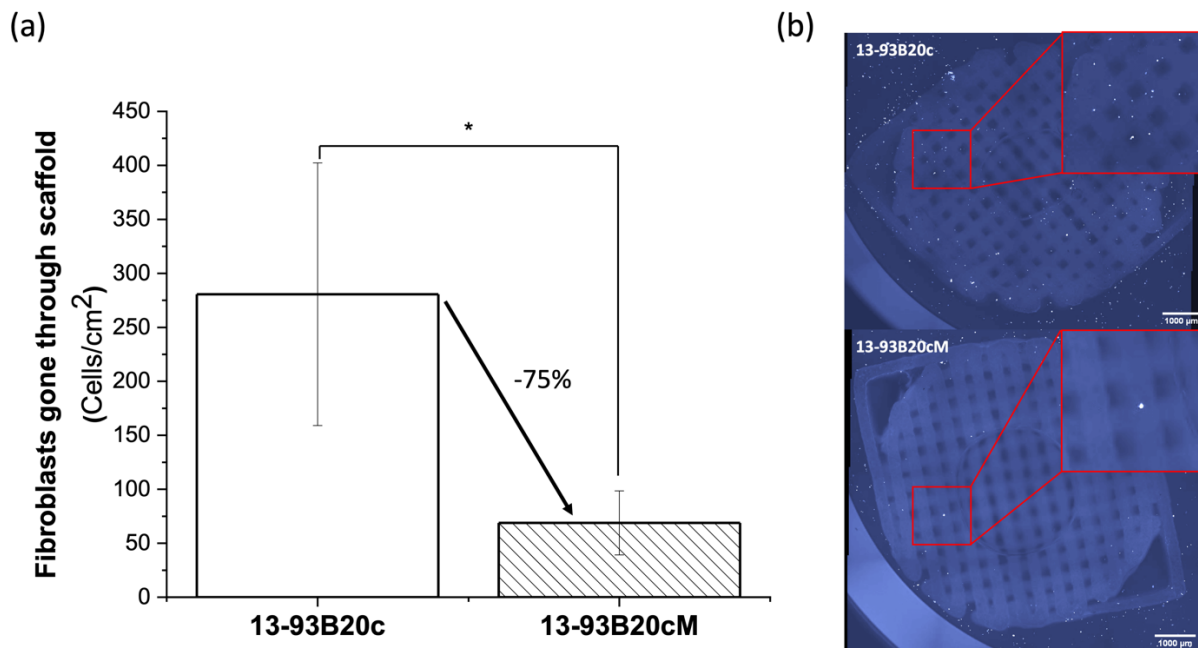
Figure 43. Number of fibroblasts passed through scaffolds 2h after cell-seeding. (a) cell density (* p < 0.05). (b) images of cells passed, scale bar 1000 μm.

After Red TTFluor HDFs seeding at the scaffolds surfaces and 2h of incubation, the upper surfaces of the scaffolds with and without membrane were imaged and the metabolic activity of the cells was determined (**Figure 44a**). More Red TTFluor HDFs can be seen on the surface of the 13-93B20cM compared to that of the 13-93B20M. Their metabolic activity seems to be preserved when compared to that of cells seeded on the surface of a cell culture well plate. On the other hand, cells at the surface of the 13-93B20 have a drastic drop of their metabolic activity. In the plausible scenario of minimal chemical toxicity from the substrates, this may be attributed to the surface topography of the scaffold without a membrane. Indeed, the roughness is known to be an essential feature to control on scaffolds for tissue engineering since it can greatly influence cell behavior. Different cells can have a different affinity and behavior when in contact with varying levels of roughness [213]. Pertaining to fibroblasts, they are known to adhere and proliferate better on smooth surface [214], [215]. Therefore, it is not surprising to find their metabolic activity diminished on the scaffold without membrane since it has quite a high roughness, around 4 μm (**Figure 32b**). Indeed, the presence of the membrane allows to

obtain a kind of "coat" on the rough surface of the 13-93B20c, which minimizes the impact of the scaffold initial roughness and therefore allows the cells to maintain their metabolic activity on the membrane/13-93B20c assembly.

In addition to the upper surface of the scaffold, the bottom part of the scaffolds' surfaces was visualized and the metabolic activity of MC3T3 cells beneath the scaffolds was determined (**Figure 44b**).Although the metabolic activity of the MC3T3 is higher compared to that of the fibroblasts, it seems constrained by the presence of the scaffold. Indeed, for bone tissue engineering, it is commonly admitted that for osteoblasts to survive and proliferate at the implant surface, the implant surface roughness should be high [213], [215]. Although the roughness of the scaffolds was not measured on the bottom part of our scaffolds, the SEM images of the scaffold's surface (**Figure 32**) give us a glimpse of what could be on the 3D printed strut forming the scaffold structure underneath. Indeed, we can hypothesize that those filaments present, like on the surface, a layer with precipitates giving it a rocky shape and therefore, probably a high roughness, suitable for osteoblasts-like cells attachment.
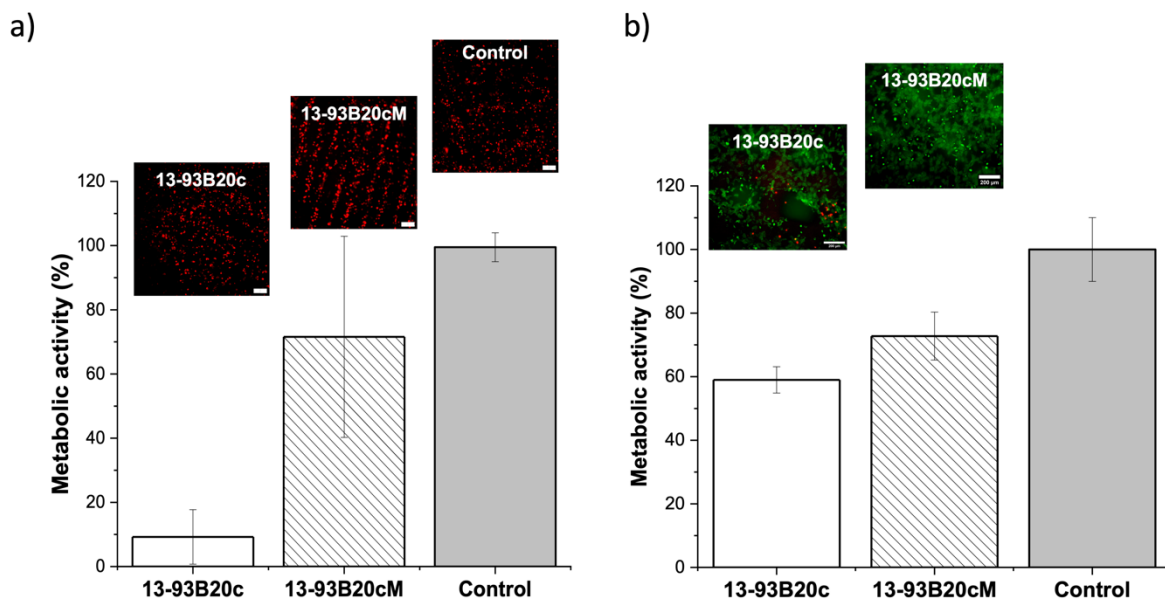
Figure 44. a) HDF behavior in contact with the upper part of the scaffold, with membrane or not: Metabolic activity of control HDF and HDF in contact for with the upper part of the scaffold 2h and fluorescence images of control HDF and HDF in contact with the upper part of the scaffold for 2h, scale bar = 400 μm (b). b) MC3T3 behavior in contact with the lower part of the scaffold, with membrane or not: Metabolic activity of control MC3T3 monolayer and MC3T3 monolayer in contact with the lower

part of the scaffolds for 2h and fluorescence images of MC3T3 monolayer in contact with the lower part of the scaffolds for 2h, scale bar = 200 µm

However, when comparing the metabolic activity of the MC3T3 in contact with the 13-93B20c and membrane/13-93B20c assembly, the presence of the membrane on the surface of the scaffold seems to preserve the metabolic activity of the cells below, which, in a clinical context, are the cells that we are looking forward to promote with the utilization of the BG. The slightly lower metabolic activity of the cells could be due to the boron release. Boron has a recognized cell toxicity at certain concentrations. Although it wasn't quantified in this study, the concentration of boron that was dissolved into the culture media as a result of the scaffolds' degradation might be inferred from the kinetics of degradation reported in **section B2** of this manuscript. In TRIS buffer solution, after 3h of immersion, the boron concentration in the solution was no higher than 10 mg/mL, and in SBF after 2h of immersion the boron concentration is inferior to 20 mg/mL. In the literature, concentration of 50 ppm, which corresponds to 50 mg/mL, was found to reduce the cell viability at the surface of borosilicate BG [31]. This could explain the lower metabolic activity of the cells (MC3T3 and Red TTFluor HDFs) in contact with the materials. Nevertheless, Fu et al. [104] in their study emphasize that, regardless of the potential cytotoxic effect of boron containing BG in-vitro, those boron-containing BG support soft tissue infiltration and extracellular matrix formation in-vivo. This is attributed to a more dynamic microenvironment in the body which facilitates the rapid metabolism of boron in-vivo [31], [104].

Overall, the results of this section show that, it is possible to generate a HC membrane at the surface of functionally graded 3D printed BG-based scaffolds. Subsequently, the bioactivity of the scaffolds with and without membrane was demonstrated. And finally, it has been shown that the HC membrane generated at the surface of the 13-93B20c fulfills its role as barrier membrane and avoid most of the fibroblastic cells to go through the scaffold. In addition, it has been demonstrated that the presence of the membrane seems to have a beneficial effect on the behavior of the fibroblasts at the surface of the membrane/13-93B20c assembly allowing them to maintain their metabolic activity, while osteoblast-like cells also seem to maintain a favorable behavior and their metabolic activity in contact with the bottom part of the scaffold. Overall, those preliminary results are encouraging regarding the cell fate in contact with the membrane/13-93B20c assembly. It is known that inorganic synthetic matrices are a great alternative to the gold standard autograft in bone reconstruction. However, another option is the use of allograft or xenograft for the reconstruction of bone. Therefore, it seems relevant to investigate the potential of generating a honeycomb membrane at the surface of cortical bone pieces. In the following section, preliminary results on the generation of a HC membrane on xenogenic decellularized bone matrix (DBM) will be presented.

E. Membrane generation on bone matrix: proof of concept

1. Cortical bone matrix

Nowadays, there are more and more options available to surgeons for bone repair. One of which is the use of allograft from compatible human donors or the use of xenogenic bone matrix. In this field, the company BIOBank has developed a unique process to upcycle femoral heads taken from living human donors, after total hip prothesis placement, and xenogeneic bones that would otherwise go to waste. The process Supercrit® allows to produce high safety DBM for bone grafting procedure. In brief, the

Supercrit® process uses CO_2 in a "supercritical state" where the CO_2 is in an intermediary state between gas and liquid which impart it with a very low viscosity and a high solvent power. These properties make supercritical CO_2 a high-performance fluid for delipidating bone tissue. Supercritical CO_2 is also non-toxic and neutral to the bone tissue allowing to keep most of the natural properties of the bone, notably its architecture and density. The Supercrit® process, after a step in supercritical CO_2, also uses a chemical oxidation to remove residual proteins. Nevertheless, and like with the other grafting materials options, this material can still be invaded during healing by fibrous tissue which can eventually impair bone regeneration. Therefore, the generation of the HC membrane through the BFM process was attempted at the surface xenogenic DBM, treated with the Supercrit®, kindly supplied by BIOBank. **Figure 45** presents macroscopic and SEM images of the cortical bone prior and post-membrane generation.
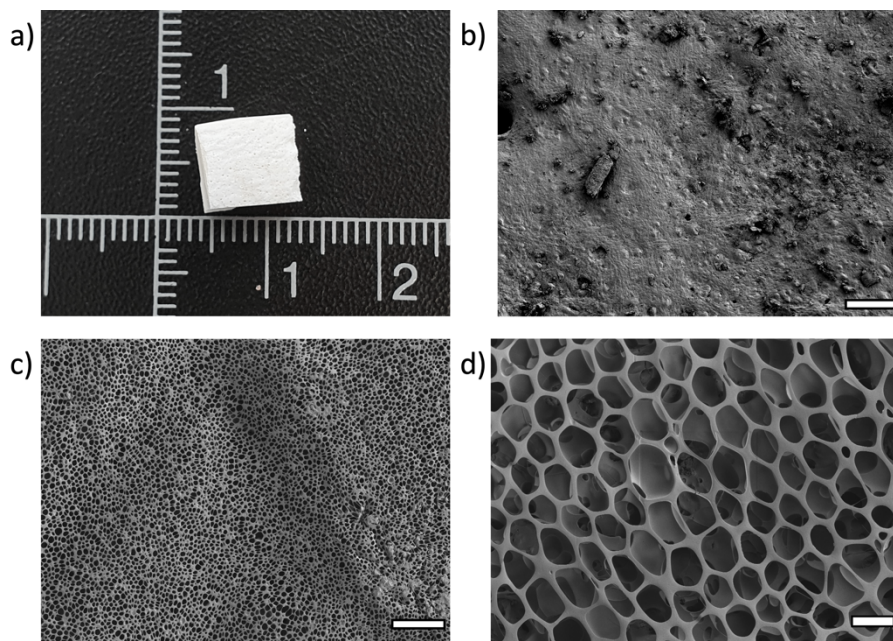
Figure 45. a) macroscopic photo of a DBM piece used for the membrane generation, b) SEM image of the surface of the cortical DBM, scale bar = 50 μm, c) SEM images of the HC membrane created at the surface of a DBM, scale bar = 50 μm for and d) higher magnification SEM images of the HC membrane created at the surface of a DBM, scale bar = 10 μm.

As one can see the surface of the cortical bone matrix seems relatively smooth and with few pores or holes. We found that the bone surface roughness varied between 1 and 6 μm with and average roughness

around 2 µm (data not shown). This smooth surface with only a few small pores allows, like for the 13-93B20c to keep most of the solution at the surface and therefore create HC membrane with a narrow pore size distribution. It was found that the pore diameter of the HC membrane on bone varies between 5 and 7 µm with an average around 6µm (data not shown). The average pore size, while being slightly higher than those reported for membrane deposited on 3D BG scaffolds, remain in a similar range. The higher average pore size on bone might be attributed, to some extent, to the surface topography of the DBM. Indeed, providing a relatively flat surface with a low porosity allows to obtain lower variability in the HC pore structure, although many parameters can still influence the HC organization and shape as stated above [44].

Just like the membrane/3D-printed scaffolds assemblies, the bone and the membrane/bone assembly were immersed in TRIS buffer solution and SBF up to 28 days and 14 days, respectively. The membranes were subsequently imaged, and the results are presented in **Figure 46**.
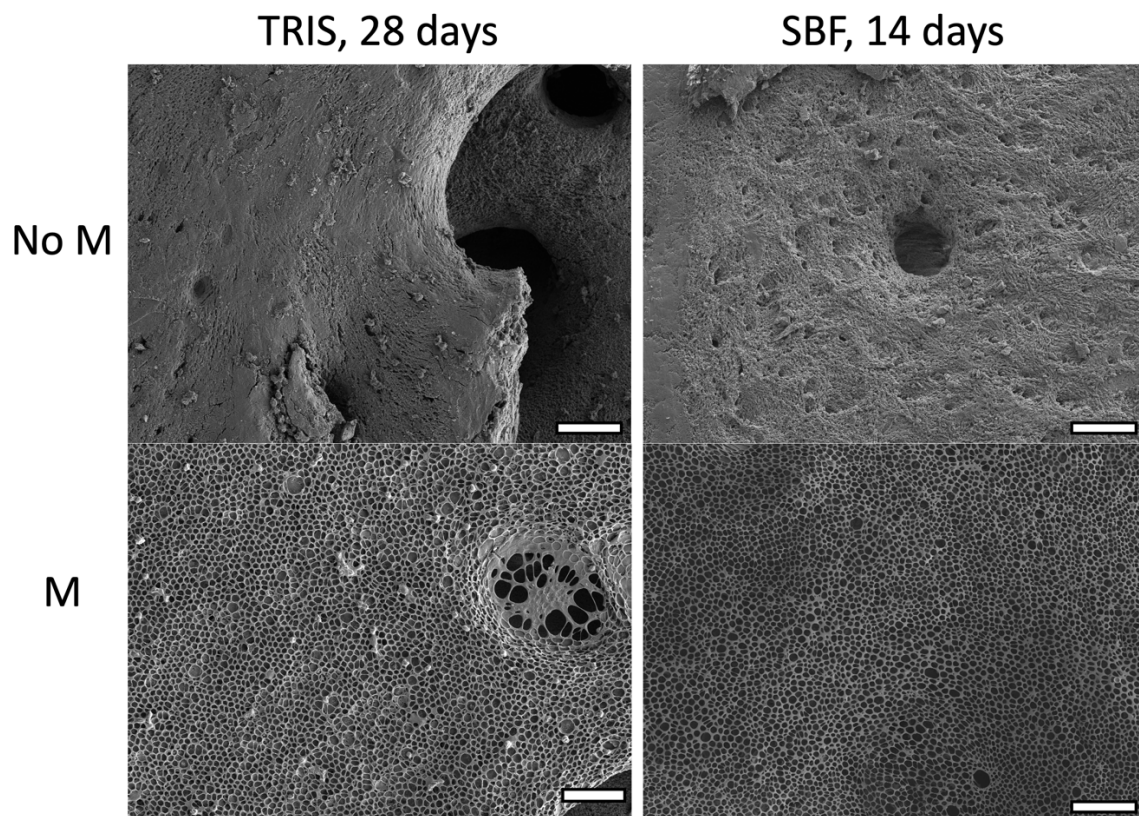
Figure 46. SEM images of the bone and membrane/bone assembly after 28 days of immersion in TRIS buffer solution and 14 days of immersion in SBF. Scale bar = 50 µm.

First of all, in TRIS buffer solution, after 28 days, one can see that the bone matrix without membrane seems slightly damaged and presents some small cracks on the surface. On the membrane/bone assembly, the membrane seems intact with a honeycomb-like structure. On both samples, whether they have a membrane or not, small round structures of unknown nature can be observed. Further experiments should be conducted to identify the origin of these structures. On the other hand, after 14 days in SBF, the bone seems a bit less damaged compared to the immersion in TRIS for 28 days. This might be due to the length of the immersion which is half that in TRIS buffer solution. After SBF immersion, the membrane seems intact and presents a neat surface with a honeycomb-like structure. Those results demonstrate the stability of the membrane generated at the surface of cortical bone matrix upon immersion in aqueous environment.

> **As a summary, the HC membrane was successfully generated at the surface of cortical DBM and its stability upon immersion in aqueous solutions has been proved since, even after 28 days of immersion, the membrane did not detach from its substrate. Cortical bone is an interesting matrix to show that it is possible to generate a HC membrane on natural bone matrix. However, contrary to cancellous bone, cortical bone has a low porosity which is less interesting for neovascularization purposes while it is a crucial element in the success of bone implant. For this purpose, cancellous bone seems to be an interesting matrix with a higher porosity. Therefore, the generation of a honeycomb membrane was attempted at the surface of cancellous bone and the results are presented in the following section.**

2. Cancellous bone matrix

This section's experiments were conducted by Rose Emilien, in the context of her 1st year Master's internship. The cancellous bone was again kindly supplied by BIOBank for the purpose of these experiments.

The generation of the HC membrane directly at the surface of the cancellous bone revealed impossible due to the high porosity of the bone, as can be seen in **Figure 47** (sample bone/membrane). Therefore,

methods to fill-in the pores were investigated. initially the idea was to freeze the cancellous bone, to create a thin layer of ice, onto which the HC membrane could be deposited. While, membrane could be deposited, the variability in the membrane quality, between samples, was too great to be considered a feasible solution (data not shown).

In a second time, the idea was to use a hydrogel between the bone and the membrane as a "biological glue". Several variations were investigated. The first consisting of the use of the hydrogel as a separate material. The hydrogel was then deposited on top of the cortical bone and the membrane was, either, generated directly on the gel (bone + hydrogel/membrane) or as a third material then deposited on the gel (bone + hydrogel + membrane). Another strategy consisted in directly combining the bone and the hydrogel during the hydrogel crosslinking and either adding the membrane generated separately (bone/hydrogel + membrane) or creating the membrane directly on the hydrogel already combined to the bone (bone/hydrogel/membrane). The hydrogels were produced with a solution at 10% gelatine and 1 mM genipine (which gives the blue color) for crosslinking and left to crosslink for 24h at RT.

The membrane created separately (samples with "+membrane" in **Figure 47**) revealed a HC structure with a homogeneous repartition of the pores with a size of approximately 4 μm which is similar to what can be found in the literature [42], [201]. This HC membrane was successfully adsorbed on the hydrogel although it stays mobile at the surface. The membrane created directly on the hydrogel (samples with "/membrane" in **Figure 47**) revealed an heterogeneous HC-like porous structure with a pore size varying from 2.5 to 5 μm which is similar to what can be found in the literature [42], [201]. The poor homogeneity of the pores in the membranes created directly at the surface of the hydrogel can be related to the high humidity and water content of the hydrogel. Indeed, and as mentioned before, small changes in the humidity can greatly impact the formation of the HC structure and the membrane porosity [44].
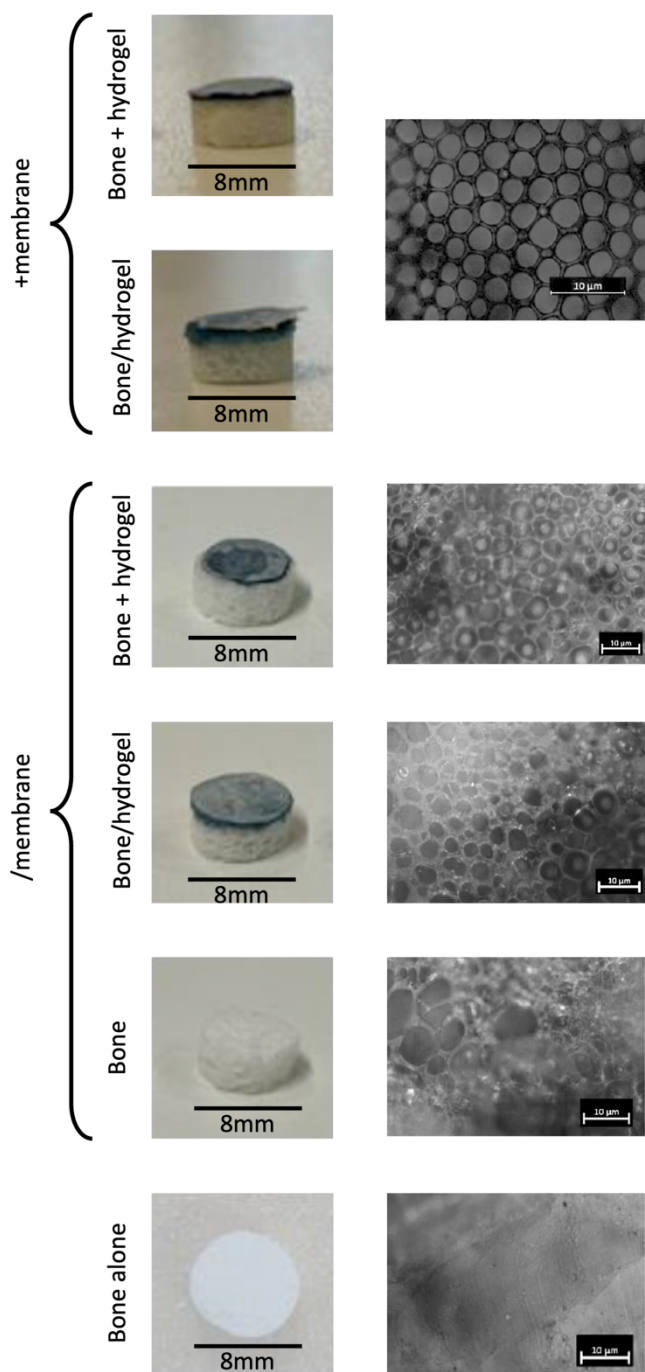
Figure 47. Macroscopic images of produced assemblies (left pane) and optical microscopic images (right pane) of the membranes obtained. Scale bar of microscopic images = 10 µm. Samples with a name structure as "material 1 + material 2" means that material 2 (either hydrogel or membrane) has been produced separately and added at the surface of material 1 (either bone or hydrogel). Samples with a name structure "material 1/ material 2" means that material 2 (either hydrogel or membrane) has been produced directly on material 1 (either hydrogel or bone). This figure is modified from Mrs. Rose Emilien's internship report.

Following the association of the membrane, the hydrogel and the bone, the constructs were immersed in distilled water to observe the behavior of the materials and especially the membrane stability at the surface of the construct. The results are presented in **Figure 48**.

During the first 48h of immersion, the hydrogel swells regardless of the association with the bone or the presence of the membrane. For the samples where the membrane was simply adsorbed on the hydrogel (bone + hydrogel + membrane and bone/hydrogel + membrane), the hydrogel has completely dissolved after 7 days and the membrane is therefore not attached anymore to the construct. For the membrane created directly on the hydrogel and then associated with the bone (bone + hydrogel/membrane), the hydrogel has not completely dissolved after 7 days. However, for this construct, the membrane has detached from the hydrogel. On the other hand, for the sample's bone/hydrogel/membrane, after 7 days, not only the hydrogel is not completely dissolved but the membrane is still partly attached to the hydrogel revealing a higher stability of this construct upon immersion.
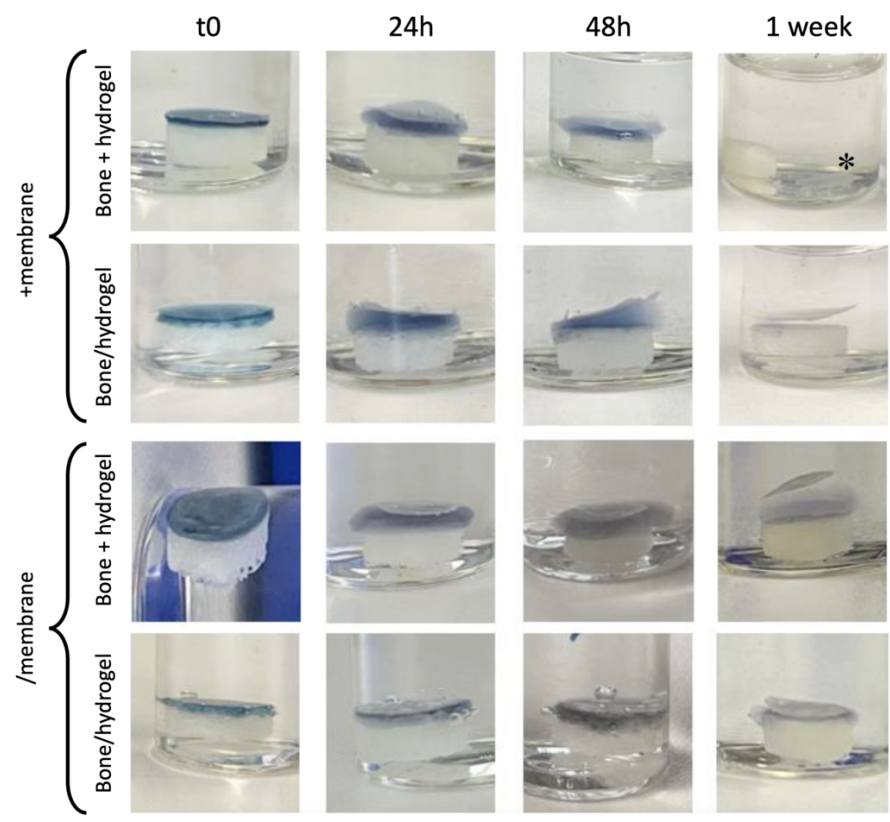
Figure 48. Photographs of the assemblies during immersion in distilled water (6mL) under mild agitation at 37°C. * membrane

All together, these results suggest that it is possible to combine cancellous bone with a hydrogel and create a porous HC-like membrane at the surface of the construct, creating a "tri-phasic" material. However, the HC is not very homogeneous and with a high-water content hydrogel, this seems inevitable. Furthermore, in order to obtain a good attachment of the membrane and ensure the cohesiveness of the construct, some parameters must be tailored. For instance, the crosslinking time of the hydrogel might be adjusted to offer a substrate with a higher cohesiveness and lower water content which could influence the HC formation [216].

VI. Conclusion and perspectives

The perfect bone grafting material does not exist… Yet. There are hundreds, if not thousands, of possibilities available to surgeons for the bone repair of their patient. Therefore, the choice of material is driven by patients' specifics mostly. Nevertheless, one major problem is common with all grafting material: they do not prevent fibrous tissue in growth in the bone defect. This common, and yet deleterious, phenomena during the bone healing can lead to serious complications including implant failure due to an insufficient bone regeneration. The main aim of this thesis was to investigate the feasibility of producing a single material with two phases affixed including an osteogenic compound on one side, and a honeycomb-like structured barrier membrane on the other that would prevent the fibrous tissue invasion while promoting bone regeneration.

Bioactive compounds, such as BGs, are of great interest since they are capable to promote the formation of HA through their dissolution by-products. Many compositions of BGs have been put on the market but one of the first was the S53P4, which has been used in clinic for decades now. On the other hand, S53P4 is not a composition that can be used for the preparation of 3D porous structure because of its high tendency to crystalize upon sintering. A new composition, the 13-93B20, has revealed to be of great interest. Indeed, thanks to its composition that incorporates boron notably, its processing window is larger than the one of the S53P4 and allows to produce 3D porous structures through 3D printing. Furthermore, the boron is known to have beneficial effects on angiogenesis notably. On the other hand, honeycomb structured membranes and films have been investigated for years for different applications in tissue engineering. Honeycomb structured polymer membranes have been revealed to be of great interest to enhance cell adhesion and proliferation.

Combining a inorganic phase made of BG with a honeycomb barrier membrane in a single material has never been reported before this work. Therefore, the main aim of this thesis was to give a proof of concept of the feasibility of the association of an inorganic material like BG with a polymeric

barrier membrane structured in honeycomb in a single material and investigate its physicochemical properties as long as its interactions with cells.

The association of bulk discs of BG with the HC membrane was found to be highly affected by the chemical and surface features of the BG discs. However, with the appropriate treatment, namely conditioning, it has been demonstrated that it was possible to obtain a strong link between the bulk BG disc and the HC membrane either in dry or aqueous conditions. Furthermore, the presence of the membrane did not impair the dissolution of the BGs, which is essential to promote the bone regeneration in-vivo. In addition, the membranes were found to support precipitation of CaP.

One objective that presented itself during the thesis was to ensure the safety of the material, even after sterilization. Nowadays, gamma sterilization is one of the most used methods for the sterilization of biomaterials in industry. Therefore, the materials were subjected to gamma irradiation for sterilization purposes and the impact of the treatment was assessed. The gamma irradiation was found to provoke the appearance of defects in the molecular structure of the BG. Those defects are well known in the scientific community and did not influence the BG dissolution behavior in aqueous condition. Furthermore, although the polymer of the HC membrane suffered from a diminution in its molecular weight due to the irradiation, it did not overly affect the strength of the link between the membrane and the bulk BG disc. In addition, it was demonstrated that the physicochemical changes observed in the BGs did not deleteriously affect the material-cell interactions. Therefore, it was found the gamma irradiation is a suitable method for the sterilization of the assemblies.

The next objective was to be able to create the membrane at the surface of a 3D porous structure. To mimic the bone organization, a functionally graded 3D porous 13-93B20-based scaffold was printed by robocasting and sintered. The HC membrane was successfully created at its surface and showed similar properties compared to a free-standing HC membrane. Then, following immersion in aqueous solutions, the assemblies were found to support potentially bone-like apatite formation, which is encouraging for the use of the material in-vivo. In addition, when put in contact with osteoblast-like or fibroblasts cells, the assembly was found to support cell adhesion and growth, while preventing fibroblasts passage through the scaffold demonstrating the barrier effect of the HC membrane. Although

the cells metabolic activity was diminished, probably because of the boron release notably, it is known that in in-vitro conditions, the boron might impact the cells growth and proliferation because it is not metabolized and eliminated like in the dynamic microenvironment of the human body.

Overall, this thesis demonstrates the possibility to successfully combine an inorganic phase made of BG with a HC structured barrier membrane in a single material that could be used in a single step procedure for bone reconstruction. However, one should keep in mind that complex fabrication methods were used in this work. For such material to reach the market several adaptations should be considered, notably to obtain 100% reproducible BG scaffold morphology by 3D printing and in a shorter time. Furthermore, the use of high temperatures remains a limitation in terms of energy cost in the production process of the BG scaffolds and the brittleness of the scaffold obtain is an important limitation of the construct as such. In addition, the HC membrane generated here was prepared from a solution containing a highly dangerous organic solvent which is a huge drawback of the method. One should consider the possibility to generate the HC membrane with less dangerous and "eco-friendly" solvent which would allow a greater safety for the material and for the experimenter. Additionally, the use of a "biological glue" as a way to combine a highly porous structure, like cancellous bone, and the honeycomb membrane can be considered as revealed by the results presented in the last part of this manuscript. Furthermore, important efforts must be put in the investigation of the material cell-interaction in-vitro and in-vivo. Indeed, the results obtained here are insufficient to guaranty all the beneficial effects expected from such materials. Animal experimentations should be conducted to assess 1) the "real world" barrier effect of the membrane, 2) the biocompatibility of the construct and 3) the beneficial effects compared to the available marketed solutions.

In my opinion, this kind of material could be a great addition to arsenal of grafting materials available to surgeons. It has the potential to ensure a greater bone regeneration without the downside of the fibrous tissue ingrowth. However, numerous experiments are still needed to find the appropriate, cost effective and safe conditions for the preparation of such material.

I think we will never find THE perfect grafting material for bone regeneration. On the contrary I think that having several viable options for the surgeons is more valuable to adapt their strategy to the specifics of their patients and perform personalized, cutting-edge medicine.

References

[1] S. Standring, N. Ananad, H. Gray, and H. Gray, Eds., *Gray's anatomy: the anatomical basis of clinical practice ; [get full access and more at ExpertConsult.com]*, 41. ed. Philadelphia, Pa.: Elsevier, 2016.

[2] R. K. Fuchs, W. R. Thompson, and S. J. Warden, "Bone biology," in *Bone Repair Biomaterials*, Elsevier, 2019, pp. 15–52. doi: 10.1016/B978-0-08-102451-5.00002-0.

[3] W. Wang and K. W. K. Yeung, "Bone grafts and biomaterials substitutes for bone defect repair: A review," *Bioactive Materials*, vol. 2, no. 4, pp. 224–247, Dec. 2017, doi: 10.1016/j.bioactmat.2017.05.007.

[4] R. Dimitriou, E. Jones, D. McGonagle, and P. V. Giannoudis, "Bone regeneration: current concepts and future directions," *BMC Med*, vol. 9, no. 1, p. 66, Dec. 2011, doi: 10.1186/1741-7015-9-66.

[5] A. Oryan, S. Alidadi, A. Moshiri, and N. Maffulli, "Bone regenerative medicine: classic options, novel strategies, and future directions," *J Orthop Surg Res*, vol. 9, no. 1, p. 18, 2014, doi: 10.1186/1749-799X-9-18.

[6] R. Tevlin, G. G. Walmsley, O. Marecic, M. S. Hu, D. C. Wan, and M. T. Longaker, "Stem and progenitor cells: advancing bone tissue engineering," *Drug Deliv. and Transl. Res.*, vol. 6, no. 2, pp. 159–173, Apr. 2016, doi: 10.1007/s13346-015-0235-1.

[7] M. W. Archunan and S. Petronis, "Bone Grafts in Trauma and Orthopaedics," *Cureus*, Sep. 2021, doi: 10.7759/cureus.17705.

[8] A. R. Amini, C. T. Laurencin, and S. P. Nukavarapu, "Bone Tissue Engineering: Recent Advances and Challenges," p. 59, 2013.

[9] H.-S. Sohn and J.-K. Oh, "Review of bone graft and bone substitutes with an emphasis on fracture surgeries," *Biomater Res*, vol. 23, no. 1, p. 9, Dec. 2019, doi: 10.1186/s40824-019-0157-y.

[10] S. Nour *et al.*, "Bioactive Materials: A Comprehensive Review on Interactions with Biological Microenvironment Based on the Immune Response," *J Bionic Eng*, vol. 16, no. 4, pp. 563–581, Jul. 2019, doi: 10.1007/s42235-019-0046-z.

[11] M. Navarro, A. Michiardi, O. Castaño, and J. A. Planell, "Biomaterials in orthopaedics," *J. R. Soc. Interface.*, vol. 5, no. 27, pp. 1137–1158, Oct. 2008, doi: 10.1098/rsif.2008.0151.

[12] L. L. Hench, R. J. Splinter, W. C. Allen, and T. K. Greenlee, "Bonding mechanisms at the interface of ceramic prosthetic materials," *J. Biomed. Mater. Res.*, vol. 5, no. 6, pp. 117–141, Nov. 1971, doi: 10.1002/jbm.820050611.

[13] L. L. Hench and J. M. Polak, "Third-Generation Biomedical Materials," *Science*, vol. 295, no. 5557, pp. 1014–1017, Feb. 2002, doi: 10.1126/science.1067404.

[14] F. Baino, "Bioactive glasses – When glass science and technology meet regenerative medicine," *Ceramics International*, vol. 44, no. 13, pp. 14953–14966, Sep. 2018, doi: 10.1016/j.ceramint.2018.05.180.

[15] R. Detsch, P. Stoor, A. Grünewald, J. A. Roether, N. C. Lindfors, and A. R. Boccaccini, "Increase in VEGF secretion from human fibroblast cells by bioactive glass S53P4 to stimulate angiogenesis in bone: VEGF Secretion of Fibroblasts by Bioactive Glass S53P4," *J. Biomed. Mater. Res.*, vol. 102, no. 11, pp. 4055–4061, Nov. 2014, doi: 10.1002/jbm.a.35069.

[16] A. Hoppe, N. S. Güldal, and A. R. Boccaccini, "A review of the biological response to ionic dissolution products from bioactive glasses and glass-ceramics," *Biomaterials*, vol. 32, no. 11, pp. 2757–2774, Apr. 2011, doi: 10.1016/j.biomaterials.2011.01.004.

[17] P. Balasubramanian, T. Büttner, V. Miguez Pacheco, and A. R. Boccaccini, "Boron-containing bioactive glasses in bone and soft tissue engineering," *Journal of the European Ceramic Society*, vol. 38, no. 3, pp. 855–869, Mar. 2018, doi: 10.1016/j.jeurceramsoc.2017.11.001.

[18] R. Moonesi Rad, A. Z. Alshemary, Z. Evis, D. Keskin, K. Altunbaş, and A. Tezcaner, "Structural and biological assessment of boron doped bioactive glass nanoparticles for dental tissue applications," *Ceramics International*, vol. 44, no. 8, pp. 9854–9864, Jun. 2018, doi: 10.1016/j.ceramint.2018.02.230.

[19] A. Shearer, M. Montazerian, J. J. Sly, R. G. Hill, and J. C. Mauro, "Trends and perspectives on the commercialization of bioactive glasses," *Acta Biomaterialia*, vol. 160, pp. 14–31, Apr. 2023, doi: 10.1016/j.actbio.2023.02.020.

[20] Ö. H. Andersson, G. Liu, K. H. Karlsson, L. Niemi, J. Miettinen, and J. Juhanoja, "In vivo behaviour of glasses in the SiO2-Na2O-CaO-P2O5-AI2O3- B2O3 system," *Journal of Materials science : Materials in Medicine*, vol. 1, pp. 219–227, 1990, doi: https://doi.org/10.1007/BF00701080.

[21] D. J. Hulsen, N. A. van Gestel, J. A. P. Geurts, and J. J. Arts, "S53P4 bioactive glass," in *Management of Periprosthetic Joint Infections (PJIs)*, Elsevier, 2017, pp. 69–80. doi: 10.1016/B978-0-08-100205-6.00004-5.

[22] O. Leppäranta *et al.*, "Antibacterial effect of bioactive glasses on clinically important anaerobic bacteria in vitro," *J Mater Sci: Mater Med*, vol. 19, no. 2, pp. 547–551, Feb. 2008, doi: 10.1007/s10856-007-3018-5.

[23] A. A. Gorustovich, J. A. Roether, and A. R. Boccaccini, "Effect of Bioactive Glasses on Angiogenesis: A Review of *In Vitro* and *In Vivo* Evidences," *Tissue Engineering Part B: Reviews*, vol. 16, no. 2, pp. 199–207, Apr. 2010, doi: 10.1089/ten.teb.2009.0416.

[24] M. Fabert *et al.*, "Crystallization and sintering of borosilicate bioactive glasses for application in tissue engineering," *J. Mater. Chem. B*, vol. 5, no. 23, pp. 4514–4525, 2017, doi: 10.1039/C7TB00106A.

[25] P. Sinitsyna, O. Karlström, C. Sevonius, and L. Hupa, "In vitro dissolution and characterisation of flame-sprayed bioactive glass microspheres S53P4 and 13–93," *Journal of Non-Crystalline Solids*, vol. 591, p. 121736, Sep. 2022, doi: 10.1016/j.jnoncrysol.2022.121736.

[26] Q. Fu, M. N. Rahaman, B. S. Bal, W. Huang, and D. E. Day, "Preparation and bioactive characteristics of a porous 13–93 glass, and fabrication into the articulating surface of a proximal tibia," *J. Biomed. Mater. Res.*, vol. 82A, no. 1, pp. 222–229, Jul. 2007, doi: 10.1002/jbm.a.31156.

[27] M. Brink, "The influence of alkali and alkaline earths on the working range for bioactive glasses," *J. Biomed. Mater. Res.*, vol. 36, no. 1, pp. 109–117, Jul. 1997, doi: 10.1002/(SICI)1097-4636(199707)36:1<109::AID-JBM13>3.0.CO;2-D.

[28] R. F. Brown *et al.*, "Effect of borate glass composition on its conversion to hydroxyapatite and on the proliferation of MC3T3-E1 cells," *J. Biomed. Mater. Res.*, vol. 88A, no. 2, pp. 392–400, Feb. 2008, doi: 10.1002/jbm.a.31679.

[29] A. Houaoui, I. Lyyra, R. Agniel, E. Pauthe, J. Massera, and M. Boissière, "Dissolution, bioactivity and osteogenic properties of composites based on polymer and silicate or borosilicate bioactive glass," *Materials Science and Engineering: C*, vol. 107, p. 110340, Feb. 2020, doi: 10.1016/j.msec.2019.110340.

[30] M. Ojansivu *et al.*, "The effect of S53P4-based borosilicate glasses and glass dissolution products on the osteogenic commitment of human adipose stem cells," *PLoS ONE*, vol. 13, no. 8, p. e0202740, Aug. 2018, doi: 10.1371/journal.pone.0202740.

[31] P. Balasubramanian *et al.*, "Ion Release, Hydroxyapatite Conversion, and Cytotoxicity of Boron-Containing Bioactive Glass Scaffolds," *Int J Appl Glass Sci*, vol. 7, no. 2, pp. 206–215, Jun. 2016, doi: 10.1111/ijag.12206.

[32] G. Gillispie, S. J. Lee, and J. J. Yoo, "Bone and Cartilage Tissue Engineering," in *Reference Module in Biomedical Sciences*, Elsevier, 2018, p. B978012801238365849X. doi: 10.1016/B978-0-12-801238-3.65849-X.

[33] R. Dimitriou, G. I. Mataliotakis, G. M. Calori, and P. V. Giannoudis, "The role of barrier membranes for guided bone regeneration and restoration of large bone defects: current experimental and clinical evidence," *BMC Med*, vol. 10, no. 1, p. 81, Dec. 2012, doi: 10.1186/1741-7015-10-81.

[34] S. Jiang *et al.*, "Radially Porous Nanocomposite Scaffolds with Enhanced Capability for Guiding Bone Regeneration In Vivo," *Adv Funct Materials*, vol. 32, no. 18, p. 2110931, May 2022, doi: 10.1002/adfm.202110931.

[35] F. Stavropoulos, J. C. Nale, and J. D. Ruskin, "Guided Bone Regeneration," *Oral and Maxillofacial Surgery Clinics of North America*, vol. 14, no. 1, pp. 15–27, 2002, doi: https://doi.org/10.1016/S1042-3699(02)00013-4.

[36] C. Dahlin, A. Linde, J. Gottlow, and S. Nyman, "Healing of Bone Defects by Guided Tissue Regeneration," *Plastic and Reconstructive Surgery*, vol. 81, no. 5, pp. 672–676, 1988, doi: 10.1097/00006534-198805000-00004.

[37] M. C. Bottino *et al.*, "Recent advances in the development of GTR/GBR membranes for periodontal regeneration—A materials perspective," *Dental Materials*, vol. 28, no. 7, pp. 703–721, Jul. 2012, doi: 10.1016/j.dental.2012.04.022.

[38] I. Elgali, O. Omar, C. Dahlin, and P. Thomsen, "Guided bone regeneration: materials and biological mechanisms revisited," *Eur J Oral Sci*, vol. 125, no. 5, pp. 315–337, Oct. 2017, doi: 10.1111/eos.12364.

[39] R. A. Perez and G. Mestres, "Role of pore size and morphology in musculo-skeletal tissue regeneration," *Materials Science and Engineering: C*, vol. 61, pp. 922–939, Apr. 2016, doi: 10.1016/j.msec.2015.12.087.

[40] P. Aprile, D. Letourneur, and T. Simon-Yarza, "Membranes for Guided Bone Regeneration: A Road from Bench to Bedside," *Adv. Healthcare Mater.*, vol. 9, no. 19, p. 2000707, Oct. 2020, doi: 10.1002/adhm.202000707.

[41] G. Narayanan, V. N. Vernekar, E. L. Kuyinu, and C. T. Laurencin, "Poly (lactic acid)-based biomaterials for orthopaedic regenerative engineering," *Advanced Drug Delivery Reviews*, vol. 107, pp. 247–276, Dec. 2016, doi: 10.1016/j.addr.2016.04.015.

[42] M. T. Calejo, T. Ilmarinen, H. Skottman, and M. Kellomäki, "Breath figures in tissue engineering and drug delivery: State-of-the-art and future perspectives," *Acta Biomaterialia*, vol. 66, pp. 44–66, Jan. 2018, doi: 10.1016/j.actbio.2017.11.043.

[43] G. Widawski, M. Rawiso, and B. François, "Self-organized honeycomb morphology of star-polymer polystyrene films," *Nature*, vol. 369, no. 6479, pp. 387–389, Jun. 1994, doi: 10.1038/369387a0.

[44] A. Zhang, H. Bai, and L. Li, "Breath Figure: A Nature-Inspired Preparation Method for Ordered Porous Films," *Chem. Rev.*, vol. 115, no. 18, pp. 9801–9868, Sep. 2015, doi: 10.1021/acs.chemrev.5b00069.

[45] L. M. Pineda, M. Busing, and R. P. Mei, "Bone regeneration with resorbable polymeric membranes. 111. Effect of poly(L-lactide) membrane pore size on the bone healing process in large defects," *J. Biomed. Mat. Res.*, vol. 31, pp. 385–394, 1996.

[46] G. Troiano, K. Zhurakivska, L. Lo Muzio, L. Laino, M. Cicciù, and L. Lo Russo, "Combination of Bone Graft and Resorbable Membrane for Alveolar Ridge Preservation: a Systematic Review, Meta-analysis and Trial Sequential Analysis," *Journal of Periodontology*, pp. 1–17, Sep. 2017, doi: 10.1902/jop.2017.170241.

[47] Y. Wang *et al.*, "Mechanical and degradative properties of PLDLA biodegradable pins with bioactive glass fibers in a beagle model," *Biomed. Mater.*, vol. 15, no. 3, p. 035010, Mar. 2020, doi: 10.1088/1748-605X/ab772d.

[48] R. Florencio-Silva, G. R. da S. Sasso, E. Sasso-Cerri, M. J. Simões, and P. S. Cerri, "Biology of Bone Tissue: Structure, Function, and Factors That Influence Bone Cells," *BioMed Research International*, vol. 2015, pp. 1–17, 2015, doi: 10.1155/2015/421746.

[49] J. Compston, "Bone marrow and bone: a functional unit," *Journal of Endocrinology*, vol. 173, no. 3, pp. 387–394, Jun. 2002, doi: 10.1677/joe.0.1730387.

[50] R. Marsell and T. A. Einhorn, "The biology of fracture healing," *Injury*, vol. 42, no. 6, pp. 551–555, Jun. 2011, doi: 10.1016/j.injury.2011.03.031.

[51] M. S. Jones and B. Waterson, "Principles of management of long bone fractures and fracture healing," *Surgery (Oxford)*, vol. 38, no. 2, pp. 91–99, Feb. 2020, doi: 10.1016/j.mpsur.2019.12.010.

[52] N. L. Fazzalari, "Bone fracture and bone fracture repair," *Osteoporos Int*, vol. 22, no. 6, pp. 2003–2006, Jun. 2011, doi: 10.1007/s00198-011-1611-4.

[53] G. Zhu *et al.*, "Bone physiological microenvironment and healing mechanism: Basis for future bone-tissue engineering scaffolds," *Bioactive Materials*, vol. 6, no. 11, pp. 4110–4140, Nov. 2021, doi: 10.1016/j.bioactmat.2021.03.043.

[54] E. H. Schemitsch, "Size Matters: Defining Critical in Bone Defect Size!," *Journal of Orthopaedic Trauma*, vol. 31, no. 5, pp. S20–S22, Oct. 2017, doi: 10.1097/BOT.0000000000000978.

[55] L. Montez, "Regeneration osseuse et ingenierie tissulaire Une eponge formee par la reticulation du chitosan avec une adenosine diphosphate est-elle un support adequat pour l encapsulation de cellules osseuses," Université Claude Bernard Lyon 1, Faculté de Pharmacie, 2018. [Online]. Available: https://bibnum.univ-lyon1.fr/nuxeo/nxfile/default/4fdebedd-f650-4ada-b88a-97b5f50accb5/blobholder:0/THph_2018_MONTEZ_Louise.pdf?mimetype=application/pdf

[56] Y. Li, S.-K. Chen, L. Li, L. Qin, X.-L. Wang, and Y.-X. Lai, "Bone defect animal models for testing efficacy of bone substitute biomaterials," *Journal of Orthopaedic Translation*, vol. 3, no. 3, pp. 95–104, Jul. 2015, doi: 10.1016/j.jot.2015.05.002.

[57] J. C. Reichert *et al.*, "The challenge of establishing preclinical models for segmental bone defect research," *Biomaterials*, vol. 30, no. 12, pp. 2149–2163, Apr. 2009, doi: 10.1016/j.biomaterials.2008.12.050.

[58] H. Stephen, *The Musculoskeletal System*, 3rd Edition. Jeremy Bowes, 2023. [Online]. Available: https://clinicalkeymeded.elsevier.com/reader/books/9780702084515/epubcfi/6/18%5B%3Bvnd. vst.idref%3DCH0001_1-21.e1_B9780702083808000017%5D!/4

[59] R. McRae and M. Esser, *Practical Fracture Treatment*, 5th edition. Elsevier Health Sciences, 2008. [Online]. Available: https://clinicalkeymeded.elsevier.com/reader/books/9781455725236/epubcfi/6/8%5B%3Bvnd.v st.idref%3DaB9780443068768100450%5D!/4/2/8/3:75%5B%20or%2C%20by%5D

[60] P. Bejon and E. Robinson, "Bone and joint infection," *Medicine*, vol. 49, no. 11, pp. 710–713, Nov. 2021, doi: 10.1016/j.mpmed.2021.08.011.

[61] D. Clark, M. Nakamura, T. Miclau, and R. Marcucio, "Effects of Aging on Fracture Healing," *Curr Osteoporos Rep*, vol. 15, no. 6, pp. 601–608, Dec. 2017, doi: 10.1007/s11914-017-0413-9.

[62] T. Sozen, L. Ozisik, and N. Calik Basaran, "An overview and management of osteoporosis," *Eur J Rheumatol*, vol. 4, no. 1, pp. 46–56, Mar. 2017, doi: 10.5152/eurjrheum.2016.048.

[63] T. D. Rachner, S. Khosla, and L. C. Hofbauer, "Osteoporosis: now and the future," *The Lancet*, vol. 377, no. 9773, pp. 1276–1287, Apr. 2011, doi: 10.1016/S0140-6736(10)62349-5.

[64] L. G. Kindblom, "Classification, Pathology," *Bone Tumors*.

[65] E. I. Hauben, "Epidemiology of primary bone tumors and economical aspects of bone metastases".

[66] J. L. Ferguson, S. P. Turner, and S. Barracks, "Bone Cancer:Diagnosis and Treatment Principles," *BONE CANCER*, vol. 98, no. 4, 2018.

[67] A. Houaoui, "Développement de matériaux composites et hybrides à base de verre bioactif pour la bio-ingénierie osseuse," CY Cergy Paris Université, 2021. [Online]. Available: http://www.theses.fr/2021CYUN1033/document

[68] R. S. Chaughule and R. Dashaputra, Eds., *Advances in Dental Implantology using Nanomaterials and Allied Technology Applications*. Cham: Springer International Publishing, 2021. doi: 10.1007/978-3-030-52207-0.

[69] D. F. Williams, "On the nature of biomaterials," *Biomaterials*, vol. 30, no. 30, pp. 5897–5909, Oct. 2009, doi: 10.1016/j.biomaterials.2009.07.027.

[70] F. J. O'Brien, "Biomaterials & scaffolds for tissue engineering," *Materials Today*, vol. 14, no. 3, pp. 88–95, Mar. 2011, doi: 10.1016/S1369-7021(11)70058-X.

[71] P. V. Giannoudis, H. Dinopoulos, and E. Tsiridis, "Bone substitutes: An update," *Injury*, vol. 36, no. 3, pp. S20–S27, Nov. 2005, doi: 10.1016/j.injury.2005.07.029.

[72] C. T. Laurencin and S. F. El-Amin, "Xenotransplantation in Orthopaedic Surgery:," *Journal of the American Academy of Orthopaedic Surgeons*, vol. 16, no. 1, pp. 4–8, Jan. 2008, doi: 10.5435/00124635-200801000-00002.

[73] H. Qu, H. Fu, Z. Han, and Y. Sun, "Biomaterials for bone tissue engineering scaffolds: a review," *RSC Adv.*, vol. 9, no. 45, pp. 26252–26262, 2019, doi: 10.1039/C9RA05214C.

[74] G. H. Altman *et al.*, "Silk-based biomaterials," *Biomaterials*, vol. 24, no. 3, pp. 401–416, 2003, doi: https://doi.org/10.1016/S0142-9612(02)00353-8.

[75] S. Abtahi, X. Chen, S. Shahabi, and N. Nasiri, "Resorbable Membranes for Guided Bone Regeneration: Critical Features, Potentials, and Limitations," *ACS Mater. Au*, p. acsmaterialsau.3c00013, Jun. 2023, doi: 10.1021/acsmaterialsau.3c00013.

[76] E. A. de Rezende Duek and A. Cristina Motta, "Bioresorbable Polymers ☆," in *Reference Module in Materials Science and Materials Engineering*, Elsevier, 2017, p. B9780128035818022815. doi: 10.1016/B978-0-12-803581-8.02281-5.

[77] G. Pertici, "Introduction to bioresorbable polymers for biomedical applications," in *Bioresorbable Polymers for Biomedical Applications*, Elsevier, 2017, pp. 3–29. doi: 10.1016/B978-0-08-100262-9.00001-X.

[78] H. R. Fernandes, A. Gaddam, A. Rebelo, D. Brazete, G. E. Stan, and J. M. F. Ferreira, "Bioactive Glasses and Glass-Ceramics for Healthcare Applications in Bone Regeneration and Tissue Engineering," *Materials*, vol. 11, no. 12, p. 2530, Dec. 2018, doi: 10.3390/ma11122530.

[79] Q. Fu, E. Saiz, M. N. Rahaman, and A. P. Tomsia, "Bioactive glass scaffolds for bone tissue engineering: state of the art and future perspectives," *Materials Science and Engineering: C*, vol. 31, no. 7, pp. 1245–1256, Oct. 2011, doi: 10.1016/j.msec.2011.04.022.

[80] S. Erden and K. Ho, "Fiber reinforced composites," in *Fiber Technology for Fiber-Reinforced Composites*, Elsevier, 2017, pp. 51–79. doi: 10.1016/B978-0-08-101871-2.00003-5.

[81] P. K. Vallittu, "Bioactive glass-containing cranial implants: an overview," *J Mater Sci*, vol. 52, no. 15, pp. 8772–8784, Aug. 2017, doi: 10.1007/s10853-017-0888-x.

[82] P. K. Vallittu *et al.*, "Biomaterial and implant induced ossification: in vitro and in vivo findings," *J Tissue Eng Regen Med*, vol. 14, no. 8, pp. 1157–1168, Aug. 2020, doi: 10.1002/term.3056.

[83] S. R. Dutta, D. Passi, P. Singh, and A. Bhuibhar, "Ceramic and non-ceramic hydroxyapatite as a bone graft material: a brief review," *Ir J Med Sci*, vol. 184, no. 1, pp. 101–106, Mar. 2015, doi: 10.1007/s11845-014-1199-8.

[84] F. Baino, G. Novajra, and C. Vitale-Brovarone, "Bioceramics and Scaffolds: A Winning Combination for Tissue Engineering," *Front. Bioeng. Biotechnol.*, vol. 3, Dec. 2015, doi: 10.3389/fbioe.2015.00202.

[85] G. Fernandez De Grado *et al.*, "Bone substitutes: a review of their characteristics, clinical use, and perspectives for large bone defects management," *J Tissue Eng*, vol. 9, p. 204173141877681, Jan. 2018, doi: 10.1177/2041731418776819.

[86] M. Bohner, B. L. G. Santoni, and N. Döbelin, "β-tricalcium phosphate for bone substitution: Synthesis and properties," *Acta Biomaterialia*, vol. 113, pp. 23–41, Sep. 2020, doi: 10.1016/j.actbio.2020.06.022.

[87] H. Granel *et al.*, "Optimized Bioactive Glass: the Quest for the Bony Graft," *Adv. Healthcare Mater.*, vol. 8, no. 11, p. 1801542, Jun. 2019, doi: 10.1002/adhm.201801542.

[88] L. L. Hench, "The story of Bioglass®," *J Mater Sci: Mater Med*, vol. 17, no. 11, pp. 967–978, Nov. 2006, doi: 10.1007/s10856-006-0432-z.

[89] L. L. Hench and O. Andersson, "BIOACTIVE GLASSES," *An Introduction to Bioceramics*, p. 22.

[90] J. R. Jones, "Review of bioactive glass: From Hench to hybrids," *Acta Biomaterialia*, vol. 9, no. 1, pp. 4457–4486, Jan. 2013, doi: 10.1016/j.actbio.2012.08.023.

[91] Ö.H. Anderson, K.H. Karlson, G. Liu, and L. Niemi, "In vivo behavior of glasses in the SiO2-NaO2-CaO-P2O5-Al2O3-B2O3 system," *J. Mater. Sci. Mater. Med.*, vol. 1, no. 4, pp. 219–227, 1990.

[92] S. Fagerlund and L. Hupa, "Chapter 1. Melt-derived Bioactive Silicate Glasses," in *Smart Materials Series*, A. R. Boccaccini, D. S. Brauer, and L. Hupa, Eds., Cambridge: Royal Society of Chemistry, 2016, pp. 1–26. doi: 10.1039/9781782622017-00001.

[93] L. Hupa, "Composition-property relations of bioactive silicate glasses," in *Bioactive Glasses*, Elsevier, 2018, pp. 1–35. doi: 10.1016/B978-0-08-100936-9.00001-0.

[94] O. D. Abodunrin, K. El Mabrouk, and M. Bricha, "A review on borate bioactive glasses (BBG): effect of doping elements, degradation, and applications," *J. Mater. Chem. B*, vol. 11, no. 5, pp. 955–973, 2023, doi: 10.1039/D2TB02505A.

[95] V.-V. Välimäki and H. T. Aro, "Molecular Basis for Action of Bioactive Glasses as Bone Graft Substitute," *Scand J Surg*, vol. 95, no. 2, pp. 95–102, Jun. 2006, doi: 10.1177/145749690609500204.

[96] L.-C. Gerhardt and A. R. Boccaccini, "Bioactive Glass and Glass-Ceramic Scaffolds for Bone Tissue Engineering," *Materials*, vol. 3, no. 7, pp. 3867–3910, Jul. 2010, doi: 10.3390/ma3073867.

[97] N. C. Lindfors, I. Koski, J. T. Heikkila, K. Mattila, and A. J. Aho, "A prospective randomized 14-year follow-up study of bioactive glass and autogenous bone as bone graft substitutes in benign bone tumors," vol. 94, no. 1, 2010.

[98] O. Peitl, E. Dutra Zanotto, and L. L. Hench, "Highly bioactive P2O5–Na2O–CaO–SiO2 glass-ceramics," *Journal of Non-Crystalline Solids*, vol. 292, no. 1–3, pp. 115–126, Nov. 2001, doi: 10.1016/S0022-3093(01)00822-5.

[99] S. Fagerlund, J. Massera, N. Moritz, L. Hupa, and M. Hupa, "Phase composition and in vitro bioactivity of porous implants made of bioactive glass S53P4," *Acta Biomaterialia*, vol. 8, no. 6, pp. 2331–2339, Jul. 2012, doi: 10.1016/j.actbio.2012.03.011.

[100] W. Huang, D. E. Day, K. Kittiratanapiboon, and M. N. Rahaman, "Kinetics and mechanisms of the conversion of silicate (45S5), borate, and borosilicate glasses to hydroxyapatite in dilute phosphate solutions," *J Mater Sci: Mater Med*, vol. 17, no. 7, pp. 583–596, Jul. 2006, doi: 10.1007/s10856-006-9220-z.

[101] S. B. Jung, "Bioactive Borate Glasses," in *Bio-Glasses*, J. R. Jones and A. G. Clare, Eds., Chichester, UK: John Wiley & Sons, Ltd, 2012, pp. 75–95. doi: 10.1002/9781118346457.ch6.

[102] A. Yao, D. Wang, W. Huang, Q. Fu, M. N. Rahaman, and D. E. Day, "In Vitro Bioactive Characteristics of Borate-Based Glasses with Controllable Degradation Behavior," *J American Ceramic Society*, vol. 90, no. 1, pp. 303–306, Jan. 2007, doi: 10.1111/j.1551-2916.2006.01358.x.

[103] R. Jugdaohsingh, L. D. Pedro, A. Watson, and J. J. Powell, "Silicon and boron differ in their localization and loading in bone," *Bone Reports*, vol. 1, pp. 9–15, Jan. 2015, doi: 10.1016/j.bonr.2014.10.002.

[104] Q. Fu, M. N. Rahaman, B. S. Bal, L. F. Bonewald, K. Kuroki, and R. F. Brown, "Silicate, borosilicate, and borate bioactive glass scaffolds with controllable degradation rate for bone tissue engineering applications. II. In vitro and in vivo biological evaluation," *J. Biomed. Mater. Res.*, vol. 95A, no. 1, pp. 172–179, Oct. 2010, doi: 10.1002/jbm.a.32823.

[105] L. L. Hench, "Chronology of Bioactive Glass Development and Clinical Applications," *NJGC*, vol. 03, no. 02, pp. 67–73, 2013, doi: 10.4236/njgc.2013.32011.

[106] P. I. J. M. Wuisman and S. T.H., "PART II: CLINICAL APPLICATIONS OF DEGRADABLE IMPLANTS," in *Degradable Polymers for Skeletal Implants*, New York: Nova Science Publishers, 2009.

[107] L. S. Nair and C. T. Laurencin, "Biodegradable polymers as biomaterials," *Progress in Polymer Science*, vol. 32, no. 8–9, pp. 762–798, Aug. 2007, doi: 10.1016/j.progpolymsci.2007.05.017.

[108] O. S. Zaroog, M. A. Satgunam, and L. C. Wei, "Biomaterials for Bone Tissue Engineering: Properties and Applications," in *Reference Module in Materials Science and Materials Engineering*, Elsevier, 2019. doi: 10.1016/B978-0-12-803581-8.11394-3.

[109] S. V. Gohil, S. Suhail, J. Rose, T. Vella, and L. S. Nair, "Polymers and Composites for Orthopedic Applications," in *Materials for Bone Disorders*, Elsevier, 2017, pp. 349–403. doi: 10.1016/B978-0-12-802792-9.00008-2.

[110] C. Vepari and D. L. Kaplan, "Silk as a biomaterial," *Progress in Polymer Science*, vol. 32, no. 8–9, pp. 991–1007, Aug. 2007, doi: 10.1016/j.progpolymsci.2007.05.013.

[111] J. Melke, S. Midha, S. Ghosh, K. Ito, and S. Hofmann, "Silk fibroin as biomaterial for bone tissue engineering," *Acta Biomaterialia*, vol. 31, pp. 1–16, Feb. 2016, doi: 10.1016/j.actbio.2015.09.005.

[112] L. Meinel *et al.*, "Silk implants for the healing of critical size bone defects," *Bone*, vol. 37, no. 5, pp. 688–698, Nov. 2005, doi: 10.1016/j.bone.2005.06.010.

[113] H. J. Kim, U.-J. Kim, G. Vunjak-Novakovic, B.-H. Min, and D. L. Kaplan, "Influence of macroporous protein scaffolds on bone tissue engineering from bone marrow stem cells," *Biomaterials*, vol. 26, no. 21, pp. 4442–4452, Jul. 2005, doi: 10.1016/j.biomaterials.2004.11.013.

[114] I.-Y. Kim *et al.*, "Chitosan and its derivatives for tissue engineering applications," *Biotechnology Advances*, vol. 26, no. 1, pp. 1–21, Jan. 2008, doi: 10.1016/j.biotechadv.2007.07.009.

[115] P. Zhai, X. Peng, B. Li, Y. Liu, H. Sun, and X. Li, "The application of hyaluronic acid in bone regeneration," *International Journal of Biological Macromolecules*, vol. 151, pp. 1224–1239, May 2020, doi: 10.1016/j.ijbiomac.2019.10.169.

[116] A. Baldini, D. Zaffe, and G. Nicolini, "Bone-defects healing by high-molecular hyaluronic acid: preliminary results," *Annali di Stomatologia*.

[117] C. Scholz, *Chapter 1: THE MOLECULAR STRUCTURE OF DEGRADABLE POLYMERS from Degradable Polymers for Skeletal Implants*, New York: Nova Science Publishers. 2009.

[118] J. C. Middleton and A. J. Tipton, "Synthetic biodegradable polymers as orthopedic devices," *Biomaterials*, vol. 21, no. 23, pp. 2335–2346, Dec. 2000, doi: 10.1016/S0142-9612(00)00101-0.

[119] A. B. Balaji, H. Pakalapati, M. Khalid, R. Walvekar, and H. Siddiqui, "Natural and synthetic biocompatible and biodegradable polymers," in *Biodegradable and Biocompatible Polymer Composites*, Elsevier, 2018, pp. 3–32. doi: 10.1016/B978-0-08-100970-3.00001-8.

[120] A. C. B. Benatti *et al.*, "Bioreabsorbable polymers for tissue engineering: PLA, PGA, and their copolymers," in *Materials for Biomedical Engineering*, Elsevier, 2019, pp. 83–116. doi: 10.1016/B978-0-12-816901-8.00004-3.

[121] G. S. Ciambelli *et al.*, "Characterization of poly (L-co-D,L Lactic Acid) and a study of polymer-tissue interaction in subcutaneous implants in wistar rats," *Mat. Res.*, vol. 16, no. 1, pp. 28–37, Oct. 2012, doi: 10.1590/S1516-14392012005000146.

[122] J. Kangas *et al.*, "Comparison of strength properties of poly-L/D-lactide (PLDLA) 96/4 and polyglyconate (Maxon) sutures:In vitro, in the subcutis, and in the achilles tendon of rabbits," *J. Biomed. Mater. Res.*, vol. 58, no. 1, pp. 121–126, 2001, doi: 10.1002/1097-4636(2001)58:1<121::AID-JBM180>3.0.CO;2-Z.

[123] M. Grazia Raucci, D. Giugliano, and L. Ambrosio, "Fondamental Properties of Bioceramics and Biocomposites," in *Handbook of bioceramics and biocomposites*, New York, NY: Springer Berlin Heidelberg, 2016.

[124] G. Turnbull *et al.*, "3D bioactive composite scaffolds for bone tissue engineering," *Bioactive Materials*, vol. 3, no. 3, pp. 278–314, Sep. 2018, doi: 10.1016/j.bioactmat.2017.10.001.

[125] R. Sergi, D. Bellucci, and V. Cannillo, "A Review of Bioactive Glass/Natural Polymer Composites: State of the Art," *Materials*, vol. 13, no. 23, p. 5560, Dec. 2020, doi: 10.3390/ma13235560.

[126] T. Long, J. Yang, S.-S. Shi, Y.-P. Guo, Q.-F. Ke, and Z.-A. Zhu, "Fabrication of three-dimensional porous scaffold based on collagen fiber and bioglass for bone tissue engineering: IDEAL SCAFFOLD FOR BONE TISSUE ENGINEERING," *J. Biomed. Mater. Res.*, vol. 103, no. 7, pp. 1455–1464, Oct. 2015, doi: 10.1002/jbm.b.33328.

[127] X. Du, D. Wei, L. Huang, M. Zhu, Y. Zhang, and Y. Zhu, "3D printing of mesoporous bioactive glass/silk fibroin composite scaffolds for bone tissue engineering," *Materials Science and Engineering: C*, vol. 103, p. 109731, Oct. 2019, doi: 10.1016/j.msec.2019.05.016.

[128] J. Yang, T. Long, N.-F. He, Y.-P. Guo, Z.-A. Zhu, and Q.-F. Ke, "Fabrication of a chitosan/bioglass three-dimensional porous scaffold for bone tissue engineering applications," *J. Mater. Chem. B*, vol. 2, no. 38, pp. 6611–6618, 2014, doi: 10.1039/C4TB00940A.

[129] H. H. Lu, S. F. El-Amin, K. D. Scott, and C. T. Laurencin, "Three-dimensional, bioactive, biodegradable, polymer-bioactive glass composite scaffolds with improved mechanical properties support collagen synthesis and mineralization of human osteoblast-like cellsin vitro," *J. Biomed. Mater. Res.*, vol. 64A, no. 3, pp. 465–474, Mar. 2003, doi: 10.1002/jbm.a.10399.

[130] V. Maquet, A. R. Boccaccini, L. Pravata, I. Notingher, and R. Jérôme, "Porous poly(α-hydroxyacid)/Bioglass® composite scaffolds for bone tissue engineering. I: preparation and in vitro characterisation," *Biomaterials*, vol. 25, no. 18, pp. 4185–4194, Aug. 2004, doi: 10.1016/j.biomaterials.2003.10.082.

[131] J. J. Blaker, V. Maquet, R. Jérôme, A. R. Boccaccini, and S. N. Nazhat, "Mechanical properties of highly porous PDLLA/Bioglass® composite foams as scaffolds for bone tissue engineering," *Acta Biomaterialia*, vol. 1, no. 6, pp. 643–652, Nov. 2005, doi: 10.1016/j.actbio.2005.07.003.

[132] F. Baino *et al.*, "Processing methods for making porous bioactive glass-based scaffolds—A state-of-the-art review," *Int J Appl Ceram Technol*, vol. 16, no. 5, pp. 1762–1796, Sep. 2019, doi: 10.1111/ijac.13195.

[133] J. CESARANO III, "Robocasting of Ceramics and Composites Using Fine Particle Suspensions," United States, Oct. 1999. [Online]. Available: http://inis.iaea.org/search/search.aspx?orig_q=RN:33058481

[134] J. Franco, P. Hunger, M. E. Launey, A. P. Tomsia, and E. Saiz, "Direct write assembly of calcium phosphate scaffolds using a water-based hydrogel," *Acta Biomaterialia*, vol. 6, no. 1, pp. 218–228, Jan. 2010, doi: 10.1016/j.actbio.2009.06.031.

[135] G. Murray, R. Holden, and W. Roschlau, "Experimental and clinical study of new growth of bone in cavity," *American journal of Surgery*, vol. 93, pp. 385–387, 1957.

[136] D. Buser, Ed., "Chapter 1: The development of Guided Bone Regeneration over the past 30 Years," in *30 years of guided bone regeneration*, Third edition., Batavia, IL: Quintessence Publishing Co, Inc, 2021.

[137] M. Retzepi and N. Donos, "Guided Bone Regeneration: biological principle and therapeutic applications: Guided bone regeneration," *Clinical Oral Implants Research*, vol. 21, no. 6, pp. 567–576, Mar. 2010, doi: 10.1111/j.1600-0501.2010.01922.x.

[138] J. Liu and D. G. Kerns, "Mechanisms of guided bone regeneration: a review," *Open Dent J*, vol. 8, pp. 56–65, mai 2014, doi: 10.2174/1874210601408010056.

[139] Z. Yang *et al.*, "Advances in Barrier Membranes for Guided Bone Regeneration Techniques," *Front. Bioeng. Biotechnol.*, vol. 10, p. 921576, Jun. 2022, doi: 10.3389/fbioe.2022.921576.

[140] Y. Ren *et al.*, "Barrier Membranes for Guided Bone Regeneration (GBR): A Focus on Recent Advances in Collagen Membranes," *IJMS*, vol. 23, no. 23, p. 14987, Nov. 2022, doi: 10.3390/ijms232314987.

[141] S. M. Kuo, S. J. Chang, T. W. Chen, and T. C. Kuan, "Guided tissue regeneration for using a chitosan membrane: An experimental study in rats," *J. Biomed. Mater. Res.*, vol. 76A, no. 2, pp. 408–415, Feb. 2006, doi: 10.1002/jbm.a.30534.

[142] S.-Y. Shin *et al.*, "Biological Evaluation of Chitosan Nanofiber Membrane for Guided Bone Regeneration," *Journal of Periodontology*, vol. 76, no. 10, pp. 1778–1784, Oct. 2005, doi: 10.1902/jop.2005.76.10.1778.

[143] D. Lee *et al.*, "Preparation of antibacterial chitosan membranes containing silver nanoparticles for dental barrier membrane applications," *Journal of Industrial and Engineering Chemistry*, vol. 66, pp. 196–202, Oct. 2018, doi: 10.1016/j.jiec.2018.05.030.

[144] Archana R Sankar, Sheela Kumar Gujjari, Kulkarni PK, and Akhila AR, "Development of biodegradable silkworm cocoon derived silk membrane for GTR in the treatment of grade II furcation," *ijrps*, vol. 11, no. 2, pp. 1551–1561, Apr. 2020, doi: 10.26452/ijrps.v11i2.2033.

[145] S.-W. Lee and S.-G. Kim, "Membranes for the Guided Bone Regeneration," *Maxillofacial Plastic and Reconstructive Surgery*, vol. 36, no. 6, pp. 239–246, Nov. 2014, doi: 10.14402/jkamprs.2014.36.6.239.

[146] S. Ghafouri, A. R. Sadeghi-avalshahr, A. M. Molavi, and H. Hassanzadeh, "Fabrication of Functionally Graded Electrospun Membranes Based on Silk Fibroin for Using as Dental Barrier Membranes in Guided Bone Regeneration," *Fibers Polym*, vol. 23, no. 9, pp. 2549–2556, Sep. 2022, doi: 10.1007/s12221-022-4304-z.

[147] T. Osathanon, P. Chanjavanakul, P. Kongdecha, P. Clayhan, and N. C.-N. Huynh, "Polycaprolactone-Based Biomaterials for Guided Tissue Regeneration Membrane," in *Periodontitis - A Useful Reference*, P. Arjunan, Ed., InTech, 2017. doi: 10.5772/intechopen.69153.

[148] P. Gentile, V. Chiono, C. Tonda-Turo, A. M. Ferreira, and G. Ciardelli, "Polymeric membranes for guided bone regeneration," *Biotechnology Journal*, vol. 6, no. 10, pp. 1187–1197, Oct. 2011, doi: 10.1002/biot.201100294.

[149] A. Hoomaert, P. Layrolle, and J. Sohier, "Bone regeneration membrane and method for forming a bone regeneration membrane," EP 2 404 627 A1 [Online]. Available: https://patentimages.storage.googleapis.com/4b/63/f3/ce2f59298f2378/EP2404627A1.pdf

[150] Q. Zhang *et al.*, "Bioinspired engineering of honeycomb structure – Using nature to inspire human innovation," *Progress in Materials Science*, vol. 74, pp. 332–400, Oct. 2015, doi: 10.1016/j.pmatsci.2015.05.001.

[151] M. T. Calejo, T. Ilmarinen, H. Jongprasitkul, H. Skottman, and M. Kellomäki, "Honeycomb porous films as permeable scaffold materials for human embryonic stem cell-derived retinal pigment epithelium: Porous films as scaffolds for hESC-RPE," *J. Biomed. Mater. Res.*, vol. 104, no. 7, pp. 1646–1656, Jul. 2016, doi: 10.1002/jbm.a.35690.

[152] A. Shiohara, B. Prieto-Simon, and N. H. Voelcker, "Porous polymeric membranes: fabrication techniques and biomedical applications," *J. Mater. Chem. B*, vol. 9, no. 9, pp. 2129–2154, 2021, doi: 10.1039/D0TB01727B.

[153] E. H. Min, "Fabrication of Honeycomb Structured Porous Membranes for Biological Applications," University of New South Wales, 2010. [Online]. Available: https://doi.org/10.26190/unsworks/22991

[154] J. Massera, A. Mishra, S. Guastella, S. Ferraris, and E. Verné, "Surface functionalization of phosphate-based bioactive glasses with 3-aminopropyltriethoxysilane (APTS)," *Biomedical glasses*, vol. 2, no. 1, Jan. 2016, doi: 10.1515/bglass-2016-0007.

[155] M. T. Calejo, T. Ilmarinen, H. Skottman, and M. Kellomäki, "Breath figures in tissue engineering and drug delivery: State-of-the-art and future perspectives," *Acta Biomaterialia*, vol. 66, pp. 44–66, Jan. 2018, doi: 10.1016/j.actbio.2017.11.043.

[156] *T. Luxbacher, The ZETA guide, principles of the streaming potential technique, Anton Paar.*

[157] M. R. Lin, J. E. Ritter, L. Rosenfeld, and T. J. Lardner, "Measuring the interfacial shear strength of thin polymer coatings on glass," *J. Mater. Res.*, vol. 5, no. 5, pp. 1110–1117, May 1990, doi: 10.1557/JMR.1990.1110.

[158] T. Kokubo, H. Kushitani, S. Sakka, T. Kitsugi, and T. Yamamuro, "Solutions able to reproduce in vivo surface-structure changes in bioactive glass-ceramic A-W3," *J. Biomed. Mater. Res.*, vol. 24, no. 6, pp. 721–734, Jun. 1990, doi: 10.1002/jbm.820240607.

[159] S. Ferraris, A. Nommeots-Nomm, S. Spriano, E. Vernè, and J. Massera, "Surface reactivity and silanization ability of borosilicate and Mg-Sr-based bioactive glasses," *Applied Surface Science*, vol. 475, pp. 43–55, mai 2019, doi: 10.1016/j.apsusc.2018.12.218.

[160] S. Ferraris *et al.*, "Bioactive materials: In vitro investigation of different mechanisms of hydroxyapatite precipitation," *Acta Biomaterialia*, vol. 102, pp. 468–480, Jan. 2020, doi: 10.1016/j.actbio.2019.11.024.

[161] H. H. Lu, S. R. Pollack, and P. Ducheyne, "45S5 Bioactive glass surface charge variations and the formation of a surface calcium phosphate layer in a solution containing fibronectin," p. 8.

[162] H. H. Lu, S. R. Pollack, and P. Ducheyne, "Temporal zeta potential variations of 45S5 bioactive glass immersed in an electrolyte solution," p. 8, 1999.

[163] A. Doostmohammadi *et al.*, "Preparation, chemistry and physical properties of bone-derived hydroxyapatite particles having a negative zeta potential," *Materials Chemistry and Physics*, vol. 132, no. 2–3, pp. 446–452, Feb. 2012, doi: 10.1016/j.matchemphys.2011.11.051.

[164] Q. Fu, M. N. Rahaman, H. Fu, and X. Liu, "Silicate, borosilicate, and borate bioactive glass scaffolds with controllable degradation rate for bone tissue engineering applications. I. Preparation and in vitro degradation," *J. Biomed. Mater. Res.*, vol. 95A, no. 1, pp. 164–171, Oct. 2010, doi: 10.1002/jbm.a.32824.

[165] L. Varila, S. Fagerlund, T. Lehtonen, J. Tuominen, and L. Hupa, "Surface reactions of bioactive glasses in buffered solutions," *Journal of the European Ceramic Society*, vol. 32, no. 11, pp. 2757–2763, Aug. 2012, doi: 10.1016/j.jeurceramsoc.2012.01.025.

[166] J. Massera and L. Hupa, "Influence of SrO substitution for CaO on the properties of bioactive glass S53P4," *J Mater Sci: Mater Med*, vol. 25, no. 3, pp. 657–668, Mar. 2014, doi: 10.1007/s10856-013-5120-1.

[167] J. M. Tainio *et al.*, "Structure and in vitro dissolution of Mg and Sr containing borosilicate bioactive glasses for bone tissue engineering," *Journal of Non-Crystalline Solids*, vol. 533, p. 119893, Apr. 2020, doi: 10.1016/j.jnoncrysol.2020.119893.

[168] K. Schuhladen, X. Wang, L. Hupa, and A. R. Boccaccini, "Dissolution of borate and borosilicate bioactive glasses and the influence of ion (Zn, Cu) doping in different solutions," *Journal of Non-Crystalline Solids*, vol. 502, pp. 22–34, Dec. 2018, doi: 10.1016/j.jnoncrysol.2018.08.037.

[169] E. Bormashenko, "Breath-Figure Self-Assembly, a Versatile Method of Manufacturing Membranes and Porous Structures: Physical, Chemical and Technological Aspects," *Membranes*, vol. 7, no. 3, p. 45, Aug. 2017, doi: 10.3390/membranes7030045.

[170] D. Meroni *et al.*, "A Close Look at the Structure of the TiO_2-APTES Interface in Hybrid Nanomaterials and Its Degradation Pathway: An Experimental and Theoretical Study," *J. Phys. Chem. C*, vol. 121, no. 1, pp. 430–440, Jan. 2017, doi: 10.1021/acs.jpcc.6b10720.

[171] Y. Lai, Y. Zeng, X. Tang, H. Zhang, J. Han, and H. Su, "Structural investigation of calcium borosilicate glasses with varying Si/Ca ratios by infrared and Raman spectroscopy," *RSC Adv.*, vol. 6, no. 96, pp. 93722–93728, 2016, doi: 10.1039/C6RA20969F.

[172] S. Zhou *et al.*, "Hydrogen Bonding Interaction of Poly(D , L -Lactide)/hydroxyapatite Nanocomposites," *Chem. Mater.*, vol. 19, no. 2, pp. 247–253, Jan. 2007, doi: 10.1021/cm0619398.

[173] A. A. El-Rashidy, J. A. Roether, L. Harhaus, U. Kneser, and A. R. Boccaccini, "Regenerating bone with bioactive glass scaffolds: A review of in vivo studies in bone defect models," *Acta Biomaterialia*, vol. 62, pp. 1–28, Oct. 2017, doi: 10.1016/j.actbio.2017.08.030.

[174] M. Brink, T. Turunen, R.-P. Happonen, and A. Yli-Urpo, "Compositional dependence of bioactivity of glasses in the system Na2O-K2O-MgO-CaO-B2O3-P2O5-SiO2," p. 8.

[175] Y. Yu, B. Stevensson, and M. Edén, "Medium-Range Structural Organization of Phosphorus-Bearing Borosilicate Glasses Revealed by Advanced Solid-State NMR Experiments and MD Simulations: Consequences of B/Si Substitutions," *J. Phys. Chem. B*, vol. 121, no. 41, pp. 9737–9752, Oct. 2017, doi: 10.1021/acs.jpcb.7b06654.

[176] A. Mishra, J. Rocherullé, and J. Massera, "Ag-doped phosphate bioactive glasses: thermal, structural and in-vitro dissolution properties," *Biomedical glasses*, vol. 2, no. 1, Jan. 2016, doi: 10.1515/bglass-2016-0005.

[177] M. Bohner and J. Lemaitre, "Can bioactivity be tested in vitro with SBF solution?," *Biomaterials*, vol. 30, no. 12, pp. 2175–2179, Apr. 2009, doi: 10.1016/j.biomaterials.2009.01.008.

[178] M. Ouis, A. Abdelghany, and H. Elbatal, "Corrosion mechanism and bioactivity of borate glasses analogue to Hench's bioglass," *PAC*, vol. 6, no. 3, pp. 141–149, 2012, doi: 10.2298/PAC1203141O.

[179] S. Prasad S. *et al.*, "Effect of boron oxide addition on structural, thermal, in vitro bioactivity and antibacterial properties of bioactive glasses in the base S53P4 composition," *Journal of Non-Crystalline Solids*, vol. 498, pp. 204–215, Oct. 2018, doi: 10.1016/j.jnoncrysol.2018.06.027.

[180] J. Massera, L. Hupa, and M. Hupa, "Influence of the partial substitution of CaO with MgO on the thermal properties and in vitro reactivity of the bioactive glass S53P4," *Journal of Non-Crystalline Solids*, vol. 358, no. 18–19, pp. 2701–2707, Sep. 2012, doi: 10.1016/j.jnoncrysol.2012.06.032.

[181] M. Kopani *et al.*, "On determination of properties of ultrathin and very thin silicon oxide layers by FTIR and X - ray reflectivity," *MRS Proc.*, vol. 1066, pp. 1066-A07-03, 2008, doi: 10.1557/PROC-1066-A07-03.

[182] S. Koutsopoulos, "Synthesis and characterization of hydroxyapatite crystals: A review study on the analytical methods," *J. Biomed. Mater. Res.*, vol. 62, no. 4, pp. 600–612, Dec. 2002, doi: 10.1002/jbm.10280.

[183] E. I. Kamitsos, A. P. Patsis, M. A. Karakassides, and G. D. Chryssikos, "Infrared reflectance spectra of lithium borate glasses," *Journal of Non-Crystalline Solids*, vol. 126, no. 1–2, pp. 52–67, Dec. 1990, doi: 10.1016/0022-3093(90)91023-K.

[184] J. Fournier *et al.*, "Luminescence study of defects in silica glasses under near-UV excitation," *Physics Procedia*, vol. 8, pp. 39–43, 2010, doi: 10.1016/j.phpro.2010.10.009.

[185] H. Nishikawa, T. Shiroyama, R. Nakamura, Y. Ohki, K. Nagasawa, and Y. Hama, "Photoluminescence from defect centers in high-purity silica glasses observed under 7.9-eV excitation," *Phys. Rev. B*, vol. 45, no. 2, pp. 586–591, Jan. 1992, doi: 10.1103/PhysRevB.45.586.

[186] S. Munekuni *et al.*, "Various types of nonbridging oxygen hole center in high-purity silica glass," *Journal of Applied Physics*, vol. 68, no. 3, pp. 1212–1217, Aug. 1990, doi: 10.1063/1.346719.

[187] A. M. Fayad, W. M. Abd-Allah, and F. A. Moustafa, "Effect of Gamma Irradiation on Structural and Optical Investigations of Borosilicate Glass Doped Yttrium Oxide," *Silicon*, vol. 10, no. 3, pp. 799–809, May 2018, doi: 10.1007/s12633-016-9533-6.

[188] P. Rautiyal *et al.*, "Gamma irradiation-induced defects in borosilicate glasses for high-level radioactive waste immobilisation," *Journal of Nuclear Materials*, vol. 544, p. 152702, Feb. 2021, doi: 10.1016/j.jnucmat.2020.152702.

[189] D. L. Griscom, "Properties and Structure of Defects in Silica Glass," *Journal of The Ceramic Society of Japan*, no. 99, p. 20, 1991.

[190] J. H. Mackey, H. L. Smith, and A. Halperin, "Optical studies in x-irradiated high purity sodium silicate glasses," *Journal of Physics and Chemistry of Solids*, vol. 27, no. 11–12, pp. 1759–1772, Nov. 1966, doi: 10.1016/0022-3697(66)90107-7.

[191] D. L. Griscom, "E.S.R. studies of radiation damage and structure in oxide glasses not containing transition group ions: A contemporary overview with illustrations from the alkali borate system,"

Journal of Non-Crystalline Solids, vol. 13, no. 2, pp. 251–285, Jan. 1974, doi: 10.1016/0022-3093(74)90095-7.

[192] A. A. El-Kheshen, "Glass as Radiation Sensor," *Current Topics in Ionizing Radiation Research*, p. 26, 2012.

[193] D. Möncke and D. Ehrt, "Irradiation induced defects in glasses resulting in the photoionization of polyvalent dopants," *Optical Materials*, vol. 25, no. 4, pp. 425–437, May 2004, doi: 10.1016/j.optmat.2003.11.001.

[194] D. L. Griscom, G. H. Sigel, and R. J. Ginther, "Defect centers in a pure-silica-core borosilicate-clad optical fiber: ESR studies," *Journal of Applied Physics*, vol. 47, no. 3, pp. 960–967, Mar. 1976, doi: 10.1063/1.322687.

[195] J. Mao *et al.*, "Structural changes on the surfaces of borosilicate glasses induced by gamma-ray irradiation," *J Am Ceram Soc.*, vol. 105, no. 8, pp. 5178–5189, Aug. 2022, doi: 10.1111/jace.18492.

[196] N. Ollier, B. Boizot, B. Reynard, D. Ghaleb, and G. Petite, "Analysis of molecular oxygen formation in irradiated glasses: a Raman depth profile study," *Journal of Nuclear Materials*, vol. 340, no. 2–3, pp. 209–213, Apr. 2005, doi: 10.1016/j.jnucmat.2004.11.011.

[197] R. Procházka *et al.*, "A comparison of natural and experimental long-term corrosion of uranium-colored glass," *Journal of Non-Crystalline Solids*, vol. 355, no. 43–44, pp. 2134–2142, Oct. 2009, doi: 10.1016/j.jnoncrysol.2009.06.032.

[198] P. Nugroho, H. Mitomo, F. Yoshii, and T. Kume, "Degradation of poly(l-lactic acid) by g-irradiation," *Polymer Degradation and Stability*, p. 7, 2001.

[199] H.-E. Shim *et al.*, "Preliminary Study on the Simulation of a Radiation Damage Analysis of Biodegradable Polymers," *Materials*, vol. 14, no. 22, p. 6777, Nov. 2021, doi: 10.3390/ma14226777.

[200] H.-E. Shim *et al.*, "Preliminary Study on the Simulation of a Radiation Damage Analysis of Biodegradable Polymers," *Materials*, vol. 14, no. 22, p. 6777, Nov. 2021, doi: 10.3390/ma14226777.

[201] A. Deraine *et al.*, "Polymer-Based Honeycomb Films on Bioactive Glass: Toward a Biphasic Material for Bone Tissue Engineering Applications," *ACS Appl. Mater. Interfaces*, p. acsami.1c03759, Jun. 2021, doi: 10.1021/acsami.1c03759.

[202] R. A. Gittens *et al.*, "A review on the wettability of dental implant surfaces II: Biological and clinical aspects," *Acta Biomaterialia*, vol. 10, no. 7, pp. 2907–2918, Jul. 2014, doi: 10.1016/j.actbio.2014.03.032.

[203] M. S. Kim *et al.*, "Adhesion Behavior of Human Bone Marrow Stromal Cells on Differentially Wettable Polymer Surfaces," *Tissue Engineering*, vol. 13, no. 8, pp. 2095–2103, Aug. 2007, doi: 10.1089/ten.2006.0062.

[204] Y. Fukuhira *et al.*, "Biodegradable honeycomb-patterned film composed of poly(lactic acid) and dioleoylphosphatidylethanolamine," *Biomaterials*, vol. 27, no. 9, pp. 1797–1802, Mar. 2006, doi: 10.1016/j.biomaterials.2005.10.019.

[205] W. Wang *et al.*, "Enhancing the Hydrophilicity and Cell Attachment of 3D Printed PCL/Graphene Scaffolds for Bone Tissue Engineering," *Materials*, vol. 9, no. 12, p. 992, Dec. 2016, doi: 10.3390/ma9120992.

[206] W. Cui, X. Li, C. Xie, H. Zhuang, S. Zhou, and J. Weng, "Hydroxyapatite nucleation and growth mechanism on electrospun fibers functionalized with different chemical groups and their combinations," *Biomaterials*, vol. 31, no. 17, pp. 4620–4629, Jun. 2010, doi: 10.1016/j.biomaterials.2010.02.050.

[207] M. A. Elsawy, K.-H. Kim, J.-W. Park, and A. Deep, "Hydrolytic degradation of polylactic acid (PLA) and its composites," *Renewable and Sustainable Energy Reviews*, vol. 79, pp. 1346–1352, Nov. 2017, doi: 10.1016/j.rser.2017.05.143.

[208] W. Wang *et al.*, "Development of X-ray opaque poly(lactic acid) end-capped by triiodobenzoic acid towards non-invasive micro-CT imaging biodegradable embolic microspheres," *European Polymer Journal*, vol. 108, pp. 337–347, Nov. 2018, doi: 10.1016/j.eurpolymj.2018.09.018.

[209] A. L. B. Maçon *et al.*, "A unified in vitro evaluation for apatite-forming ability of bioactive glasses and their variants," *J Mater Sci: Mater Med*, vol. 26, no. 2, p. 115, Feb. 2015, doi: 10.1007/s10856-015-5403-9.

[210] A. Houaoui *et al.*, "New Generation of Hybrid Materials Based on Gelatin and Bioactive Glass Particles for Bone Tissue Regeneration," *Biomolecules*, vol. 11, no. 3, p. 444, Mar. 2021, doi: 10.3390/biom11030444.

[211] K. Magyari, L. Baia, A. Vulpoi, S. Simon, O. Popescu, and V. Simon, "Bioactivity evolution of the surface functionalized bioactive glasses: Surface Functionalized Bioactive Glasses," *J. Biomed. Mater. Res.*, vol. 103, no. 2, pp. 261–272, Feb. 2015, doi: 10.1002/jbm.b.33203.

[212] C. Drouet, "Apatite Formation: Why It May Not Work as Planned, and How to Conclusively Identify Apatite Compounds," *BioMed Research International*, vol. 2013, pp. 1–12, 2013, doi: 10.1155/2013/490946.

[213] A. M. Ross, Z. Jiang, M. Bastmeyer, and J. Lahann, "Physical Aspects of Cell Culture Substrates: Topography, Roughness, and Elasticity," *Small*, vol. 8, no. 3, pp. 336–355, Feb. 2012, doi: 10.1002/smll.201100934.

[214] T. P. Kunzler, T. Drobek, M. Schuler, and N. D. Spencer, "Systematic study of osteoblast and fibroblast response to roughness by means of surface-morphology gradients," *Biomaterials*, vol. 28, no. 13, pp. 2175–2182, May 2007, doi: 10.1016/j.biomaterials.2007.01.019.

[215] Ł. Kaniuk, Z. J. Krysiak, S. Metwally, and U. Stachewicz, "Osteoblasts and fibroblasts attachment to poly(3-hydroxybutyric acid-co-3-hydrovaleric acid) (PHBV) film and electrospun scaffolds," *Materials Science and Engineering: C*, vol. 110, p. 110668, May 2020, doi: 10.1016/j.msec.2020.110668.

[216] H.-C. Liang, W.-H. Chang, H.-F. Liang, M.-H. Lee, and H.-W. Sung, "Crosslinking structures of gelatin hydrogels crosslinked with genipin or a water-soluble carbodiimide," *J. Appl. Polym. Sci.*, vol. 91, no. 6, pp. 4017–4026, Mar. 2004, doi: 10.1002/app.13563.

[217] P. Sepulveda, J. R. Jones, and L. L. Hench, "Bioactive sol-gel foams for tissue repair," *J. Biomed. Mater. Res.*, vol. 59, no. 2, pp. 340–348, Feb. 2002, doi: 10.1002/jbm.1250.

[218] K. Deshmukh, T. Kovářík, T. Křenek, D. Docheva, T. Stich, and J. Pola, "Recent advances and future perspectives of sol–gel derived porous bioactive glasses: a review," *RSC Adv.*, vol. 10, no. 56, pp. 33782–33835, 2020, doi: 10.1039/D0RA04287K.

[219] R. A. Martin *et al.*, "Characterizing the hierarchical structures of bioactive sol–gel silicate glass and hybrid scaffolds for bone regeneration," *Phil. Trans. R. Soc. A.*, vol. 370, no. 1963, pp. 1422–1443, Mar. 2012, doi: 10.1098/rsta.2011.0308.

[220] P. Valerio, M. H. R. Guimaráes, M. M. Pereira, M. F. Leite, and A. M. Goes, "Primary osteoblast cell response to sol-gel derived bioactive glass foams," *J Mater Sci: Mater Med*, vol. 16, no. 9, pp. 851–856, Sep. 2005, doi: 10.1007/s10856-005-3582-5.

[221] G. Poologasundarampillai, P. D. Lee, C. Lam, A.-M. Kourkouta, and J. R. Jones, "Compressive Strength of Bioactive Sol-Gel Glass Foam Scaffolds," *Int J Appl Glass Sci*, vol. 7, no. 2, pp. 229–237, Jun. 2016, doi: 10.1111/ijag.12211.

[222] K. Schwartzwalder, and A. V. Somers, "Method of making porous ceramic articles," 3,090,094, May 21, 1963 [Online]. Available: https://patentimages.storage.googleapis.com/38/a2/dd/65c66c3a7cac4c/US3090094.pdf

[223] T. Fukasawa, M. Ando, T. Ohji, and S. Kanzaki, "Synthesis of Porous Ceramics with Complex Pore Structure by Freeze-Dry Processing," *Journal of the American Ceramic Society*, vol. 84, no. 1, pp. 230–232, Jan. 2001, doi: 10.1111/j.1151-2916.2001.tb00638.x.

[224] J. J. Beaman and C. R. Deckard, "Selective laser sintering with assisted powder handling," 4 938 816, Jul. 03, 1990 [Online]. Available: https://patents.google.com/patent/US4938816A/en

[225] J. Delgado, L. Serenó, K. Monroy, and J. Ciurana, "Selective Laser Sintering," in *Modern Manufacturing Processes*, M. Koç and T. Özel, Eds., Hoboken, NJ, USA: John Wiley & Sons, Inc., 2019, pp. 481–499. doi: 10.1002/9781119120384.ch20.

[226] F. P. W. Melchels, J. Feijen, and D. W. Grijpma, "A review on stereolithography and its applications in biomedical engineering," *Biomaterials*, vol. 31, no. 24, pp. 6121–6130, Aug. 2010, doi: 10.1016/j.biomaterials.2010.04.050.

[227] C. W. Hull and S. Gabriel, "APPARATUS FOR PRODUCTION OF THREE-DMENSONAL OBJECTS BY STEREO THOGRAPHY," 4 575 330, Mar. 11, 1986 [Online]. Available: https://patentimages.storage.googleapis.com/5c/a0/27/e49642dab99cf6/US4575330.pdf

[228] P. Tesavibul *et al.*, "Processing of 45S5 Bioglass® by lithography-based additive manufacturing," *Materials Letters*, vol. 74, pp. 81–84, May 2012, doi: 10.1016/j.matlet.2012.01.019.

[229] N. Kooy, K. Mohamed, L. T. Pin, and O. S. Guan, "A review of roll-to-roll nanoimprint lithography," *Nanoscale Res Lett*, vol. 9, no. 1, p. 320, Dec. 2014, doi: 10.1186/1556-276X-9-320.

[230] D. Qin, Y. Xia, and G. M. Whitesides, "Soft lithography for micro- and nanoscale patterning," *Nat Protoc*, vol. 5, no. 3, pp. 491–502, Mar. 2010, doi: 10.1038/nprot.2009.234.

[231] X.-H. Hu and S. Xiong, "Fabrication of Nanodevices Through Block Copolymer Self-Assembly," *Front. Nanotechnol.*, vol. 4, p. 762996, Feb. 2022, doi: 10.3389/fnano.2022.762996.

[232] A. H. Hofman, G. Ten Brinke, and K. Loos, "Hierarchical structure formation in supramolecular comb-shaped block copolymers," *Polymer*, vol. 107, pp. 343–356, Dec. 2016, doi: 10.1016/j.polymer.2016.08.021.

Annexes

# Annex 1: Bone filling synthetic scaffolds fabrication methods

1) Common techniques

The common technologies for the fabrication of scaffolds included all the manufacturing method that are not based on the reproduction of a virtual model by CAD. These methods allow to produce glass, glass-ceramic and polymer/glass composite scaffolds. Among the numerous conventional techniques, sol-gel foaming, organic phase burning-out, foam replication and freeze casting are going to be detailed.

a) Sol-gel foaming

The sol-gel foaming method was first introduced by Sepulveda et al. in the beginning of the 21st century [217]. This method has been developed because of the lack of melt-derived BG that could withstand the sintering process without crystallization. Sol-gel foaming is a method that combines mechanical frothing with sol-gel technology, a chemical-based wet synthesis approach that transforms a solution containing ceramic precursors (sol) into a network of covalently bound silica by inorganic polymerization processes. In the process, to tune the pore size and organization, a surfactant is added which also helps to stabilize the bubble formation which eventually creates the pores [84], [132]. Furthermore, the gelation step on the process can be long, up to a few days. Therefore, an accelerator agent is added to the sol to reduce the gelation time. Once the gelation is induced, it is possible to cast the mixture in molds to give a certain shape to the scaffold. The gels are then allowed to age then dry and finally are stabilized at high temperature. A representation of the process can be found in **Figure 49**. The resulting scaffold from this process have an interconnected macropore (10 to 500 μm) and mesopore (2 to 50 nm) structure which is believed to be a beneficial structure for the tissue and cell response because it mimics their natural environment [79], [84], [132], [218].

142
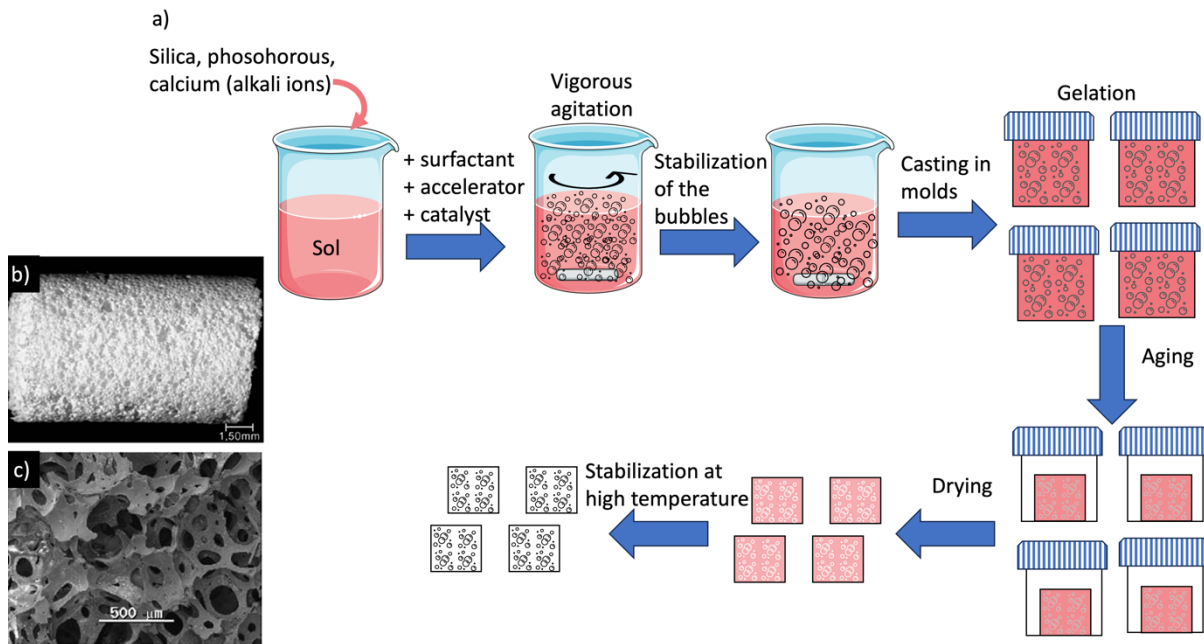
Figure 49. a) Schematic representation of the sol-gel process, adapted and modified from [219], b) macroscopic view of a sol-gel foam and c) SEM image of the microstructure of the sol-gel foam. Photo and SEM images adapted and modified from [220].

The structure of sol-gel based foams presents real advantages when considering the cell response to the material since the structure of the scaffold mimics closely the natural structure of bone. However, the biggest drawback of these materials is their intrinsic brittleness due to their nanoporous porosity which does not make them suitable for load barring applications [98, 146]. However, recent advances have allowed to produce sol-gel based scaffolds with a compressive strength of 5 MPa which would make those scaffolds suitable for load-barring applications [221].

b) Organic phase burning-out

In this method, the particles of BG are mixed with a sacrificial phase (a porogen), that will be burned-out during sintering to produce the porous structure. The porogen particles are usually natural (e.g. starch, rice husk) or synthetic (e.g. polyethylene particles) polymers [79], [132]. Typically, the BG particles and porogen are mixed and molded into a green-body and this green-body will then be sintered to allow the BG particles to link together while the porogen will be eliminated leaving pores behind. The porosity can be tailored by adapting the porogen quantity but it is complicated to obtain high

porosity (>70%) scaffolds with this method [132]. However, the higher the porogen concentration the higher the porosity and the higher the risk of cracks formation. Indeed, with a high content of porogen, the gas formation will be important which can lead to the formation of cracks in the scaffold [84].

c) Foam replication

Researchers began using polymeric foams as templates for creating biomedical scaffolds in order to attain a higher level of porosity with interconnecting macropores. It is well established that it is possible to create polymeric foams with extremely controlled 3D porous architecture with up to 90% of void. The principle of the foam replication method is based on using a natural (e.g. marine sponges) or synthetic (e.g. polyurethane) sponge as template and coat it with a glass slurry (containing a binding agent like polyvinyl alcohol) and then consolidate the structure. The foam replication method can be achieved via two different routes: 1) coating the foam template and not removing it, therefore obtaining a composite scaffold with a polymeric core coated with glass, and 2) polymer foam replication which consist of the reproduction of the foam that is only used as a template for the inorganic phase during sintering. In the later method, the composite, made of the foam coated with the glass slurry, is subjected to a double-thermal treatment to achieve the full burn-out of the polymer phase and consolidation of the glass phase [84], [132]. This polymer foam replication method, also called sponge replica method, has been patented by Schwartzwalder and Somers in 1963 [222]. Thanks to its simplicity of implementation, since it is usable with any ceramic that can be appropriately dispersed in a solution, the sponge replica method has become known as the most popular and efficient technique for creating ceramic scaffolds that resemble foam for tissue engineering. One of the greatest advantages of this method is that the polymer sponge used as template can be precisely shaped to match the bone defect characteristics which means that, in ideal circumstances, it is possible to produce personalized scaffolds according to the patients' needs [84]. Nevertheless, the scaffold's low strength, which is typically in the range described for trabecular bone, restricts its usage to low-load bearing applications [79].

d) Freeze casting

The porous structure of the scaffold can be created by utilizing the creation of ice crystals as a porogen agent rather than an organic template. Fukasawa et al. [223] invented this process in order to produce

porous industrial ceramics in an environmentally acceptable manner. The freeze casting method consists of a stable colloidal suspension of glass particles poured in mold and subsequently quickly frozen. The cooling process is typically not the same in all directions and therefore results in the creation of oriented and elongated ice crystals [132]. Sublimation under vacuum is used to extract the frozen solvent at a quite "cold" temperature of about -20°C. This step is critical since an uncontrolled sublimation of the solvent might destroy the porous architecture of the scaffold. Following a drying step, the obtained scaffolds are sintered to consolidate the structure. This method has successfully been used to produce porous polymer, ceramic and glass scaffolds [79], [132]. Compared to a scaffold with a random 3D architecture, the scaffolds obtained by freeze casting, thanks to the oriented structure of the pores, allow to have a material with a higher strength in the direction of the orientation. It has been reported in hydroxyapatite scaffolds for example that, compared to a scaffold with a random pore organization, the scaffold has a strength up to 4 times higher in the direction of the orientation of the pores and is similar to the highest strength of human trabecular bone [79], [164]. The major drawback of this method is that the scaffolds obtained from aqueous solutions only allow to obtain small pores, in the range of 10 to 40 µm, which is considered too small for appropriate tissue ingrowth. However, this can be tackled by using a mixture of water and organic solvent or organic solvent alone, like 1,4-dioxane or camphene [79], [132].

Conventional techniques are usually simple to implement to produce glass-based scaffolds. However, they do not allow for a precise control of the porosity of each material prepared or the preparation of patient specific scaffolds. Furthermore, the use of organic solvent is a huge downside of some of those methods since organic solvents are deadly to humans, therefore limiting their development industrially. Other methods, regrouped under the terms "advance techniques" or "additive manufacturing" and are available to researchers to produce porous scaffolds with a highly controlled and reproducible structure. Those methods will be described in the following section.

2) Advance techniques

Additive manufacturing technologies (AMT) can also be referred to as "rapid prototyping" (RP) or "solid freeform fabrication" (SFF). AMTs provide the ability to carefully manage how an object is put together "layer by layer" or "piece by piece", giving researchers and industrial companies the chance to design shapes and details that are not possible with the conventional technologies. AMTs, compared to the conventional methods, offer a tremendous amount of customization, industrial scalability, and flexibility [132]. For those methods, it is necessary to start with a CAD or, sometimes when it is possible, a computed tomography (CT) model of the object we meant to replicate. It is then divided into layers along one of its axes, and the AMT constructs the object by adding each layer one at a time. Using AMTs, it is possible to produce all kinds of materials based on metals, polymers, ceramic, glasses and even living cells [132].

AMTs have a lot of potential in the biomedical industry because they can create devices that are customized for individual patients. In addition, unlike conventional methods previously mentioned, they frequently do not employ harmful solvents that could get trapped in the structure. AMTs were not initially widely employed in biomedicine due to the expensive equipment investment costs, but recently, they have become more widely available and are now used, particularly in maxillo-facial surgery and dentistry [132].

In this section only a few of the available methods in additive manufacturing will be described, namely selective laser sintering (SLS), stereolitography and robocasting.

a) Selective laser sintering (SLS)

SLS is a method developed and patented by Beaman et al. in 1990 [224]. Briefly, using laser energy, the SLS selectively sinters powder into a predetermined shape, layer by layer. The machinery is composed of a computer that controls the system, a laser with a scanning mechanism made of mirrors, a system to disperse the material, the feeding platform, and the construction platform (**Figure 50**). An inert environment is necessary during the entire process due to the high propensity for oxidation [225].

In a simplified manner, the SLS starts with a CAD either created or imported from medical data from a scanner like computer tomography (CT) or magnetic resonance imaging (MRI) for instance. The model

is then imported to the machine and roller starts to spread a controlled amount of powder from the feeding platform to the building platform. The roller also allows to level the powder bed on the building platform to obtain a compact and homogeneous layer. In the process, the powder is also preheated bellow the melting temperature, by either infrared or resistive heaters for instance, which is crucial to reduce shrinkage, thermal distortion and laser power requirements [225]. The next step is to generate a high-power laser beam that scans a specific area that corresponds to the surface of the sliced CAD model. A computer-controlled laser beam that is integrated with a scanning system heats the area being irradiated to the point where the material's particles partially or completely melt, yielding a stable two-dimensional part. When a particular layer has been processed to completion, the spreading mechanism deposits a new layer of powder in the building platform while the material platform moves up and the building platform moves down [225]. The process is then repeated until the whole CAD model has been sintered.
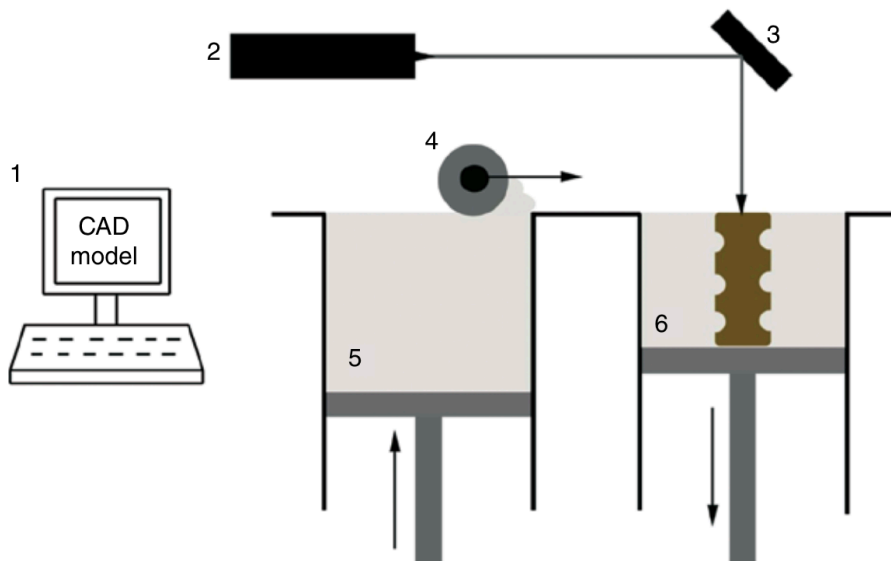

Figure 50. Schematic of the basic components of selective laser sintering. 1) computer, 2) laser, 3) scanning mirrors, 4) roller, 5) material platform, 6) building platform [225].

With this method, any powder material capable of absorbing electromagnetic radiation can be used to produce part or whole products. The simplicity of the process of the SLS can shorten the production time and costs compared to traditional technologies. Furthermore, SLS allows to produce much more complex structures than the conventional method with minimal waste [225]. However, despite its

advantages there are some limitations to the use of SLS. Indeed, theoretically, all powdered materials can be used with SLS but in reality, that is not the case. Indeed, some materials, like metals, are not necessarily produced in powdered form and thus need to be crushed before use. Furthermore, the particle size must be carefully controlled since it influences tremendously the processability ans sinterability of the material[225]. Using SLS, materials based on nano-HA, β-TCP as well as ceramic/polymer composites have been prepared [84], [225].

b) Stereolitography (SLA)

SLA was the first SFF technology commercially available and is considered to be among the most powerful AMT available on the market with the finest resolution – it is possible to produce materials with features as small as 20 μm [132], [226]. Furthermore, this method can be used with various materials like polymers, ceramics, glasses and even hydrogels or cells. As of today, there are two different approaches for SLA, either top-down or bottom-up. The first one developed and patented by Hull et al. in 1986 [227] consists a design lighted on the surface of a photocurable resin using a computer-controlled laser beam or a digital light projector with a computer-driven building stage. This causes the resin to solidify to a specific depth, which causes it to attach to the support platform. The platform is then moved away from the surface and the built layer is then recoated with the liquid resin. The second layer is then cured and so on until the whole structure of the scaffold has been created [226]. On the other hand, in the top-down method, the platform rises while the polymer is lit from the transparent bottom of the vessel. The set-ups for both methods are described in **Figure 51**. It provides a number of benefits over the earlier method, including the requirement for less feedstock, protection from oxidation because the object is submerged, and the absence of the need to recoat the surface [132]. Following the curation of the resin and the removing of the excess material, the 3D construct produced can be sintered to obtain the final object [84].
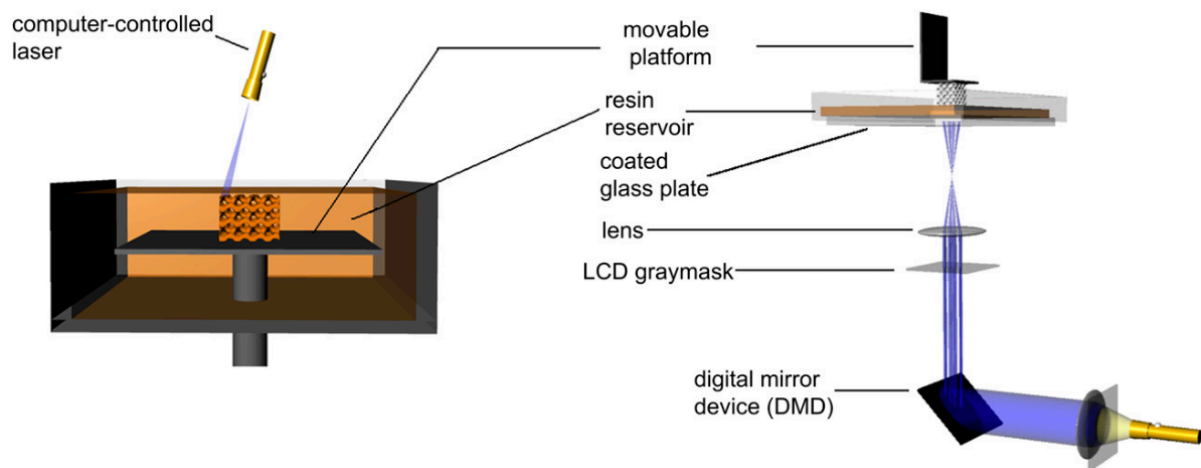
Figure 51. Schematic of the two types of stereolitography. Left: a bottom-up system with scanning laser. Right: a top-down setup with digital light projection [226].

The major limitation of the SLA method is linked to the photocurable resins. Indeed, there are only few options of resins that allow to have a sufficiently low viscosity yet the ability to solidify quickly after the photo irradiation. The most commonly used resins in SLA include monomers and low-weight oligomers. However, those resins revealed to become glassy, brittle, and rigid materials. Nevertheless, researchers are constantly developing new promising elastomeric resins [132].

SLA has been extensively used with HA or calcium phosphates to produce scaffolds for hard tissue engineering [84]. In 2012 Tesavibul et al. [228] reported on the fabrication of scaffold based on 45S5 Bioglass® with stereolitography. They produced a scaffold with a porosity close to 500 μm, similar to that of trabecular bone, and a compressive strength of 0.33 MPa, close to the structures that can be obtained from foam replica methods.

# Annex 2: Fabrication methods of porous polymeric membrane

1) Top-down approaches

    a) Photo nanoimprint lithography

Photo nanoimprint lithography, or photolithography, is based on the principle of nanoimprinting that uses of a stamp or mold as template which is pressed against a deformable resist layer that has been formed on a substrate, such as a silicon (Si) wafer or a metallic surface. In photolithography, a photoresist is used and cured using UV to induce the resist solidification by polymer crosslinking (**Error! Reference source not found.**) [152]. This method has several advantages, notably it can be conducted at room temperature and the resists does not need to be very viscous which allows it to fill in the master mold cavity quite fast and result in a high process throughput [229]. Photolithography is one of the most used conventional method to fabricate porous membrane and porous films with a resolution of less than 100 nm can be obtained with this approach [153].

However, the technique presents some limitations. Notably, it requires the use of a clean room to control the presence of dusts in the atmosphere which increases the costs considerably. Furthermore, the chemical used have an important toxicity which then influences the potential grafting of biomolecules at the material's surface [153]. Furthermore, the creation of free-standing permeable membranes with this method is still difficult because the pores frequently retain a very thin layer at the bottom, and the membrane can be damaged by separation from the substrate. This issue can be overcome by adding a sacrificial layer between the polymer and the substrate. In addition, in the nanoimprinting lithography process, the master mold is one of the critical factors to control since its accuracy and definition are the key to define the pattern on the imprinted polymer [152]. Nevertheless, the fabrication of such master mold is quite expensive due to the materials and precision required to fabricate them [152], [153].
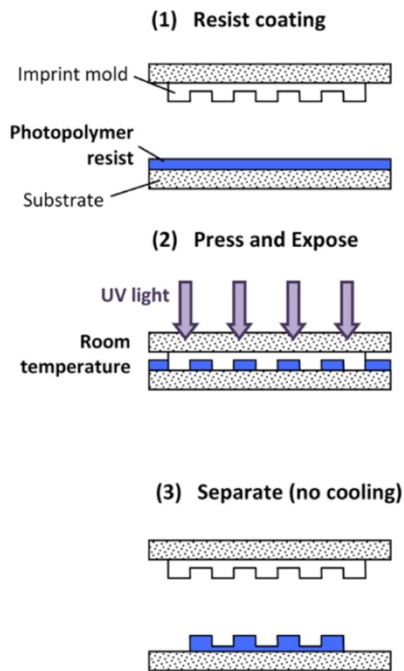
Figure 52. Schematic of a typical photolithography process. Adapted from [229]

b) Soft lithography

Soft lithography regroups several techniques that, contrary to photolithography, are based on the printing, molding, and embossing using an elastomeric stamp as template. Some example of soft lithography techniques includes microcontact printing (µCP), replica molding (REM), micro-molding in capillary (MIMIC) or solvent-assisted micro-molding (SAMIM) for example[153], [230] (**Error! Reference source not found.**). The most important element of soft lithography is the elastomeric stamp with the patterns as embossment structures on its surface. Typically, a liquid precursor is cast against a master whose surface has been imprinted with the complimentary structures to create the stamp [230]. Soft lithographic techniques allow to produce surfaces with a molecular-level detail, particularly thanks to the stamps that are mainly produced from poly(dimethyl siloxane) (PDMS) whose elastomeric properties allows it to conform to a surface with an atomic-level contact precision [230]. However, one downside of the use of such elastic polymer is its easy decomposition, therefore necessitating a frequent replacement. Nevertheless, one very advantageous property of the technique is the possibility to use it in ambient environment, therefore reducing the costs [153].
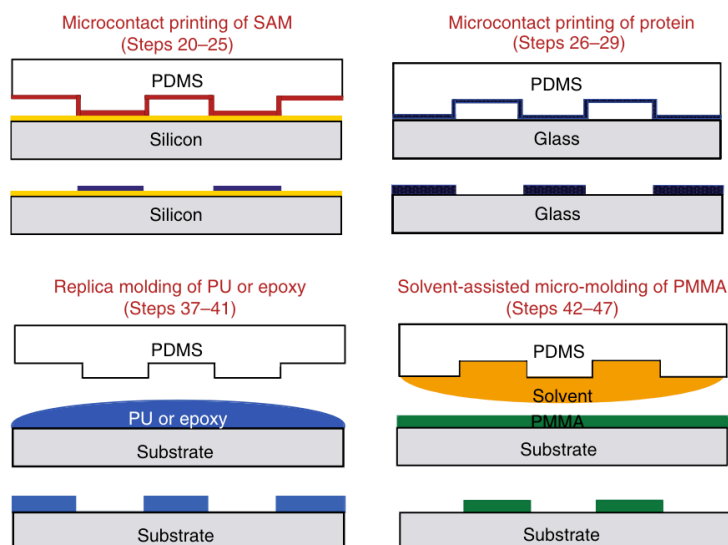
Figure 53. Schematic of the major soft lithographic techniques: microcontact printing (µCP), replica molding (REM) and solvent-assisted micro-molding (SAMIM). SAM = self-assembled monolayer, PU = polyurethane, PMMA = Poly(methyl methacrylate) Adapted from [230]

Accurate and small designs can be produced using any lithographic technique. However, it is currently difficult to fabricate larger features with nano-size resolution for commercialization and other applications. Furthermore, although soft lithographic techniques allow a very precise control over the size and distribution of the porous pattern, they lack flexibility. Indeed, if the pattern needs to change, it is necessary to produce new mast molds which is costly. In addition, the geometry of the membrane is restricted to a flat-plane because it is difficult to imprint on spherical objects due to the process' constraints [152], [153].

2) Bottom-up technique

a) Block copolymer (BCP) self-assembly

Block copolymer (BCP) self-assembly, also called self-assembled non-solvent induced phase separation (SNIPS), is a method using two or more chemically distinct homopolymers that are covalently linked together in the form of a BCP, i.e. block A and block B linked through a covalent c bond in this manner A-c-B [152]. Phase separation happens during self-assembly to reduce the contact energy between the segments of the copolymer due to their thermodynamic incompatibility. Self-assembly typically takes place in either a pure block copolymer or a composite made of a block

copolymer and other elements. BCP can be used to create porous membranes in two ways: (1) as a template for pore development, or (2) as the framework for the membrane.

As the pore template, the BCP is used in combination with other components that will be left after the BCP removal. For instance, those substances can be what is called "prepolymers" or other polymer precursors of homopolymers different from that of the BCP that will interact with the BCP. Only through non-covalent interactions [152]. These methods, although it can be interesting to produce inorganic materials, based on silica or carbon for instance, it has several limitations. The first one is that the BCP must be amphiphilic with a domain that must interact non-covalently with the prepolymers. The second is that the prepolymers must be able to crosslink further together and for a stable structure without affecting the BCP that should also have the possibility to be easily removed. Often the prepolymers are thermally treated to stabilize the structure which removes the BCP at the same time [152].

In contrast to the method that uses BCP as the pore template, in which the BCP is totally removed for pore formation, when BCP is used as the membrane framework, a portion of the BCP is used to build the porous membrane and only one of the blocks is removed, in some cases with additional components [152].

Through BCP self-assembly, a variety of pore morphology can be obtained. This is governed by three different parameters inherent to the BCP: 1) the degree of polymerization (N), 2) the volume fraction of block A (f_A) and what is called the Flory-Huggins interaction parameter of two blocks (χ). While N and f_A are determined through BCP synthesis, χ depend on the nature of the monomer combination chosen [231]. Those parameters can be represented in a theoretical phase diagram using the self-consistent field theory (SCFT), that can allow to predict how a deblock A-c-B copolymer will arrange (**Error! Reference source not found.**).
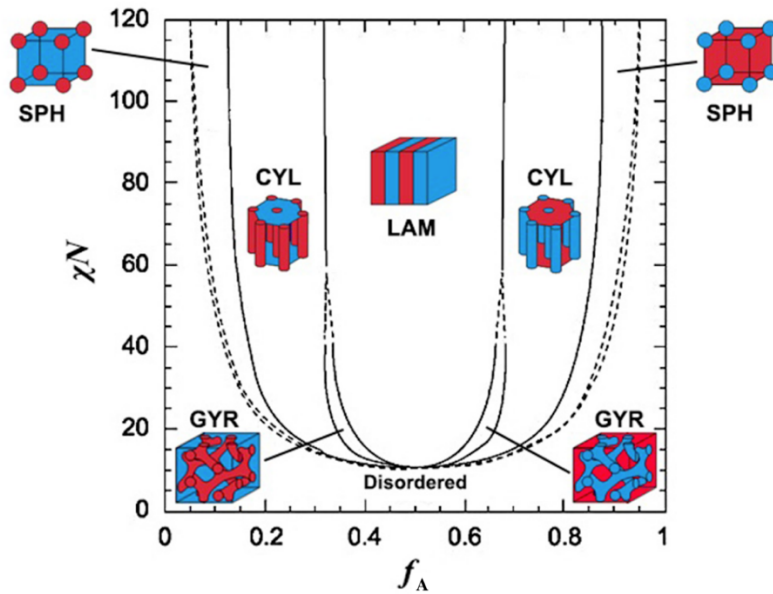
Figure 54. Theoretical diagram representing the possible organizations of diblock copolymer during BCP self-assembly calculated using the SCFT. [232]

Despite the advantages of BCP self-assembly, such as versatility in surface chemistry and fine control of pore size in the low-nanoscale region, obtaining pores larger than 100 nm in diameter remains difficult. In addition, it is extremely challenging to create cylindrical pores across the membrane. Furthermore, due to the laborious and drawn-out preparation steps, this technique further struggles for scale-up [152].

Appendices

Appendix 1
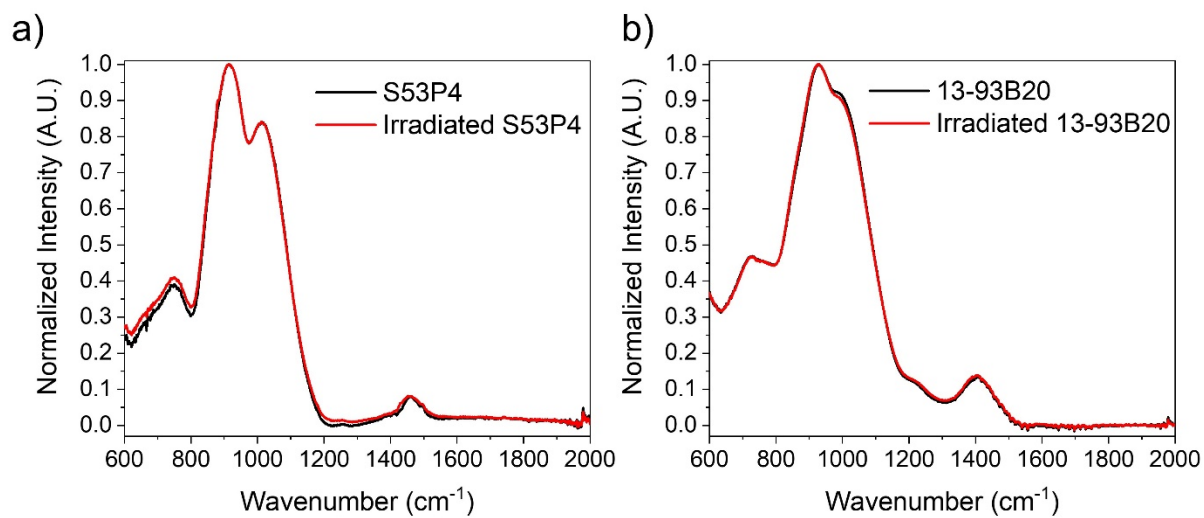
Appendix 1. FTIR-ATR spectra of S53P4 (a) and 13-93B20 (b) before (black curve) and after (red curve) irradiation.

Publications

Polymer-Based Honeycomb Films on Bioactive Glass: Toward a Biphasic Material for Bone Tissue Engineering Applications

A. Deraine, M. T. Rebelo Calejo, R. Agniel, M. Kellomäki, E. Pauthe, M. Boissière, and J. Massera*

Cite This: https://doi.org/10.1021/acsami.1c03759

Read Online

ACCESS | Metrics & More | Article Recommendations | SI Supporting Information

ABSTRACT: The development of innovative materials for bone tissue engineering to promote bone regeneration while avoiding fibrous tissue infiltration is of paramount importance. Here, we combined the known osteopromotive properties of bioactive glasses (BaGs) with the biodegradability, biocompatibility, and ease to shape/handle of poly-L-co-D,L-lactic acid (PLDLA) into a single biphasic material. The aim of this work was to unravel the role of the surface chemistry and topography of BaG surfaces on the stability of a PLDLA honeycomb membrane, in dry and wet conditions. The PLDLA honeycomb membrane was deposited using the breath figure method (BFM) on the surface of untreated BaG discs (S53P4 and 13-93B20), silanized with 3-aminopropyltriethoxysilane (APTES) or conditioned (immersed for 24 h in TRIS buffer solution). The PLDLA membranes deposited onto the BaG discs, regardless of their composition or surface treatments, exhibited a honeycomb-like structure with pore diameter ranging from 1 to 5 μm. The presence of positively charged amine groups (APTES grafting) or the precipitation of a CaP layer (conditioned) significantly improved the membrane resistance to shear as well as its stability upon immersion in the TRIS buffer solution. The obtained results demonstrated that the careful control of the substrate surface chemistry enabled the deposition of a stable honeycomb membrane at their surface. This constitutes a first step toward the development of new biphasic materials enabling osteostimulation (BaG) while preventing migration of fibrous tissue inside the bone defect (honeycomb polymer membrane).

KEYWORDS: bioactive glass, honeycomb membrane, biphasic material, bone tissue engineering, in vitro stability
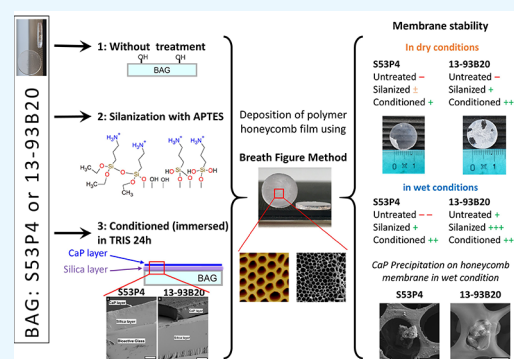
1. INTRODUCTION

It is commonly accepted that bone tissue regeneration requires innovative materials, with various properties, i.e., biocompatibility, osteoconductivity/osteoinductivity, while promoting angiogenesis.[1−3] In addition, newly developed biomaterials should have a structural organization mimicking the natural bone. One challenge that is often encountered when using bone grafts (natural or synthetic) is the invasion of implants by soft/fibrous tissue before proper bone regeneration occurs. This is due to the faster proliferation rate of cells involved in the wound healing process (e.g., fibroblasts) compared to that of the bone cells.[4] Therefore, invasion of the bone defect by soft tissue will ultimately lead to incomplete bone regeneration.[5,6] To prevent this negative outcome, membranes have been used to cover the bone defect and thus prevent fibrous tissue ingrowth.[5,7] Many types of membranes have been developed, either made from synthetic polymers (either degradable, i.e., aliphatic acids such as poly-L-lactic acid (PLLA), poly-L-lactide-co-glycolide (PLGA) or not degradable such as polytetrafluorethylene (PTFE)) or natural polymers (collagen or chitosan, for example).[5,8] As of today, the majority of commercially available membranes are based on synthetic degradable polymers or collagen.[9] These membranes exhibit

high biocompatibility, favor cell adhesion, and do not necessitate to be retrieved during a second surgery. However, they have an unpredictable degradation rate, leading to a mismatch between the membrane degradation and the new bone formation rate.[9] There is still important work to be done to achieve the production of the ideal protective membrane, but there is a consensus on their required properties. The ideal barrier membrane should (1) be biocompatible, (2) be cell-occlusive, (3) allow space-making ("define the volume of bone that can be regenerated"[10]), (4) allow tissue integration, (5) be easy to handle, and (6) have an appropriate pore size and pore interconnectivity to facilitate bone regeneration but preventing excessive fibrous tissue penetration.[5,10−12] While initially the membrane was only used to direct the bone regeneration (without the use of bone grafts), the review by Dimitriou et al.[5] reports the use of barrier membranes associated with a bone

graft (natural or synthetic) since the early 2000s. Since then, researchers have focused on understanding the impact of using a membrane in addition to the bone graft on bone regeneration.[13−16] In such cases, the membrane and the graft are two materials that are not in direct contact. While the use of a membrane alone protects the defect from fibrous tissue ingrowth, the addition of a bone graft underneath the membrane was associated with a faster bone regeneration.[16−18]

In the present study, a proof of concept for a new biphasic material where a biodegradable polymer-based barrier membrane was directly deposited on a synthetic osteostimulative substrate is proposed for the first time, to the best of the authors' knowledge. One phase, made of a honeycomb-structured poly-L-co-D,L-lactic acid (PLDLA) barrier membrane, providing protection from fibrous tissue ingrowth while still allowing exchange of ions and nutrients and a second phase, made of dense bioactive glasses (BaG), promoting bone regeneration. Indeed, such approach could allow the design of patient-specific graft providing a 2 in 1 solution, easy to use, in complex surgery for large bone defect (e.g., mandibulectomy, wide palatal defect, etc.). PLDLA was chosen as the material forming the barrier membrane. As mentioned previously, membrane porosity must be carefully controlled as it is one of the key factors to achieve good tissue integration while avoiding fibrous tissue ingrowth. One successful method to control the membrane porosity is the breath figure method (BFM).[19] This method allowed us to create highly organized honeycomb-like porous surfaces through a simple process. In short, (1) the desired polymer is mixed with a volatile water-immiscible solvent, (2) the solution is cast on a substrate under a high relative humidity (RH) airflow which allows water condensation at the polymer solution surface, while the solvent evaporates (3) when water and solvent have completely evaporated, a membrane with a highly ordered porous surface is formed.[19,20] Its low cost and its ease of implementation make the BFM a widely used method to produce porous polymer membranes.[19,21] Furthermore, it has been shown that membranes prepared using BFM and having appropriate pore sizes can adequately support cell adhesion and proliferation.[21−23] In addition, in this study, BaG was chosen as the substrate onto which the membrane was deposited. BaGs have been extensively studied for their ability to promote osteoconduction or even osteoinduction.[24,25] The composition of BaGs can be tailored, to ensure the release of the most therapeutically relevant ions for the intended application.[26] Over the years, BaGs have been found to be osteostimulative, to favor angiogenesis,[27] and to have antimicrobial properties.[28,29] Due to their high interest in bone regeneration, the surface chemistry of BaGs, as well as their ability to be functionalized in view of increasing the adsorption rate of biomolecules or to increase the connectivity between the glass and the polymeric phase, have been widely studied.[30−33]

In this manuscript, we reported the deposition of a PLDLA membrane, processed by BFM, onto a bioactive glass. PLDLA was chosen for its ease of processing into a honeycomb membrane with controlled surface porosity,[19,34] while BaG was used for its bioactivity. Two substrates have been studied, i.e., S53P4 and 13-93B20. The S53P4, also known as BoneAlive S53P4, is a well-known and widely used silicate BaG which has the US Food and Drug Administration approval,[35,36] while the glass 13-93B20 is an experimental glass composition already reported as part of composites in ref [37]. The impact of substrate surface physicochemical properties (surface charge,

ion release, etc.) on the interfacial stability of the membrane was assessed. The aim of this work is to design a promising biphasic material that can retain its bioactivity (through controlled ion release) while maintaining the membrane integrity. The controlled pore size of the membrane and its stability over time will expectedly allow ion transfer while preventing fibroblasts from migrating within the graft.

2. MATERIALS AND METHODS

2.1. BaG Material Synthesis and Surface Treatments. S53P4 and 13-93B20 BaG were prepared from analytical grade K_2CO_3 (Alfa Aesar, Thermo Fischer, Kandel, Germany), Na_2CO_3, $NH_4H_2PO_4$, $(CaHPO_4)(2(H_2O))$, $CaCO_3$, MgO, H_3BO_3 (Sigma-Aldrich, Saint-Louis, MS), and Belgian quartz sand. The nominal oxide compositions of the experimental BaGs are presented in Table 1 in mol %.

Table 1. Composition of the BaGs in mol %

glass	mol %						
	Na_2O	CaO	P_2O_5	SiO_2	K_2O	MgO	B_2O_3
S53P4	22.66	21.77	1.72	53.85			
13-93B20	6.0	22.1	1.7	43.7	7.9	7.7	10.9

The reagents were melted in a platinum crucible at 1450 °C in an electrical furnace. The molten glass was then cast into a preheated graphite mold to obtain a rod with a diameter of 14 mm. The glass rods were then annealed overnight at 500 °C and let to cool down to room temperature. The rods were then cut into 2 mm thick discs and polished with SiC paper (grit #320, #500, #800, #1200, #2400, and #4000, from Struers, Copenhagen, Denmark). All samples were dried and kept in a desiccator until further use.

Membranes were directly deposited onto untreated or surface-modified BaG discs. Discs with both BaGs composition were surface treated by either silanization or conditioning. The surface treatment protocols are as follows.

2.1.1. Silanization with 3-Aminopropyltriethoxysilane (APTES). Polished BaG discs were silanized with 3-aminopropyltriethoxysilane (APTES) (Thermo Fischer Scientific, Germany), according to the protocol used by Massera et al.[38] Briefly, the BaG discs were first washed for 5 min in acetone and distilled water (three times), in a sonicating bath. After washing, the BaG discs were immersed in ethanol (150 mL) with APTES (70 μL) for 6 h and, successively, dried at 100 °C for 1 h. To remove the loosely bound APTES, the BaG discs were then washed again in ethanol for 5 min in the sonicating bath and further dried for 30 min at 100 °C.

2.1.2. Conditioning. Polished BaG discs were immersed in TRIS buffer solution and incubated at 37 °C for 24 h. TRIS solution was prepared from Trisma base and Trisma HCl (Sigma-Aldrich, Saint-Louis, MS) at pH 7.38 ± 0.02 at 37 ± 0.2 °C. After incubation, the solution was removed, and the BaG discs were allowed to dry in a fume hood overnight before membrane deposition.

2.2. Honeycomb Membrane Deposition. Honeycomb membranes were fabricated from a 10 mg·mL⁻¹ solution of 96/04 L-lactide/D-lactide copolymer (PLDLA) containing 0.1 mg·mL⁻¹ of the surfactant dioleoyl phosphatidylethanolamine (DOPE) in chloroform. PLDLA purified, medical grade, PURASORB PLD 9620 was purchased from Corbion Purac, The Netherlands and DOPE from Sigma-Aldrich, Japan.

The honeycomb membranes were produced by the BFM as described in Figure 1 and as previously reported in ref [19]. Briefly, the polymer solution was deposited drop by drop onto BaG discs (untreated, silanized, and conditioned) and then the solvent was allowed to evaporate in a humidity chamber at 80 ± 5% RH, under airflow. The samples were air-dried at room temperature and then washed twice with 70% ethanol to remove the surfactant. Samples were air-dried again and stored in a desiccator until further use.
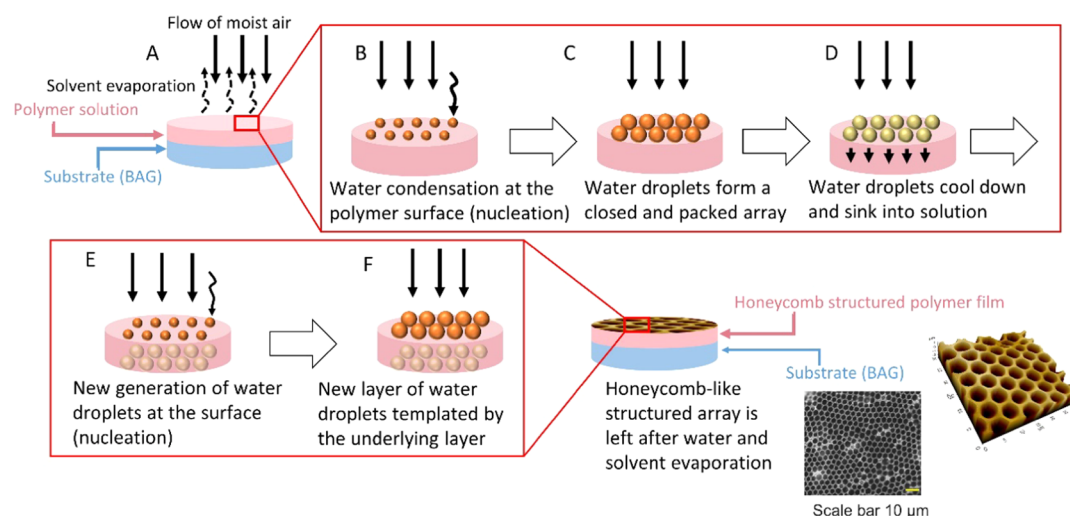
Figure 1. Schematic of the membrane deposition process, using the BFM. (A) Deposition of the polymer solution on the substrate (BaG) and placing the construct under a flow of moist air, (B) water droplets start to condense at the surface of the polymer solution, (C) water droplets grow and form a closed and packed array, (D) droplets cool down and sink into the solution, (E) new generation of water droplets is formed at the surface, (F) process continues until the end of the reaction under the flow of moist air, and each new generation of water droplets is templated by the underlying layer.

Table 2. ζ-Potential of Untreated, Silanized, and Conditioned BaG Disc Surfaces at pH 7 (Streaming Potential)

	S53P4			13-93B20		
	untreated	silanized	conditioned	untreated	silanized	conditioned
ζ-potential (mV)	-47.8 ± 0.5	-30.6 ± 2.0	-16.9 ± 0.4	-53.2 ± 1.9	-12.2 ± 0.4	-15.5 ± 0.4

2.3. Material Characterization. *2.3.1. ζ-Potential.* An electrokinetic analyzer for solid surfaces (SurPASS 3, Anton Paar, Austria) was employed to measure the ζ-potential of untreated and treated BaG discs by means of the streaming potential technique.[39] An adjustable gap cell was used for the measurements, and a 1 mM KCl solution was used as the electrolyte. Measurements were carried out at pH = 7.

2.3.2. Shear Stress Test. Two aluminum plates were clamped to a TA1 texture analyzer (Lloyd materials testing, AMETEK, Pennsylvania) equipped with a 20 or 100 N load cell, depending on the force to be applied. The specimen to be tested was fixed in-between the plates, by solvent-free double-sided tape (tesa ECO FIXATION). Freshly prepared samples were used for the measurement. Shear force on the membrane was created by pulling the upper plate at 1 mm·min^{-1} while the bottom aluminum plate remained fixed. The design of the setup can be found in ref 40. The test was performed on five to seven samples.

2.3.3. BaG Disc Surface Topography and Composition. Scanning electron microscopy–energy-dispersive X-ray spectroscopy analysis (SEM/EDX) was conducted using a Gemini SEM 300 (Carl Zeiss, Germany) equipped with an EDS Bruker Quantax (Bruker) for EDX spectroscopy. Samples were metalized with nickel (for EDX) 4 times 30 s at 30 mA (for EDX analysis) or with a 4 nm thick platinum layer using a Leica ACE600 (Leica, Wetzlar, Germany) (for SEM imaging).

2.3.4. Structural Property. The infrared (IR) absorption spectra of untreated or treated BaG discs were recorded using a Bruker Alpha FTIR in attenuated total reflectance (ATR), to see the effect of treatments on their surface chemical properties. All IR spectra were recorded within the range 400−4000 cm^{-1} with a resolution of 2 cm^{-1} and 64 accumulation scans. All spectra were corrected for Fresnel losses and normalized to the band with maximum intensity.

2.3.5. Stability Tests. The membrane stability was studied in dry and wet conditions.

2.3.5.1. In Dry Conditions. Samples ($n = 3$) were dried and kept at room temperature in a desiccator (20−40% RH) inside multiwell plates for up to 4 weeks. Topographical features of honeycomb films were analyzed using an atomic force microscope (AFM) XE-100 Park

System Corp. An image size of 30 μm × 30 μm was scanned in noncontact mode, under air and at room temperature. Acquired images were analyzed using image analysis software (XEI, Park System). The pore size was estimated from the AFM images using the software Fiji.

2.3.5.2. In Wet Conditions. Samples ($n = 12$) were immersed in 5 mL of TRIS buffer solution before being incubated at 37 °C in static conditions (without agitation). The buffer solution was refreshed at 3, 6, 24, 48 h, 5, 7, 9, 14, and 21 days to prevent saturation of the immersion solution with ions released from the BaG substrate. The assembly (membrane/BaG disc) integrity was assessed by counting the number of membranes that detached (partially or totally from the substrate) during the immersion period. At 28 days (4 weeks), samples were collected and left to dry in a fume hood overnight before further analysis.

All samples were imaged by AFM and SEM/EDX, as described above.

At each time point (3, 6, 24, 48 h, 5, 7, 9, 14, 21, and 28 days), 1 mL of the immersion solution was collected to quantify the change in ion concentration over the incubation period. Inductively coupled plasma-optical emission spectroscopy (ICP-OES) analysis was conducted with an Agilent 5110 instrument (Agilent technologies) equipped with a SPS 4 autosampler, to quantify the presence of phosphorus (P), sodium (Na), calcium (Ca), silicate (Si) (for both BaGs) and boron (B), potassium (K) and magnesium (Mg) (only for 13-93B20) in the medium collected during the immersion in TRIS buffer solution. Wavelength values for the analysis were as follows: P, 213.618 nm; Na, 589.592 nm; Ca, 317.933 nm; Si, 250.690 nm; B, 249.678 nm; K, 766.491 nm, and Mg, 279.800 nm.

3. RESULTS AND DISCUSSION

Materials were first studied in dry conditions to assess the impact of aging on the adhesion of membranes to the substrates. Samples were subsequently immersed to observe and understand the degradation process of the materials in aqueous conditions.
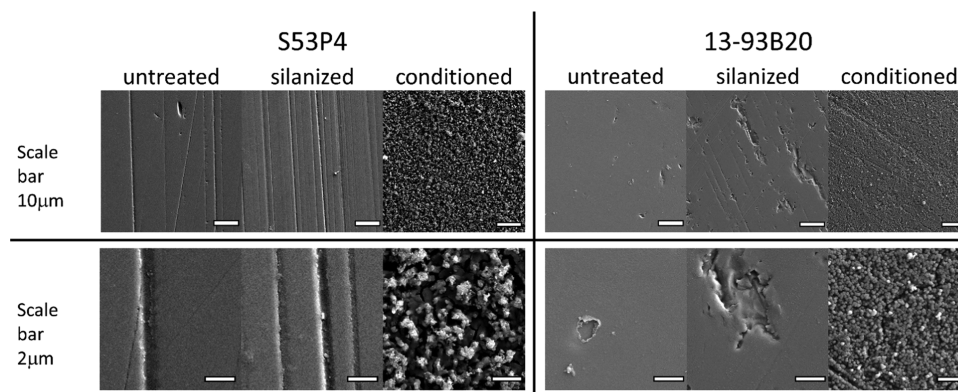
Figure 2. SEM images of the surface of untreated, silanized, and conditioned BaG discs, before membrane deposition.

3.1. BaG Disc Treatment, Deposition, and Characterization of the Stability of Membranes in Dry Conditions. 3.1.1. Surface Treatments.

First, the impact of the treatment on the surface charge of BaG discs was analyzed. ζ-Potential measurements are reported in Table 2.

As expected, with ζ-potential around -50 mV, the surface charge of the untreated samples is in agreement with the values for silicate and borosilicate glasses.[41,42] Regardless of the BaG composition, both treatments (silanized and conditioned) led to a decrease in the surface charge. In the case of silanization with APTES, the decrease in surface charge can be explained by the introduction of positively charged amine groups to the BaG disc surface at pH = 7.[41] Upon conditioning for 24 h in TRIS buffer solution, the BaG discs started to dissolve which resulted in the formation of Si–OH and Si–O$^-$ groups on their surfaces. Eventually, if the dissolution/reaction in an aqueous solution is rapid, a calcium phosphate reactive layer may start to precipitate.[35,43] Using a silicate glass model, Lu et al. reported that during immersion the measured ζ-potential presents a shift toward positive values, corresponding to the formation of an amorphous Ca–P layer, which can be detected as early as 1 day after immersion.[44] At longer immersion times, amorphous Ca–P layers crystallize. The crystalline hydroxyapatite layer has been reported to have a ζ-potential value close to -15 mV.[43,45] Based on these results, the surface charge decrease observed in our study may be explained by (1) the density of positively charged amine groups at the surface of silanized samples and (2) the nature (composition, specific surface area) of the Ca–P layer that has possibly deposited during the preincubation of the BaG discs for 24 h.

When comparing BaG compositions, it was clear that the surface charge of untreated and conditioned glass discs, respectively, was similar. However, silanization with APTES was found more efficient in reducing the electronegativity on the glass 13-93B20 than on the glass S53P4. Such variation in the surface charge between BaGs might be correlated with their dissolution rates. Indeed, borosilicate BaGs are known to possess a borate phase with higher reactivity than silicate BaGs.[46,47] Such a fast, early dissolution may lead to an increase in the density of Si–OH groups that are formed during the washing step, in turn leading to a higher density of sites onto which the APTES can be attached. The higher the concentration of amine groups, the less negative the surface will be. Indeed, Ferraris et al. have reported that upon silanization, the increase of the ζ-potential is dependent on the density of amine groups.[41] Therefore, the smaller change in surface charge seen for the S53P4 glass when compared to the

13-93B20 glass can be assigned to a greater density of positively charged amine groups at the surface of the latter composition. However, one should keep in mind that the dynamic dissolution of the BaG may also lead to the release of amine groups.

To obtain more information on the surface texture of different BaG discs and the impact of treatments on the surface composition, BaG discs were imaged by SEM/EDX (Figures 2 and 3).
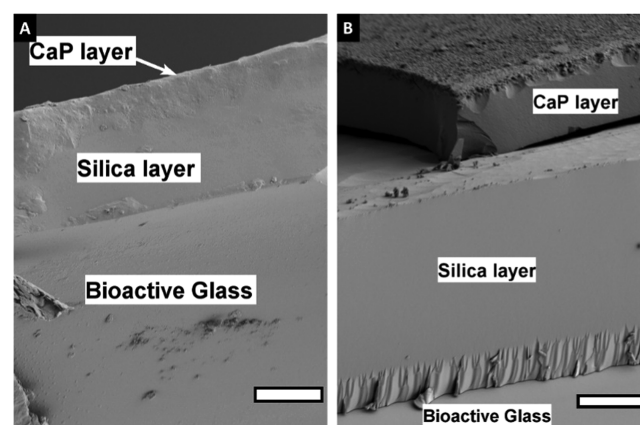

Figure 3. SEM images of cross section of S53P4 (A) and 13-93B20 (B) conditioned analyzed by EDX, scale bar: 20 μm.

At the microscopic level, silanization of S53P4 does not seem to have a significant impact on surface texture, whereas in the case of 13-93B20, the signs of surface degradation can be seen. In addition, a high density of nodules with submicrometer size can be observed on conditioned BaG discs. At higher magnification, one can see that nodules are smaller and denser at the surface of 13-93B20 than at the surface of S53P4. The cross section of samples was analyzed by EDX (Figure 3) and the top surface by Fourier transform infrared (FTIR) spectroscopy (Figure 4).

SEM/EDX analysis of conditioned samples indicated the presence of three phases: (1) the bioactive glass, (2) a silica-rich layer, and (3) a reactive layer composed mainly of Ca and P. The Ca/P ratio was found to vary between 1.4 and 1.7, regardless of the BaG composition. The large variation in the ratio can be assigned to the (1) high penetration depth of the electron beam (signal from the underneath BaG is collected) and (2) the Ca deficiency of the early apatite layer formed at the surface of BaG.[42] The formation of such layers was
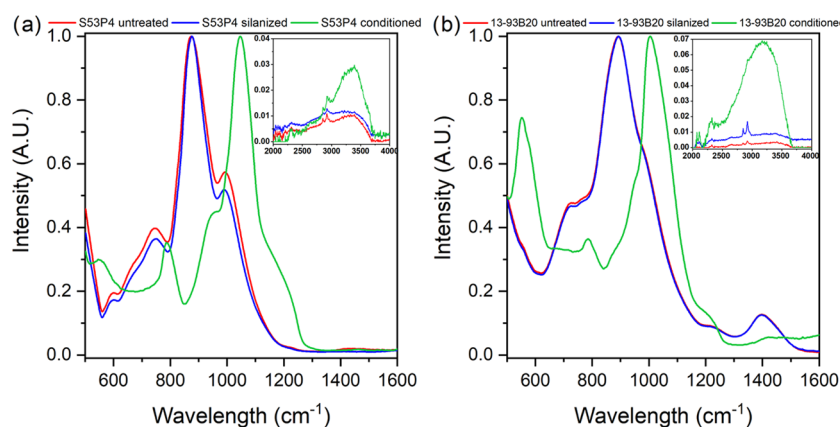
Figure 4. FTIR-ATR spectra of S53P4 (a) or 13-93B20 (b), untreated (red), silanized (blue), and conditioned (green) prior to membrane deposition. The inset in each spectrum shows the 2000-4000 cm^{-1} region.
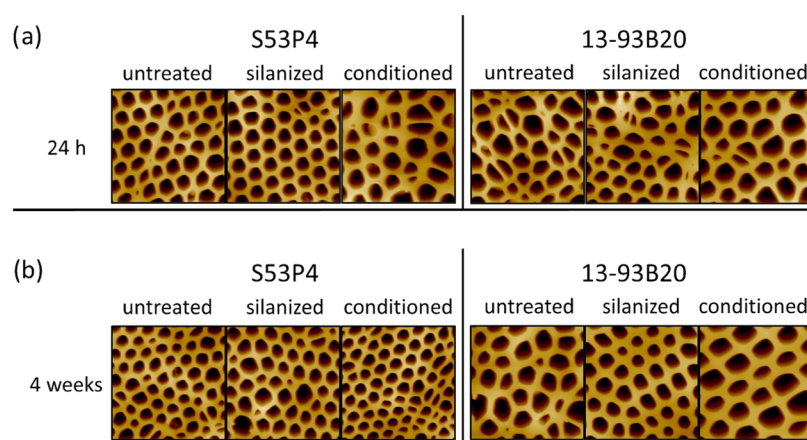
Figure 5. AFM images of the membranes deposited on the different substrates 24 h (a) or 4 weeks (b) after aging in a desiccator at 40% RH (each image is 30 μm × 30 μm).

expected upon immersion of silicate and borosilicate BaGs into aqueous solutions.[46−48] It is interesting to point out that the reactive layer at the surface of S53P4 glass had a lower density of nodules than the surface of 13-93B20 (Figure 3). Such a thin layer at the surface of S53P4, formed upon immersion in TRIS buffer solution, was also reported before by Varila et al.[49]

The FTIR-ATR spectra of the top layer are presented in Figure 4.

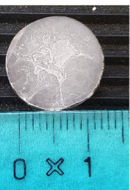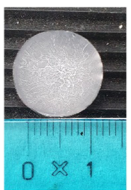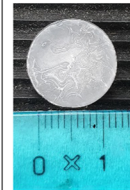The FTIR-ATR analysis was made to identify the chemical structure at the surface of the glasses.
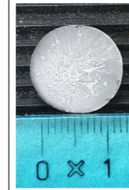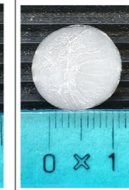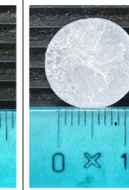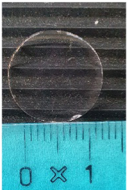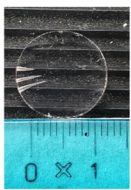
FTIR-ATR spectra of untreated S53P4 (Figure 4a) and 13-93B20 (Figure 4b) displayed bands ∼748, ∼930, and ∼1030 cm^{-1}. These bands can be attributed to Si−O bending, Si−O^{-} (nonbridging oxygen) in the [SiO$_4$] units, and to Si−O−Si asymmetric stretching in [SiO$_4$] units, respectively.[50,51] Aside from those bands, the glass 13-93B20 also exhibited bands at 1400 cm^{-1} related to BO$_3$ vibrati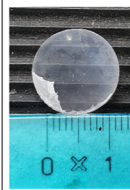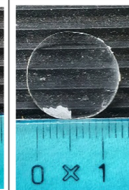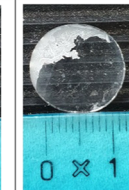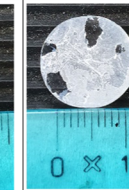ons.[51,52] Silanization did not seem to significantly impact the surface chemistry, regardless of the glass composition. While vibration related to amine groups (NH$_2$ between 1400 and 1600 cm^{-1}) could be expected, they were not visible in the FTIR-ATR spectra of silanized BaG discs. The reason may lie in the low density of amine groups at the surface of the BaG discs.[38,41] However, as an amine group signal is visible in the same region as BO$_3$ units in 13-93B20, it is possible that those bands were covered by boron bands in this glass.

Major changes in the surface structure occurred for conditioned BaG discs, as expected from SEM/EDX. The FTIR-ATR spectra of conditioned samples exhibited complete disappearance of vibration bands related to silicate and borate networks and new absorption bands at ∼560, ∼605, ∼800, and ∼1060 cm^{-1} as well as a shoulder at ∼959 cm^{-1} appeared. The shoulder at ∼959 cm^{-1} can be attributed to C−O vibration mode in CO$_3$$^{2-}$ and to P−O−P bonding.[50] The bands at ∼800 and ∼1060 cm^{-1} can be assigned to the C−O bending and P−O stretching vibration, respectively.[53] Bands at ∼560 and ∼605 cm^{-1}, in the conditioned BaG disc spectra, attributed to the P−O resonance of PO$_4$$^{3-}$, were characteristic of an apatite structure.[48] Furthermore, conditioned samples presented a band of higher intensity in the region 3000−3600 cm^{-1} corresponding to OH vibration indicating a hydrated layer at BaG disc surfaces (Figure 4a,b insets).[38]

These spectra confirmed the presence of a hydroxyapatite layer at the surface of conditioned BaG discs and revealed that there were no significant differences in the surface chemistry of silanized and untreated BaG discs.

3.1.2. Deposition of PLDLA Honeycomb Membrane. Figure 5 presents the AFM images of the membranes deposited on different BaG discs (untreated and treated). The images, taken 24 h postdeposition (Figure 5a), allowed us to assess the relationship between the physicochemical features of different BaG disc surfaces and the features of the membranes prepared by the BFM.

Table 3. Photographs of the PLDLA Membrane Deposited on BaG Discs before (Upper Row) and after (Lower Row) the Shear Stress Test[a]

	S53P4			13-93B20		
	Untreated	Silanized	Conditioned	Untreated	Silanized	Conditioned
Before						
After						
Maximum Load (N)	0.94 ± 0.46	0.83 ± 0.63	5.56 ± 5.26	1.96 ± 1.15	13.18 ± 7.65	19.88 ± 3.79

[a]Upon shear, the loss of the membrane is revealed by the appearance of the transparent glass substrate.

—: BAG untreated, ⋯: BAG silanized, - - -: BAG conditioned
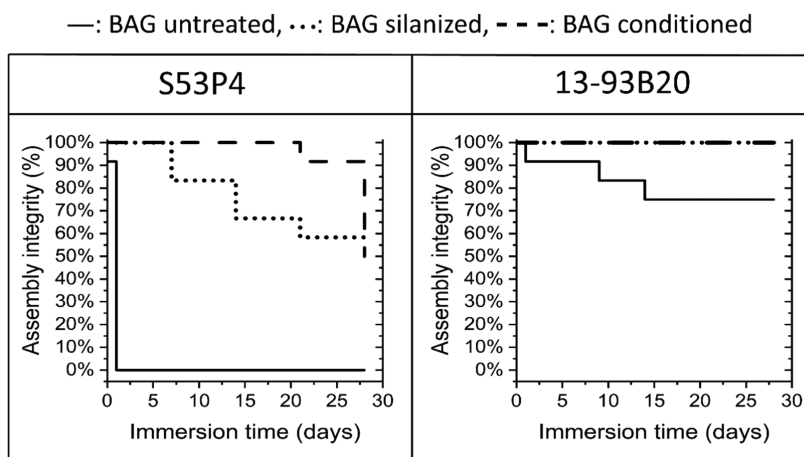
Figure 6. Assembly integrity (in %) was estimated by counting the number of membranes that did not detach (partially or totally) from their substrate, as a function of immersion time, $n = 12$.

After 24 h aging (Figure 5a), regardless of the substrate, a honeycomb-like pattern was always visible, in spite of some variation in the homogeneity of pores. The pore area was calculated and found to be 5−20 μm^2 (data not shown), and the thickness of the membrane was found to vary from 10 to 20 μm. Assuming that pores had a shape close to a circle, this corresponded to a diameter of 1−5 μm, which was similar to the values reported in the literature for PLDLA honeycomb membranes.[19] It is well known that when using the BFM, small variations in the humidity, in the viscosity of the polymer solution or in room temperature, can greatly influence the final shape of the honeycomb.[19,21,54]

3.1.3. PLDLA Membrane Resistance and Stability in Dry Conditions. The attachment of the membrane to its substrate was then evaluated by applying a shear stress on the materials and by measuring the force needed to detach the membranes. The results are shown in Table 3.

The results showed that the membranes deposited on untreated and silanized S53P4 substrates exhibited full detachment from the glass surface. In the images, almost no residues of the membrane were visible on the glass surface with a maximum load inferior to 1 N. On the other hand, the membranes deposited on the conditioned S53P4 detached only partially, and the force needed to detach them was more than 5 times higher than that needed to detach the membrane from silanized and untreated S53P4.

In the case of 13-93B20, untreated and silanized BaGs behaved similarly, i.e., part of the membrane detached from the substrate, but some residues were observable after the test. In contrast with S53P4, silanization of 13-93B20 greatly increased the resistance to shear (more than 10 times). The attachment strength of the membranes deposited on the conditioned 13-93B20 outperformed all the other substrates and treatments. In spite of the membranes becoming mildly damaged following a maximum load of 19.88 N, a large portion of the membranes remained tightly attached to the substrate after the test, with the shear force needed to achieve detachment being greater than for all other samples. It is noteworthy that, in all the cases, the standard deviation indicated a high degree of inhomogeneity between samples. Inhomogeneities on untreated samples
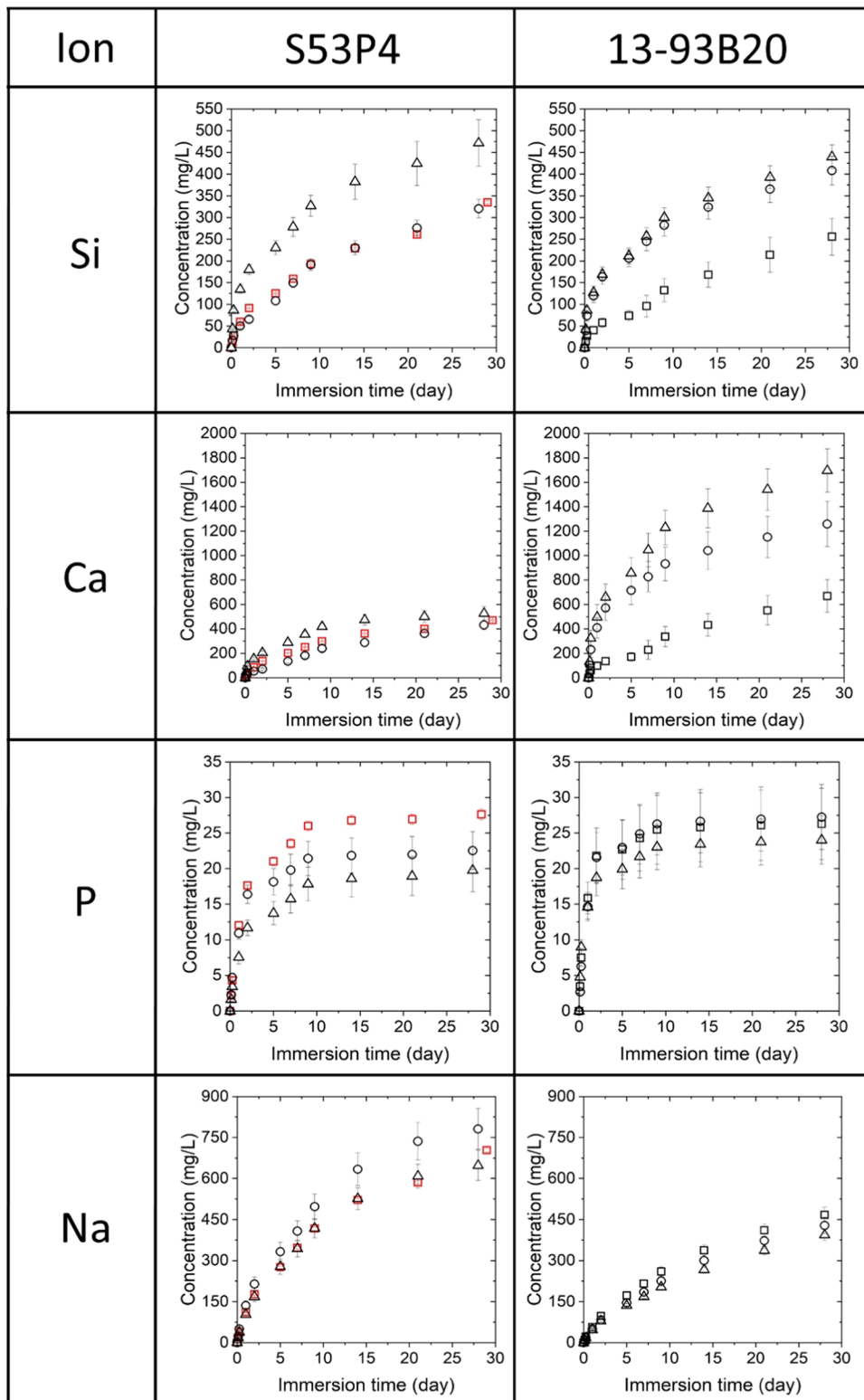
Figure 7. Silicon (Si), calcium (Ca), phosphorous (P), and sodium (Na) release profile upon immersion of the membrane/BaG disc assembly in TRIS buffer solution for up to 28 days. Red squares display the results of untreated S53P4 without a membrane.

can be attributed to small differences in the surface finish of the postpolishing of the samples. In the case of silanized samples, differences may arise from the APTES physisorption. While the

exposure of amine groups was the most likely event, one cannot overlook the possibility of the APTES being bound to the BaG disc surface by the amine group, thus revealing ethoxy
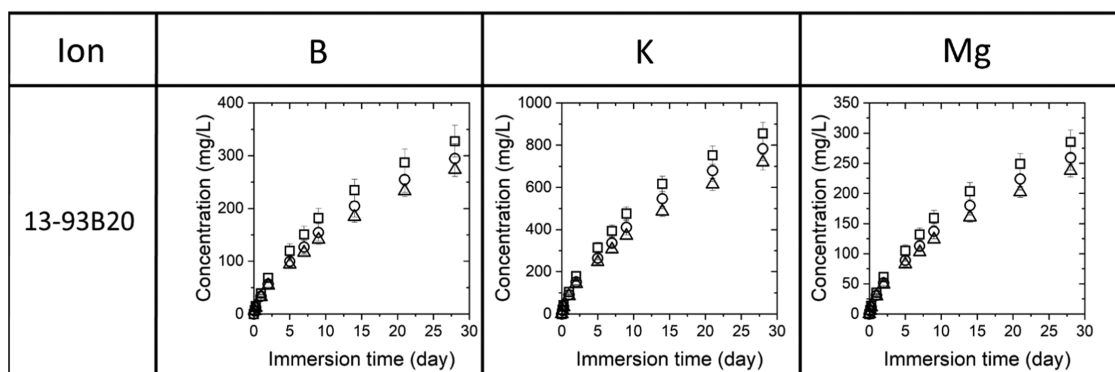
Figure 8. Ion release profile of boron (B), potassium (K), and magnesium (Mg) for the three 13-93B20-containing membrane/BaG disc assembly as a function of immersion time in TRIS buffer solution.

groups.[55] Upon conditioning, the texture, topography, and density of reactive layer across the surface of the disc cannot be precisely controlled, especially in the case of S53P4 where the precipitation was less prominent than for 13-93B20. Finally, as mentioned earlier, a small variation in membrane deposition parameters (i.e., temperature, humidity, etc.) can lead to small changes in membrane properties.[19]

The stability of membranes in dry conditions as a function of time and without external stress was also studied. Membranes deposited onto various BaG disc surfaces were imaged using the AFM, 4 weeks postdeposition, as shown in Figure 5b. When compared to Figure 5a, the honeycomb structure kept its integrity for at least 4 weeks in a dry environment (desiccator). Most of the pores were found in the range of 1−5 μm in diameter. As stated above, a large variability in the pore dimension was measured, which does not seem to be correlated with membrane aging nor with the treatment applied to the substrate, but rather with the processing methods and variables (humidity, polymer solution viscosity, temperature).

3.2. Stability of the Membrane/BaG Disc Assembly in Aqueous Conditions. *3.2.1. Assembly Integrity in Aqueous Solution.* The stability of the membrane/BaG disc assembly was then studied by immersing the material in TRIS buffer solution at 37 °C, for up to 4 weeks (Figure 6).

All membranes deposited on untreated S53P4 detached after 3 h of immersion. Membranes started to detach after 7 and 21 days on S53P4 silanized and conditioned, respectively. Compared to untreated S53P4, membranes deposited on untreated 13-93B20 were noticeably more stable. Indeed, 70% were still attached to their substrate after 28 days of immersion. While borosilicate glass is typically considered more hydrolytically unstable than silicate glass, this is solely due to the borate phase which degrades at a faster rate than the silicate phase.[51] As per the FTIR-ATR spectra in Figure 4, one can see that the silicate network in the S53P4 glass has a greater number of nonbridging oxygen (ratio between the bands at ~930 and ~1030 cm^{-1}) than the silicate network in the 13-93B20 glass.[56] Therefore, the initial dissolution of the SiO$_2$ network occurs faster for the S53P4 glass, leading to a decreased interface stability between the glass and the membrane.

Silanization improved drastically the assembly integrity, regardless of the BaG composition. It is interesting to note that membranes deposited on silanized S53P4 seemed to detach gradually over time. Sixty percent of the membranes remained attached to the substrate after 4 weeks of immersion, while 100% of the membranes were still attached to their substrate on silanized 13-93B20. As per the ζ-potential, it is believed that the surface of 13-93B20 was grafted with a higher density of amine groups leading to a higher stability of the membrane at the glass surface. Zhou et al. reported interactions between PLDLA and hydroxyapatite, thereby hydrogen bonds form between C=O and P-OH functions.[57] Similarly, in this study, it is feasible that amines and the C=O group interact through hydrogen bonding.

Finally, on the conditioned S53P4, membranes remained stably attached to the substrate for 20 days, with 50% of the membranes abruptly detaching at 27 days. Membrane attachment was found to be significantly improved when the conditioned 13-93B20 BaG was used as the substrate, with 100% of the membranes remaining attached at the end of the immersion period. As shown by the SEM/EDX (Figures 2 and 3) and FTIR-ATR analysis (Figure 4), the surface chemistry has changed during the immersion for 24 h in TRIS buffer solution, thereby a Ca−P reactive layer has formed at the surface of the glass. This is believed to be the reason for the stability of the assembly upon immersion.

ζ-Potential, mechanical testing, and immersion into TRIS buffer solution indicated that:

(1) The stability of the membrane was highly dependent on the surface reactivity, i.e., in solution, the more reactive surface will lead to a faster failure of the membrane.

(2) Silanization improved the stability of the membrane/BaG disc assembly in an aqueous solution. The improvement was a function of the amine group density (i.e., surface charge). However, only at higher silanization density, an increased shear stress is necessary to detach the membrane from the substrate (i.e., for silanized 13-93B20, Table 3).

(3) Membranes deposited on conditioned samples demonstrated improved resistance to shear, as well as higher stability in aqueous solutions. Such improvement in the membrane/BaG disc assembly stability was linked to the precipitation of a stable Ca−P reactive layer. The thicker the layer, the more stable the membrane, probably due to an increased specific surface area and/or interactions between the hydroxy groups of the reactive layer and carbonyl groups of the polymer.[57] The impact of the
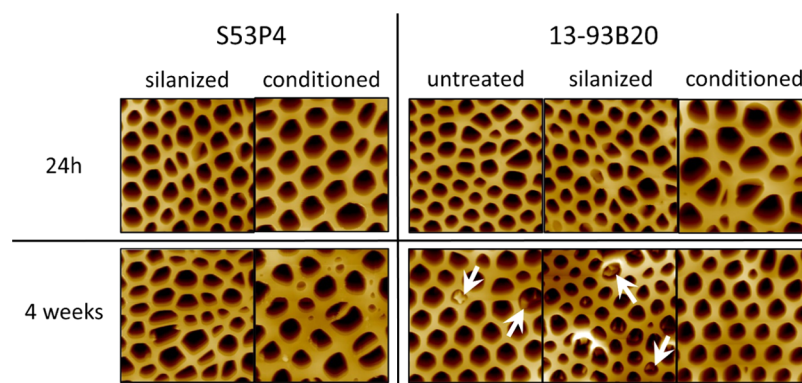
Figure 9. AFM images of the films deposited on the different substrates after incubation in TRIS buffer solution at 37 °C for 24 h and 4 weeks (each image is 30 μm × 30 μm, and each image is from different samples). The white arrows show precipitates.

specific surface area on the membrane adhesion will be studied in the future.

Overall, a controlled surface treatment of bioactive substrates led to an improvement in the assembly integrity. This is of paramount importance in view of culturing cells without the risk of the membrane detaching over time. Furthermore, when thinking of the application (i.e., a biphasic bone substitute), proper adhesion of the membrane to its substrate is crucial, up until the time the defects have been repaired.

3.2.2. BaG Ion Release, from the Assembly, in Aqueous Solution. It is well known that BaGs react and release ions upon immersion, which can have beneficial effects on cell fate.[25,52] The release profile of Si, Ca, P, and Na ions by both BaGs is presented in Figure 7, while the release profile of B, K, and Mg ions, specific to the composition of the 13-93B20 glass, is shown in Figure 8.

The ion release profiles for untreated samples are also reported in the figures. However, membranes deposited on untreated S53P4 were not studied further, due to their poor stability in aqueous conditions (Figure 7, all membranes detaching after 3 h). Therefore, the ion release from this material does not reflect the release rate of ions through the membrane but rather from the substrate alone. The data are included to allow for comparison in dissolution kinetics between the various treatments on S53P4.

As suspected, the release of Si from untreated S53P4 was slightly faster than the release rate observed for untreated 13-93B20, which confirmed that the decreased membrane stability in the aqueous solution was probably due to the rapid release of ions from the glass surface. A faster Si release from S53P4, when compared to 13-93B20, was expected. Indeed, BaG 13-93B20 was developed by substituting 20% of SiO_2 with B_2O_3 in the silicate glass 13-93.[37] The silica network, in the glass 13-93 (without boron), is more polymerized than in S53P4 and therefore 13-93 is more stable to hydrolysis.[58] In addition, the partial substitution of B_2O_3 for SiO_2, in 13-93B20, further leads to an increased polymerization of the SiO_2 network making 13-93B20 silica network less sensitive to hydrolysis compared to S53P4.[37,59] Upon silanization, one can see that the Si release for S53P4 did not significantly change, whereas it increased for 13-93B20. This can be assigned to the pretreatment of the materials during silanization and/or release of Si from the grafted APTES. Finally, the conditioned S53P4 BaG released more Si than the silanized counterpart, whereas the Si release profile from the conditioned 13-93B20 was similar to the Si

release from the silanized 13-93B20 material. The greater Si release from the conditioned S53P4 compared to 13-93B20 can be explained by the change in surface chemistry. Indeed, as the reactive layer was thinner on S53P4 BaG, more silica gel was in contact with the solution, in turn leading to higher Si release to the surrounding medium. It is important to note that after 3 days of immersion, the silicon release seemed to slow down. This phenomenon is in agreement with previous studies discussing the Si release from BaGs.[41]

The phosphorous release profile was similar for all BaGs. Phosphate concentration seemed to saturate, as soon as 1 week for all samples. The shape of the curve indicated that phosphate release followed a typical diffusion-controlled process. However, as the results are cumulative, this could also indicate the saturation of the solution with phosphate ions, leading to precipitation of a reactive layer.[60] The phosphorous release profile appeared to be independent of the surface treatment in 13-93B20. However, untreated S53P4 released more phosphorous than the surface-treated ones. This can be attributed to the absence of the membrane in this particular condition.

Sodium release from S53P4 and 13-93B20 glass samples was consistent with the dissolution mechanism described by Hench[24,61] for BaGs. Indeed, the conditioned samples seemed to release Na at a lower rate than the silanized samples. This was attributed to the fast Na^+ H^+ ion exchange occurring at the early stage of the glass dissolution, occurring during the conditioning step. The variation in concentration was less pronounced in the case of 13-93B20 due to the lower Na content in the glass composition (Table 1).

It is interesting to note that despite the two glass compositions having almost the same mol % of Ca, the release of this ion happened faster in the case of the borosilicate glass. Indeed, it has been hypothesized that Ca interacts preferentially with the borate network than with the silicate one, which is the least hydrolytically stable.[41,51] All 13-93B20 BaGs released a higher content of Ca compared to S53P4 BaGs regardless of the treatment, but this amount was significantly higher for the silanized and conditioned 13-93B20. Given the high affinity of Ca and P toward the precipitation of apatite crystals, the high release of Ca, irrespective of the treatment for the glass 13-93B20 is likely to lead to the precipitation of a reactive layer overtime[41,62]

As shown in Figure 8, 13-93B20 released B, K, and Mg, in a similar amount and kinetics regardless of the treatment. This suggested that the borate phase was the most soluble and was
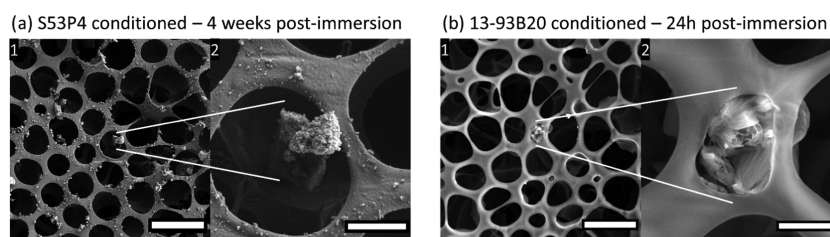
Figure 10. SEM images of the films deposited on (a) conditioned S53P4 or (b) conditioned 13-93B20 incubated in TRIS for 4 weeks and 24 h, respectively (a1 and b1 Scale bar 10 μm. Area of interest a2 and b2 are displayed on the right of the images, Scale bar 2 μm).

not affected by the silica-rich layer formation and Ca−P reactive layer precipitation.

Altogether, these results indicated that (a) the presence of the membrane did not prevent the glass from dissolving, and therefore the ions, beneficial to the cells, were still released to the medium, (b) 13-93B20 glass exhibited a rapidly dissolving borate phase and a stable silicate phase, which in turn promoted membrane stability and higher density of APTES grafting, and (c) 13-93B20 exhibited an ion release profile favorable to the precipitation of a reactive layer.

3.2.3. Membrane Surface Analysis. To assess the surface features of the membrane after immersion, samples incubated in TRIS for 4 weeks were air-dried overnight and imaged by AFM (Figure 9).

The honeycomb structure of the membrane was preserved for at least 4 weeks of immersion in TRIS buffer solution. Images were further processed with Fiji, and the pore size was estimated. Regardless of the incubation time or the substrate, pores were estimated to have a diameter in the 1−5 μm range. The pore size postincubation was similar, within the accuracy of the measurement and the accuracy of the processing, to the sample preincubation.

To illustrate the precipitation within pores, Figure 10 exhibits the membrane surface of (a) conditioned S53P4 immersed for 4 weeks in TRIS and (b) conditioned 13-93B20 immersed for 24 h in TRIS.

From the SEM images (Figure 10a), one can observe the presence of small nodules at the surface of the membranes deposited on the conditioned S53P4; similar features were also seen at the surface of the silanized S53P4 postimmersion. From Figure 10b, one can see that large aggregates were present within the pores of the membrane. Such aggregates were not visible in the postimmersion of silanized and untreated samples. The EDX analysis revealed a high concentration of Ca and P. Those nodules, both on membrane deposited on S53P4 and 13-93B20, were due to the precipitation of a CaP layer, as expected upon immersion of BaGs.[63] However, the small size and low density of the nodules did not enable unambiguous EDX analysis.

4. CONCLUSIONS

In this study, the impact of the bioactive glass surface treatment on the stability of a polymeric membrane deposited using the breath figure method was investigated.

All membranes exhibited a honeycomb-like surface topography, regardless of the BaG composition or the surface modification. The pores of the honeycomb had a diameter ranging from 1 to 5 μm, demonstrating the ability of BaG discs to support the production of a microstructured membrane.

Deposition of a PLDLA membrane on an untreated bioactive glass surface was revealed to yield suboptimal results.

Indeed, in dry conditions, membranes demonstrated low resistance to shear, irrespective of the glass composition. Upon immersion, for 4 weeks, all the membranes detached from the S53P4 substrate, while half of them detached from 13-93B20. Therefore, one may conclude that the presence of OH$^-$ groups at the material surface was not sufficient to enable strong electrostatic interactions between BaG discs and membranes, leading to early failure of the membrane/BaG disc assembly.

Upon deposition of the membrane on a silanized bioactive glass surface, the presence of amine groups led to a significant enhancement of the membrane adherent properties both in dry and wet conditions. However, it appeared that the improvement was directly linked to the density of the primary amines at the glass surface. Such treatment was found more efficient in the case of 13-93B20 BaG which is assumed to have a faster initial degradation rate. It is believed that the primary amine groups interact, through hydrogen bonds, with PLDLA carbonyl groups.

Finally, deposition of the membrane on conditioned surfaces was revealed to be more effective in reaching a stable BaG disc/membrane interface in dry and wet conditions. The reason for the increased interaction between the BaG disc surface and the membrane appeared to be mainly linked to (1) the precipitation of a reactive layer (CaP) and (2) the subsequent change in topography. Results were significantly better when the membrane was deposited on the 13-93B20 BaG disc than on the S53P4 BaG disc. This was assigned to the thicker and denser reactive layer formed at the surface of this BaG disc compared to the one at the surface of S53P4.

To conclude, this study demonstrated that a PLDLA membrane can be deposited on inorganic surfaces using the breath figure method. With appropriate surface treatment, it was possible to increase the membrane stability. This study also highlighted the capacity of BaGs to maintain a biologically relevant release of ions, even after surface treatment. Results also suggested a potential precipitation of CaP at the membrane surface upon immersion. However, further studies are required to unambiguously identify the composition of the precipitates. The results of this study are promising for the development of new biphasic materials for bone tissue engineering.

■ ASSOCIATED CONTENT

Ⓢ Supporting Information

The Supporting Information is available free of charge at https://pubs.acs.org/doi/10.1021/acsami.1c03759.

SEM micrograph of the S53P4 substrate after 24 h of immersion in TRIS buffer solution along with the EDX line scan showing the remnant glass, the SiO$_2$-rich layer, and the precipitated reactive layer (PDF)

■ AUTHOR INFORMATION

Corresponding Author

J. Massera − *Laboratory of Biomaterials and Tissue Engineering, Faculty of Medicine and Health Technology, Tampere University, 33720 Tampere, Finland;* ● orcid.org/0000-0002-1099-8420; Email: jonathan.massera@tuni.fi

Authors

A. Deraine − *ERRMECe, Equipe de Recherche sur les Relations Matrice Extracellulaire-Cellules (EA1391), Université de Cergy-Pontoise, Maison Internationale de la Recherche (MIR), 95001 Neuville sur Oise, France; Laboratory of Biomaterials and Tissue Engineering, Faculty of Medicine and Health Technology, Tampere University, 33720 Tampere, Finland;* ● orcid.org/0000-0002-3795-1593

M. T. Rebelo Calejo − *Laboratory of Biomaterials and Tissue Engineering, Faculty of Medicine and Health Technology, Tampere University, 33720 Tampere, Finland*

R. Agniel − *ERRMECe, Equipe de Recherche sur les Relations Matrice Extracellulaire-Cellules (EA1391), Université de Cergy-Pontoise, Maison Internationale de la Recherche (MIR), 95001 Neuville sur Oise, France*

M. Kellomäki − *Laboratory of Biomaterials and Tissue Engineering, Faculty of Medicine and Health Technology, Tampere University, 33720 Tampere, Finland*

E. Pauthe − *ERRMECe, Equipe de Recherche sur les Relations Matrice Extracellulaire-Cellules (EA1391), Université de Cergy-Pontoise, Maison Internationale de la Recherche (MIR), 95001 Neuville sur Oise, France*

M. Boissière − *ERRMECe, Equipe de Recherche sur les Relations Matrice Extracellulaire-Cellules (EA1391), Université de Cergy-Pontoise, Maison Internationale de la Recherche (MIR), 95001 Neuville sur Oise, France*

Complete contact information is available at:
https://pubs.acs.org/10.1021/acsami.1c03759

Notes

The authors declare no competing financial interest.

■ REFERENCES

(1) Moore, W. R.; Graves, S. E.; Bain, G. I. Synthetic Bone Graft Substitutes. *ANZ J. Surg.* **2001**, *71*, 354−361.

(2) Amini, A. R.; Laurencin, C. T.; Nukavarapu, S. P. Bone Tissue Engineering: Recent Advances and Challenges. *Biomed. Eng.* **2013**, *40*, 363−408.

(3) Wang, W.; Yeung, K. W. K. Bone Grafts and Biomaterials Substitutes for Bone Defect Repair: A Review. *Bioact. Mater.* **2017**, *2*, 224−247.

(4) Fedarko, N. S.; D'Avis, P.; Frazier, C. R.; Burrill, M. J.; Fergusson, V.; Tayback, M.; Sponseller, P. D.; Shapiro, J. R. Cell Proliferation of Human Fibroblasts and Osteoblasts in Osteogenesis Imperfecta: Influence of Age. *J. Bone Miner. Res.* **1995**, *10*, 1705−1712.

(5) Dimitriou, R.; Mataliotakis, G. I.; Calori, G. M.; Giannoudis, P. V. The Role of Barrier Membranes for Guided Bone Regeneration and Restoration of Large Bone Defects: Current Experimental and Clinical Evidence. *BMC Med.* **2012**, *10*, No. 81.

(6) Ogiso, B.; Hughes, F. J.; Melcher, A. H.; McCulloch, C. A. G. Fibroblasts Inhibit Mineralised Bone Nodule Formation by Rat Bone Marrow Stromal Cells in Vitro. *J. Cell. Physiol.* **1991**, *146*, 442−450.

(7) Meinig, R. P. Clinical Use of Resorbable Polymeric Membranes in the Treatment of Bone Defects. *Orthop. Clin. North Am.* **2010**, *41*, 39−47.

(8) Kellomäki, M.; Puumanen, K.; Ashammakhi, N.; Waris, T.; Paasimaa, S.; Törmälä, P. Bioabsorbable Laminated Membranes for Guided Bone Regeneration. *Technol. Health Care* **2002**, *10*, 165−172.

(9) Cheng, X.; Yang, F. More Than Just a Barrier—Challenges in the Development of Guided Bone Regeneration Membranes. *Matter* **2019**, *1*, 558−560.

(10) Todd, V. Scantlebuty. 1982-1992: A Decade of Technology Development for Guided Tissue Regeneration. *J. Periodontol.* **1993**, *64*, 1129−1137.

(11) Gottlow, J. Guided Tissue Regeneration Using Bioresorbable and Non-Resorbable Devices: Initial Healing and Long-Term Results. *J. Periodontol.* **1993**, *64*, 1157−1165.

(12) Gutta, R.; Baker, R. A.; Bartolucci, A. A.; Louis, P. J. Barrier Membranes Used for Ridge Augmentation: Is There an Optimal Pore Size? *J. Oral Maxillofac. Surg.* **2009**, *67*, 1218−1225.

(13) Wessing, B.; Lettner, S.; Zechner, W. Guided Bone Regeneration with Collagen Membranes and Particulate Graft Materials: A Systematic Review and Meta-Analysis. *Int. J. Oral Maxillofac. Implants* **2018**, *33*, 87−100.

(14) Sankar, A. R.; Gujjari, S. K.; Kulkarni, P. K.; Akhila, A. R. Development of Biodegradable Silkworm Cocoon Derived Silk Membrane for GTR in the Treatment of Grade II Furcation. *Int. J. Res. Pharm. Sci.* **2020**, *11*, 1551−1561.

(15) Reynolds, M. A.; Aichelmann-Reidy, M. E.; Branch-Mays, G. L.; Gunsolley, J. C. The Efficacy of Bone Replacement Grafts in the Treatment of Periodontal Osseous Defects. A Systematic Review. *Ann. Periodontol.* **2003**, *8*, 227−265.

(16) Yadav, V. S.; Narula, S. C.; Sharma, R. K.; Tewari, S.; Yadav, R. Clinical Evaluation of Guided Tissue Regeneration Combined with Autogenous Bone or Autogenous Bone Mixed with Bioactive Glass in Intrabony Defects. *J. Oral Sci.* **2011**, *53*, 481−488.

(17) Proussaefs, P.; Lozada, J. The Use of Resorbable Collagen Membrane in Conjunction with Autogenous Bone Graft and Inorganic Bovine Mineral for Buccal/Labial Alveolar Ridge Augmentation: A Pilot Study. *J. Prosthet. Dent.* **2003**, *90*, 530−538.

(18) Donos, N.; Lang, N. P.; Karoussis, I. K.; Bosshardt, D.; Tonetti, M.; Kostopoulos, L. Effect of GBR in Combination with Deprotei-nized Bovine Bone Mineral and/or Enamel Matrix Proteins on the Healing of Critical-Size Defects. *Clin. Oral Implants Res.* **2004**, *15*, 101−111.

(19) Calejo, M. T.; Ilmarinen, T.; Skottman, H.; Kellomäki, M. Breath Figures in Tissue Engineering and Drug Delivery: State-of-the-Art and Future Perspectives. *Acta Biomater.* **2018**, *66*, 44−66.

(20) Dou, Y.; Jin, M.; Zhou, G.; Shui, L. Breath Figure Method for Construction of Honeycomb Films. *Membranes* **2015**, *5*, 399−424.

(21) Zhang, A.; Bai, H.; Li, L. Breath Figure: A Nature-Inspired Preparation Method for Ordered Porous Films. *Chem. Rev.* **2015**, *115*, 9801−9868.

(22) Wu, X. H.; Wu, Z. Y.; Su, J. C.; Yan, Y. G.; Yu, B. Q.; Wei, J.; Zhao, L. M. Nano-Hydroxyapatite Promotes Self-Assembly of Honeycomb Pores in Poly(L-Lactide) Films through Breath-Figure Method and MC3T3-E1 Cell Functions. *RSC Adv.* **2015**, *5*, 6607−6616.

(23) Zhao, C.; Pan, C.; Sandstedt, J.; Fu, Y.; Lindahl, A.; Liu, J. Combination of Positive Charges and Honeycomb Pores to Promote MC3T3-E1 Cell Behaviour. *RSC Adv.* **2015**, *5*, 42276−42286.

(24) Hench, L. L. The Story of Bioglass. *J Mater. Sci.: Mater. Med.* **2006**, *17*, 967−978.

(25) El-Rashidy, A. A.; Roether, J. A.; Harhaus, L.; Kneser, U.; Boccaccini, A. R. Regenerating Bone with Bioactive Glass Scaffolds: A

Review of in Vivo Studies in Bone Defect Models. *Acta Biomater.* 2017, *62*, 1−28.

(26) Hoppe, A.; Güldal, N. S.; Boccaccini, A. R. A Review of the Biological Response to Ionic Dissolution Products from Bioactive Glasses and Glass-Ceramics. *Biomaterials* 2011, *32*, 2757−2774.

(27) Gorustovich, A. A.; Roether, J. A.; Boccaccini, A. R. Effect of Bioactive Glasses on Angiogenesis: A Review of *In Vitro* and *In Vivo* Evidences. *Tissue Eng., Part B* 2010, *16*, 199−207.

(28) Drago, L.; Toscano, M.; Bottagisio, M. Recent Evidence on Bioactive Glass Antimicrobial and Antibiofilm Activity: A Mini-Review. *Materials* 2018, *11*, No. 326.

(29) Drago, L.; Vassena, C.; Fenu, S.; Vecchi, E. D.; Signori, V.; Francesco, R. D.; Romanò, C. L. In Vitro Antibiofilm Activity of Bioactive Glass S53P4. *Future Microbiol.* 2014, *9*, 593−601.

(30) Sayed Abdelgeliel, A.; Ferraris, S.; Cochis, A.; Vitalini, S.; Iriti, M.; Mohammed, H.; Kumar, A.; Cazzola, M.; Salem, W. M.; Verné, E.; Spriano, S.; Rimondini, L. Surface Functionalization of Bioactive Glasses with Polyphenols from Padina Pavonica Algae and In Situ Reduction of Silver Ions: Physico-Chemical Characterization and Biological Response. *Coatings* 2019, *9*, No. 394.

(31) Vernè, E.; Ferraris, S.; Vitale-Brovarone, C.; Cochis, A.; Rimondini, L. Bioactive Glass Functionalized with Alkaline Phosphatase Stimulates Bone Extracellular Matrix Deposition and Calcification in Vitro. *Appl. Surf. Sci.* 2014, *313*, 372−381.

(32) Philippart, A.; Boccaccini, A. R.; Fleck, C.; Schubert, D. W.; Roether, J. A. Toughening and Functionalization of Bioactive Ceramic and Glass Bone Scaffolds by Biopolymer Coatings and Infiltration: A Review of the Last 5 Years. *Expert Rev. Med. Devices* 2015, *12*, 93−111.

(33) Stanić, V. Variation in Properties of Bioactive Glasses After Surface Modification. In *Clinical Applications of Biomaterials*; Kaur, G., Ed.; Springer International Publishing: Cham, 2017; pp 35−63.

(34) Calejo, M. T.; Ilmarinen, T.; Jongprasitkul, H.; Skottman, H.; Kellomäki, M. Honeycomb Porous Films as Permeable Scaffold Materials for Human Embryonic Stem Cell-Derived Retinal Pigment Epithelium: Porous Films as Scaffolds for HESC-RPE. *J. Biomed. Mater. Res.* 2016, *104*, 1646−1656.

(35) Hupa, L. Composition-Property Relations of Bioactive Silicate Glasses. In *Bioactive Glasses*; Elsevier, 2018; pp 1−35.

(36) Anderson, Ö.H.; Karlson, K. H.; Liu, G.; Niemi, L. In Vivo Behavior of Glasses in the SiO2-NaO2-CaO-P2O5-Al2O3-B2O3 System. *J. Mater. Sci.: Mater. Med.* 1990, *1*, 219−227.

(37) Houaoui, A.; Lyyra, I.; Agniel, R.; Pauthe, E.; Massera, J.; Boissière, M. Dissolution, Bioactivity and Osteogenic Properties of Composites Based on Polymer and Silicate or Borosilicate Bioactive Glass. *Mater. Sci. Eng., C* 2020, *107*, No. 110340.

(38) Massera, J.; Mishra, A.; Guastella, S.; Ferraris, S.; Verné, E. Surface Functionalization of Phosphate-Based Bioactive Glasses with 3-Aminopropyltriethoxysilane (APTS). *Biomed. Glasses* 2016, *2*, 51−62.

(39) Luxbacher, T. *The ZETA Guide: Principles of the Streaming Potential Technique*; Anton Paar GmbH: Graz, Austria, 2014.

(40) Lin, M. R.; Ritter, J. E.; Rosenfeld, L.; Lardner, T. J. Measuring the Interfacial Shear Strength of Thin Polymer Coatings on Glass. *J. Mater. Res.* 1990, *5*, 1110−1117.

(41) Ferraris, S.; Nommeots-Nomm, A.; Spriano, S.; Vernè, E.; Massera, J. Surface Reactivity and Silanization Ability of Borosilicate and Mg-Sr-Based Bioactive Glasses. *Appl. Surf. Sci.* 2019, *475*, 43−55.

(42) Ferraris, S.; Yamaguchi, S.; Barbani, N.; Cazzola, M.; Cristallini, C.; Miola, M.; Vernè, E.; Spriano, S. Bioactive Materials: In Vitro Investigation of Different Mechanisms of Hydroxyapatite Precipitation. *Acta Biomater.* 2020, *102*, 468−480.

(43) Lu, H. H.; Pollack, S. R.; Ducheyne, P. 45S5 Bioactive glass surface charge variations and the formation of a surface calcium phosphate layer in a solution containing fibronectin. *J. Biomed. Mater. Res.* 2001, *54*, 454−461.

(44) Lu, H. H.; Pollack, S. R.; Ducheyne, P. Temporal zeta potential variations of 45S5 bioactive glass immersed in an electrolyte solution. *J. Biomed. Mater. Res.* 1999, *51*, 80−87.

(45) Doostmohammadi, A.; Monshi, A.; Salehi, R.; Fathi, M. H.; Karbasi, S.; Pieles, U.; Daniels, A. U. Preparation, Chemistry and Physical Properties of Bone-Derived Hydroxyapatite Particles Having a Negative Zeta Potential. *Mater. Chem. Phys.* 2012, *132*, 446−452.

(46) Brown, R. F.; Rahaman, M. N.; Dwilewicz, A. B.; Huang, W.; Day, D. E.; Li, Y.; Bal, B. S. Effect of Borate Glass Composition on Its Conversion to Hydroxyapatite and on the Proliferation of MC3T3-E1 Cells. *J. Biomed. Mater. Res., Part A* 2009, *88*, 392−400.

(47) Fu, Q.; Rahaman, M. N.; Fu, H.; Liu, X. Silicate, Borosilicate, and Borate Bioactive Glass Scaffolds with Controllable Degradation Rate for Bone Tissue Engineering Applications. I. Preparation and in Vitro Degradation. *J. Biomed. Mater. Res., Part A* 2010, *95*, 164−171.

(48) Huang, W.; Day, D. E.; Kittiratanapiboon, K.; Rahaman, M. N. Kinetics and Mechanisms of the Conversion of Silicate (45S5), Borate, and Borosilicate Glasses to Hydroxyapatite in Dilute Phosphate Solutions. *J. Mater. Sci.: Mater. Med.* 2006, *17*, 583−596.

(49) Varila, L.; Fagerlund, S.; Lehtonen, T.; Tuominen, J.; Hupa, L. Surface Reactions of Bioactive Glasses in Buffered Solutions. *J. Eur. Ceram. Soc.* 2012, *32*, 2757−2763.

(50) Massera, J.; Hupa, L. Influence of SrO Substitution for CaO on the Properties of Bioactive Glass S53P4. *J. Mater. Sci.: Mater. Med.* 2014, *25*, 657−668.

(51) Tainio, J. M.; Salazar, D. A. A.; Nommeots-Nomm, A.; Roiland, C.; Bureau, B.; Neuville, D. R.; Brauer, D. S.; Massera, J. Structure and in Vitro Dissolution of Mg and Sr Containing Borosilicate Bioactive Glasses for Bone Tissue Engineering. *J. Non-Cryst. Solids* 2020, *533*, No. 119893.

(52) Balasubramanian, P.; Büttner, T.; Miguez Pacheco, V.; Boccaccini, A. R. Boron-Containing Bioactive Glasses in Bone and Soft Tissue Engineering. *J. Eur. Ceram. Soc.* 2018, *38*, 855−869.

(53) Schuhladen, K.; Wang, X.; Hupa, L.; Boccaccini, A. R. Dissolution of Borate and Borosilicate Bioactive Glasses and the Influence of Ion (Zn, Cu) Doping in Different Solutions. *J. Non-Cryst. Solids* 2018, *502*, 22−34.

(54) Bormashenko, E. Breath-Figure Self-Assembly, a Versatile Method of Manufacturing Membranes and Porous Structures: Physical, Chemical and Technological Aspects. *Membranes* 2017, *7*, No. 45.

(55) Meroni, D.; Lo Presti, L.; Di Liberto, G.; Ceotto, M.; Acres, R. G.; Prince, K. C.; Bellani, R.; Soliveri, G.; Ardizzone, S. A Close Look at the Structure of the TiO2 -APTES Interface in Hybrid Nanomaterials and Its Degradation Pathway: An Experimental and Theoretical Study. *J. Phys. Chem. C* 2017, *121*, 430−440.

(56) Lai, Y.; Zeng, Y.; Tang, X.; Zhang, H.; Han, J.; Su, H. Structural Investigation of Calcium Borosilicate Glasses with Varying Si/Ca Ratios by Infrared and Raman Spectroscopy. *RSC Adv.* 2016, *6*, 93722−93728.

(57) Zhou, S.; Zheng, X.; Yu, X.; Wang, J.; Weng, J.; Li, X.; Feng, B.; Yin, M. Hydrogen Bonding Interaction of Poly(d,l-Lactide)/ Hydroxyapatite Nanocomposites. *Chem. Mater.* 2007, *19*, 247−253.

(58) Brink, M.; Turunen, T.; Happonen, R.-P.; Yli-Urpo, A. Compositional dependence of bioactivity of glasses in the system Na2O-K2O-MgO-CaO-B2O3-P2O5-SiO2. *J. Biomed. Mater. Res.* 1997, *37*, 114−121.

(59) Yu, Y.; Stevensson, B.; Edén, M. Medium-Range Structural Organization of Phosphorus-Bearing Borosilicate Glasses Revealed by Advanced Solid-State NMR Experiments and MD Simulations: Consequences of B/Si Substitutions. *J. Phys. Chem. B* 2017, *121*, 9737−9752.

(60) Mishra, A.; Rocherullé, J.; Massera, J. Ag-Doped Phosphate Bioactive Glasses: Thermal, Structural and in-Vitro Dissolution Properties. *Biomed. Glasses* 2016, *2*, 38−48.

(61) Hench, L. L.; Andersson, O. Bioactive glasses: An Introduction to bioceramics. *Adv. Ser. Ceram.* 2011, 41−62.

(62) Bohner, M.; Lemaitre, J. Can Bioactivity Be Tested in Vitro with SBF Solution? *Biomaterials* 2009, *30*, 2175−2179.

(63) Hench, L. L. Chronology of Bioactive Glass Development and Clinical Applications. *New J. Glass Ceram.* 2013, *3*, 67−73.

RESEARCH ARTICLE

Journal
American Ceramic Society

Evaluation of the sterilization effect on biphasic scaffold based on bioactive glass and polymer honeycomb membrane

Audrey Deraine Coquen[1,2] | Bartosz Bondzior[3,4] | Laeticia Petit[2] |
Minna Kellomäki[2] | Emmanuel Pauthe[1] | Michel Boissière[1] | Jonathan Massera[2]

[1]ERRMECe, Equipe de Recherche sur les Relations Matrice Extracellulaire-Cellules (EA1391), Université de Cergy-Pontoise, Maison Internationale de la Recherche (MIR), rue Descartes, Neuville sur Oise Cedex, France

[2]Laboratory of Biomaterials and Tissue Engineering, Faculty of Medicine and Health Technology, Tampere University, Tampere, Finland

[3]Photonics Laboratory, Tampere University, Tampere, Finland

[4]Institute of Low Temperature and Structure Research PAS, Wrocław, Poland

Correspondence
Audrey Deraine Coquen and Jonathan Massera, Bioceramics, Bioglasses and Biocomposites Group, Faculty of Medicine and Health Technology, Tampere University, Korkeakoulunkatu 3, Tampere SM424 33720, Finland.
Email: audrey.deraine@tuni.fi and jonathan.massera@tuni.fi

Abstract
The sterilization is a core preoccupation when it comes to implantable biomaterials. The most common in industry is the gamma sterilization; however, the radiation used in this method can induce modifications in the material properties. This study investigates the impact of such radiations on the physicochemical properties and biological toxicity of a new biomaterial based on a poly-L-co-D,L-lactide polymer honeycomb membrane and bioactive glass (BG), combined, to form an assembly (membrane/BG assembly). The investigated BGs are the S53P4, which is FDA approved and clinically used, and 13-93B20, a BG containing boron promising for bone regeneration. Infrared and photoluminescence measurements revealed that, upon irradiation, defects are created in the BGs molecular matrix. Defects were identified to be mainly non-bridging oxygen hole center and occur in higher proportion in the 13-93B20 making it more sensitive to irradiation compared to the S53P4. However, the irradiation does not significantly impact the structure of the BGs. On the membrane side, the molecular weight is divided by two resulting in a lower shear stress resistance. However, the membrane honeycomb topography does not seem to be impacted by the irradiation. In contact with cells, no toxicity effect was observed, and BGs keep their bioactive properties by releasing ions beneficial to the cell fate and with no influence on apatite precipitation speed. Overall, this study showed that, despite some impact on the physicochemical properties, the irradiation does not induce deleterious effect on the membrane/BG assemblies and is therefore a suitable method for the sterilization of this novel biomaterial.

KEYWORDS
13-93B20, bioactive glass, gamma irradiation, honeycomb membrane, PLDLA, S53P4

1 | INTRODUCTION

In the 1970s, Larry Hench developed the first bioactive glass (BG). Due to its unique composition, it is able to release ions that stimulate the cells present in the bone to produce new bone and bond to it while degrading.[1] Following this discovery, the S53P4 was developed and is now commercialized as BonAlive (BonAlive Biomaterials Ltd.).[2] Since then, multiple BG compositions have been investigated with the goal to improve the angiogenic properties of BG. Houaoui et al.[3] demonstrated that BG 13-93B20, containing boron, is a highly promising BG for bone regeneration, whereas boron, substituted for SiO_2 in the silicate matrix, was found to be efficient in over-expressing angiogenic markers.[4] Recently, we reported on this BG in combination with a honeycomb membrane with the goal to produce a new biphasic material allowing bone regeneration while protecting the bone defect from invasion by fibrotic tissue demonstrating the promising use of this material as an implant.[5]

When it comes to biomaterials intended for implantation, sterilization is a central preoccupation as there are high risks of infection if the implants are not properly sterilized. Indeed, sterilization allows to eliminate microorganisms found on the implantable materials, therefore preventing the infection risk for the patient. The selection of the sterilization technique must be done with great care and must take into account the feasibility but also the fact that it can affect the materials properties and modify its performances.[6]

Some well-known sterilization methods comprise ethylene oxide, steam, dry heat, and radiation methods.[7] Particularly, gamma sterilization has several advantages. Indeed, sterilization through gamma rays is low cost, is performed at room temperature, fast, has a high penetration in materials, and is associated with a low risk of producing toxic residues.[8,9] Those advantages make gamma irradiation one of the most common sterilization methods, notably in the biomedical industry.[10,11] The regulation recommends the use of a dose of gamma rays that will allow to have a sterility assurance level of 10^{-6} meaning that the probability of finding a viable microorganism on an implantable device should be equal or lower than 10^{-6} to ensure that the material is sterile.[12] The usual recommended dose for medical devices to achieve sterility is 25 kGy.[6,11,13] Yet, Gamma irradiation is known to affect polymers, and particularly biodegradable polymers such as poly-L-co-D,L-lactide (PLDLA) as well as glasses.

When considering the glass, used in this study as a bioactive, osteopromotive substrate, the radiation damages can lead to a displacement of atom(s) in the BG network upon photon/atom collision and/or may induce ionization producing electron-hole pairs.[14] However, the material response to the radiation is complex. The material composition and structure as well as the nature and the dose of the radiation play an important role in the response of the material to radiation treatment.[15] Although large amount of data is available for glasses used in the immobilization of nuclear waste, such studies are not widely performed on compositions like BG. Thus, when investigating a new biomaterial, it is of outmost importance to investigate the effect of the gamma-irradiation on its physicochemical properties and its cytotoxicity when in contact with cells.

As our developed biphasic materials also possess a polymeric membrane, one should keep in mind that not only the radiation may affect the inorganic substrate but also the polymer and the interfacial bonds between the polymer and the BG. The polymeric membrane, deposited on the BG, as shown in Ref. [5], is made of PLDLA. However, it is generally accepted that high dose of gamma radiation leads to a decrease in the average molecular weight (Mw) of the PLDLA through chain scission.[16] Studies have shown that such effect typically occurs at dose greater than 25 kGy. However, already at 25 kGy, simulations have shown that the Mw of PLDLA 96/4 was decreased by almost 50%.[16] In the case of our biphasic material, it is therefore crucial to assess the change in average Mw as well as to ensure that the interface between the BG and the membrane remains stable postirradiation.

In this context, the impact of gamma radiation on the BG structure was investigated using Fourier transform infrared (FTIR), photoluminescence (PL), and UV–vis spectroscopy. The impact of radiation on the polymer membrane was assessed by size exclusion chromatography (SEC) to valuate changes in the average Mw, and scanning electron microscopy images were recorded to ensure that the honeycomb structure was maintained postirradiation. The interface stability, between the BG and the membrane, was assessed by shear stress testing. Finally, cells were cultured at the surface of the radiated biphasic material and their behavior compared to cells cultured on biphasic materials that were not exposed to radiation. This study shine light on the impact of gamma radiation, regularly used for biomaterials sterilization, on the physicochemical properties of biphasic materials as well as on the interfacial interaction between the polymer membrane and the BG substrate.

TABLE 1 Composition of the bioactive glasses (BGs) in mol%.

BG	mol%						
	Na_2O	CaO	P_2O_5	SiO_2	K_2O	MgO	B_2O_3
S53P4	22.66	21.77	1.72	53.85	–	–	–
13-93B20	6.0	22.1	1.7	43.7	7.9	7.7	10.9

2 | MATERIALS AND METHODS

2.1 | Material preparation

S53P4 and 13-93B20 BGs were prepared from analytical grade K_2CO_3 (Alfa Aesar, Thermo Fisher), Na_2CO_3, $NH_4H_2PO_4$, $(CaHPO_4)(2(H_2O))$, $CaCO_3$, MgO, H_3BO_3 (Sigma Aldrich), and Belgian quartz sand. The nominal oxide compositions (in mol%) of the experimental BGs are presented in Table 1.

The 60 g batch of S53P4's raw reagents were placed in the furnace preheated at 600°C and then temperature increased to 1200°C and kept for 1 h and then melted at 1450°C for 3 h. The 60 g batch of 13-93B20's raw reagents were placed in the furnace at RT and heated to 800°C. The temperature was kept for 15 min to decompose the raw materials and then melted at 1450°C for 1 h. Both glasses were melted in a platinum crucible in an electrical furnace, in air. The molten BGs were then casted into a preheated (400°C) graphite mold to obtain a rod with diameter 14 mm. The BGs rods were then annealed overnight at 40°C below the respective glass transition temperature of the BGs overnight and let to cool down to room temperature. After annealing, the rods were cut into 2 mm thick discs and polished with SiC paper (grit 320, 500, 800, 1200, 2400, and 4000, from Struers). All samples were kept in a desiccator until further use.

Prior to the membrane deposition, the polished BGs were immersed in TRIS buffer solution and incubated at 37°C for 24 h. TRIS solution was prepared from Trisma base and Trisma HCl (Sigma Aldrich) at pH 7.40 ± 0.02 at 37 ± 0.2°C. After incubation, the solution was removed, and BGs were allowed to dry under a fume hood over night before membrane deposition. This method is referred to as the conditioning. Conditioning has been shown to improve the membrane/BG interaction.[5]

Honeycomb membranes were fabricated from a solution of PLDLA with an M/M% ratio of 96/04 and surfactant dioleoyl phosphatidylethanolamine (DOPE) at 10 and 0.1 mg/mL respectively, in chloroform. PLDLA purified, medical grade, PURASORB PLD 9620 (inherent viscosity midpoint of 2.0 dL/g), was purchased from Corbion Purac and DOPE from Sigma Aldrich. The honeycomb membranes were produced by the breath figure method as described in Figure S1 and as previously reported in Ref. [17]. Briefly, the polymer solution was deposited drop by drop onto BG materials (untreated and conditioned), and then the solvent was allowed to evaporate in a humidity chamber at 80% ± 5% RH, under airflow. The membranes were air dried at room temperature and then washed two times with 70% ethanol in order to remove the surfactant. Samples were air-dried again and stored in a desiccator until further use.

Finally, before irradiation, the membrane/BG assemblies were disinfected in two successive EtOH 70% baths and stored in homemade individual plastic pockets and then irradiated at room temperature using a ^{60}Co gamma cell (2000 Ci) as source of gamma radiation having a dose rate under 28 kGy. The gamma irradiation was performed by IONISOS.

2.2 | Characterization

Before measuring the infrared (IR) spectra of the BGs, the membrane was removed by polishing, and they were crushed by hand in a mortar to obtain a powder. The IR spectra were recorded using a Spectrum Two FTIR spectrophotometer Perkin Elmer (PerkinElmer) in attenuated total reflectance mode with a diamond crystal puck, to assess the possible changes induced by the sterilization. All IR spectra were recorded within the range of 400–4000 cm^{-1} with a resolution of 2 cm^{-1} and 64 accumulation scans. All spectra were background corrected and normalized to the band with maximum intensity and presented from 600 cm^{-1} because of the air absorption that makes the signal below 600 cm^{-1} unreliable.

PL spectra were recorded with an FLS-1000 (Edinburgh Instruments) spectrofluorometer equipped with double excitation and emission monochromators and with a 450 W xenon lamp as excitation source. Spectra were recorded from 300 to 920 nm with a slid width of 2 mm, a step of 2 nm, and an excitation wavelength of 266 nm. The measurements were performed on bulk BGs and repeated multiple times and on different days to confirm the trends discussed in Section 3.

The UV–vis absorption spectra of the BGs were measured using a spectrophotometer (UV-3600 Plus) in the 200–1800 nm range with a step of 0.5 nm.

For the SEC, the membranes were dissolved from 12 membrane/BG assemblies in 2 mL of tetrahydrofuran (THF, Fischer scientific) and filtered before measurement in order to analyze the polymer Mw before and after irradiation. A Merck Hitachi 7000 series was used to analyze the samples, equipped with two Waters Styragel columns (HR5E and HR1), an L-7200 autosampler taking 20 µL of the solution to analyze, an L-7100 pump, an L-7350 column oven set at 35°C, and an RI 5450 detector. Solutions were

eluted in THF at 1 mL/min. The Mws were calibrated using polystyrene standards high EasiVial (Agilent).

The shear stress test was performed using two aluminum plates that were clamped to a TA1 texture analyzer (Lloyd materials testing, AMETEK) equipped with a 100 N load cell as in Ref. 5 The specimen to be tested was fixed in-between the plates, by solvent-free double-sided tape (tesa ECO FIXATION). Briefly, shear force on the membrane was created by pulling the upper plate at 1 mm/min, whereas the bottom aluminum plate remained fixed. The test was performed on five-to-six samples. The illustration of the setup can be found in Ref. [18]. The surface of detachment (SOD) was measured using the freehand selection tool from Fiji software to draw the contour of the places where the membrane detached and measure the area selected. The areas obtained for each place were then summed to obtain the total area from which the membrane detached and divided by the number of samples to obtain the average SOD.

2.3 | Material-cell interaction

Prior to cell culture, the nonirradiated samples were disinfected in two successive EtOH bath during 1 and 2 min, respectively, and then allowed to dry for 10 min before use. Between the baths, the samples were allowed to dry during 5 min under the laminar hood.

The irradiated and nonirradiated samples were preimmersed in 1 mL of cell culture medium for 24 h before seeding the cells. Pre-osteoblastic MC3T3 cells (E1 subclone 4, from ATCC, ref: CRL-2593) were cultured in minimum essential medium α (αMEM) Gibco (Thermo Fisher Scientific) supplemented with 10% fetal bovine serum and 1% penicillin/streptomycin, in a humidified atmosphere of 5% CO_2 at 37°C.

Cells were seeded at a density of 20 000 cells/samples, and three samples were used. The morphology of the cells was observed after 24 h, 72 h, and 7 days of culture. At each time point, the cells were fixed with 3% (w/v) paraformaldehyde solution dissolved in PBS (Sigma Aldrich) for 15 min and then permeabilized with 0.1% (v/v) Triton X-100 (Sigma Aldrich) for 10 min. Nonspecific binding sites were blocked by incubating the assembly in PBS containing 1% bovine serum albumin (BSA, Sigma Aldrich) for 1 h. The cytoskeleton and nuclei of the cells were stained, respectively, with 1:50 FITC-labeled phalloidin (Sigma Aldrich P5282) and 1:1000 4′,6-diamidino-2-phenylindole dihydrochloride (Sigma Aldrich D9542) in PBS-BSA 0.5% for 1 h. Each incubation with antibodies was performed in the dark in a humid atmosphere. Samples were then washed in PBS-BSA 0.5%, mounted in Prolon-

gold (Invitrogen), and observed under an LSM710 confocal microscope (Carl Zeiss).

During the cell culture, at each time point (preincubation, 24 h, 72 h, and 7 days after cells seeding), 1 mL of culture medium was collected from each sample and diluted in 9 mL of deionized water to quantify the change in ion concentration over time. The preincubation time point is presented before 0 in the curves. Inductively coupled plasma (ICP)-optical emission spectroscopy analysis was conducted with an Agilent 5110 instrument (Agilent technologies) equipped with an SPS 4 autosampler, to quantify the presence of phosphorus (P), sodium (Na), calcium (Ca), silicate (Si) (for both BGs) and boron (B), potassium (K), and magnesium (Mg) (only for 13-93B20) in the medium collected during the cell culture. Wavelength values for the analysis were as follows: P, 213.618 nm; Ca, 317.933 nm; Si, 288.158 nm; B, 249.678 nm; K, 766.491 nm, and Mg, 279.800 nm. The results are presented as cumulative data $\pm$ standard deviation (SD).

3 | RESULTS AND DISCUSSION

Before discussing the impact of the gamma irradiation on various membrane/BG assembly properties (including cell-membrane/BG assembly interactions), the structural and luminescent properties of the selected BGs, S53P4 and 13-93B20, are first presented. The IR spectrum of S53P4 BG in Figure 1a exhibits multiple bands that can mainly be related to Si–O bonds. The shoulder at $\approx$660 cm^{-1} and the band at $\approx$750 cm^{-1} can be attributed to bending vibrations of the Si–O^{-} end groupings.[19–21] The main band at $\approx$915 cm^{-1} can be assigned to Si–O^{-} (non-bridging oxygen—NBO) asymmetric stretching vibrations of the [SiO$_4$] units[22,23] followed by the band at $\approx$1010 cm^{-1} which is related to Si–O–Si asymmetric stretching vibration.[22] A faint shoulder can be seen $\approx$1250 cm^{-1} and might be connected to longitudinal asymmetric stretching of Si–O–Si according to Kopani et al.[24] The band at $\approx$1465 cm^{-1} can be associated with carbonate groups presence due to an incomplete decarbonization.[19,20,25] The spectrum of 13-93B20 has similar bands compared to that of the IR spectrum of S53P4 while also having a few differences. The band between 600 and 800 cm^{-1}, with a pick at $\approx$720 cm^{-1}, can be associated with B–O–B bending vibrations.[22] The main bands in the 800–1100 cm^{-1} region can be related to a joint contribution from the previously mentioned band related to Si–O bonds and from B–O bonds in [BO$_4$] units especially at 916 and 1010 cm^{-1}.[22] The shoulders at $\approx$1225 cm^{-1} can be related to BO$_2$O^{-} triangles and at $\approx$1400 and $\approx$1470 cm^{-1} can be associated to BO$_3$ groups and carbonate groups whose signature might be covered
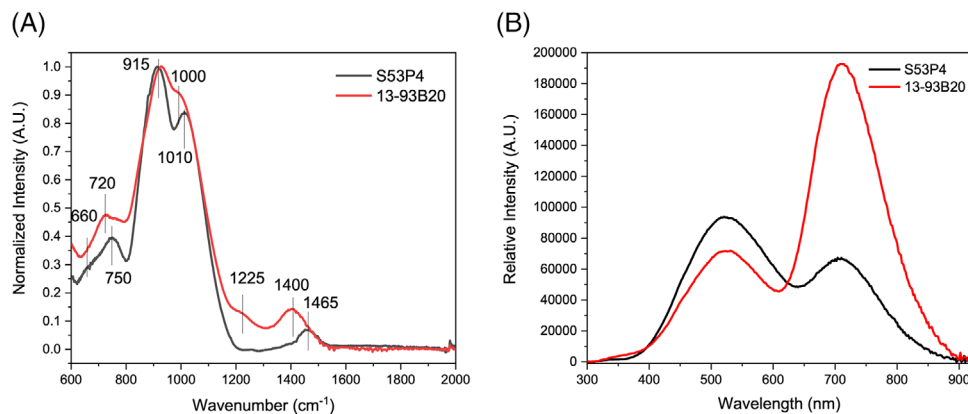
FIGURE 1 Fourier transform infrared (FTIR) (A) and photoluminescence (B) spectra of the bioactive glasses (BGs) as prepared (λ_{exc} = 266 nm).
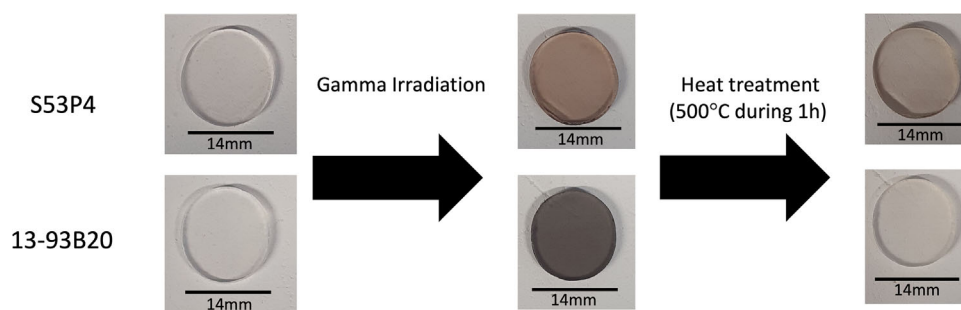
FIGURE 2 Pictures representing pictures of the bioactive glasses (BGs) before and after irradiation and after heat treatment (in that order) showing the reversibility of the color's appearances.

by the BO_3 groups signal.[19,26,27] In summary, although S53P4 spectra mainly depict the presence of SiO_4 units with bridging and NBOs, the structures of 13-93B20 present a joint contribution of the silica network, and mainly BO_3 along with BO_2^- and BO_4 units that are fully integrated within the BG structure.

The PL spectra, of the 2 investigated BGs, at 266 nm excitation are presented in Figure 1b. They exhibit two emission bands centered at 532 and 710 nm which can be assigned to oxygen deficient centers (ODCs)[28] and NBO hole center ([NBOHC], molecular structure: $\equiv$Si–O$^-$),[29,30] respectively. Although a larger amount of ODC is suspected in S53P4 than in 13-93B20, the 13-93B20 possesses a larger amount of NBOHC probably due to the presence of various borate units.[31,32]

## 3.1 | Effect of the gamma irradiation on the BG

The investigated BGs were irradiated using gamma radiations with a dose of 26–29 kGy. After irradiation, the

BGs became dark, S53P4 being less dark (Figure 2). The darker color of the BGs visible after radiation treatment is a clear sign of defect formation as demonstrated by Rautiyal et al.[14]

As in Rautiyal et al., the formation of defects is evidenced from the changes in the UV–vis absorption spectra after radiation treatment.[14] As depicted in Figure 3a,b, the absorption coefficient in the 300–1000 nm range increases after irradiation, the increase being larger in the absorption spectrum of 13-93B20 BG (Figure 3c).

The shoulder at 450–550 nm can be assigned to defects like ODC,[14,33] and the shoulder at 550–650 nm can be attributed to defects like NBOHC and/or peroxy radicals (molecular structure: $\equiv$Si–O–O$^-$).[14,33] E$^-$ centers, known to have an absorption band in the range of 600–730 nm, are also expected to form during the radiation treatment.[34] The absorption bands centered at 440 and 620 nm can be related to H_I and H_{II} defect centers, defined as trapped holes on one or two NOBs on the same SiO_4 tetrahedron,[35] respectively. Similar defects were reported in silicate glasses by El-Kheshen.[36] According to Griscom et al., ODC, peroxy linkage, and/or E$'$ centers (molecular structure: Si$^-$) with an absorption band at 300–350 nm are
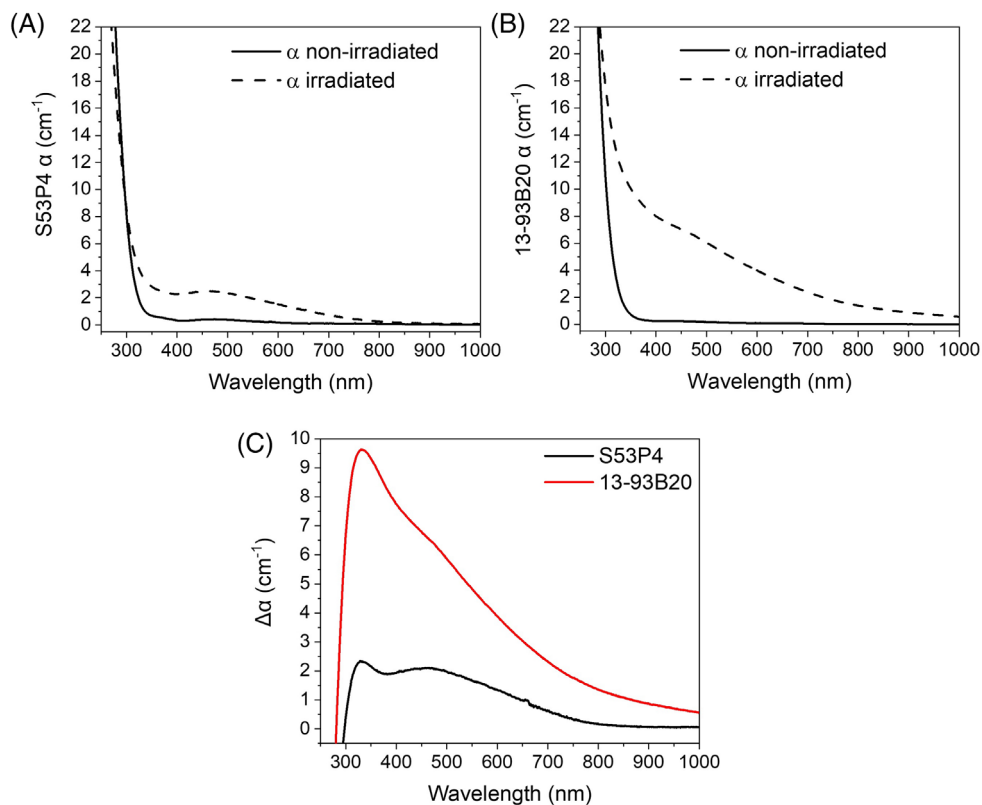
FIGURE 3 UV–vis absorption spectra represented by the absorption coefficient of S53P4 (a) and 13-93B20 (b) as prepared or after irradiation, and spectra of the difference in absorbance coefficient (α) between irradiated and nonirradiated samples (c) ($\Delta\alpha = \alpha$ [irradiated]—α [nonirradiated]).

also expected.[33] In the 13-93B20 BG, the increase in intensity of the absorption bands at 350–450 nm could be related to boron bound oxygen hole centers (BOHC, $\equiv$B–O–Si$\equiv$) according to Möncke et al.[37] BOHC's or hole trapped centers with an absorption band between 500 and 600 nm are also suspected to form.[31] As depicted in Figure 3c, a larger amount of defects are expected to be formed during the radiation treatment in the 13-93B20 indicating that this BG is more sensitive to gamma irradiation than S53P4, probably due to the presence of BO_3 and BO_4 units. Griscom et al.[38] described a core-silicate-clad-borosilicate prototype fiber that shows a higher radiation sensitivity in the cladding material compared to the core. They stated that this higher sensitivity of the borosilicate cladding material is due to the defects formed upon irradiation and particularly the "boron E′ centers." Those centers are planar BO_3 units that, upon irradiation, trap an electron and are therefore charged (−1), whereas the Si E′ centers are not charged, which make the boron E′ centers less stable than their Si counterpart. This might be what happens in our BG and can explain the higher radiation sensitivity of the 13-93B20. This is in agreement with the darker coloration of the 13-93B20 after irradiation as shown in Figure 2.

One should point out that the formation of defects has no noticeable impact on the structure of the BGs (Figure S2) although an increase in bridging oxygen (BO) at the expense of NBO was reported after radiation treatment in Refs. [39, 40]. However, the doses used in these studies were orders of magnitude higher than the dose used in our study. The radiation treatment has an impact on the spectroscopic properties but only for 13-93B20 as seen in Figure 4: The PL emission bands between 300 and 900 nm decreases after irradiating 13-93B20 revealing a decrease in the number of ODC and NBOHC in this glass in agreement with Refs. [39, 40]. 13-93B20 seems to be more sensitive to the irradiation than S53P4 most probably due the presence of BO_3, BO_2O^-, and BO_4 units and of a large amount of NBO in its network.

Nevertheless, the identification of the defects presented here requires more investigation with other methods than FTIR and PL such as Raman spectroscopy or electron paramagnetic resonance spectroscopy to provide more information and precisely determine the nature of each defect.

To assess the reversibility of the color change postirradiation, the irradiated samples were reheated at 500°C for 1 h
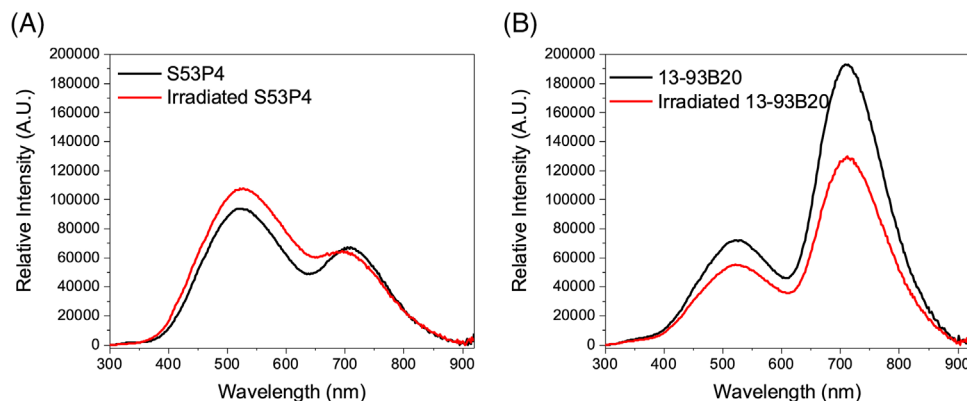
FIGURE 4 Photoluminescence spectra of S53P4 (a) and 13-93B20 (b) before (black curve) and after (red curve) irradiation.
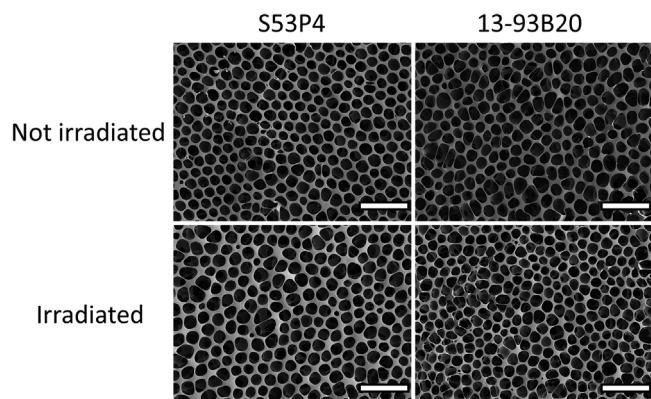

FIGURE 5 Scanning electron microscopy (SEM) images of the membranes deposited on the S53P4 and 13-93B20 substrates both before and after irradiation (scale bar 20 μm).

(Figure 2). This temperature was chosen because it is lower than the T_g of the BGs and would allow relaxation without damaging the BG structure. In Figure 2, it can be seen that all samples recovered a color similar to their original one. This suggests that reversible structural changes are occurring during the irradiation of the samples. This reversibility of the color of the BGs induced by irradiation has already been described by Procházka et al.[41] and El-Kheshen.[36]

3.2 | Effect of the gamma irradiation on the membrane/BG assembly

As shown in Figure 5, the polymer retains the honeycomb structure after irradiation. However, the Mw of the polymer decreases from ≈350.000 to ≈175.000 g/mol after irradiation, independently of the BG composition. A similar decrease in Mw of polymer was reported by Nugroho et al.[42] and Shim et al.[16] and can be related to random chain scission. Furthermore, FTIR spectra were recorded pre- and postirradiation, and no significant difference
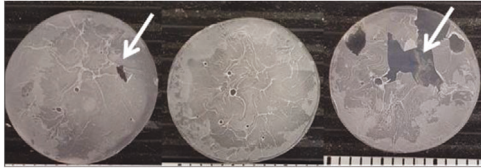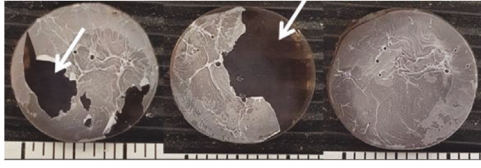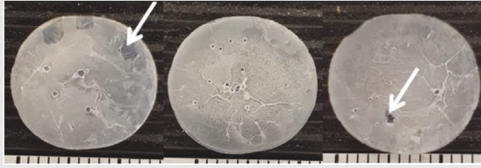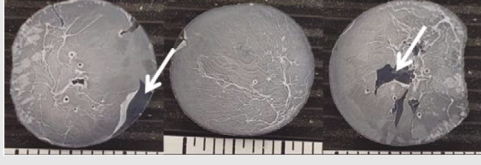
could be evidenced (data not shown). This agrees with a study by Shim et al.[16] who reported that, at gamma-rays doses ranging from 25 to 500 kGy, no significant difference in the polymer chain, and notably the polymer functional groups, before and after irradiation could be seen. In addition, Pérez Davila et al. reported a 99.8% similarity in FTIR spectra recorded pre- and postirradiation (25 kGy) of PLA 3D scaffolds.

Photographies of the membrane/BG assemblies after the shear stress test and SOD are shown in Table 2. Prior to irradiation, the SOD comprises between 2 and 10 mm^2. When comparing the SOD of the nonirradiated S53P4 and 13-93B20 membrane/BG assemblies, we can see a larger surface area detached on the S53P4 than from the 13-93B20 (9.79 vs. 2.61 mm^2), indicating that the membranes are better attached on the 13-93B20 than on the S53P4 due to the thicker apatite layer and its structure at the surface of the BG as explained in Ref. [5]. One should point out the attachment inhomogeneity of the membrane based on the photographies and the large SD for the shear stress load. After irradiation, the SOD increases while using a lower load indicating a lower attachment of the membrane to the BG. Therefore, it is plausible to think that the radiation treatment leads to a decrease of the membrane attachment points and therefore the membrane resistance to shear stress.

3.3 | Effect of the gamma irradiation on the membrane/BG assembly-cell interaction

MC3T3-E1 osteogenic progenitor cells were seeded on top of nonirradiated and gamma irradiated membrane/BG assembly. In order to estimate, and to discriminate, the potential and resulting effects of the irradiation onto the cell behavior, as controls, nonirradiated membrane/BG assembly samples were simply disinfected prior

TABLE 2 Photographies illustrating membrane/bioactive glass (BG) assemblies before and after irradiation, after the shear stress test.

Samples			Average maximum load (N)	Average SOD (mm^2)
S53P4	Before irradiation		42.60 ± 9.45	9.79 ± 10.89
	After irradiation		33.79 ± 13.05	30.40 ± 23.85
13-93B20	Before irradiation		49.17 ± 19.66	2.61 ± 3.27
	After irradiation		36.69 ± 7.26	10.97 ± 6.64

Note: Pointed by the white arrows, membrane total surface ≈154 mm^2.

Abbreviation: SOD, surface of detachment.
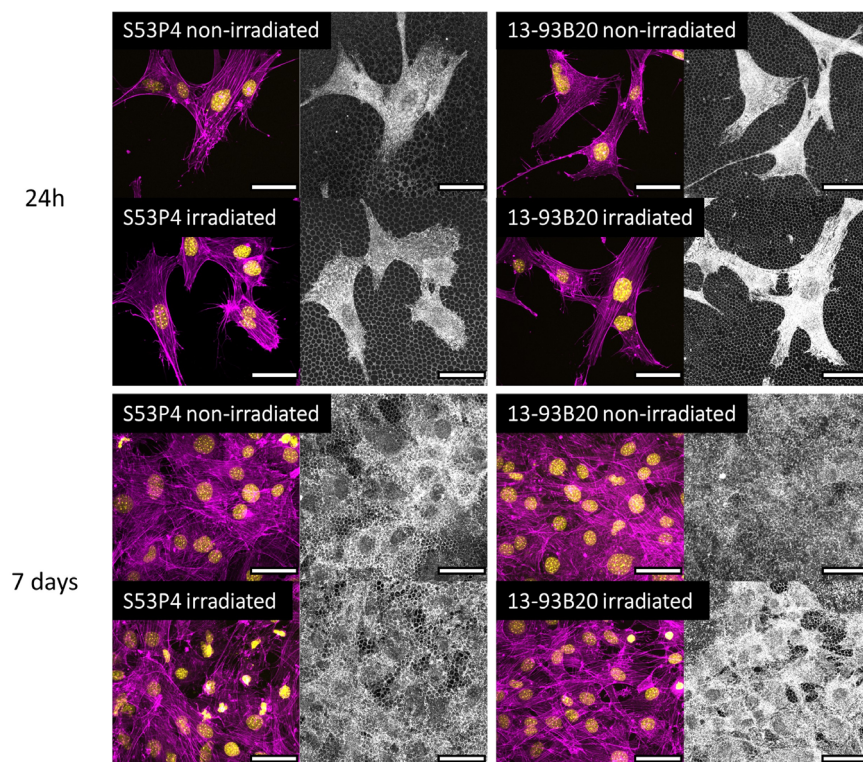
FIGURE 6 Confocal images of MC3T3 cells cultured on the membrane part of the materials nonirradiated (disinfected) or irradiated after 24 h and 7 days, scale bars 50 μm. Gray scale images show the honeycomb membrane with a shadow of the cells on it. Magenta = actin filaments, yellow = nucleus.
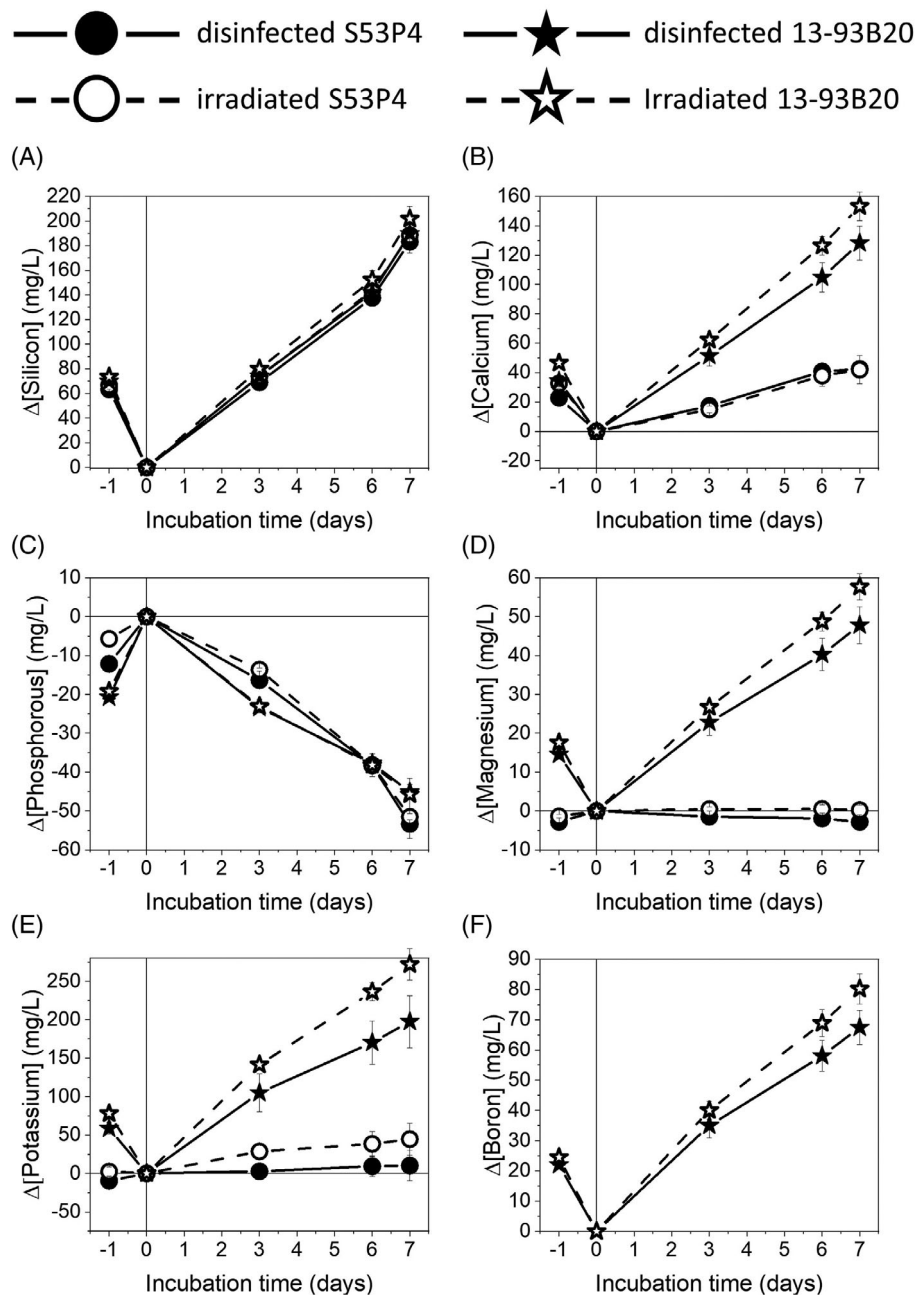
FIGURE 7 Ions release profile of silicon (a), calcium (b), phosphorous (c), magnesium (d), potassium (e), and boron (f) during cell culture up to 7 days of S53P4 nonirradiated (●) or irradiated (○) and 13-93B20 nonirradiated (★) or irradiated (☆). −1 represent the ion release during the preincubation of the materials in complete culture medium and 0 the starting point of the cell testing. Data are presented as cumulative over time.

to cell culture. Cells were cultured on the honeycomb membrane side up to 7 days and had their nucleuses and actin filaments stained and subsequently imaged through confocal microscopy to observe their morphology (Figure 6). Furthermore, the medium during the cell culture was collected and analyzed through ICP to quantify the ion release from the BGs during the experiment (Figure 7).

After 24 h, cells have adhered at the membrane surface and have spread independently of the BG composition and treatment. Actin filaments are visible and organized. Nuclei are well defined and large, showing that the cells grew at the surface of the irradiated membrane/BG assembly similarly than those on the disinfected samples. Furthermore, the honeycomb membrane, visible under the cells (gray scale images), seems to be intact,

independently of the BG composition. After 7 days, cells are confluent. Actin filament organization is well visible like nuclei. The membrane is less visible underneath the cells because of the high number of cells. These results indicate that the gamma irradiation of the membrane/BG assembly does not seem to induce deleterious or cytotoxic effect on the cells.

To confirm this finding, the medium was analyzed through ICP in order to quantify the inorganic ions released by the BGs in the medium during the experiment. The results are presented in Figure 7.

Looking at the ion release from the S53P4, for each considered ion, the release profile is similar irrespective of the treatment. This result indicates that, the defects, resulting from the gamma radiation, do not impact the dissolution rate of the S53P4 BG.

The silicon (Si) release profile of the 13-93B20 is similar to the release profile of S53P4, and no significant variation is observed between the nonirradiated and the irradiated samples. Considering the boron (B) release, we can observe a significant increase in its release when the BG is irradiated. The same pattern can be observed regarding the release profile of calcium (Ca), magnesium (Mg), and potassium (K). As said above, irradiation creates defects in the BGs, and the 13-93B20, due to the presence of borate units like BO_3 and BO_4, is more sensitive to the radiations meaning that more defects are created in this BG. This phenomenon makes the 13-93B20 slightly more soluble when irradiated resulting in a higher release in the medium of Ca, Mg, and K.

Considering the phosphorous (P) concentration, the decrease observed indicates that there is a precipitation of apatite occurring regardless of the BG.[3,20] It is worth noting that, contrary to P, Ca concentration does not decrease. This suggests that Ca ions saturate the solution, whereas P can easily be consumed to form apatite structure at the surface of the membrane/BGs assemblies. Furthermore, there is no significant difference between the irradiated and the nonirradiated samples, making clear that the irradiation does not influence the precipitation speed.

Those results, in combination with the observation from the cell culture, confirm that, even though the irradiation induces the creation of defects in the BG molecular matrix that leads to some modifications in the ion release and the Mws of the polymer membrane that decreases these modifications do not seem harming for the cells. Nevertheless, such observations are not sufficient to ensure that the membrane/BGs assemblies do not have a cytotoxic effect on the cells. Further experiments such as MTT and LDH assays are planned for a future study in order to further analyze the effect of the membrane/BG assemblies and the sterilization on the cells.

4 | CONCLUSION

In this study, the effect of gamma irradiation on scaffolds based on a honeycomb membrane and BG S53P4 and 13-93B20 was investigated.

The gamma irradiation induced the formation of defects such as NBOs and ODCs in the BG molecular matrix. Those defects appear mainly in the silicate and borate network of the BGs. However, it was demonstrated that this effect is reversible upon heat treatment. Furthermore, although the irradiation does not affect the honeycomb membrane topography, it does shorten the polymer chains length by chain scission. The polymer undergoes chain scission, and the membrane has a lower resistance to shear stress compared to the nonirradiated samples. In addition, the irradiation induces modifications in the ion release profile of the BG but does not impact the apatite precipitation speed and does not induce deleterious effect on cells cultured in contact with the membrane/BG assemblies.

Overall, despite the physicochemical modifications of the membrane/BG assemblies, those changes are negligible on the properties of the assemblies. Indeed, the membrane/BG assembly still possesses the features we intended: a honeycomb membrane, strongly attached to its substrate and a BG that maintains its bioactivity without toxic effect on the cells.

ORCID
Bartosz Bondzior https://orcid.org/0000-0002-1764-2427

REFERENCES
1. Jones JR. Bioactive glass as synthetic bone grafts and scaffolds for tissue engineering. In: Jones JR, Clare AG, editors. Bioglasses [Internet]. Chichester, UK: John Wiley & Sons, Ltd; 2012 [cited 2020 Feb 21]. p. 177–201. Available from: http://doi.wiley.com/10.1002/9781118346457.ch12
2. Hulsen DJ, van Gestel NA, Geurts JAP, Arts JJ. S53P4 bioactive glass. In: Management of periprosthetic joint infections (PJIs) [Internet]. Elsevier; 2017 [cited 2019 May 28]. p. 69–80. Available from: https://linkinghub.elsevier.com/retrieve/pii/B9780081002056000045

3. Houaoui A, Lyyra I, Agniel R, Pauthe E, Massera J, Boissière M. Dissolution, bioactivity and osteogenic properties of composites based on polymer and silicate or borosilicate bioactive glass. Mater Sci Eng C. 2020;107:110340.

4. Ojansivu M, Mishra A, Vanhatupa S, Juntunen M, Larionova A, Massera J, et al. The effect of S53P4-based borosilicate glasses and glass dissolution products on the osteogenic commitment of human adipose stem cells. PLoS One. 2018;13(8): e0202740.

5. Deraine A, Rebelo Calejo MT, Agniel R, Kellomäki M, Pauthe E, Boissière M, et al. Polymer-based honeycomb films on bioactive glass: toward a biphasic material for bone tissue engineering applications. ACS Appl Mater Interfaces. 2021;13(25):29984–95. Available from: acsami.1c03759

6. Hasirci V, Hasirci N. Sterilization of biomaterials. In: Fundamentals of biomaterials [Internet]. New York, NY: Springer New York; 2018 [cited 2022 Nov 9]. p. 187–98. Available from: http://link.springer.com/10.1007/978-1-4939-8856-3_13

7. Tipnis NP, Burgess DJ. Sterilization of implantable polymer-based medical devices: a review. Int J Pharm. 2018;544(2):455–60.

8. Dai Z, Ronholm J, Tian Y, Sethi B, Cao X. Sterilization techniques for biodegradable scaffolds in tissue engineering applications. J Tissue Eng. 2016;7:2041731416648810.

9. Jain S, Yassin MA, Fuoco T, Mohamed-Ahmed S, Vindenes H, Mustafa K, et al. Understanding of how the properties of medical grade lactide based copolymer scaffolds influence adipose tissue regeneration: sterilization and a systematic in vitro assessment. Mater Sci Eng C. 2021;124:112020.

10. Jablonská E, Horkavcová D, Rohanová D, Brauer DS. A review of in vitro cell culture testing methods for bioactive glasses and other biomaterials for hard tissue regeneration. J Mater Chem B. 2020;8(48):10941–53.

11. Pérez Davila S, González Rodríguez L, Chiussi S, Serra J, González P. How to sterilize polylactic acid based medical devices? Polymers. 2021;13(13):2115.

12. Venugopal B, Chandran S, Ajit A. ISO 11137: an overview on radiation for sterilization of medical devices and healthcare products. In: Timiri Shanmugam PS, Thangaraju P, Palani N, Sampath T, editors. Medical device guidelines and regulations handbook [Internet]. Cham: Springer International Publishing; 2022 [cited 2023 Jan 24]. p. 121–43. Available from: https://link.springer.com/10.1007/978-3-030-91855-2_8

13. Simmons A. Future trends for the sterilisation of biomaterials and medical devices. In: Sterilisation of biomaterials and medical devices [Internet]. Elsevier; 2012 [cited 2023 Jan 24]. p. 310–20. Available from: https://linkinghub.elsevier.com/retrieve/pii/B9781845699321500118

14. Rautiyal P, Gupta G, Edge R, Leay L, Daubney A, Patel MK, et al. Gamma irradiation-induced defects in borosilicate glasses for high-level radioactive waste immobilisation. J Nucl Mater. 2021;544:152702.

15. Jiang N, Silcox J. Electron irradiation induced phase decomposition in alkaline earth multi-component oxide glass. J Appl Phys. 2002;92(5):2310–16.

16. Shim HE, Yeon YH, Lim DH, Nam YR, Park JH, Lee NH, et al. Preliminary study on the simulation of a radiation damage analysis of biodegradable polymers. Materials. 2021;14(22):6777.

17. Calejo MT, Ilmarinen T, Skottman H, Kellomäki M. Breath figures in tissue engineering and drug delivery: state-of-the-art and future perspectives. Acta Biomater. 2018;66:44–66.

18. Lin MR, Ritter JE, Rosenfeld L, Lardner TJ. Measuring the interfacial shear strength of thin polymer coatings on glass. J Mater Res. 1990;5(5):1110–17.

19. Ferraris S, Nommeots-Nomm A, Spriano S, Vernè E, Massera J. Surface reactivity and silanization ability of borosilicate and Mg-Sr-based bioactive glasses. Appl Surf Sci. 2019;475:43–55.

20. Massera J, Hupa L. Influence of SrO substitution for CaO on the properties of bioactive glass S53P4. J Mater Sci: Mater Med. 2014;25(3):657–68.

21. Ouis M, Abdelghany A, Elbatal H. Corrosion mechanism and bioactivity of borate glasses analogue to Hench's bioglass. PAC. 2012;6(3):141–49.

22. Prasad SS, Datta S, Adarsh T, Diwan P, Annapurna K, Kundu B, et al. Effect of boron oxide addition on structural, thermal, in vitro bioactivity and antibacterial properties of bioactive glasses in the base S53P4 composition. J Non-Cryst Solids. 2018;498:204–15.

23. Massera J, Hupa L, Hupa M. Influence of the partial substitution of CaO with MgO on the thermal properties and in vitro reactivity of the bioactive glass S53P4. J Non-Cryst Solids. 2012;358(18–19):2701–7.

24. Kopani M, Jergel M, Kobayashi H, Takahashi M, Brunner R, Mikula M, et al. On determination of properties of ultrathin and very thin silicon oxide layers by FTIR and X-ray reflectivity. MRS Online Proc Libr. 2008;1066:10660703.

25. Koutsopoulos S. Synthesis and characterization of hydroxyapatite crystals: a review study on the analytical methods. J Biomed Mater Res. 2002;62(4):600–612.

26. Kamitsos EI, Patsis AP, Karakassides MA, Chryssikos GD. Infrared reflectance spectra of lithium borate glasses. J Non-Cryst Solids. 1990;126(1–2):52–67.

27. Tainio JM, Salazar DAA, Nommeots-Nomm A, Roiland C, Bureau B, Neuville DR, et al. Structure and in vitro dissolution of Mg and Sr containing borosilicate bioactive glasses for bone tissue engineering. J Non-Cryst Solids. 2020;533:119893.

28. Fournier J, Néauport J, Grua P, Jubera V, Fargin E, Talaga D, et al. Luminescence study of defects in silica glasses under near-UV excitation. Phys Procedia. 2010;8:39–43.

29. Nishikawa H, Shiroyama T, Nakamura R, Ohki Y, Nagasawa K, Hama Y. Photoluminescence from defect centers in high-purity silica glasses observed under 7.9-eV excitation. Phys Rev B. 1992;45(2):586–91.

30. Munekuni S, Yamanaka T, Shimogaichi Y, Tohmon R, Ohki Y, Nagasawa K, et al. Various types of nonbridging oxygen hole center in high-purity silica glass. J Appl Phys. 1990;68(3):1212–17.

31. Fayad AM, Abd-Allah WM, Moustafa FA. Effect of gamma irradiation on structural and optical investigations of borosilicate glass doped yttrium oxide. Silicon. 2018;10(3):799–809.

32. Schuhladen K, Wang X, Hupa L, Boccaccini AR. Dissolution of borate and borosilicate bioactive glasses and the influence of ion (Zn, Cu) doping in different solutions. J Non-Cryst Solids. 2018;502:22–34.

33. Griscom DL. Optical properties and structure of defects in silica glass. J Ceram Soc Jpn. 1991;99(1154):923–42.

34. Mackey JH, Smith HL, Halperin A. Optical studies in x-irradiated high purity sodium silicate glasses. J Phys Chem Solids. 1966;27(11–12):1759–72.

35. Griscom DL. E.S.R. studies of radiation damage and structure in oxide glasses not containing transition group ions: a contemporary overview with illustrations from the alkali borate system. J Non-Cryst Solids. 1974;13(2):251–85.

36. El-Kheshen AA. Glass as radiation sensor. In: Current topics in ionizing radiation research. Vol. 26. London: IntechOpen; 2012. p. 579–602.

37. Möncke D, Ehrt D. Irradiation induced defects in glasses resulting in the photoionization of polyvalent dopants. Opt Mater. 2004;25(4):425–37.

38. Griscom DL, Sigel GH, Ginther RJ. Defect centers in a pure-silica-core borosilicate-clad optical fiber: ESR studies. J Appl Phys. 1976;47(3):960–67.

39. Mao J, Yang K, Chen X, Zhu S, Zhang G, Yang F, et al. Structural changes on the surfaces of borosilicate glasses induced by gamma-ray irradiation. J Am Ceram Soc. 2022;105(8):5178–89.

40. Ollier N, Boizot B, Reynard B, Ghaleb D, Petite G. Analysis of molecular oxygen formation in irradiated glasses: a Raman depth profile study. J Nucl Mater. 2005;340(2–3):209–13.

41. Procházka R, Ettler V, Goliáš V, Klementová M, Mihaljevič M, Šebek O, et al. A comparison of natural and experimental long-term corrosion of uranium-colored glass. J Non-Cryst Solids. 2009;355(43–44):2134–42.

42. Nugroho P, Mitomo H, Yoshii F, Kume T. Degradation of poly(l-lactic acid) by γ-irradiation. Polym Degrad Stab. 2001;7(2):337–43

SUPPORTING INFORMATION

Additional supporting information can be found online in the Supporting Information section at the end of this article.

How to cite this article: Coquen AD, Bondzior B, Petit L, Kellomäki M, Pauthe E, Boissière M, et al. Evaluation of the sterilization effect on biphasic scaffold based on bioactive glass and polymer honeycomb membrane. J Am Ceram Soc. 2023;1–12. https://doi.org/10.1111/jace.19406